FACULTY OF SCIENCES

Development of the oscillation analysis framework for the SoLid experiment

Author
Ianthe Michiels

Promotors
Prof. Dr. Dirk Ryckbosch
Prof. Dr. Didar Dobur

Jury
Prof. Dr. Philippe Smet (Universiteit Gent)
Prof. Dr. Natalie Jachowicz (Universiteit Gent)
Prof. Dr. Matthieu Boone (Universiteit Gent)
Prof. Dr. Nick van Remortel (Universiteit Antwerpen)
Prof. Dr. Mathieu Bongrand (Université de Nantes)

GHENT UNIVERSITY

SoLiD

Introduction

Ever since its origin, mankind has developed a natural curiosity that drives us to wanting to understand how the world around us works, from the tiniest particles to the largest galaxy clusters. The field of research that is dedicated to the understanding of the laws of nature, on every possible scale, is physics. On the smallest scale, the field of Elementary Particle Physics examines particles that are, as far as we know, not divisible into smaller pieces. These particles are therefore called *elementary* and are assumed to be the building blocks of all matter.

In this thesis, we will consider one type of these elementary particles, that is probably the most enigmatic of them all: the neutrino.

As will be described in chapter 1, neutrinos showed the first evidence of physics beyond the Standard Model of Particle Physics. This was due to the non-zero neutrino masses, that were needed to explain the observed oscillations between the three different neutrino flavours. Although the 3-flavour oscillation theory nicely explained the results from solar and atmospheric neutrino experiments, tensions with this model were found at the end of the 20th century. One of these is the so-called *reactor antineutrino anomaly* (RAA), that refers to a number of short-baseline reactor experiments which measured an antineutrino rate that deviated from the predicted rate at the 98.6% C.L.. One possible explanation for the RAA is that of an eV-scale sterile neutrino, that would cause oscillations at a few meter distance from the source. Recently, a new generation of neutrino experiments arose that will evaluate the anomaly and sterile neutrino hypothesis at reactor-detector baselines of about 10 m.

In chapter 2, we will introduce the SoLid experiment, that is one of the new very-short-baseline experiments. The experiment uses a novel technique to detect reactor antineutrinos via inverse beta decay (IBD) interactions. The

construction of the first full scale SoLid detector started in December 2016 and took place at Ghent University. In December 2017, the detector was installed at the BR2 research reactor site of the SCK•CEN in Mol, Belgium, where it took data until June 2020. A first part of the work for this thesis existed in the organisation of these detector construction and installation efforts.

In chapter 3 we will look at all inputs that are required for the simulation of the processes taking place in a nuclear reactor. For the SoLid experiment, the necessary outputs of this simulation are the resulting antineutrino flux and energy spectrum as a function of time. This reactor information is linked to the SoLid detector simulation to generate a predicted set of IBD events in the SoLid detector volume.

Then, in chapter 4, all steps that are needed for a simulation of the detector response will be discussed. These encompass the simulations of the particle transport and interactions in the detector materials, the response of the readout electronics to light pulses, as well as the signal reconstruction of the recorded waveforms. In the scope of this thesis, a mathematical object that encapsulates the full detector response, called the *migration matrix*, was developed and implemented.
The detector simulations allow a full prediction of the rate and signatures of the inverse beta decays in the SoLid detector. This prediction is needed for the development of selection criteria for the discrimination of the IBD signal from background events, as described in chapter 5. The IBD event selection codes and the currently achievable detection efficiencies and signal-to-background ratios will be discussed as well.

In chapter 6, the final step of the SoLid analysis will be treated. This step exists of the comparison of the signal excess from data to the predicted excess from simulation, in order to reject or confirm the sterile neutrino oscillation hypothesis. The main work of this thesis existed in the development of the framework that is used to perform this so-called *oscillation analysis*. The different statistical tests that were implemented for this analysis will therefore be discussed in detail, using illustrations based on a simulated SoLid dataset.

A precise knowledge of the uncertainties on the model and the data is of crucial importance for a correct interpretation of the outcome of their comparison. The methods to determine the statistical and systematic uncertainties are described in chapter 7.

Finally, chapter 8 will show a first oscillation analysis result, based on a small sample of the SoLid Phase I dataset. The production of this result

serves as an important validation of the work performed for this thesis, as it combines all different elements of the SoLid analysis chain. The final steps that are necessary for the completion of the analysis of the full Phase I dataset will be listed too, for future reference.

This thesis will conclude with a small outlook on Phase II of the SoLid experiment, that is presented in chapter 9.

Contents

Neutrinos: from standard to sterile

1

Since the discovery of the neutrino, back in 1956, the world of particle physics has drastically changed. A vast number of theories and experiments first paved the way towards the Standard Model of particle physics. In the following years, the Standard Model was proven not only to describe very accurately the zoo of particles and their behaviour, but even to *predict* some of these. Later, however, other experimental results also created some tensions in the neutrino sector of the model and thus demonstrated the need for extensions of this renowned framework. This chapter starts with an introduction to the Standard Model and the elementary particles and forces it describes. It continues discussing the history of the neutrino and further on explains in which ways this elusive particle does and does not fit in the standard framework.

1.1 The Standard Model

The Standard Model (SM) of elementary particle physics is a theory that bundles all known elementary particles and defines how these interact with each other. This model grew from a combination of known fundamental physics, new experimental observations and the need for simplification and unification. More specifically, it originated from the attempt to unify the electroweak theory, which itself is a unification of the mathematics describing electromagnetism and the weak force, and the theory of quantum chromodynamics (QCD), which describes the strong nuclear force. The framework was cast in its final form in the mid-1970s and thus comprises three of the four fundamental forces: the electromagnetic (EM) force, and the weak and strong nuclear forces. The fourth force, gravity, is not included in this Standard Model. The lack of a theory unifying all four forces, often solemnly referred

to as the Theory of Everything, is one of the biggest unsolved problems in theoretical physics. For the study of elementary particles, however, gravity is of so little effect that this force can be neglected in almost every particle physics experiment.

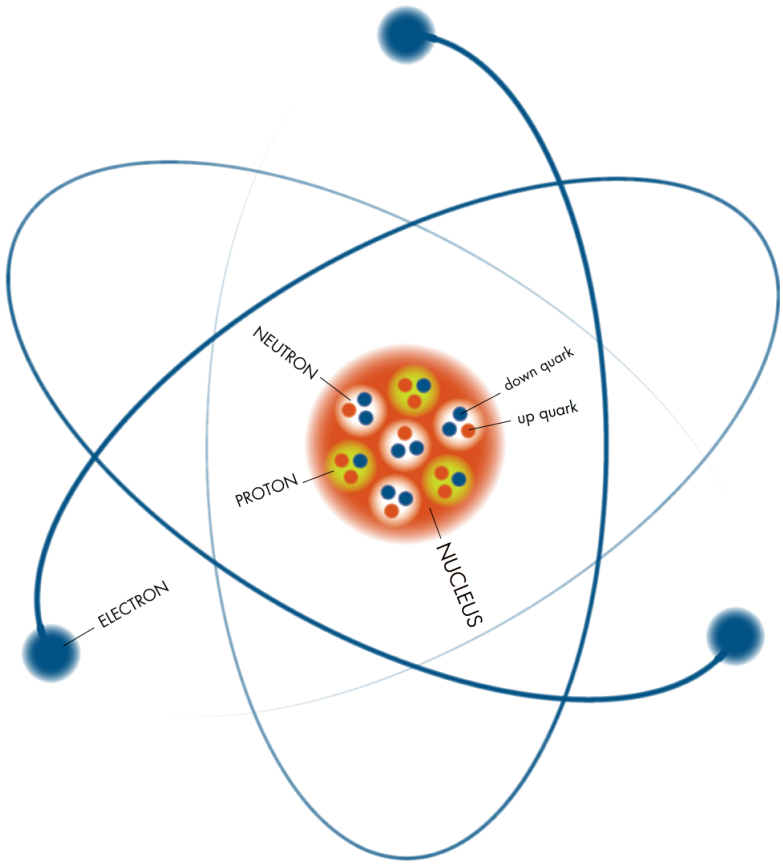

Figure 1.1: The buildup of matter. [1]

1.1.1 Particles

Let us take a step back and first have a look at the elementary *particles*. They are dubbed elementary, to stress the fact that as far as we know, they are not divisible into smaller pieces. They thus are both the building blocks of the Standard Model and of the world as we know it.
Figure 1.1 shows how ordinary matter - an atom - is built up out of a cloud of electrons and a core - or nucleus - of protons and neutrons, which in turn

exist of closely packed quarks. In this atom, the electron and the up and down quarks are *elementary* particles.
Both the electron and quarks belong to the class of *fermions*, particles with half-integer spin[1]. The class of fermions can be divided in two groups, where the up and down quarks in the atom are part of a larger group of *quarks*, and the electron is part of a second group called *leptons*. The fermions can also be classified in three generations (across lepton and quark groups), which are all identical except for the particle masses. Each generation combines an electrically charged lepton [e; μ; τ], an electrically neutral lepton [ν_e ; ν_μ ; ν_τ], called neutrino, and two quarks [(u, d); (c, s); (t, b)], as illustrated in the first three columns of figure 1.2 (top). The particles of the first generation are stable and they build up all matter, as it was described above. The higher generation particles are created in high energy processes and can have a relatively long lifetime, but most of them eventually decay to lower mass particles of the first generation.

Next to the fermions, there is a second type of particles, called (gauge) *bosons*, that have integer spin. Each of these fundamental particles is linked to a particular fundamental force, as a consequence of which they are also often referred to as force carriers. The photons (γ) carry the electromagnetic force, the W and Z^+/Z^- mediate the weak force, and the gluons (g) are the carriers of the strong force. They are illustrated in the fourth column of figure 1.2 (top). Following this principle, it can be assumed that also the gravitational force acts via a corresponding boson. This hypothetical "graviton", however, has not been found yet.
In 2012, an additional boson, that had been predicted in the 1960's by Robert Brout and François Englert [3] and independently also by Peter Higgs [4, 5], was discovered [6, 7]. This Brout-Englert-Higgs-boson is the carrier of the Higgs-field that drives the mechanism through which the elementary particles obtain their mass.

1.1.2 Particle interactions

The Standard Model does not only describe what matter is made of, it also, and maybe more importantly, tells us how the various elementary particles interact. The three forces between SM particles allow three types of interactions.

The **strong interaction** is responsible for quarks binding together to form hadrons, such as protons and neutrons. As a residual effect, it creates the nuclear force that binds the latter particles to form atomic nuclei. The **weak**

[1] "Spin" is a quantum number that refers to a particle's intrinsic angular momentum.

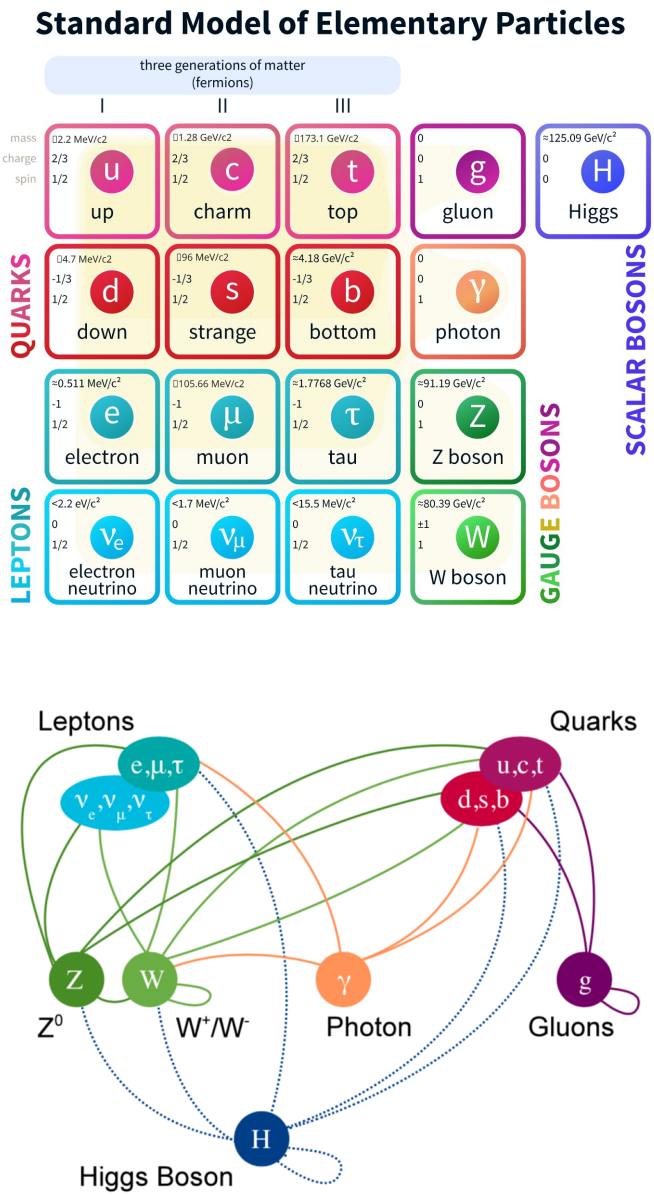

Figure 1.2: The Standard Model of particle physics (top) and the fundamental interactions between the Standard Model particles (bottom). Adapted from [2].

interaction acts on the nucleus of atoms, mediating some forms of radioactive decay. The **electromagnetic force** governs electric and magnetic fields. These fields are responsible for the attraction between orbital electrons and atomic nuclei and thus hold atoms together. On a larger scale, this also provides the chemical bonding between atoms.

As mentioned already, for each of these forces working on the level of elementary particles, there is at least one corresponding boson that mediates the particle interactions. These bosons are the quanta of the force they are related to and the elementary forces can be mathematically described by quantum fields. All elementary particles have specific properties or quantum numbers linked to these fields and those quantum numbers govern how particles behave in the related interactions:

- The electromagnetic interaction works on particles that carry an *electromagnetic charge*, Q. It is *charge* as we most commonly know it. The value Q can be positive or negative and can have different magnitudes. It is a conserved quantity.
- The weak interaction works on particles via their *weak isospin*, T. For a fermion, the weak charge depends on its *chirality*.[2] The third component of the weak isospin, T_3, is conserved by all weak, strong and electromagnetic interactions.[3]
- The strong interaction works via the *color charge*, which can take the values *blue*, *red* or *green*. The opposite "negative" charges are *antiblue*, *antired* or *antigreen*. All quarks come in any of the three colours. The leptons have no colour charge and thus they cannot interact via the strong force.

Figure 1.2 (bottom) gives a schematic overview of the possible interactions, and table 1.1 summarizes the quantum numbers of the SM fermions. Each fermion has a corresponding antifermion, i.e. a particle of the same mass, but with opposite quantum numbers.

[2]Chirality is a quantum mechanical property, related to Dirac fields. A particle's chirality can be positive (+1) or negative (-1). [8]

[3]Weak isospin and electromagnetic charge are combined in a property called *weak hypercharge*: $Y_W = 2(Q - T_3)$, in the unified framework of electroweak theory.

Table 1.1: The fermions in the Standard Model and their quantum numbers related to the three fundamental interactions.

Fermions	Generation 1	2	3	EM charge (e)	Weak isospin left-hd.	right-hd.	Colour charge
Leptons	ν_e	ν_μ	ν_τ	0	1/2	—	—
	e	μ	τ	-1		0	
Quarks	u	c	t	+2/3	1/2	0	r, g, b
	d	s	b	-1/3		0	

1.2 Standard Model neutrinos

1.2.1 Postulation of the neutrino

Table 1.1 indicates that the neutrinos can only interact via the weak force, since they have zero electric and colour charge. Because they only interact weakly, the experimental detection of neutrinos can only happen indirectly, in processes where charged particles are created. By recording the directly detectable charged particles and applying conservation laws, the properties of the neutrino, which appear as "missing" energy, momentum, spin, ... can be studied.

It was through this signature of a "missing" particle, that the neutrino was first postulated in 1930, by the Austrian-born physicist Wolfgang Pauli. He had been studying the process of beta decay, that describes the radioactive decay of an atomic nucleus (A, Z) to a lighter one $(A, Z+1)$ by the emission of an electron. This essentially boils down to the conversion of a neutron to a proton inside the nucleus:

$$n \rightarrow p + e^{-}. \tag{1.1}$$

The laws of momentum and energy conservation state that for such a two-body decay, the outgoing particles should have a fixed energy and their sum should be equal to the Q-value of the reaction, which is related to the mass difference between the original nucleus and the reaction products:

$$Q = M_N(A, Z) - M_N(A, Z+1) - m_{e^-}. \tag{1.2}$$

In radioactive decay, the proton will stay confined in the nucleus and the much lighter electron will escape, carrying nearly all available energy. Experiments, however, showed that the electron energy did not have a fixed

value Q, but instead was found to have a continuous energy spectrum, with electron energies ranging from zero to just under the Q-value (cf. figure 1.3).

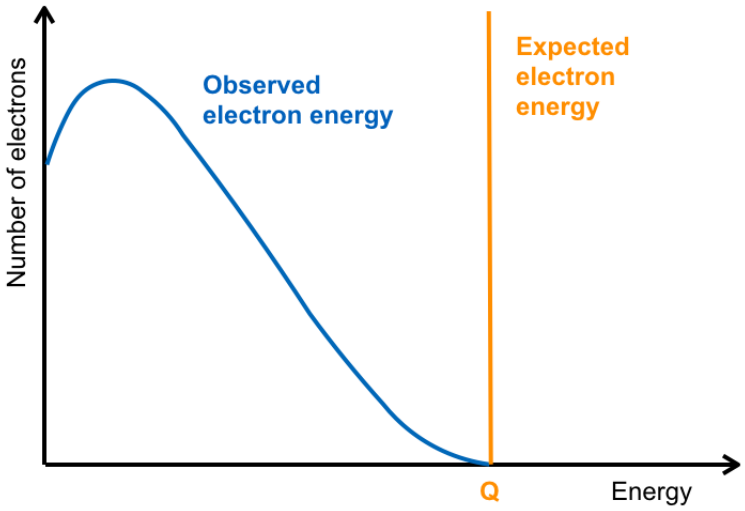

Figure 1.3: The expected and observed energy spectra for the electron in β-decay.

To explain these results, Pauli suggested that - besides the electron - a second light, but neutral particle was emitted in the reaction. The available energy would thus be distributed over these two particles, leading to a continuous energy spectrum as seen in the experiments. The neutral particle had to be very light, since the maximal detected electron energy did not deviate much from the Q-value calculated from equation 1.2. At that time there were no known particles that could fit these requirements and Pauli stated that a new particle had to be involved. However, it was not Pauli, but the Italian physicist Enrico Fermi who created a first fully comprehensive theory of beta decay and it was Edoardo Amaldi who jokingly baptised the new particle *neutrino*.

1.2.2 Discovery of the neutrino

After Fermi had developed a mature theory of weak interactions in 1934, it took another two decades until neutrinos were experimentally observed.

The weak interaction theory predicted that antineutrinos would be able to interact with protons and undergo a reaction called inverse beta decay (IBD):

$$\overline{\nu}_e + p \rightarrow e^+ + n. \tag{1.3}$$

However, soon after Fermi had published his theory, Bethe and Peierls made a first estimation of the cross section (σ) of this process and they found that $\sigma < 10^{-44}\text{cm}^2$ [9]. To be able to detect such a feeble reaction, the combination of a highly intense source of neutrinos and a very large amount of detector material would thus be needed.

It was only after the Second World War, when scientists had discovered nuclear fission, that neutrino detection came in reach. The physicists Clyde Cowan and Frederick Reines, who had been working at the famous Los Alamos site, believed that an atomic bomb explosion was the best antineutrino source for a first attempt to detect these, up to then, elusive particles. They would detect the IBD process by letting the antineutrinos from the explosion interact with protons of a liquid organic scintillator volume. This scintillator would also serve as detection medium of the charged positron, emitting light when the positron would deposit its energy and annihilate. The plans for their experiment were becoming very concrete, see figure 1.4, when Cowan and Reines realized that they could improve the signal-to-background discrimination by also detecting the neutron from the IBD interaction. This significantly reduced the required flux of antineutrinos, such that a nuclear fission reactor would be a sufficiently intense source of antineutrinos for the experiment to succeed.

This new inspiration made the experiment much more feasible and the set-up was soon installed at the Savannah River reactor, where the first experimental evidence of the neutrino was recorded in 1956 [11].

A few years later, in 1962, L.M. Lederman and his co-workers were able to discover the muon neutrino [12]. They conducted an experiment to see whether neutrinos produced in reactions that involve muons differ from the neutrinos created in association with electrons and positrons. They used the brand new Alternating Gradient Synchrotron (AGS) of the Brookhaven National Laboratory to create pions and study their decay:

$$\pi^{\pm} \rightarrow \mu^{\pm} + \nu_{\mu}. \tag{1.4}$$

If the neutrinos produced in the decay were similar to the ones produced in β-decay, it should be possible to convert them into electrons. The experiment found, however, that only muons were produced by these neutrinos and therefore proved that the electron neutrino and muon neutrino are distinct particles.

The discovery of the muon neutrino gave an indication that leptons come in flavour doublets, each of which seemed to couple a charged lepton with a certain neutrino. In the development of the Standard Model in the sub-

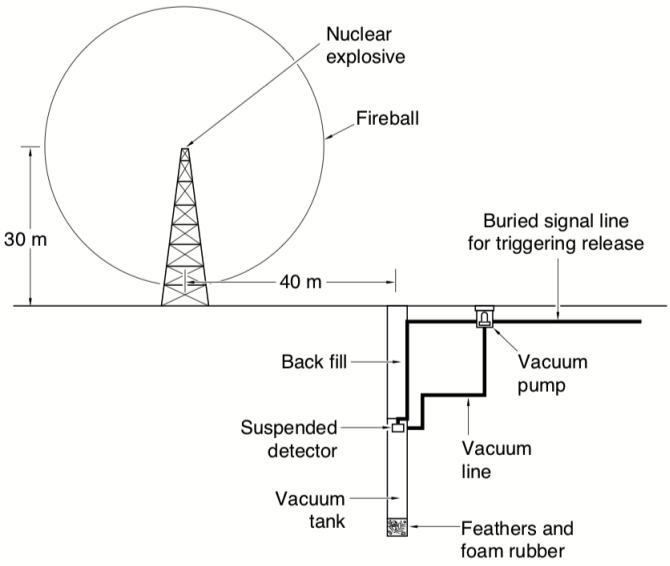

Figure 1.4: Physicists Cowan and Reines would detect antineutrinos from a nuclear bomb explosion with a liquid scintillator detector. [10]

sequent years, this doublet form was nicely incorporated and generally accepted. This meant that, when the τ-lepton was discovered at the Stanford electron-positron collider by M. Perl and his collaborators in 1977 [13], the community strongly expected the existence of a third neutrino: the ν_τ. However, it lasted another 23 years, before there was an experimental observation of this neutrino by the DONUT Collaboration at Fermilab [14]. For this experiment, the Tevatron accelerator was used as the source of tau neutrinos. The DONUT detector then recorded the neutrino interactions using a large volume of nuclear emulsion sheets that acted as a tracker for charged particles. The resulting particle tracks were analysed with image recognition techniques to select the tau neutrino candidates.

With the discovery of the third generation, all lepton flavours were now known, as it was determined by the Large Electron-Positron (LEP) collider experiments that there would be only three light neutrinos. This was done by measuring the decay of the Z-boson: the number of decay channels that is available for this boson, influences the lifetime and thus the width of the Z-resonance [15]. Every additional decay channel of the type

$$Z \rightarrow \nu_l + \overline{\nu}_l \tag{1.5}$$

makes the resonance wider by some hundreds of MeV. It can be seen from figure 1.5 that a value $N_\nu = 3$ best matches the experimental results.

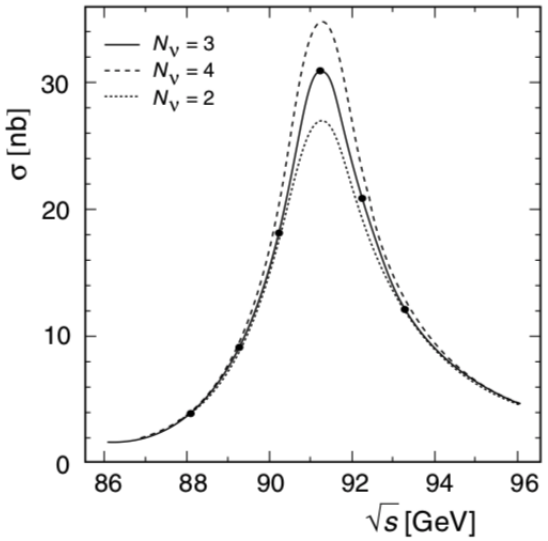

Figure 1.5: The results of the OPAL experiment, conducted at the LEP collider at CERN, show that the Z boson couples to 3 types of neutrino flavours. [16]

1.3 Neutrino oscillations

1.3.1 Solar and atmospheric neutrinos

In the late 1960s chemist Ray Davis set up an experiment to study the processes that fuel the Sun. Inspired by Hans Bethe, who had suggested these processes were driven by nuclear fusion reactions, Davis wanted to measure the resulting flux of electron neutrinos. His experimental set-up existed of a tank filled with chlorine, that was placed deep underground in the Homestake gold mine [17]. The results of this first solar neutrino experiment were compared with John Bahcall's theoretical predictions of the Standard Solar Model (SSM), which gave a description of the chain of thermonuclear reactions in the Sun [18]. The neutrino flux that Davis had detected was only 1/3 of the predicted flux, an inconsistency that was dubbed *the solar neutrino problem*. Various explanations were proposed; the problem could be related to flaws in the tedious calculations on the SSM theory or it could come from

a misunderstanding of the detector operation or efficiency. However, Davis' observations were confirmed by other solar neutrino experiments that were performed in the 1980s (KamiokaNDE II [19]) and 1990s (GALLEX [20] and SAGE [21]). The solar neutrino problem persisted and seemed to reveal unknown neutrino physics.

Moreover, studies of atmospheric neutrinos were showing a similar problem. These atmospheric neutrinos are created in two consecutive decay reactions that originate from the pion production by energetic cosmic particles - mostly protons - that interact with the Earth's atmosphere:

$$\pi^{\pm} \rightarrow \mu^{\pm} + \nu_{\mu} \tag{1.6}$$

$$\mu^{\pm} \rightarrow e^{\pm} + \nu_{e} + \nu_{\mu} \tag{1.7}$$

The decay processes imply that for every pion decay, two muon neutrinos and one electron neutrino are produced. Different experiments (Irvine-Michigan-Brookhaven [22], Kamiokande [23]) aimed to measure both muon and electron neutrino fluxes to verify the expected 2:1 ratio, but instead recorded a much lower muon versus electron neutrino rate. This deficit was referred to as the *atmospheric neutrino anomaly*.

The solar neutrino problem and atmospheric neutrino anomaly were the first experimental indications of neutrino flavour oscillations. The decisive evidence for these flavour oscillations finally came in 1998, with the results of the Super-Kamiokande experiment [24]. This experiment measured the distribution of atmospheric muon neutrinos for different zenith angles: a variable that is related to the distance travelled between the point of creation in the atmosphere and the point of detection in the water tank. The results, shown in figure 1.6, indicated that more muon neutrinos enter the detector from above than from below, what can be translated to a higher survival probability for neutrinos travelling a shorter distance.

A few years later, the Sudbury Neutrino Observation (SNO) experiment, was able to confirm that oscillations of electron neutrinos to other flavour states were the cause of the solar neutrino problem [26]. The SNO detector was built such that it was sensitive to all three types (e, μ, τ) of neutrinos interacting in the detector volume. The measured rate of electron neutrinos was still much lower than the one predicted by the solar model, but the total rate, combining all three flavour types, was nicely in line with the predicted number of neutrinos arriving from the Sun. Knowing that the fusion processes in the Sun only produce neutrinos of the electron flavour and none of the other flavours, this result clearly showed that neutrinos change flavour when travelling long distances.

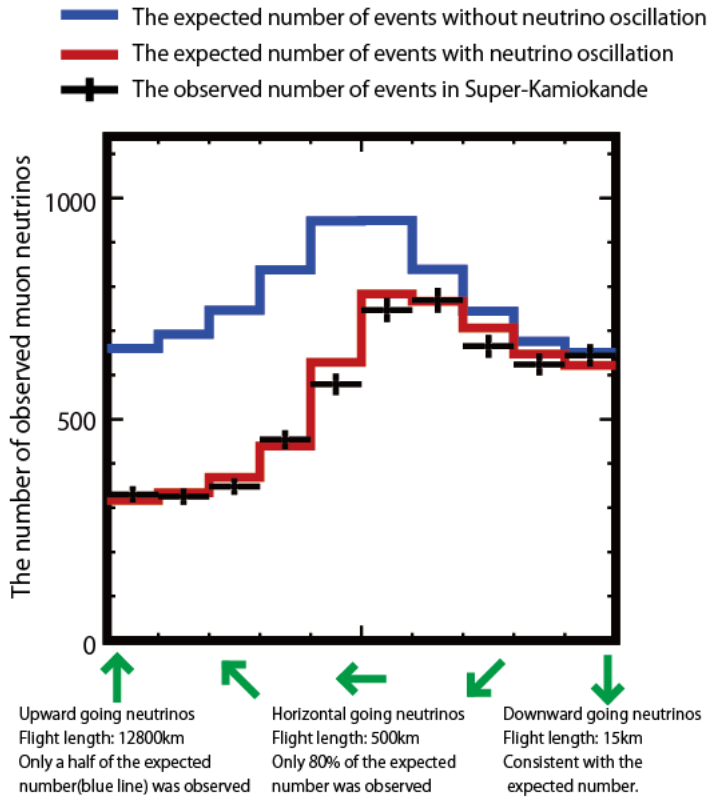

Figure 1.6: The discovery of atmospheric neutrino oscillation in Super-Kamiokande. The observed number of the muon neutrinos going up to the detector through the Earth was only half of the observed number of the muon neutrinos going down to the detector. [25]

1.3.2 Mathematical framework

Although neutrino oscillations were only experimentally confirmed at the end of the 20th century, a mathematical framework for the flavour oscillations was already developed in the 1960s. It was physicist Bruno Pontecorvo who first suggested that neutrinos might not conserve lepton number, changing flavour as they travel through space [27]. This was in 1967, a few years after the muon neutrino was discovered. The idea implies that neutrinos should be superpositions of different mass eigenstates, each state propagating with its own velocity, which results in a different superposition of mass states and thereby also a different flavour at distinct moments in time.

The full mathematical framework for the mixing of three neutrino flavours, was developed by Pontecorvo, Maki, Nakagawa and Sakata. It describes the transformation of neutrinos with a definite mass ($|\nu_i\rangle$, with i = 1, 2, 3) to neutrinos with a definite flavour ($|\nu_\alpha\rangle$, with α = e, μ, τ) via the PMNS-matrix [28]:

$$\begin{pmatrix} \nu_e \\ \nu_\mu \\ \nu_\tau \end{pmatrix} = \begin{pmatrix} U_{e1} & U_{e2} & U_{e3} \\ U_{\mu 1} & U_{\mu 2} & U_{\mu 3} \\ U_{\tau 1} & U_{\tau 2} & U_{\tau 3} \end{pmatrix} \begin{pmatrix} \nu_1 \\ \nu_2 \\ \nu_3 \end{pmatrix} \tag{1.8}$$

This matrix includes three mixing angles θ_{12}, θ_{23}, θ_{13} and a CP-violating[4] phase δ:

$$U_{PMNS} = \begin{pmatrix} c_{12}c_{13} & s_{12}c_{13} & s_{13}e^{-i\delta} \\ -s_{12}c_{23} - c_{12}s_{23}s_{13}e^{i\delta} & c_{12}c_{23} - s_{12}s_{23}s_{13}e^{i\delta} & s_{23}c_{13} \\ s_{12}s_{23} - c_{12}c_{23}s_{13}e^{i\delta} & -c_{12}s_{23} - s_{12}c_{23}s_{13}e^{i\delta} & c_{23}c_{13} \end{pmatrix} \tag{1.9}$$

where $c_{ij} = \cos\theta_{ij}$ and $s_{ij} = \sin\theta_{ij}$.

One can thus describe one specific flavour α as the superposition of three different mass eigenstates

$$|\nu_\alpha\rangle = \sum_i U_{\alpha i}|\nu_i\rangle \tag{1.10}$$

and vice versa

$$|\nu_i\rangle = \sum_\alpha U^*_{\alpha i}|\nu_\alpha\rangle. \tag{1.11}$$

We note that the PMNS-matrix is a unitary matrix and that careful tests of this unitarity, based on precision measurements, provide a powerful tool for

[4]When CP symmetry is valid, the simultaneous application of spatial reflection (P) and particle-antiparticle substitution (C) leads to a physically allowed state [8].

the evaluation of the mixing model. Any deviation from this unitarity could for example reveal the existence of new, unknown neutrino states.

Given the U_{PMNS} transformation matrix, it can be deduced that neutrino oscillations can occur, provided that the mixing angles are not zero and that at least two of the three neutrinos have non-zero mass. If all neutrinos were massless, all three mass eigenstates would propagate at the speed of light and never get out of phase. As a consequence, there would be no neutrino flavour oscillations. This is demonstrated in the following simplified derivation of the probability of flavour oscillations in vacuum, limited to the case of two neutrino flavours (ν_e, ν_μ) and two mass states (ν_1, ν_2).

Let us start by considering the creation of an electron neutrino by the weak force. This neutrino is a pure flavour state, but a linear combination of the two mass states:

$$|\nu_e\rangle = \cos\theta\,|\nu_1\rangle + \sin\theta\,|\nu_2\rangle \tag{1.12}$$

The mass eigenstates of this neutrino will propagate in time, according to the plane wave solution of the Schrödinger equation:

$$|\nu_i(t)\rangle = e^{-iE_i t/\hbar}|\nu_i(0)\rangle. \tag{1.13}$$

The flavour state of the neutrino at a time t can thus be written as:

$$|\nu_e(t)\rangle = \cos\theta\, e^{-iE_1 t/\hbar}|\nu_1(0)\rangle + \sin\theta\, e^{-iE_2 t/\hbar}|\nu_2(0)\rangle \tag{1.14}$$

The probability to find a muon neutrino after a time t is calculated as:

$$P_{\nu_e\to\nu_\mu} = |\langle\nu_\mu(t)|\nu_e(0)\rangle|^2 = \left[\sin(2\theta)\,\sin\left(\frac{E_2 - E_1}{2\hbar}t\right)\right]^2 \tag{1.15}$$

For relativistic particles with fixed momentum p and a mass $m_i << E_i$ the energy can be written as $E_i = p + m_i^2/2p$. Substituting the energy term and rewriting t to the travelled distance L/c, eq. 1.15 becomes:

$$P_{\nu_e\to\nu_\mu} = \left[\sin(2\theta)\,\sin\left(1.27\,\frac{m_2^2 - m_1^2}{E}\,L\right)\right]^2 \tag{1.16}$$

for m_i^2 expressed in $(\mathrm{eV/c^2})^2$, L in meters and E in MeV [29].
In general, the probability for a neutrino of flavour α and energy E, to be

detected as a neutrino of flavour β after travelling a distance L, is given by [30]

$$P_{\nu_\alpha \to \nu_\beta} = \sum_i |U_{\alpha i}|^2 |U_{\beta i}|^2 + 2\,\mathrm{Re} \sum_{i>j} U^*_{\alpha i} U_{\beta i} U_{\alpha j} U^*_{\beta j} \exp\left(-i \frac{\Delta m^2_{ij} L}{2E}\right). \quad (1.17)$$

The difference of the squared neutrino masses, or so-called *mass splitting* parameter, is written here as Δm^2_{ij}. This equation is valid for any number of neutrinos and proves that neutrino oscillations can only take place if the neutrino masses are different.

Various oscillation experiments have been conducted to precisely determine the values of the different mixing angles and squared mass differences for the three SM neutrinos. The current best fit values are reported in table 1.2. The mixing angle θ_{13} and mass difference Δm^2_{12} are measured to be both very small, and as a consequence the simplified model of two-flavour mixing can be applied to both solar ($\nu_e \to \nu_\mu$) and atmospheric ($\nu_\mu \to \nu_\tau$) neutrino oscillations. The two distinct mass splittings, $\Delta m^2_{21} = m^2_2 - m^2_1$ and $\Delta m^2_{32} = m^2_3 - m^2_2$, are thus well determined from experiments, but the sign of the mass differences, that tells us which neutrino is the lightest and which is the most heavy one, can not be resolved. This *mass hierarchy problem* is depicted in figure 1.7, showing the two possible options; the normal hierarchy, with $m_{1,2} < m_3$, and an inverted one, with $m_3 < m_{1,2}$.

Table 1.2: Current best fit values for three-flavour neutrino oscillations. For Δm^2_{32} and $\sin^2\theta_{23}$ the upper (lower) row corresponds to the normal (inverted) neutrino mass hierarchy [34].

Parameter	**Best fit $\pm$ 1σ**
$\Delta m^2_{21}[10^{-5}\mathrm{eV}^2]$	7.53 ± 0.18
$\Delta m^2_{32}[10^{-3}\mathrm{eV}^2]$	2.453 ± 0.034
	2.546 ± 0.040
$\sin^2\theta_{12}$	0.307 ± 0.013
$\sin^2\theta_{23}$	0.545 ± 0.021
	0.547 ± 0.021
$\sin^2\theta_{13}$	0.0218 ± 0.0007
δ	$1.36\pi \pm 0.17\pi$

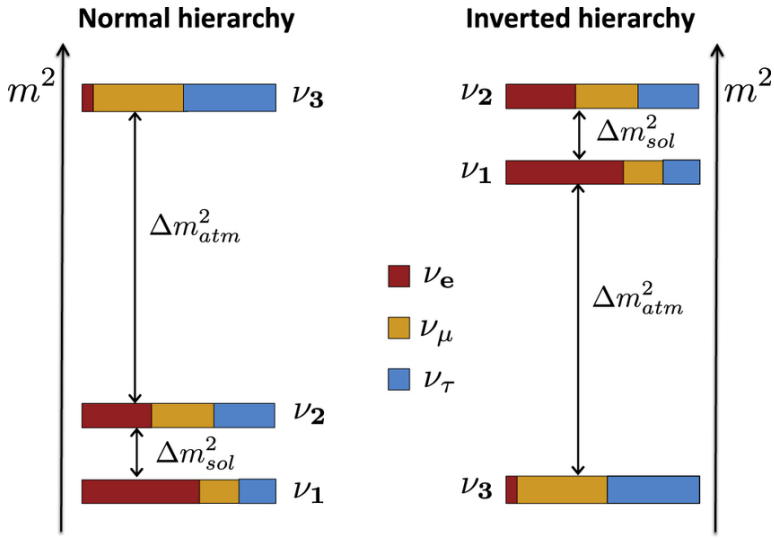

Figure 1.7: The normal (left) and inverted (right) mass hierarchy for the SM model neutrinos [31]. For both cases $m_1 < m_2$, something that is determined by the observation of neutrino oscillations in matter: the *MSW effect* [32, 33].

1.4 Neutrino anomalies

Although the framework of three-flavour neutrino oscillations has proven to be capable of explaining the results of various types of experiments, some tensions with this picture have also occurred in more recent years. The three different sectors in which those neutrino *anomalies* are observed, are discussed in the following sections.

1.4.1 Accelerator anomaly

The first experimental result that could not be explained in the framework of three-neutrino mixing was observed in 1989 by the LSND experiment [35]. This experiment studied highly energetic muon antineutrinos, produced in an accelerator facility, and found a controversial indication in favour of short-baseline $\overline{\nu}_\mu \to \overline{\nu}_e$ transitions. Given that $L/E \approx 1\,\text{eV}^{-2}$ for the LSND experiment, the measured oscillations resulted in a $\Delta m^2 \geqslant 0.1\,\text{eV}^2$; values that were far larger than those obtained from solar and atmospheric neutrino oscillations (cf. table 1.2).

However, the KARMEN experiment, that conducted a similar search at a slightly shorter baseline [36], contradicted the LSND results and their anomaly

stayed unconfirmed for some time. In 2007, the MiniBooNE Collaboration designed a new experiment to specifically match the search region of the LSND experiment. Initially, they observed a similar short-baseline oscillation for $\overline{\nu}_\mu \to \overline{\nu}_e$, but *only* for $\nu_\mu \to \nu_e$ transitions below 475 MeV [37]. Two years later, after conducting a new search, the MiniBooNE experiment unexpectedly did see an excess, consistent with the LSND result, over the entire energy range in both neutrino and antineutrino mode [38]. The combined significance of the LSND and MiniBooNE observations results in an excess of 6σ [39], and is known as the *accelerator anomaly*.

1.4.2 Gallium anomaly

Another anomaly in neutrino physics was found in the source calibration measurements of the SAGE [40] and GALLEX [41] experiments. They both made use of a gallium detector to study solar neutrinos, via the reaction:

$$^{71}\mathrm{Ga} + \nu_e \to {}^{71}\mathrm{Ge} + e^-. \tag{1.18}$$

To calibrate these gallium detectors, intense ^{51}Cr and ^{37}Ar sources were used. Both sources decay via electron capture, emitting electron neutrinos with energies below 1 MeV, and this mimics the solar neutrino signal. The radioactive sources, with well-known activities, were placed inside the detector and the produced electron neutrinos were measured. Calibration results were then obtained by comparing the measured and predicted detection rates and gave an average ratio of 0.84 ± 0.05, as shown in figure 1.8. This 2.9σ deficit of measured neutrinos is reduced to 2.3σ, when taking into account a possible overestimation of the cross section of the reaction 1.18 [42]. However, a clear deficit remains and it is known as the *gallium anomaly*.

1.4.3 Reactor anomaly

In nuclear reactor experiments, the $\overline{\nu}_e$'s coming from the reactor can be used to study oscillations by measuring the survival probability $P_{\overline{\nu}_e \to \overline{\nu}_e}$, which can be derived from the PMNS matrix and formula 1.17 [44]:

$$\begin{aligned} P_{\overline{\nu}_e \to \overline{\nu}_e} =& 1 - \cos^4(\theta_{13})\, \sin^2(2\theta_{12})\, \sin^2\left(\frac{\Delta m^2_{21} L}{4E}\right) \\ & - \sin^2(2\theta_{13})\, \sin^2\left(\frac{\Delta m^2_{32} L}{4E}\right). \end{aligned} \tag{1.19}$$

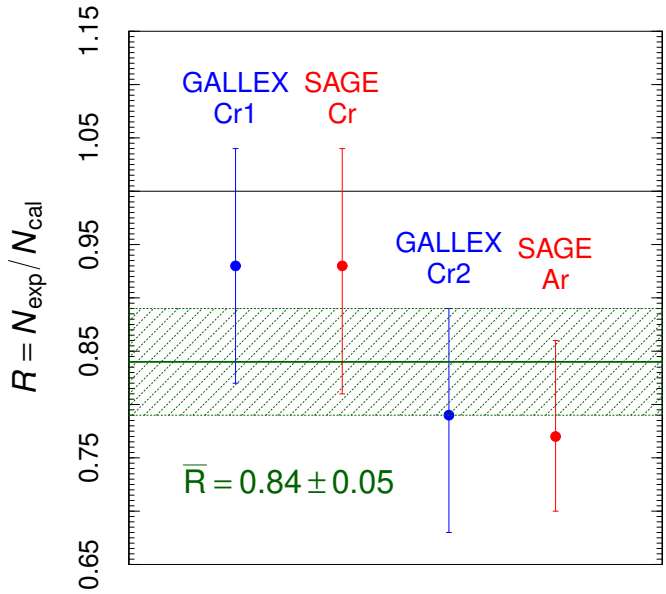

Figure 1.8: The calibration of the GALLEX and SAGE experiments resulted in an unexpectedly low average ratio R of detected-over-calculated neutrino events. The result is known as the gallium anomaly. [43]

Figure 1.9 plots the survival probability as a function of the detector distance L, together with data points of different experiments.

From the figure, we see that experiments with a baseline L of the order of 1 km are sensitive to the shorter wavelength oscillation, that is governed by Δm^2_{32}. For these distances and a neutrino energy of the order 3 MeV, the term in Δm^2_{21} becomes negligible, and formula 1.19 simplifies to

$$P_{\overline{\nu}_e \to \overline{\nu}_e} \approx 1 - \sin^2(2\theta_{13}) \sin^2\left(\frac{\Delta m^2_{32} L}{4E}\right). \tag{1.20}$$

This implies that these experiments are most sensitive to measure the θ_{13} mixing angle. Examples of such short baseline experiments are Daya Bay [45, 46], Double Chooz [47] and RENO [48, 49].

For experiments with $L \geqslant 100$ km, the rapid oscillations due to Δm^2_{32} average out:

$$\left\langle \sin^2\left(\frac{\Delta m^2_{32} L}{4E}\right) \right\rangle = \frac{1}{2} \tag{1.21}$$

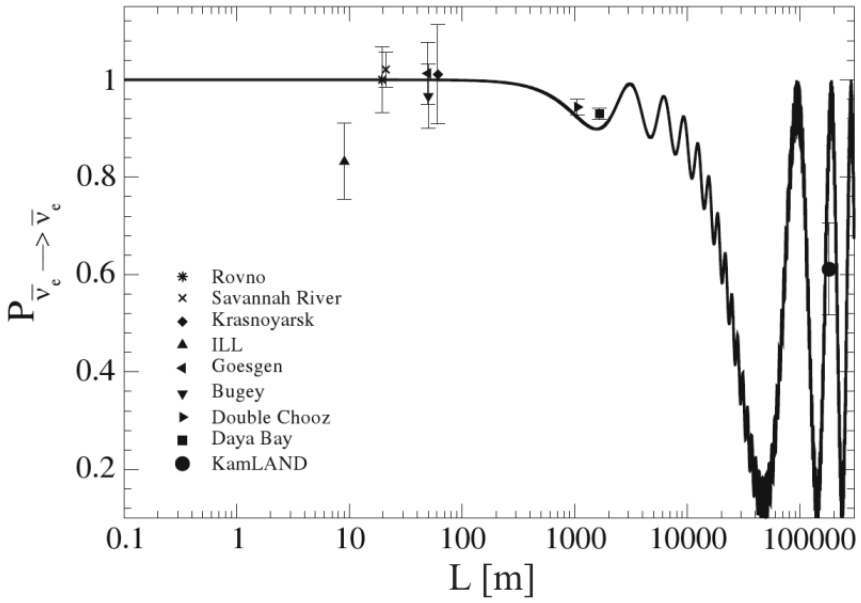

Figure 1.9: Oscillation curve for a 3 MeV reactor antineutrino in the 3-flavour neutrino model. The relative $\overline{\nu}_e$ fluxes, measured by various experiments are indicated. Adapted from [16].

and the dominant oscillation becomes the one determined by Δm^2_{21}:

$$P_{\overline{\nu}_e \to \overline{\nu}_e} \approx 1 - \frac{1}{2}\,\sin^2(2\theta_{13}) \; - \cos^4(\theta_{13})\,\sin^2(2\theta_{12})\,\sin^2\left(\frac{\Delta m^2_{21} L}{4E}\right) \tag{1.22}$$

$$\approx \cos^4(\theta_{13}) + \sin^4(\theta_{13}) \; - \cos^4(\theta_{13})\,\sin^2(2\theta_{12})\,\sin^2\left(\frac{\Delta m^2_{21} L}{4E}\right) \tag{1.23}$$

$$\approx \cos^4(\theta_{13}) \left[1 - \sin^2(2\theta_{12})\,\sin^2\left(\frac{\Delta m^2_{21} L}{4E}\right)\right], \tag{1.24}$$

where we have applied some trigonometric identities to go from eq. 1.22 to eq. 1.23 and have neglected the very small term $\sin^4(\theta_{13})$ to come to eq. 1.24.

This type of search was conducted by the long baseline experiment KamLAND, that found results consistent with the solar neutrino measurements [50].

A third type of experiments, also depicted in figure 1.9, are the ones measuring at *very* short baselines, ranging from 10 to 100 meters: Bugey [51],

Goesgen [52], ILL-Grenoble [53], Rovno [54], ... For such small source-to-detector distances, we expect $P_{\overline{\nu}_e \to \overline{\nu}_e} \approx 1$ and thus also a ratio, R, of expected-to-predicted $\overline{\nu}_e$-flux compatible with 1.

For some time, the combined data of a range of very short baseline experiments indeed resulted in a value $R = 0.980 \pm 0.024$, consistent with unity. However, in 2011, a new set of theoretical reactor antineutrino spectra were published, based on a novel calculation method.[5] This updated prediction model resulted in an increase of the predicted reactor flux by about 3%, moving the expected-to-observed $\overline{\nu}_e$ ratio down to $R = 0.927 \pm 0.023$, see figure 1.10. This 2.9σ deficit is known as the *reactor antineutrino anomaly* (RAA) [55].

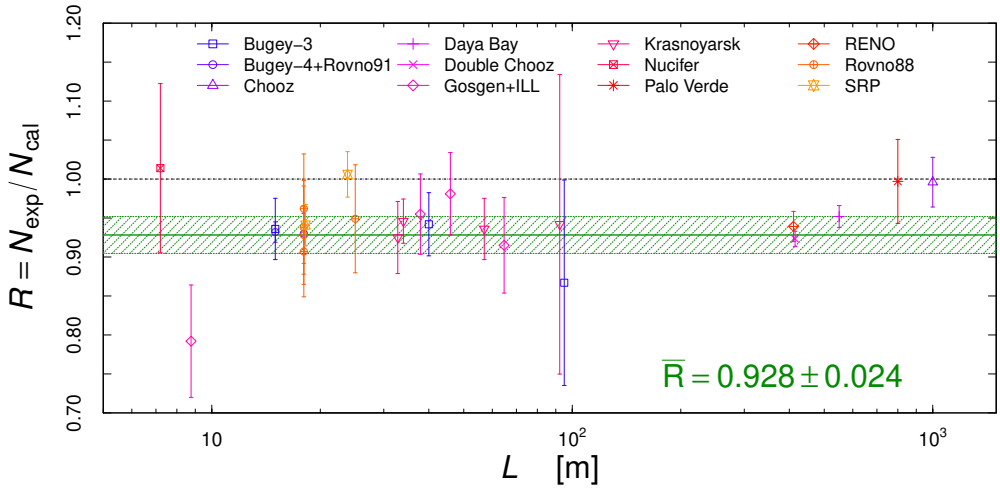

Figure 1.10: The results of multiple (very) short baseline reactor experiments, leading to the reactor antineutrino anomaly after a re-evaluation of the reactor flux calculations in 2011. [43]

1.4.4 Spectral distortion at 5 MeV

The RAA problem that is described above is a pure normalisation problem, i.e. the total number of events does not match the prediction, but the qualitative features of the measurements are within expectations. In recent years,

[5] More details on the existing calculation methods for reactor antineutrino spectra are given in chapter 3.

however, the analysis of the prompt energy spectra from reactor antineutrino data sets revealed an unexpected distortion. An excess in antineutrino events with a visible energy of roughly 5 MeV was first reported by the Double Chooz experiment [56]. The spectrum, with a 3.0σ excesss in the energy range from 4.25 to 6 MeV, is shown in figure 1.11. This *5 MeV bump* was confirmed by RENO [57], Daya Bay [58] and other experiments and thus seems to be a common feature for most nuclear reactor neutrino experiments, however with varying amplitudes. Moreover, most experiments have indicated that the size of the excess is correlated with the reactor power. As a consequence, there is a widespread expectation that the spectral distortion is created by inaccurate antineutrino flux calculations for one or more fissile isotopes. By performing measurements at a reactor over a longer period of time, taking into account the fuel evolution, or simply by measuring at different reactors, each with a different fuel composition, the influence of the fissile isotopes on the spectral distortion is being surveyed [59, 60, 61].

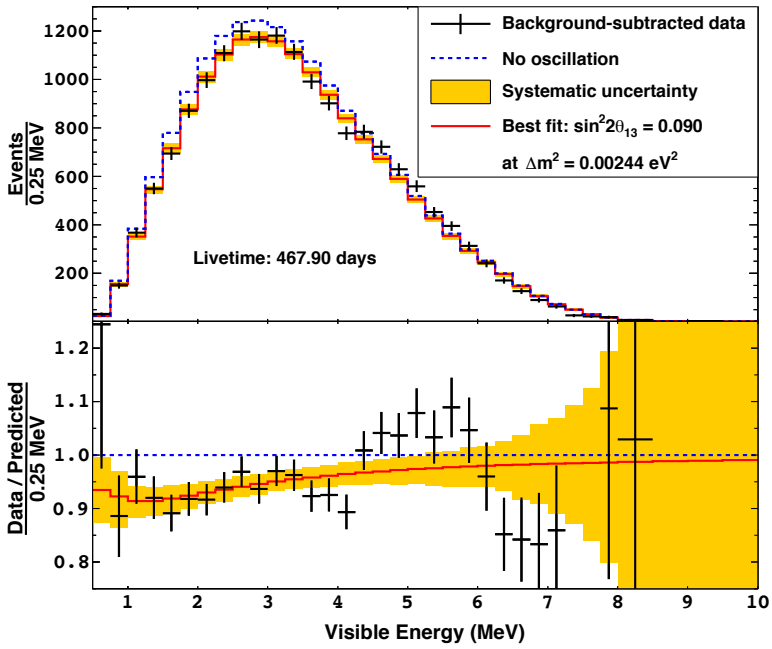

Figure 1.11: Prompt energy spectrum measured by the Double Chooz experiment (black points), compared to the no-oscillation prediction (blue dashed line) and the best fit model (red solid line) [62].

1.5 Sterile neutrino solution

As the tensions with the picture of three oscillating weak neutrinos became more profound, new theoretical concepts arose to extend the known physics and match the experimental data. One of the proposed solutions, and probably the most popular one, is that of the sterile neutrino.

1.5.1 Sterile neutrino model

Like the deficits in the solar and atmospheric neutrino flux had previously been successfully attributed to flavour oscillations, a similar solution has been proposed to solve the RAA, Gallium and accelerator anomalies. Since the three anomaly types each require oscillations over short distances (or relatively low L/E values), they can only be explained by new neutrino oscillations with a Δm^2 of a few eV^2, which is a much larger mass splitting than the ones known from the 3-neutrino model.

The hypothetical fourth neutrino would have to be a "sterile" particle. This is indicated by the LEP-results, as shown in figure 1.5, which prohibit the existence of an additional neutrino that couples to the Z boson. A new kind of neutrino therefore should not interact weakly, in contrast with the three active neutrinos that are currently known. As a result, such a neutrino does not interact via any of the SM forces and it is said to be *sterile*.

The introduction of a fourth neutrino extends the PMNS matrix from equation 1.8 with a new flavour ν_s and an additional mass eigenstate ν_4:

$$U_{\alpha i} = \begin{pmatrix} U_{e1} & U_{e2} & U_{e3} & U_{e4} \\ U_{\mu 1} & U_{\mu 2} & U_{\mu 3} & U_{\mu 4} \\ U_{\tau 1} & U_{\tau 2} & U_{\tau 3} & U_{\tau 4} \\ U_{s1} & U_{s2} & U_{s3} & U_{s4} \end{pmatrix} \tag{1.25}$$

With a required mass splitting value that is so large compared to the known mass splittings, it appears likely that the sterile neutrino will be mainly composed of the fourth mass eigenstate ν_4. The extension of the existing oscillation model with one sterile neutrino is often referred to as the 3+1-oscillation model.

1.5.2 Sterile neutrino searches

Because of the sterile property, the 3+1-hypothesis can only be tested by measuring the disappearance probability of one of the active neutrinos, for example in very short baseline nuclear reactor experiments. For those experiments the $\overline{\nu}_e$-disappearance probability, like equation 1.16, becomes

$$P_{\overline{\nu}_e \to \overline{\nu}_e} = 1 - \sin^2(2\theta_{14}) \sin^2\left(\frac{\Delta m^2_{41} L}{4E}\right). \tag{1.26}$$

The parameters $\sin^2(2\theta_{14})$ and Δm^2_{41} have been probed by various gallium and reactor experiments. In 2011, a global fit of all available data from reactor and gallium calibration experiments was published by Mention *et al.* [55]. The analysis resulted in $\Delta m^2_{41} > 1.5$ eV^2 and $\sin^2(2\theta_{14}) = 0.14 \pm 0.08$, while disfavouring the no-oscillation case at more than 3σ confidence level. Sterile neutrino searches in the ν_μ sector, however, showed strong tensions with the 3+1-model and ruled out this hypothesis as an explanation of the LSND and MiniBooNE anomalies [63].

These contradicting results triggered a new wave of experimental efforts towards the search for light sterile neutrinos. Much of this new activity is situated in the $\overline{\nu}_e$-disappearance channel, one example of which is the SoLid experiment, that is the topic of this work. The SoLid detector site and principle will be discussed in detail in the following chapter. In addition, a short description of the other very short baseline nuclear reactor experiments that are currently taking data will be given in section 2.7.

1.6 Summary

In section 1.1 of this chapter we have described how the Standard Model of particle physics encompasses all known elementary particles and the fundamental forces acting between them. The first proof for physics beyond this model was found with the discovery of neutrino oscillations, treated in section 1.3, implying that neutrinos have non-zero mass.

Although the framework of three oscillating neutrinos was able to describe the measured neutrino fluxes from various sources, such as the Sun, the atmosphere, accelerators and nuclear reactors, this picture was distorted at the end of the 20th century. Three different sectors of neutrino experiments have shown tensions with the 3-flavour model, and led to the so-called *accelerator*, *Gallium* and *reactor antineutrino anomalies*, that are discussed in section 1.4.

One proposed solution for the neutrino anomalies is that of a *sterile* neutrino, that induces additional oscillations. We have seen in section 1.5 that an oscillation driven by a mass splitting of the order of 1 eV^2 should manifest itself most clearly in a very short baseline region, below 10 m from the neutrino source.

Many new reactor neutrino experiments aim to explore $\overline{\nu}_e$-disappearance at this baseline with high precision and accuracy. When placed at a highly enriched ^{235}U core, these experiments would also be capable to give additional input on the 5 MeV spectral distortion. The SoLid experiment is one of the new projects, specifically designed to examine the reactor antineutrino anomaly at very short baselines. It is the topic of this thesis and will be discussed at length in the following chapter.

The SoLid experiment 2

SoLid, short for *Search for oscillations with a ^{6}Li detector*, is an experiment designed to investigate the sterile neutrino hypothesis, as well as to perform a precise ^{235}U $\overline{\nu}_e$-flux measurement. To be able to perform such studies, the experiment has to fulfil some specific technological requirements. This chapter describes how the reactor, detection principle and detector design are chosen and developed for the SoLid experiment, in order to enable a competitive search.

2.1 Reactor site

The SoLid experiment uses the Belgian Reactor 2 (BR2) of the *Studiecentrum voor Kernenergie*, SCK•CEN, in Mol, Belgium, as its source of antineutrinos. As one of the most powerful research reactors in the world, BR2 plays an important role in nuclear material and fuel research. It is also one of the main players in the production of medical isotopes and the irradiation of silicon for high-quality semi-conductor production [64].

BR2 is a pool-type reactor, using light water as its moderator and coolant. One of the advantages of light water reactors (LWR) is that they can have a very compact design [65], a feature that is even more pronounced for the BR2 reactor, by the twisted geometry of the channels containing its fuel rods, as illustrated in figure 2.1. The core is thereby reduced to have a diameter of $\sim$50 cm, serving as an almost point-like source of antineutrinos. This greatly reduces the smearing of the short wavelength neutrino oscillations that we study.

The reactor operates on highly enriched fuel, with an enrichment in ^{235}U of 93.5%. This corresponds to ^{235}U contributing to more than 99% of the induced fissions. Such a high purity allows for a precise measurement of the

^{235}U $\overline{\nu}_e$-flux, giving information on the origin of the 5 MeV spectral distortion.

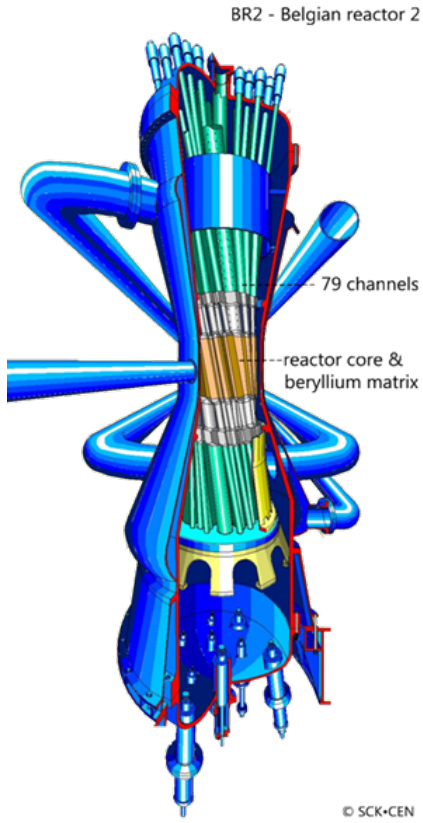

Figure 2.1: The BR2 reactor core has a unique design with inclined channels, making it very compact. [66]

The SoLid detector is located in the BR2 containment building, at the floor level that is on-axis with the core center, see figure 2.2. This figure also illustrates the reference frame used by the SoLid collaboration: facing the reactor, the x-axis points to the right side of the detector, the y-axis points upwards and the z-axis points away from the reactor, parallel to the baseline of the experiment.

Due to the compact core, the closest possible approach of the detector is less than 6 meters. Operating that close to a reactor unfortunately induces a significant amount of background, as the reactor is an intense source of neutrons and γ-rays. For the SoLid experiment, the reactor induced background radiation is reduced and stabilised, since it operates on a floor where

there are no other active experiments. This allows for all beam ports to remain closed and shielded with a thick layer of lead. Nonetheless, the fact that the experiment is located above ground makes it subject to cosmogenic backgrounds.

The BR2 reactor mostly operates at a thermal power of 50 to 60 MW, with a full possible range of 40 to 80 MW. It runs in cycles of 3 to 4 weeks, alternating with *reactor-OFF* periods of the same duration. Per year, there are a total of 6 cycles or ∼150 days of *reactor-ON* time. The reactor shut down periods are used by the SoLid experiment to precisely measure and evaluate the rates of the different background components.

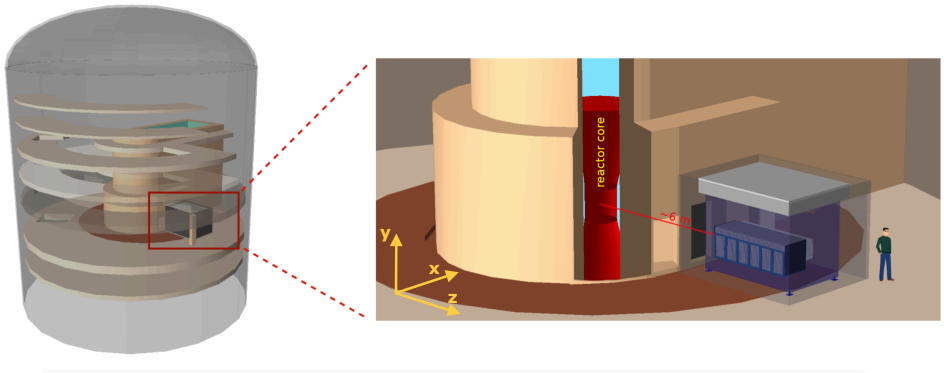

Figure 2.2: Model of the BR2 reactor building, illustrating the position of the SoLid detector (left) and the reference frame and baseline coverage of the experiment (right).

2.2 Reactor $\overline{\nu}_e$ detection

The general process to study reactor antineutrinos is the Inverse Beta Decay (IBD) reaction:

$$\overline{\nu}_e + p \rightarrow e^+ + n. \tag{2.1}$$

Here, the antineutrino interacts with a proton of the detector material and creates a positron and a neutron, resulting in a two-component signature when the detector is sensitive to both particles. This *coincidence technique* was developed and first used by Cowan and Reines, as discussed in section 1.2.2.

By considering the mass difference of the reaction products in equation 2.1, we can see that there is a threshold value for the IBD reaction:

$$E_{\overline{\nu}_e} = E_{e^+} + m_n + m_e - m_p = E_{e^+} + 1.804\,\text{MeV}, \tag{2.2}$$

where we have neglected the kinetic energy of the neutron as most of the released energy is carried away by the much lighter positron. This means that the antineutrino needs to have a kinetic energy of at least 1.804 MeV for the IBD reaction to take place.

It also follows from this calculation, that the energy deposited by the positron is a probe for the incoming antineutrino energy.

We should first note that, as the positron will promptly deposit its energy in the reaction medium, it will not take long before it annihilates with an electron, which results in two annihilation γ's of 511 keV each. In case these γ's are also seen, the relation between the deposited energy and that of the antineutrino becomes

$$E_{\text{dep, }2\gamma} = E_{e^+} + 2 \times 511\,\text{keV} = E_{\overline{\nu}_e} - 0.782\,\text{MeV}. \tag{2.3}$$

In case one or both γ's from the positron annihilation escape the detector, the energy relation becomes:

$$E_{\text{dep, }1\gamma} = E_{e^+} + 511\,\text{keV} = E_{\overline{\nu}_e} - 1.293\,\text{MeV} \tag{2.4}$$

$$\text{or} \quad E_{\text{dep, }0\gamma} = E_{e^+} = E_{\overline{\nu}_e} - 1.804\,\text{MeV}, \tag{2.5}$$

respectively.

A measure for the probability of the IBD reaction to take place is its cross section σ_{IBD}. The value of σ_{IBD} increases with antineutrino energy, but is generally of the order of $10^{-44}\,\text{cm}^2$. A more rigorous treatment of the determination of this cross section will be given in section 3.1.4.

Given the IBD threshold, the rising cross section and the falling energy spectrum of reactor antineutrinos[1], the spectrum of detected antineutrinos starts from 1.804 MeV and it reaches up to about 9 MeV, peaking around 3.5 MeV, as illustrated in figure 2.3.

[1]The precise antineutrino energy spectrum emitted by the BR2 core depends on the fuel loading and operation power. According to the methods discussed in chapter 3, the spectrum will be calculated for each reactor cycle, providing a reference for the antineutrino detection with the SoLid experiment.

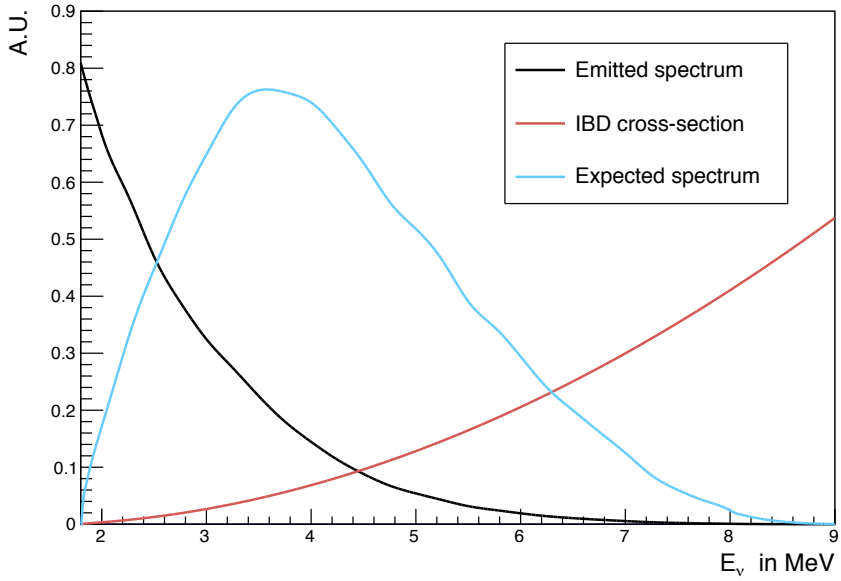

Figure 2.3: The detected $\overline{\nu}_e$-spectrum from ^{235}U fission, assuming no oscillations (blue), in arbitrary units. Its shape follows from the folding of the rising IBD cross section (red) and falling emitted antineutrino spectrum (black).

To calculate the expected number of detected antineutrinos from a point-like reactor, additional information on the detector, such as the number of target protons N_p and the energy dependent detector response R, is needed. Per energy interval $[E_i\ ;\ E_{i+1}]$ and for fission isotope k and exposure time T, we find:

$$N_k = T\frac{N_p}{4\pi L^2}\ n_f\ \int_{E_i}^{E_{i+1}} R(E_{\bar{\nu}})\ S_k(E_{\bar{\nu}})\ \sigma_{IBD}(E_{\bar{\nu}})\ dE_{\bar{\nu}}. \tag{2.6}$$

Here, L is the reactor-detector distance, n_f is the number of fissions per time unit and S_k is the emitted spectrum for isotope k. Formula 2.6 indicates that the signal prediction of reactor experiments, N_k, requires the knowledge of a lot of different parameters. The precision of this calculation is crucial, since the RAA anomaly and possible sterile neutrino oscillations under investigation are an effect of only a few percent. This subject of reactor spectra and rate predictions is treated more extensively in chapter 3.

2.3 SoLid detector concept

The SoLid detector is designed to be highly segmented and is therefore constructed out of many small detector cells. The identical cubical cells are instrumented with two types of scintillator for the antineutrino detection. One is polyvinyl toluene (PVT), a solid plastic that is machined into $(5 \times 5 \times 5)$ cm^3 blocks. The second scintillator consists of thin sheets of ^{6}LiF:ZnS(Ag) deposited on a plastic, reflective backing. Here, the ^{6}Li is used for neutron capture:

$$n + {}^6\mathrm{Li} \rightarrow {}^3\mathrm{H} + {}^4\mathrm{He} + 4.78\,\mathrm{MeV}. \tag{2.7}$$

The neutron detection sheets are cut into squares of (5×5) cm^2 and are placed on two adjacent faces of a PVT cube.

PVT is rich in protons, which makes it a very effective $\overline{\nu}_e$ target. When an IBD reaction takes places, the resulting positron almost instantly deposits all of its energy in the plastic scintillator, creating a prompt and pulsed scintillation signal. It will then annihilate and create two γ's of 511 keV, that also cause a scintillation.

The IBD neutron first thermalises, while elastically scattering through the PVT, until it gets captured in one of the inorganic scintillator sheets[2]. The triton and alpha particle that are produced in the neutron capture reaction (eq. 2.7), are energetic enough to cause excitation of the electrons in the ZnS crystal. The de-excitation of these states, in its turn, results in the neutron scintillation signal. Due to the time taken for the neutron to scatter before capture, this second scintillation signal is delayed with respect to the signal from the positron. The typical time interval between the positron and neutron signals Δt is about 60 μs. In general, the IBD neutrons do not travel a large distance in the PVT cubes before they are captured by the ^{6}Li and so the neutron signal is usually seen in the same or one of the neighbouring cubes as the positron signal. In addition, because of the finite lifetime of the ZnS excited states, which is significantly larger than the decay time of the PVT scintillator, the resulting waveforms of positron and neutron signals will have a distinct shape. Comparing the waveforms can thus help in discriminating positrons from neutrons [67]. Figure 2.4 sketches the described SoLid antineutrino detection concept.

[2]The PVT also acts as a neutron moderator. Simulations have shown that a neutron scatters through the PVT over a period of maximally hundreds of microseconds, travelling at most about 15 cm or 3 cubes from the antineutrino interaction point before they are captured in a lithium screen.

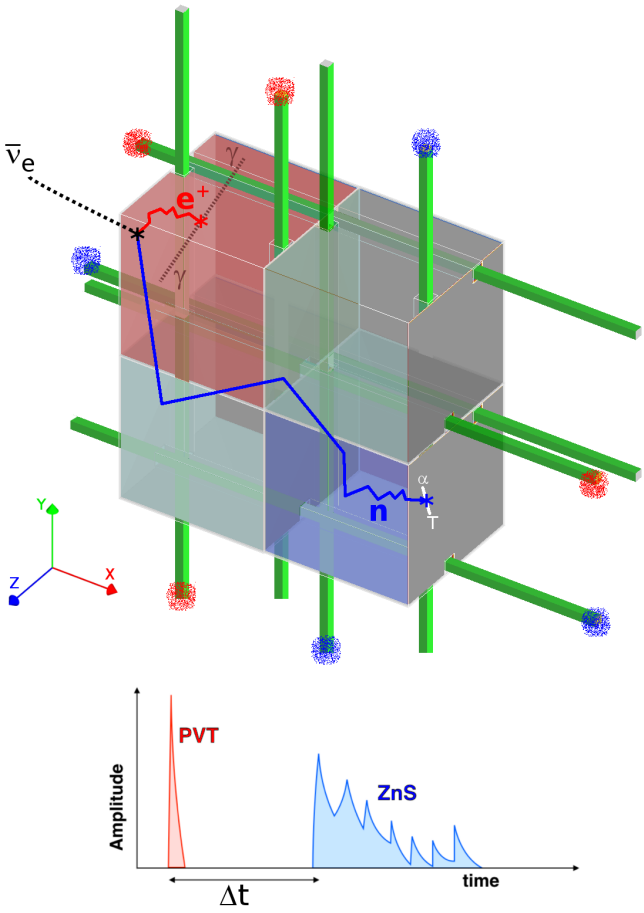

Figure 2.4: Illustration of the topology of an IBD event in the SoLid detector (top) and the corresponding scintillation signals (bottom).

To preserve the position information of the scintillation signals, each detector cell is optically isolated by a wrapping of reflective Tyvek paper. The light pulses are transported from the respective cubes to the photodetector by wavelength shifting (WLS) fibres. These fibres fit through (5×5) mm^2 grooves, that are machined in 4 different faces of each plastic scintillator cube, as illustrated in figure 2.5. The raster lay-out of the fibres enables position reconstruction, since any specific combination of two horizontal and two vertical fibres points to a unique cube. The fibres shift the wavelength of the blue PVT (ZnS(Ag)) scintillation light of 425 nm (450 nm) to green light with a wavelength of 500 nm. This longer wavelength lies in the optimal response region of the silicon photomultipliers (SiPMs) that are placed at one end of each WLS fibre and translate the photons to an electronic signal. At the other end of the fibres an aluminium mirror is placed to reflect as much light as possible towards the SiPM side. Both the mirror and SiPM are placed in a 3D-printed plastic housing to ensure a good connection with the WLS fibre, see figure 2.5.

The type of photomultiplier used for the SoLid detector is a multi-pixel photon counter (MPPC) with a surface of (3×3) mm^2, that consists of 3600 pixels. Each pixel detects photons and amplifies the signal based on the principle of charge avalanche in Geiger mode.[3] The total current coming from the MPPC is the sum of the currents from its individual pixels and is therefore proportional to the number of pixels that detected photons and triggered subsequent avalanches. The scintillation light produced in the detector and transported to the MPPCs is thus measured in units of pixel avalanches (PA). The MPPC signals are then amplified and digitised by the external readout electronics. The analogue-to-digital conversion (ADC) happens with 14 bit resolution, and a 40 MHz sampling frequency, resulting in waveform samples of 25 ns each. The amplification or *gain* is set such that one PA corresponds to ~ 32 ADC counts.

Table 2.1 gives an overview of all key components of the SoLid detector, including references to the data sheets provided by the producers.

[3] Photons of high energy create charge carriers when they hit a silicon pixel. In Geiger mode, a high enough electric potential is maintained such that the electrons produce an avalanche in which they are multiplied [68]. For MPPCs this multiplication factor is about 10^6 and the typical photon detection efficiency (PDE) is roughly 35%.

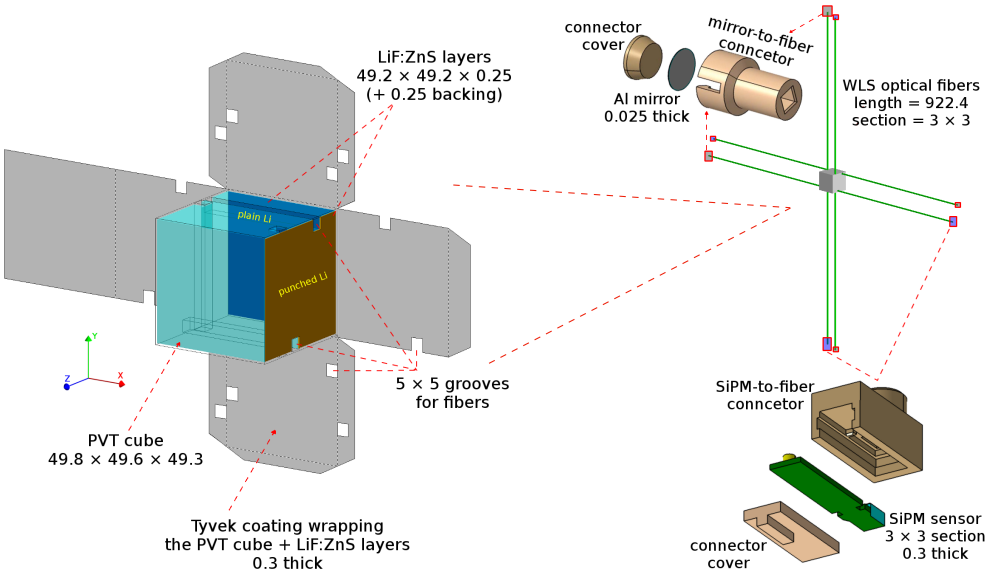

Figure 2.5: Technical illustration of the specifications of a SoLid detector cell (left) and the configuration of the readout instruments (right). All values are in mm and are summarised in table 2.1.

Table 2.1: Summary of the SoLid detector materials and their respective dimensions. For each component, the producers and product code plus a reference are added as well.

Detector material	Dimensions [mm]	Producer (product type)
PVT	$49.8 \times 49.6 \times 49.3$	ELJEN (EJ200) [69]
^{6}LiF:ZnS(Ag)	surf.: 49.2×49.2	Scintacor (ND) [70]
″	thick.: 0.225 (+ 0.225)*	″
Tyvek	thickness: 0.3	Dupont (1082D) [71]
WLS fibres	$3 \times 3 \times 922.4$	St.-Gobain (BCF-91A) [72]
SiPM	3×3	Hamamatsu (S12572-050P) [73]

*Most detector cells are equipped with lithium screens that have a plastic backing that is 0.225 mm thick. The cells on the detector edge, however, have an older version of the screens, without backing. Cf. section 2.5.

2.4 SoLid detectors

The specific layout described in the previous section is the one of the current SoLid detector, called *Phase I*. The construction of this large scale detector, the procedure of which is shortly described in section 2.5, started in december 2016. The full detector was operational since the spring of 2018 and has run continuously in data-taking mode until July 2020. Before that, the SoLid experiment successfully took data with two prototype detectors: first with NEMENIX and later with SubModule 1. Each of the different SoLid detectors is shortly described below and their main properties, or differences, are summarised in table 2.2.

2.4.1 NEMENIX

The NEMENIX detector was an 8 kg prototype constructed in 2013. It served as a proof of principle for the SoLid detection technique. NEMENIX had a basic layout of 4 by 4 by 4 stacked PVT cubes. Each cube was assembled with only one ^{6}LiF:ZnS(Ag) screen of 225 µm thick, that had no plastic backing, and was read out by only one horizontal and one vertical WLS fibre. This resulted in 32 fibres and corresponding readout channels. The cubes were also wrapped in Tyvek paper, but a thinner one than that used for Phase I.

NEMENIX was surrounded by four muon veto panels; two smaller ones, of (35×35) cm^2, on the left and right sides and two large ones, of (70×70) cm^2, on the top and bottom. The detector, along with its two small muon veto panels, was enclosed in a neutron shield made of high density polyethylene (HDPE). The two large muon veto panels, above and below the detector, were deployed outside the HDPE shielding, see figure 2.6.

The NEMENIX detector started taking data at BR2 in August 2013 and ran up to spring 2014. It demonstrated the feasibility of neutron detection using pulse shape discrimination and was able to perform a coincidence-based signal selection. This data also allowed the collaboration to measure the background conditions at the SoLid site for the first time, giving an indication of the expected rates for the large scale detectors [74].

2.4.2 SubModule 1

The positive outcome of the tests performed with NEMENIX gave green light for the construction of a larger scale prototype detector. The construction of a 288 kg SubModule 1 (SM1) started in the summer of 2014. The detector cells had the same configuration as the ones used in NEMENIX; a PVT cube and

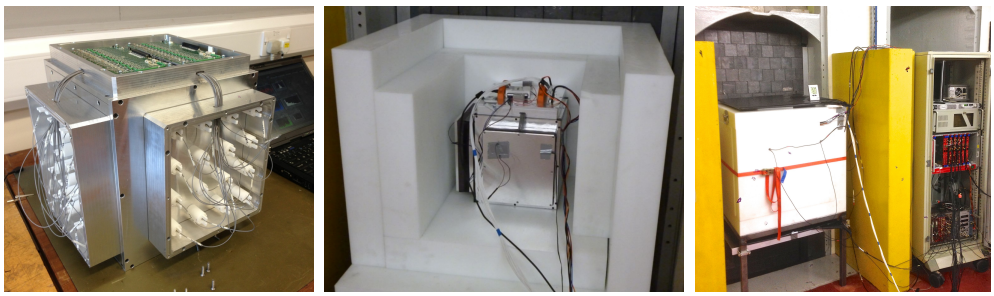

Figure 2.6: The NEMENIX detector in the lab, equipped with 32 readout channels (left). The detector installed at the BR2 reactor site with part of the HDPE shielding (middle) and with the full shielding and outer muon veto panels (right).

Table 2.2: Summary of the main properties of the first three SoLid detectors.

Property	**NEMENIX**	**SubModule 1**	**Phase I**
Construction year	2013	2014	2017
Mass	8 kg	288 kg	1.6 tonne
Nr. of detector cells ($x \times y \times z$)	$4 \times 4 \times 4$	$16 \times 16 \times 9$	$16 \times 16 \times 50$
^{6}LiF:ZnS(Ag) plastic backing	no	no	yes*
Nr. of ^{6}LiF:ZnS(Ag)-sheets/cell	1	1	2
WLS cladding	single	single	double
Nr. of WLS fibres/cell	$1\,x, 1\,y$	$1\,x, 1\,y$	$2\,x, 2\,y$
Tyvek wrapping	$75\,\mathrm{g\,m^{-2}}$	$75\,\mathrm{g\,m^{-2}}$	$105\,\mathrm{g\,m^{-2}}$

*Except the cells on the detector edge. Cf. section 2.5.

one neutron detection screen, wrapped in $75\,\mathrm{g}\cdot\mathrm{m}^{-2}$ Tyvek paper and read out by one pair of an x- and y-fibre. The fibres are coupled on one end to a Hamamatsu MPPC and are covered with thin aluminium tape, acting as a mirror, on the other end.

All cubes were stacked 16 by 16 in a vertical detection plane, supported by an aluminium frame. The inside of the frame was lined with 2 cm thick black HDPE, serving as a reflector for the neutrons created at the edges. Each detection plane was covered on both sides with a black HDPE sheet.

The full module had a total of 9 detection planes or 2304 detection cubes and was instrumented with passive shielding of 9 cm thick HDPE. The configuration of the SM1 detector cells and module is illustrated in figure 2.7.

The SM1 prototype was installed at the reactor site in the winter of 2014-2015. It was able to take a few days of reactor-ON data, before the BR2 reactor was shut down in February 2015 for a long maintenance period of 1.5 year. The SoLid experiment used this period for background and source calibration measurements. [75]

2.4.3 Optimisation of the detector design

The data and experience gained with the SM1 prototype was used by the SoLid collaboration to adapt and optimise the design of the full scale experiment. The largest drawback of SM1 was the sub-optimal performance of its front-end electronics. A new design of the readout system for Phase I resulted in a more stable system with improved detection efficiency. A detailed description of the current SoLid readout system is given in [76]. To further reduce the level of noise on the detected signals, in particular the dark count rate, the detector is placed in a cooled environment. The trigger system was also upgraded, with the addition of a dedicated neutron trigger based on pulse shape discrimination.

In order to improve the scintillation photon collection or *light yield*, a number of design changes were made. These changes include the use of double cladded[4] WLS fibres and using a double amount of these readout fibres. The aluminium tape mirror at one end of the fibres is replaced by a mirror layer deposited on Mylar foil that has a better reflectivity. The HDPE bars lining the frames are changed from black to white and are thicker, again to increase the reflectivity. In addition, thicker Tyvek wrappers of $105\,\mathrm{g}\cdot\mathrm{m}^{-2}$ are chosen. A study of the light yield as a function of these changes is presented in [77].

[4]The *cladding* of an optical fibre is a layer around the fibre core that causes light to be confined to the core by total internal reflection.

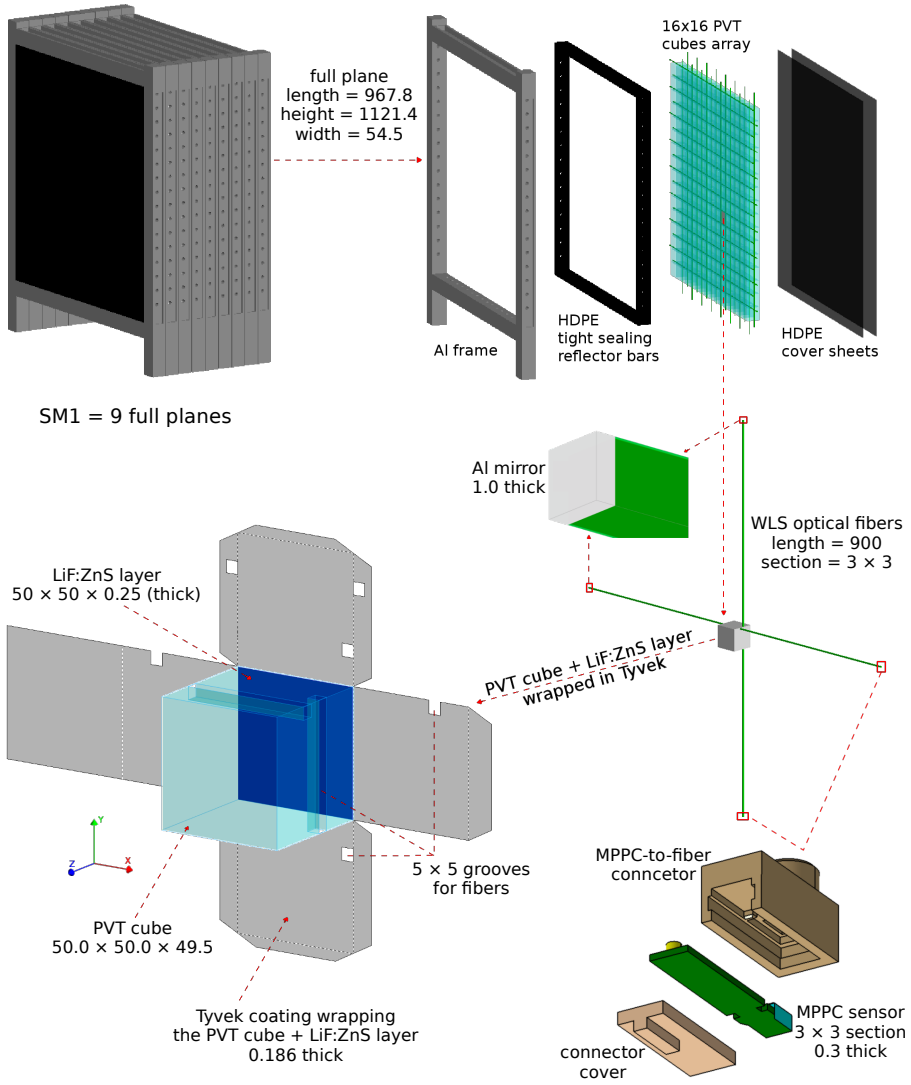

Figure 2.7: Illustration of the SM1 detector showing the frame and module design (top) and the detector cell configuration (bottom) [75].

Furthermore, Phase I contains twice the amount of ^{6}LiF:ZnS(Ag) screens, reducing the neutron capture time and improving the neutron detection efficiency [78]. In addition, the neutron screens get a plastic backing of 225 µm. Lastly, the amount of passive shielding is increased to reduce the cosmic and reactor induced backgrounds.

2.4.4 Phase I

The Phase I detector is built up out of 12 800 of the detection cells described in section 2.3. The cells are stacked per 256 (16 by 16) in vertical aluminium frames and each row and each column of cells is read out by the same pair of optical fibres, amounting to a total of 64 optical fibres per frame. The inner borders of the aluminium frames are lined with white HDPE bars with a thickness of 46.0 and 46.8 mm in the vertical and horizontal directions, respectively. As mentioned before, these bars act as a reflector for neutrons created in the edge cubes of the detector. Large Tyvek sheets are attached to each side of the filled frame improving the optical isolation. The MPPCs are connected to twisted pair ribbon cables carrying the bias voltage and outgoing signal. These cables all run through the inside of the hollow aluminium frames and towards one side of the frame, where they are attached per 16 to a connector. On that side, the so-called electronics box (EB) is mounted, which is an aluminium encasing with the front-end electronics [78].

Figure 2.8 shows the different components of a Phase I detector frame and how these frames are grouped per 10 in a so-called module. With a total of 5 modules, the active volume thus is $80 \times 80 \times 250\,\mathrm{cm}^3$, with a fiducial mass of 1.6 tonne.

At the reactor site, the Phase I detector is placed in a light-tight and cooled (10°C) cargo container, to improve the performance of the electronics. In that container, the modules are each placed on a cart that can slide over a rail system installed on the floor, as shown in figure 2.9. Mechanical actuators enable the modules to be moved remotely, which is useful for the in-situ calibration of the detector, as described in section 2.6. In this configuration, the closest approach of the Phase I detector to the BR2 reactor core is 6.325 m.

In order to attenuate the atmospheric and cosmic backgrounds, the container is surrounded by passive shielding. On top there is a 50 cm layer of HDPE and on all four sides there is a 50 cm thick water wall. In addition, thin cadmium sheets are placed on the top, the back (reactor side) and below the container as a neutron shield. Pictures of the detector shielding are shown

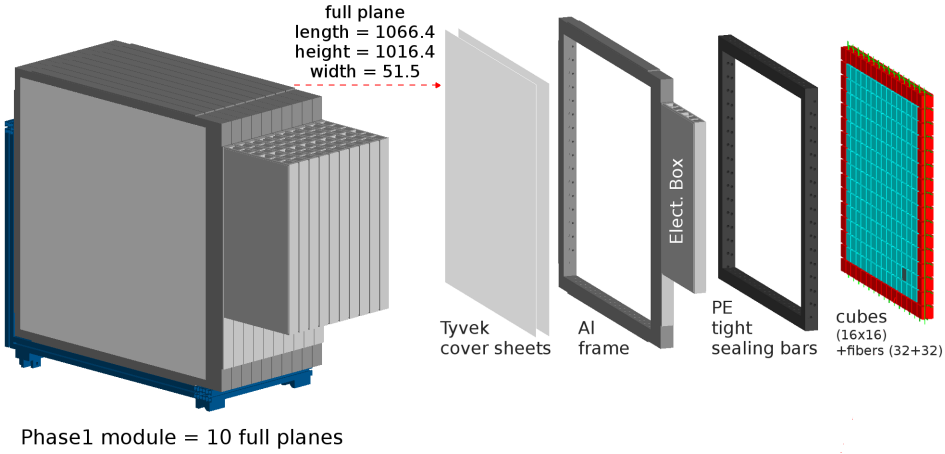

Figure 2.8: Exploded view of the Phase I detector modules.

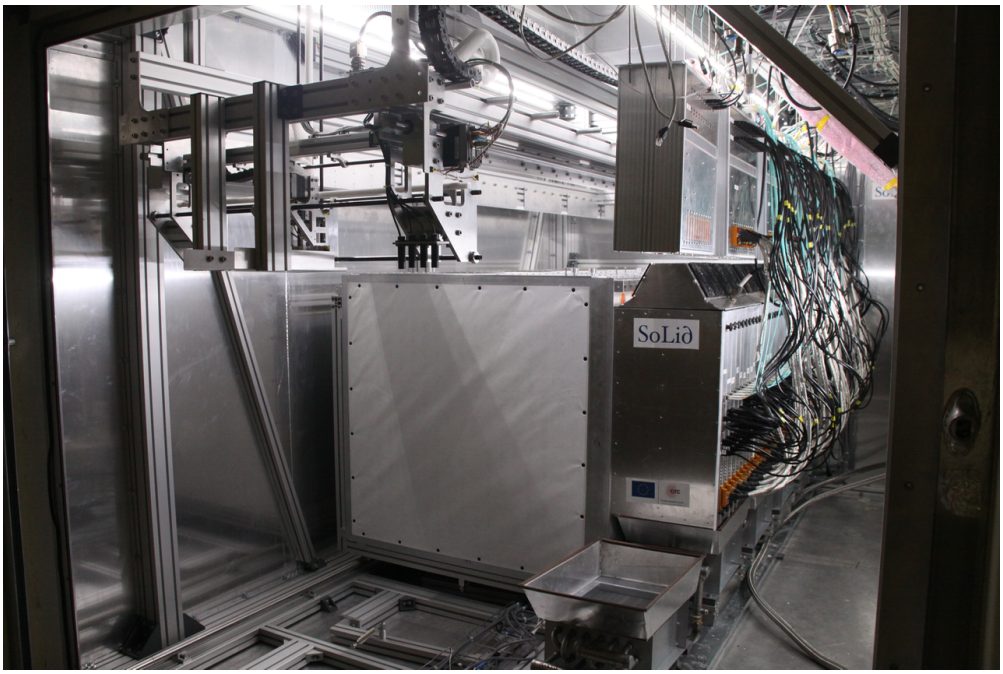

Figure 2.9: Four out of five Phase I modules installed in the SoLid container. The modules are mounted on a rail system.

in figure 2.10.

Figure 2.10: The SoLid experiment at the BR2 reactor site with HDPE shielding on top of the container (left and top right) and a wall of water bricks surrounding it (left and bottom right).

2.5 Phase I construction

At the end of 2016, the construction of the full SoLid Phase I detector was started. The construction process took over one year and large parts of it were carried out in the labs at Ghent University. These involved the cube wrapping and frame assembly procedures, quality assurance tests and the final installation of the modules, the electronics, the cooling circuit, ... in the container. The timeline of the different processes is shown in figure 2.11. This section aims to give a brief overview of the construction procedures. A more in-depth explanation can be found in the PhD thesis of Céline Moortgat, see reference [74].

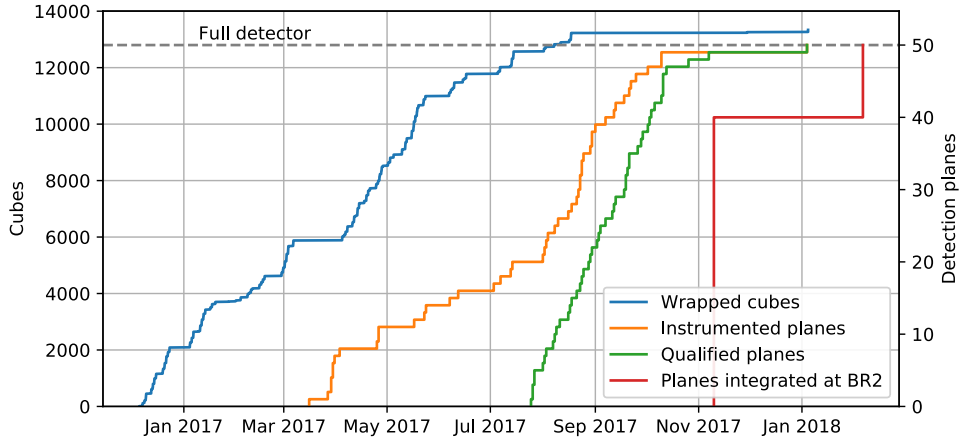

Figure 2.11: The evolution over time of the different steps in the Phase I construction process.

2.5.1 Cube wrapping

The cube wrapping procedure consisted in combining all detection cell components: a PVT cube, two ^{6}LiF:ZnS(Ag) screens and a Tyvek wrapper. Before the wrapping, the PVT cubes were washed with water and detergent and left on microfibre towels to dry. The lithium screens were carefully cut from the bigger sheets delivered by the producer. Two types of screen were made; a *plain* one and a *punched* one, to match the fibre grooves of the scintillator cubes, see figure 2.5. During these preparations, it was tracked from which production batch each component came using paper tags with dedicated barcodes. For the tracking of the individual detection cells, a sticker with a unique barcode was applied to the Tyvek wrappers.

For the cube assembly, one person gathered the 4 components on a tray and registered their individual weights, batch codes and cube code in the construction database. The tray with components was then passed to a second person, who first checked the cube dimensions and determined the correct cube orientation with an aluminium mall. This person wrapped the cube, together with the lithium screens in the Tyvek paper, closing it with tape. The cube was returned to the first person, who registered the total cube weight and put it away in a light-tight box. Pictures of the wrapping process are shown in figure 2.12.

Figure 2.12: Pictures of the wrapping set-up in the Ghent lab from [74, 79]. From top to bottom, left to right: The precision scale and scanner connected to a computer running the database scripts. - The tray with the detector cell components. - The wrapping room. - The aluminium mall for cube measurement and orientation behind a cube that is being wrapped. - The box storing the finished detector cells.

2.5.2 Frame filling

For the assembly of a detector plane, the aluminium frame was laid flat on a wooden plate on top of a table adjustable in height. A first large sheet of Tyvek was attached to the frame with plastic rivets, the frame was flipped over and instrumented with the white HDPE bars, placed on the edges.

The frame could then be filled with the wrapped cubes. The outer rows and columns were constructed of cells with SM1-type lithium screens, and all inner cubes had the new, thicker screens. The filling was guided by a computer program, checking the type of cube when its barcode was scanned and saving this code and position information in the construction database. This database allowed the collaboration to keep track of all elements and, if necessary, to trace back problems in the detector performance. It also provided a valuable overview of the detector properties, such as the weights of the different components as shown in figure 2.13.

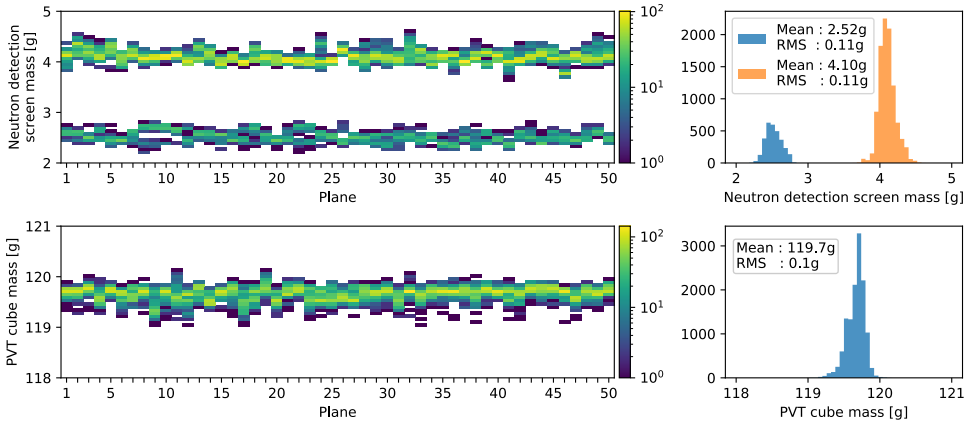

Figure 2.13: Distributions of the PVT cube masses (bottom) and ^{6}LiF:ZnS(Ag) masses (top), per plane (left) and in total (right). There are two mass distributions for the lithium screens; one for the new type of screens, with plastic backing, and one for the older type of screens, without backing, that are used in the outer layer of the detector planes.

When all cubes were installed, the ribbon cables were inserted in the frame and then the WLS fibres were gently pushed through the grooves. Next, the MPPCs were connected to the cables, noting down their serial number and position, based on the cable's color code, on a construction sheet. Then the MPPCs were placed in the plastic connectors and inserted in the frame,

making contact with the optical fibres. On the other end of the fibres, the mirror connectors were inserted. Thereafter, the fully instrumented planes were closed on the sides by screwing on small aluminium plates and were finished with the second Tyvek sheet.

2.5.3 Quality assurance with CALIPSO

Before a finished frame was ready to be inserted in a module, quality assurance (QA) tests were performed with the CALIPSO system, shown in figure 2.14. This system consists of a robot holding a radioactive source that can automatically scan a SoLid plane in both horizontal and vertical direction. Two types of sources were employed for the quality control; a β^+ source and a neutron source.

As β^+ source, ^{22}Na was used, that decays to ^{22}Ne, as illustrated in figure 2.15. In fact, the β^+ decay almost always results in the first excited state of ^{22}Ne, that will subsequently decay with the emission of a 1.27 MeV γ, and the signal of the ^{22}Na source is thus twofold. For scans with this source a special robot head was made, that would cause the annihilation of the emitted β^+ and detect it with a built-in γ trigger. The events detected in the SoLid plane that were in coincidence with this external trigger should then be related to the 1.27 MeV γ's, that were used to determine the light yield of the detector cells.

To determine the relative neutron response over a detector plane, a ^{252}Cf or AmBe source, emitting neutrons with a mean energy of respectively 2.1 MeV and 4.2 MeV, was used. The source was placed in a dedicated semi-sphere HDPE collimator to reflect the neutrons towards the SoLid plane. Around the plane HDPE plates were placed as well, acting as a moderator, again to increase the neutron interactions in the frame.

By scanning with these sources at different xy-positions, the homogeneity and performance of a frame could be tested. This QA process enabled the collaboration to detect and correct issues such as missing neutron detection screens, bad WLS fibre connections, defective MPPCs and swapped cables, before integration of the plane in a detector module. Two examples of such cases are shown in figure 2.16.

Since the detector planes in CALIPSO were read out by a prototype electronics box, the scans also allowed testing the readout electronics before the manufacturing of all fifty boxes.

A full treatment of the CALIPSO results is given in reference [81].

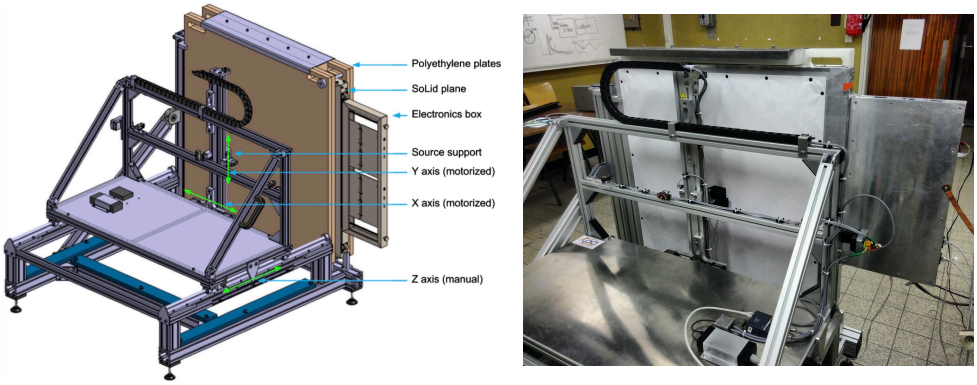

Figure 2.14: Mechanical design of the CALIPSO robot (left). Scanning of a SoLid detector plane with a β^+ source in CALIPSO (right).

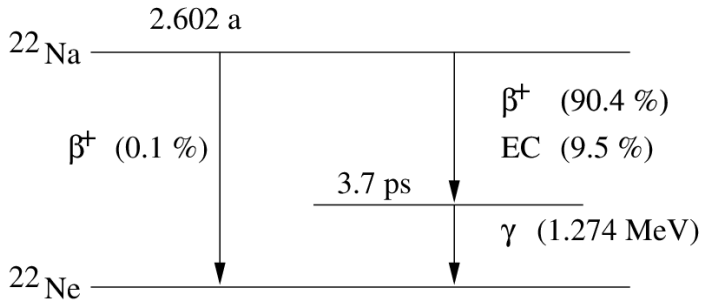

Figure 2.15: The decay scheme of ^{22}Na. In 90.4% of the cases, the decay happens via β^+ emission that results in the first excited state of ^{22}Ne. Another 9.5% of the decays happens via electron capture to this excited state, while only 0.1% of the cases gives a β^+ decay to the ^{22}Ne ground state. The excited state of ^{22}Ne decays to its ground state with the emission of a 1.27 MeV γ. [80]

2.6 Phase I calibration

As described above, the QA before commissioning with the CALIPSO system gave some first calibration results. However, a more precise calibration of the full SoLid detector is performed every few months *in situ* with the CROSS system. This system is mounted on the ceiling inside the SoLid container as illustrated in figure 2.17 (left). As described in section 2.4.4, the SoLid detector modules can be moved over a rail system by remote-controlled actuators. By doing so, small gaps between two modules can be created, in which the

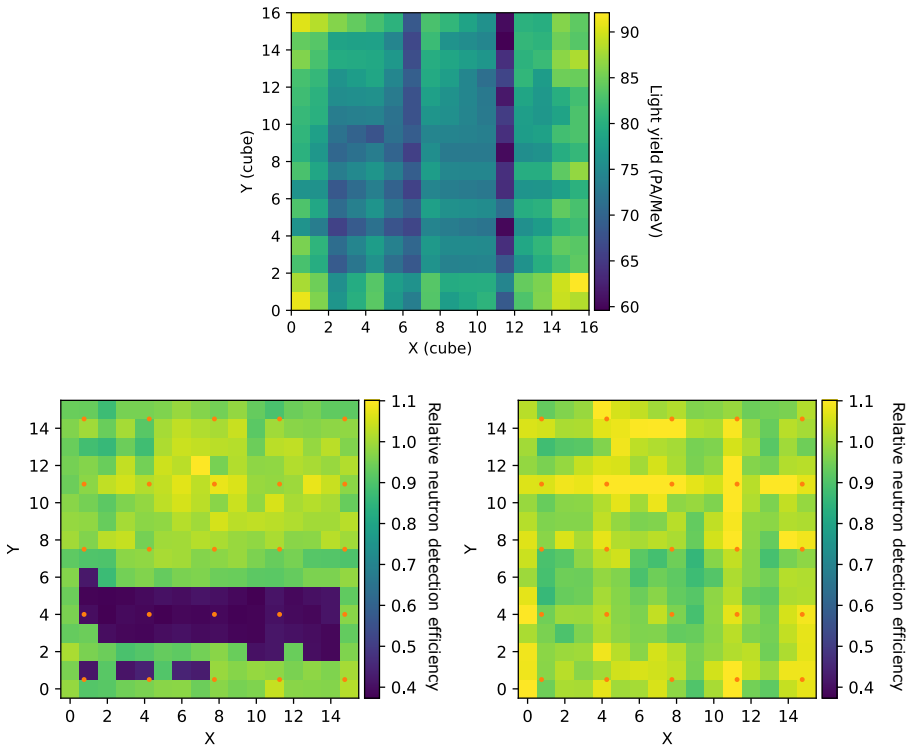

Figure 2.16: Examples of detector faults revealed by the quality assurance process with CALIPSO. Top: Column 11 of frame number 13 showed a significantly lower light yield, which was caused by a bad coupling between the corresponding fibre and the MPPC. Bottom: Looking at the relative neutron detection efficiency per cube, based on a ^{252}Cf scan, some cubes showed a clear deficiency (left). These cubes appeared to come from one batch of screens with a too low ^{6}Li doping and were replaced by other cubes (right).

CROSS calibration head can be lowered to insert a radioactive source. This is possible at each side of every module, resulting in the six possible calibration planes that are shown in figure 2.17 (right). The CROSS robot can be moved towards the different gaps, along the z-axis, and can scan in both x- and y-direction within each gap over an area that is also represented in figure 2.17 (right) in blue.

A full study of the CROSS calibration data is presented in the PhD thesis of Valentin Pestel, see reference [82]. The main results are summarised here.

2.6.1 Neutron detection efficiency

As it directly impacts the IBD detection efficiency, a precise determination of the neutron detection efficiency ϵ_{det} is needed. This ϵ_{det} is in fact a combination of the neutron capture efficiency and the neutron reconstruction efficiency, the latter of which is again a combination of the neutron trigger and identification efficiencies:

$$\epsilon_{\text{det}} = \epsilon_{\text{capt}} \times \epsilon_{\text{trig}} \times \epsilon_{\text{ID}}. \tag{2.8}$$

The neutron capture efficiency defines the probability for an IBD neutron to be captured by ^{6}Li in one of the detection screens. It is determined from Monte Carlo simulations of the neutron interactions in the detector, taking into account the neutron energy, the SoLid detector geometry, the hydrogen and ^{6}Li content and the capture cross section, and is found to be $\epsilon_{\text{capt}} = 71\%$ on average.

For the determination of $\epsilon_{\text{reco}} = \epsilon_{\text{trig}} \times \epsilon_{\text{ID}}$, the results of neutron calibration runs are used. These calibrations are performed with both the ^{252}Cf and AmBe source, using the CROSS system. Given the source activity[5] and a detailed Monte Carlo simulation of the capture processes for both sources, the number of reconstructed neutrons can be compared to the predicted number of captured neutrons, resulting in the reconstruction efficiency ϵ_{reco}. The results of the neutron scans are shown in figure 2.18. A first remarkable feature is the systematic shift of about 7% between the efficiencies for the two sources. So far it has remained unclear what causes this. However, the trend of the efficiency per plane is similar for both scans, and for now the average of the two scans is used, being $\epsilon_{\text{reco}}^{(\text{abs})} \approx 73.9^{+4.0}_{-3.3}\%$. The uncertainties on this value are dominated by the uncertainty on the source activity and the Monte Carlo detector model. Combining the neutron reconstruction efficiency with the average neutron capture efficiency, the total IBD neutron detection efficiency becomes $\epsilon_{\text{det}} \approx 52\%$.

2.6.2 Light yield

The light yield of the SoLid detector, i.e. the detected number of PA for a given energy deposit, was determined from calibration runs with a ^{22}Na source. As mentioned above, ^{22}Na undergoes β^+ decay to the first excited stated of ^{22}Ne, that de-excites with the emission of a 1.27 MeV γ. The energy calibration is based on the detection of the γ's from β^+ annihilations

[5] The activities of both sources have been determined with 2% precision at the National Physical Laboratory in the UK.

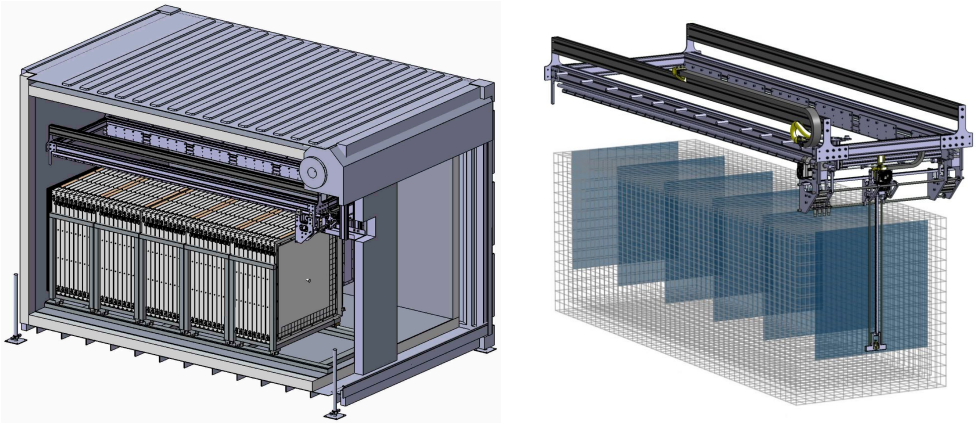

Figure 2.17: Left: Illustration of the CROSS calibration system in the SoLid container (left). The areas between the SoLid modules, in blue, that are accessible for a calibration scan, shown relative to the position of the SoLid detector cubes that are represented by the grey matrix (right).

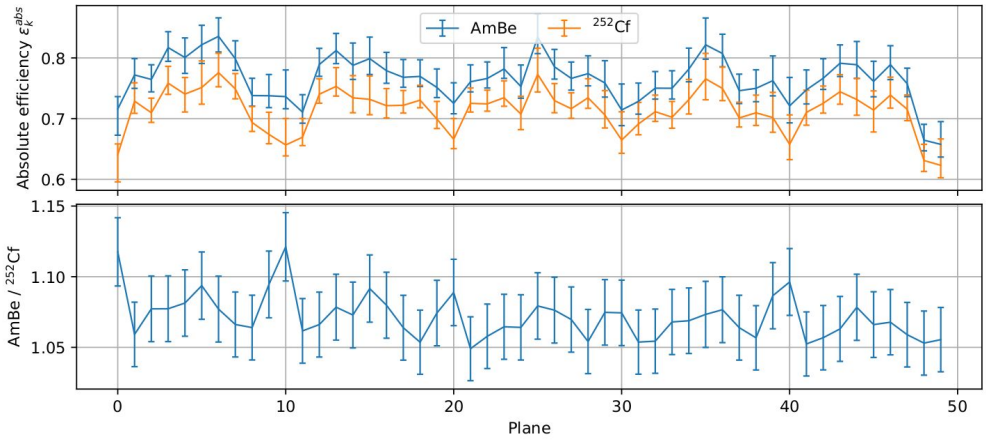

Figure 2.18: The absolute neutron reconstruction efficiency per SoLid detector plane, measured with a ^{252}Cf and AmBe source (top panel). A shift of about 7% is seen between the two resulting efficiencies (bottom panel).

and ^{22}Ne de-excitations, and is calculated with two methods. One method is based on an analytical fit of the Compton edge in the Compton scattering spectrum of the 1.27 MeV γ. The second exists in comparing the recorded ^{22}Na γ-spectrum to the spectrum determined with a dedicated Monte Carlo simulation, using a Kolmogorov-Smirnov (K-S) test. This test computes the largest vertical distance between the measured cumulative distribution and a simulated cumulative distribution, and uses this value as a *goodness-of-fit* parameter. The detector light yield values in the simulation are each time adjusted, until the best result of the K-S test is obtained, see figure 2.19. The values resulting from both methods are in very good agreement and the average light yield of the detector is determined to be about 96.7 PA/MeV. A light yield estimation per plane is shown in figure 2.20. In practice, the LY value was determined within 3% uncertainty for each of the 12 800 detector cells, taking into account attenuation effects according to the cell's position along the crossing WLS fibres, and a fibre-MPPC coupling correction.

We should note that the obtained LY values still need to be corrected for crosstalk in the photodetectors[6], which is on average $\sim$ 20%, resulting in a reduced average LY value of 81 PA/MeV.

The energy resolution of the detector is mainly driven by fluctuations in the collected photon statistics and, accordingly, in the detected number of PAs. The statistical uncertainty on the light yield, or so-called stochastic energy resolution term is determined as $\sigma_{st}(E) = \sqrt{LY \times E}$ and is thus about 11-12% at 1 MeV.

2.6.3 Energy linearity

One important feature of solid plastic as scintillator material that has not been addressed yet, is its linear energy response. This greatly simplifies the energy reconstruction and reduces the related systematic errors. This energy linearity was tested by determining the detector light yield from the γ's emitted by different calibration sources:

- ^{22}Na: This source emits γ's of 1.27 MeV, as explained above.
- ^{207}Bi: This element decays to ^{207}Pb via electron capture, accompanied by the emission of 1.063 MeV and 1.770 MeV γ's.
- AmBe: In this source ^{241}Am produces α's which interact with ^{9}Be via: $\alpha + {}^{9}\text{Be} \rightarrow \text{n} + {}^{12}\text{C}$. The resulting ^{12}C is often produced in an excited

[6] Optical crosstalk is the phenomenon where an avalanche induced by a primary photon and created in one pixel, accidentally triggers a secondary avalanche in a neighbouring pixel of the photosensor, thereby increasing the signal strength. The determination of the amount of crosstalk in the SoLid electronics is described in reference [77].

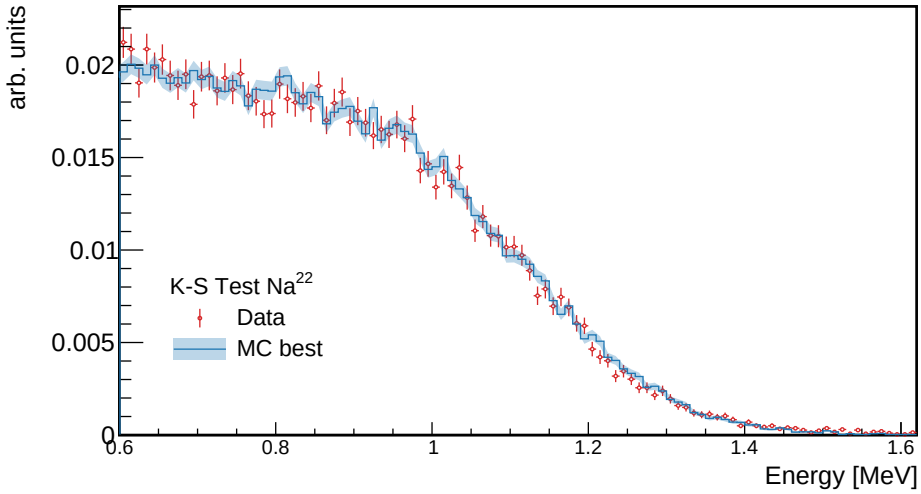

Figure 2.19: Light yield determination from a Kolmogorov-Smirnov test comparing a measured ^{22}Na spectrum with a spectrum simulated by a Monte Carlo code.

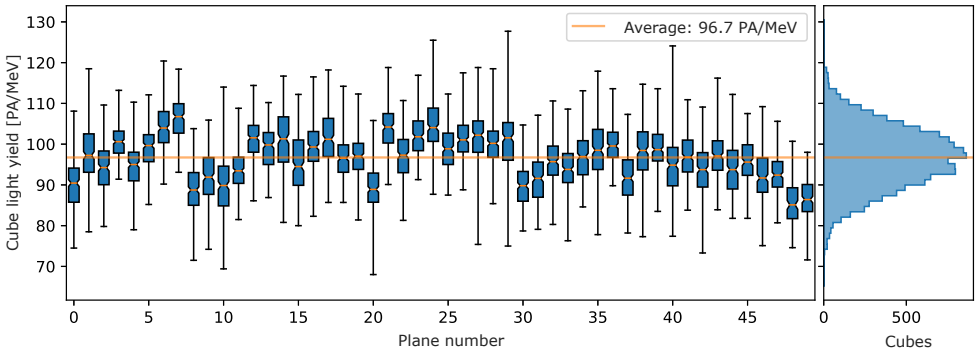

Figure 2.20: Distribution of the cube light yield measured with a ^{22}Na source during a calibration campaign in September 2018. The orange line shows the detector average. The blue boxes represent the 50% percentiles and are each "split" by a small orange line indicating the average value for that plane. The black lines represent outliers below the first and above the third quartile.

state, which decays with the emission of a 4.4 MeV γ.

- Muons: Muons are highly energetic particles from atmospheric origin which cross the SoLid detector at a relatively high rate. The ionising behaviour of muons is well known and their energy deposited per path length is about 2 MeV cm^{-1}. By calculating the path length of a muon in the detector, the deposited energy can be calculated and compared to the detected number of PAs.

The calibration measurements confirm the assumed linear response, as can be seen in figure 2.21, where the resulting light yield is plotted as a function of the deposited energy for the three calibration sources and a cosmic muon sample.

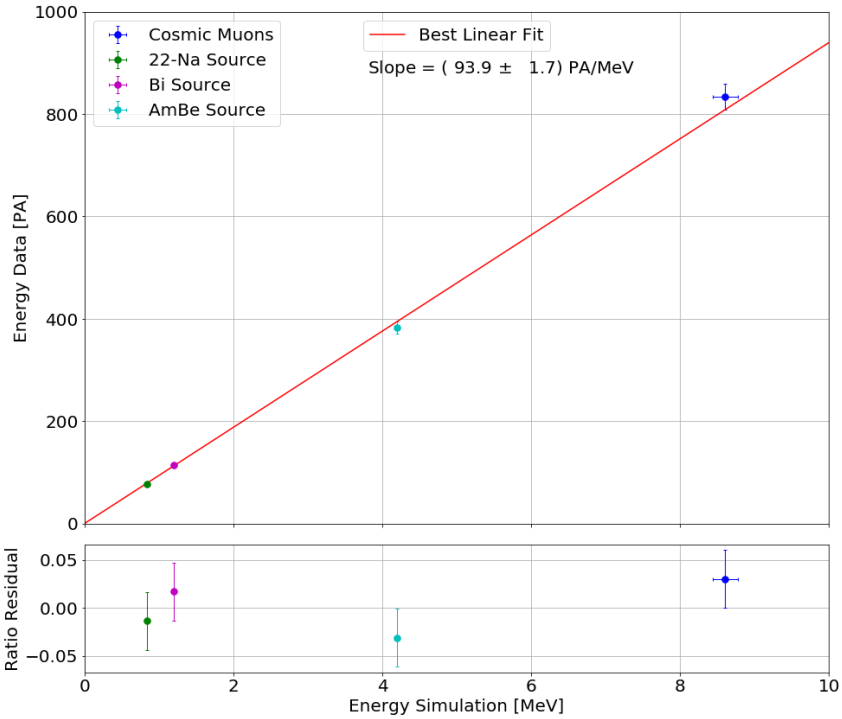

Figure 2.21: The energy linearity of the PVT scintillator material demonstrated with calibration data from different radioactive sources and detected muon tracks.

2.7 Other sterile neutrino experiments

Apart from the SoLid experiment, a number of other sterile neutrino projects are currently running or under construction. The closest competitors of the SoLid experiment are, because of their similar reactor siting and baseline, Neutrino-4, PROSPECT and STEREO.

Neutrino-4 is installed near the SM-3 research reactor of the SSC-RIAR centre in Dimitrovgrad, Russia, with a baseline of 6 to 12 m. The reactor has a thermal power of 90 MW and uses ^{235}U as its main fuel element. The Neutrino-4 detector is constructed out of 5×10 sections filled with Gd-doped liquid scintillator [83]. Based on 480 days of reactor-ON data, the Neutrino-4 collaboration published their first results in 2019, which showed that a relative fit of the data over the different detector cells favoured the sterile oscillation hypothesis with $\sin^2(2\theta_{14}) = 0.26$ and $\Delta m^2_{41} = 7.25$ eV^2 at 3σ confidence level, while rejecting the parameter region with $\sin^2(2\theta_{14}) > 0.1$ and $\Delta m^2_{41} < 3$ eV^2.

The **PROSPECT** experiment is located between 7 and 12 m from the Oak Ridge National Laboratory (ORNL) research reactor in Tennessee, USA. It is a High Flux Isotope Reactor (HFIR) with a maximal power of 85 MW and ^{235}U as the dominant fission isotope. The experiment uses a total of $\sim$4 tonnes of ^{6}Li-doped liquid scintillator divided over 11 by 14 isolated segments, for the antineutrino detection [84]. In June 2020, PROSPECT published the latest results of their short-baseline oscillation search using 96 days of reactor-ON data. These indicate a best fit to the data for parameters $(\sin^2(2\theta_{14}), \Delta m^2_{41}) = (0.11, 1.78 \text{ eV}^2)$, that is however only slightly preferred with respect to the no-oscillation hypothesis [85].

STEREO operates over a range of 9.4 to 11.1 m from the core of the Institute Laue-Langevin (ILL) research reactor in Grenoble, France. The ILL reactor has an operating power of about 58 MW and is also highly enriched in ^{235}U. The detector consists of 6 vertical cells, filled with Gd-doped liquid scintillator [86]. The STEREO collaboration has presented their analysis of 179 days of reactor-ON data at the end of 2019. They reject the best-fit point of the RAA at more than 99.9% confidence level and find that the data is compatible with the null oscillation hypothesis [87].

Other short baseline reactor experiments include DANSS [88] and NEOS, that operate near a commercial power reactor. They benefit from a higher flux of antineutrinos, but can not get as close to the reactor core and the oscillation pattern is more subject to smearing because of the larger size of the core.

The **NEOS** experiment takes place at the Hanbit nuclear reactor plant in South Korea. The detector consists of a tank filled with approximately one tonne of Gd-doped liquid scintillator and is located at a distance of 23.7 m from one of the 2.8 GW reactors. NEOS published a first sterile neutrino oscillation search in 2017, using the Daya Bay spectrum as a reference [89]. The experiment was able to exclude the RAA best fit point at more than 90% confidence level and found no strong evidence for a 3+1 neutrino oscillation.

DANSS is an experiment located near a 3.1 GW commercial power reactor at Kalinin, Russia. The detector is installed under the reactor core and can be moved up and down over distances ranging from 10.3 to 12.3 m from the reactor core. The experiment uses PVT scintillator, segmented into bars of $1 \times 4 \times 100$ cm^3, for the detection of the reactor antineutrinos. In 2018, the DANSS collaboration presented a first oscillation search that excluded the RAA best fit point, but favoured the 3+1 oscillation hypothesis with a best fit at $\sin^2(2\theta_{14}) = 0.05$ and $\Delta m^2_{41} = 1.4\text{eV}^2$ [90].

The results of the five experiments presented above are combined in figure 2.22. Each of the experiments excludes large parts of the allowed parameter space and rejects the RAA best fit value with at least 90% confidence level. Some of the results are however controversial; in specific the remarkable result of Neutrino-4, which announces an oscillation signal around $\sin^2(2\theta_{14}) = 0.26$ and $\Delta m^2_{41} = 7.25$ eV^2, and the result of DANSS, that favoured the oscillation scenario with $\sin^2(2\theta_{14}) = 0.05$ and $\Delta m^2_{41} = 1.4$ eV^2.

In 2018, global fits of all available ν_e-disappearance data, including the NEOS and DANSS results, were published by Gariazzo *et al.* [91] and by Dentler *et al.* [92] which resulted in $\Delta m^2_{41} = 1.29$ eV^2 and $\sin^2(2\theta_{14}) = 0.049$ or $\sin^2(2\theta_{14}) = 0.0089$, respectively. The allowed regions in the $\sin^2(2\theta_{14})$-Δm^2_{41} plane are shown in figure 2.23 for both analyses. The overall conclusion obtained from these analyses of short baseline ν_e-disappearance data was that there was an indication in favour of oscillations into sterile neutrinos at the 3σ level [43].

More recently, however, a study by C. Giunti [93] has shown that the statistical significance of the combined NEOS and DANSS results in favour of sterile oscillations becomes much smaller when using a Monte Carlo driven method for a correct interpretation of the χ^2 test statistic[7]. In addition, the DANSS collaboration has communicated that a new analysis of their data, in-

[7] A detailed discussion and motivation for the use of Monte Carlo toys for the correct interpretation of the χ^2 test statistic is given in section 6.5.3 of this thesis.

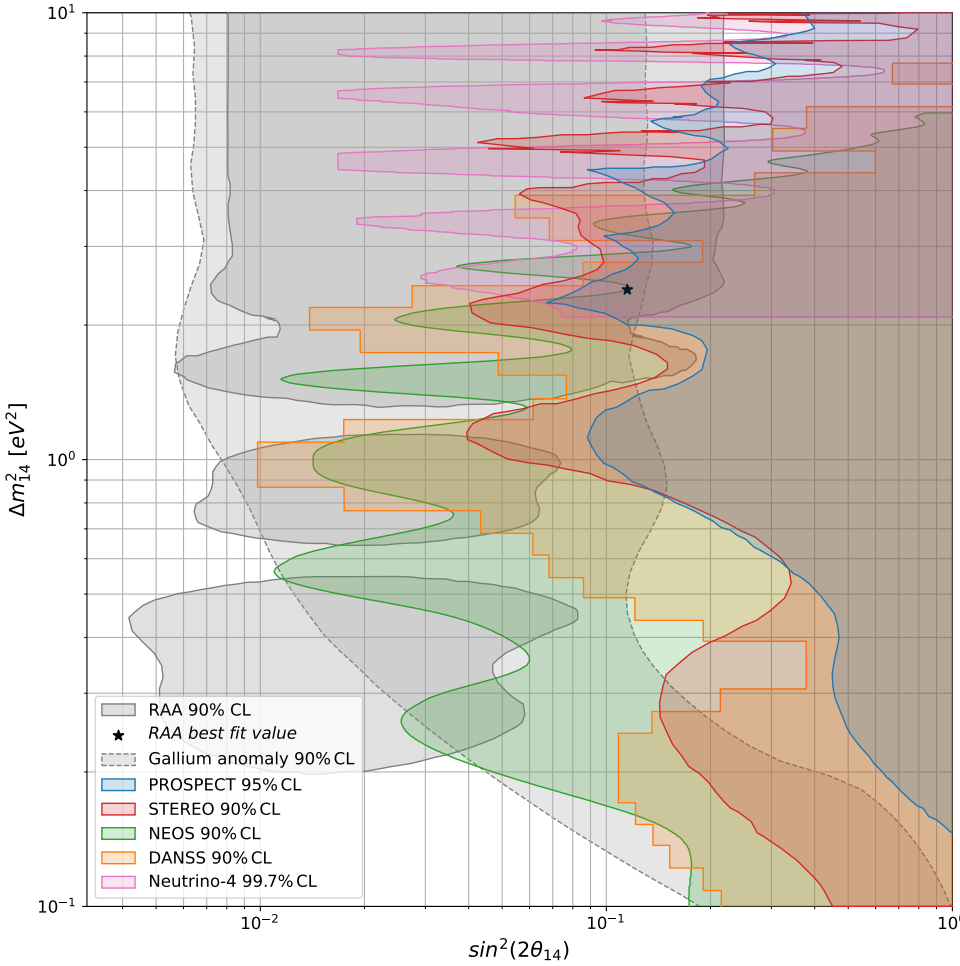

Figure 2.22: The exclusion contours for the 3+1 neutrino oscillation searches presented by PROSPECT [85], STEREO [87], NEOS [89], DANSS [90] and Neutrino-4 [83], together with the Gallium anomaly and RAA 90% confidence levels and the RAA best fit point. Thanks to V. Pestel.

cluding all systematic uncertainties, gives a result that is compatible with the no-oscillation hypothesis [94]. The remaining tensions with the Neutrino-4 result will hopefully be resolved by the data that is currently being collected by the ongoing reactor experiments.

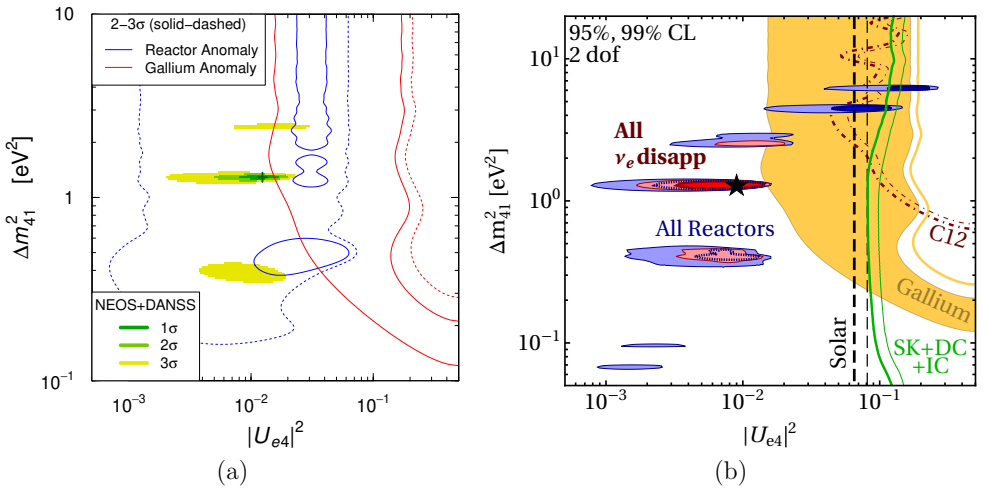

Figure 2.23: Results of short baseline ν_e disappearance analyses by Gariazzo *et al.* [91] (a) and Dentler *et al.* [92] (b). The best fit points are indicated with + (a) and ⋆ (b). Although the two analyses consider different data sets, their allowed regions are in good agreement with each other, because both data sets are dominated by the NEOS/Daya Bay and DANSS spectral ratio data. [43]

Other types of experiments with a sterile neutrino program, some of which are already taking data or will start in the next few years, are source experiments such as BEST, $\nu_\mu \rightarrow \nu_e$ appearance and ν_μ disappearance experiments such as the SBN program at Fermilab, the neutrino mass precision experiment KATRIN, and the IceCube experiment giving constraints on the mixing of the sterile with active neutrinos [43].

2.8 Summary

This chapter described the strategy used by the SoLid collaboration to meet the particular requirements needed to tackle the RAA anomaly and the 5 MeV spectral distortion.

It was chosen, as described in section 2.1, to conduct the experiment at the BR2 reactor site because of the reactor's very small and symmetric core. This makes it an ideal source of antineutrinos, as the compactness implies a minimal smearing of the oscillation signal and allows a measurement on a very short baseline from the source. The SoLid detector consists of small cells of a composite scintillator technology, with PVT cubes for the detection of electromagnetic interactions and ^{6}LiF:ZnS(Ag) screens for the capture and detection of neutrons, as discussed in section 2.3.

Two prototype detectors, NEMENIX and SubModule 1, preceded the full scale detector. From the construction and commissioning of these prototypes a lot of valuable lessons were learned and the detector design was optimised, see section 2.4. Section 2.5 dealt with the construction of the full Phase I detector, that started in december 2016 and involved the wrapping of 12 800 detector cells and assembly of 50 detector frames. Valuable quality assurance tests were performed after assembly in the lab with the CALIPSO system. Phase I was installed in the winter of 2017-2018 and has been taking data since then. During reactor-off periods, on-site calibrations are performed with the dedicated CROSS system, the methods and results of which were covered in section 2.6.

Signal prediction

3

This chapter describes how the antineutrino flux coming from a nuclear reactor can be predicted. It gives an overview of the methods that are generally used today and continues with an explanation of the specific case of the flux prediction from the BR2 reactor. The interaction probability of an antineutrino with a proton is taken into account via the IBD cross section. In combination with the specificities of the SoLid detector, such as its dimensions and proton content, this leads to an estimation of the expected IBD signal for the data taking period of the experiment.

3.1 Reactor $\overline{\nu}_e$ flux prediction

Let us consider equation 2.6 again, which gives the expected number of detected $\overline{\nu}_e$'s over a period T, in a certain energy interval $[E_i\ ;\ E_{i+1}]$ and for a certain fission isotope k, for a point-like reactor:

$$N_k = T\frac{N_p}{4\pi L^2}\ n_f\ \int_{E_i}^{E_{i+1}} R(E)\ S_k(E)\ \sigma_{IBD}(E)\ dE \tag{3.1}$$

where N_p is the number of target protons in the detector, L is the reactor-detector distance, n_f is the number of fissions per time unit, R is the detector response, S_k is the emitted spectrum for isotope k and σ_{IBD} is the IBD cross section.

This equation gives the prediction for the number of *detected* reactor antineutrinos, based on different reactor and detector parameters. We will leave out the most important detector parameter for now, which is its response R, and look at the number of *interacting* antineutrinos first. Note that the detector response includes the IBD capture and reconstruction efficiencies, energy

resolution and smearing effects. Since these parameters can vary with energy and from one detector cell to another, the response R actually depends on both energy E and on the position of the IBD interaction in the detector, which we will characterise by the length L between the centre of the reactor core and the interaction point. The function $R(E, L)$ is determined using a Monte Carlo detector simulation, which is the main topic of chapter 4.

Rewriting the formula to the expected number of $\overline{\nu}_e$ interactions over a time interval $[t\ ;\ t+T]$ and for the same energy interval $[E_i\ ;\ E_{i+1}]$ thus gives

$$N_k(t) = \frac{N_p}{4\pi L^2} \int_{E_i}^{E_{i+1}} \int_{t}^{t+T} n_f(t)\ \alpha_k(t)\ S_k(E)\ \sigma_{IBD}(E)\ dt\ dE \tag{3.2}$$

where the number of fissions n_f now depends on the time t and an additional parameter $\alpha_k(t)$ denoting the time-dependent fraction of the fissions that is due to isotope k comes into play.

The following paragraphs will further discuss the inputs to equation 3.2, in an order that follows the path of a neutrino from its emission from the reactor to its interaction in the detector.

3.1.1 Reactor fission rate

The basic principle of a nuclear reactor is the production of energy via neutron-induced fission. Let us consider ^{235}U as the target nucleus. In general, the resulting fission reaction then looks like:

$$n + {}^{235}\mathrm{U} \rightarrow {}^{236}\mathrm{U}^* \rightarrow \mathrm{X}_1^* + \mathrm{X}_2^* + xn + E \tag{3.3}$$

where the released energy E is about 200 MeV. It can be seen that, apart from energy, fission reactions also produce neutron-rich daughter nuclides X* and a number of fast neutrons xn, with $x = 2.3$ on average. The daughter nuclides in turn undergo β^--decay in order to reach a stable nuclear state:

$${}^{\mathrm{A}}_{\mathrm{Z}}\mathrm{X}^* \rightarrow {}^{\mathrm{A}}_{\mathrm{Z+1}}\mathrm{X}' + e^- + \overline{\nu}_e \tag{3.4}$$

where Z is the number of protons in the nucleus and A its mass number. In these decay processes, a lot of antineutrinos are produced, making nuclear reactors an ideal source for neutrino experiments.

A large fraction of the released neutrons from fissions like 3.3 thermalises by scattering in the reactor moderator or outside the core and are lost. During normal reactor operation, about one released neutron per fission *will* interact

in the reactor material, inducing a new fission reaction and as such continuing a stable reactor cycle.

It is important to note that the reaction in equation 3.3 can have many possible outcomes for the fission products. The nuclide distribution of the fragments from a ^{235}U fission is shown in figure 3.1. One fission example is shown in figure 3.2, illustrating the operation chain of a nuclear reactor.

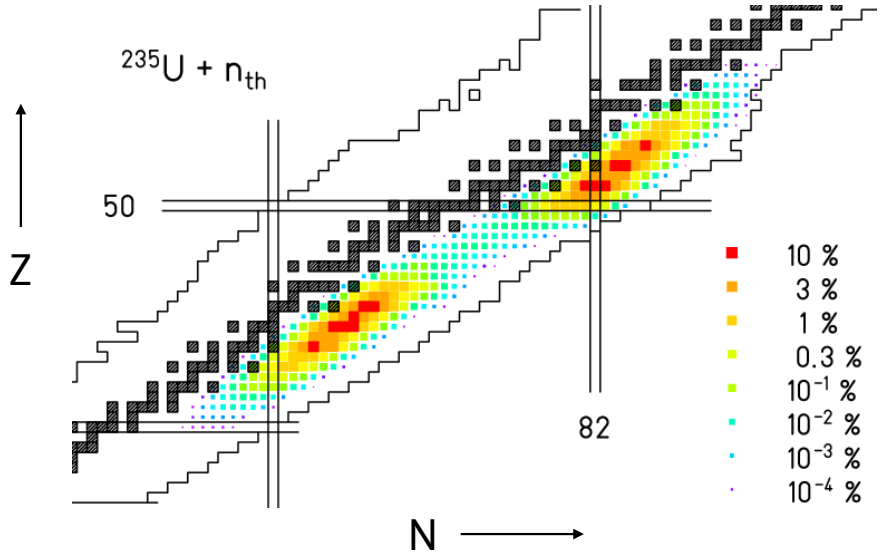

Figure 3.1: Distribution of the fission products according to their proton number (Z) and neutron number (N) for a ^{235}U fission induced by thermal neutrons. Adapted from [95].

In general, a nuclear reactor operates based on the consumption of four principal fuel nuclides: ^{235}U, ^{238}U, ^{239}Pu and ^{241}Pu. Fissions of other isotopes contribute less than 0.3% to the total fission rate. Fresh fuel elements, however, only contain the uranium isotopes and for highly enriched reactors they mainly contain ^{235}U and a little ^{238}U. During operation, the plutonium isotopes are gradually generated by neutron capture on ^{238}U (see figure 3.2). Thus while running, a reactor core burns uranium isotopes and accumulates plutonium isotopes instead. However, a reactor like BR2, with an enrichment

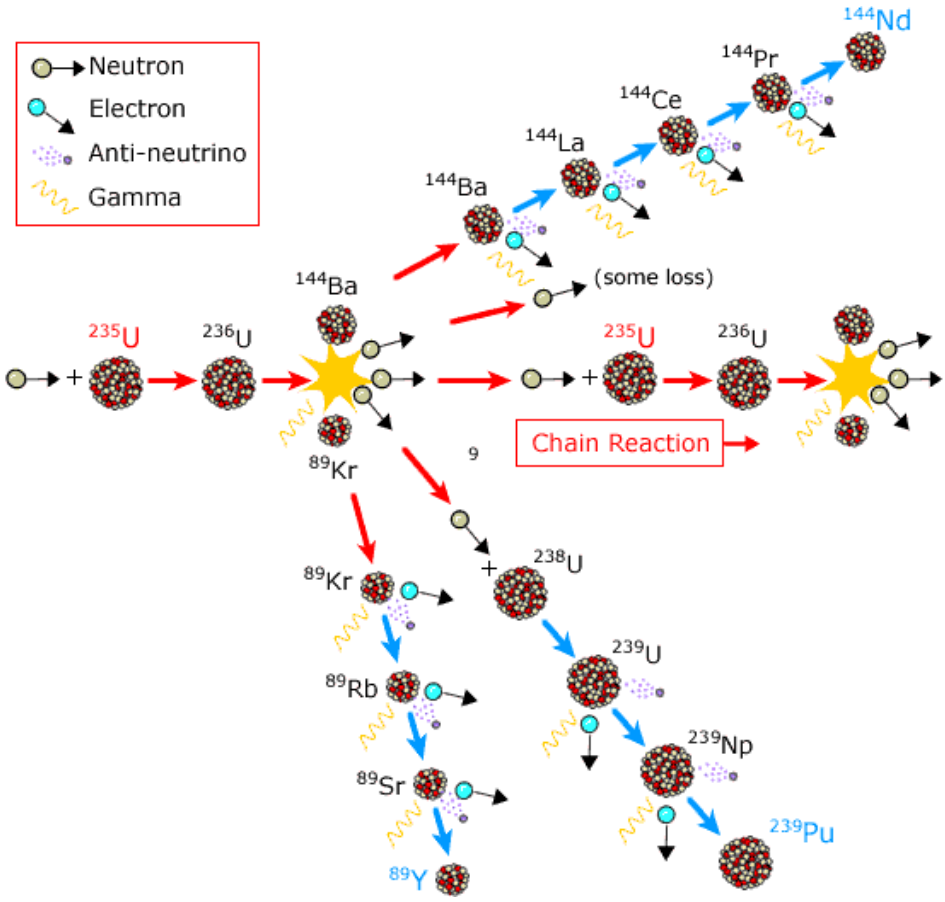

Figure 3.2: A neutron-induced fission reaction with ^{235}U as the target nuclide. The middle row shows how the released neutrons feed the nuclear chain reaction. The bottom right reaction chain illustrates the production of ^{239}Pu through neutron capture on ^{238}U. [96]

of $\sim$ 93.5% ^{235}U, has very little ^{238}U and as a consequence only a minuscule amount of the ^{239}Pu and ^{241}Pu fissile isotopes are produced. For these reactors, the fission fraction of ^{235}U - i.e. the number of fissions coming from ^{235}U with respect to the total number of fissions - is over 99%.

In general, the fission fraction of isotope k at time t can be determined from the relative fission rates, f_k, and is written as

$$\alpha_k(t) = \frac{f_k(t)}{\sum_{k=1}^{4} f_k(t)} \tag{3.5}$$

The precise number of fissions, generated in a reactor core at a time t, can be calculated using the formula:

$$n_f(t) = \frac{P_{th}(t)}{\sum_k \alpha_k(t) \langle E_f \rangle_k} \tag{3.6}$$

where $P_{th}(t)$ is the thermal power of the reactor at time t and $\langle E_f \rangle_k$ is the average released energy per fission of isotope k. The nominator is often rewritten as follows

$$n_f(t) = \frac{P_{th}(t)}{\langle E_f \rangle(t)} \tag{3.7}$$

where $\langle E_f \rangle$ represents the mean released energy per fission, averaged over all fissile isotopes.

Given that the average energy released per fission is about 200 MeV, one can easily calculate that a 60 MW reactor, like BR2, generates about 10^{18} fissions/s. However, in order to perform a sterile neutrino search, the SoLid experiment needs a very precise value for $n_f(t)$. Therefore, the different parameters in formula 3.6 and the corresponding uncertainties need to be assessed with care.

The thermal power $P_{th}(t)$ of the BR2 reactor is monitored by the personnel at SCK•CEN and is determined by two methods. One is based on the enthalpy balance in the reactor's water cooling circuits that is calculated based on measurements of the water flow and temperature in these circuits. The second method makes use of the ^{16}O present in the cooling water that is activated by fast neutrons through the reaction $^{16}\mathrm{O} + n \rightarrow {}^{16}\mathrm{N} + p$. By measuring the activity of ^{16}N, the thermal power evolution can be derived. The thermal power, together with other operation parameters, is stored in the

BIDASSE database (BR2 Integrated Data Acquisition System for Survey and Experiments) to which the SoLid collaboration has access. We will use the results of the first method, which has an estimated uncertainty on the thermal power calculation of 5 to 8%. This uncertainty is driven by uncertainties on the calibration of the devices measuring the cooling water temperature and flow, and by offsets introduced during the processing of these measurements [97].

The values $\langle E_f \rangle_k$, giving the mean energy released per fission of isotope k, are calculated from nuclear theory and can be retrieved from dedicated databases. The corresponding estimated uncertainties are 0.5% at most [98].

The fission rates and their spatial distribution are based on the known power evolution and calculated by a detailed simulation of the neutron flux inside the BR2 core. The reactor core model includes the positions of the beryllium matrix, the fuel elements, possible samples under irradiation and the control bars and is illustrated in figure 3.3. The neutron transport is run with the MCNPX code [99], that is coupled to the CINDER90 evolution module [100], giving the fission rates as a result. Note that in this step, we no longer assume a point-like reactor core, but include its finite dimensions and thus

$$n_f(t) = \int_R n_f(\vec{x}, t)\, dx^3 = \int_R \frac{P_{th}(t)}{\sum_k \alpha_k(\vec{x}, t) \langle E_f \rangle_k}\, dx^3 \tag{3.8}$$

where the fission fractions $\alpha_k(\vec{x}, t)$ now depend both on the time and spatial fission distribution. In practice, the simulation output lists the spatial distributions of each of the fissile isotopes, as well as their temporal evolutions during the cycle. The combined statistical and systematic errors on the fission rates during burn up are calculated to be less than 3% for ^{235}U, ^{238}U and ^{239}Pu and about 10% for ^{241}Pu. The dominant systematic sources come from the geometrical approximation, the treatment of beryllium poisoning[1] and the limited number of unique fuel materials in the simulation [101].

The inputs for the BR2 reactor simulation model that have an impact on the expected fission rate and their associated uncertainties for the ^{235}U isotope are summarised in table 3.1. The statistical uncertainty on this MC simulation can be minimised to less than 1% by increasing the number of simulated

[1] Beryllium poisoning is the process where the strong neutron absorbers ^{3}He and ^{6}Li are created from the interaction of reactor neutrons with beryllium, which causes a reduction of the reactivity.

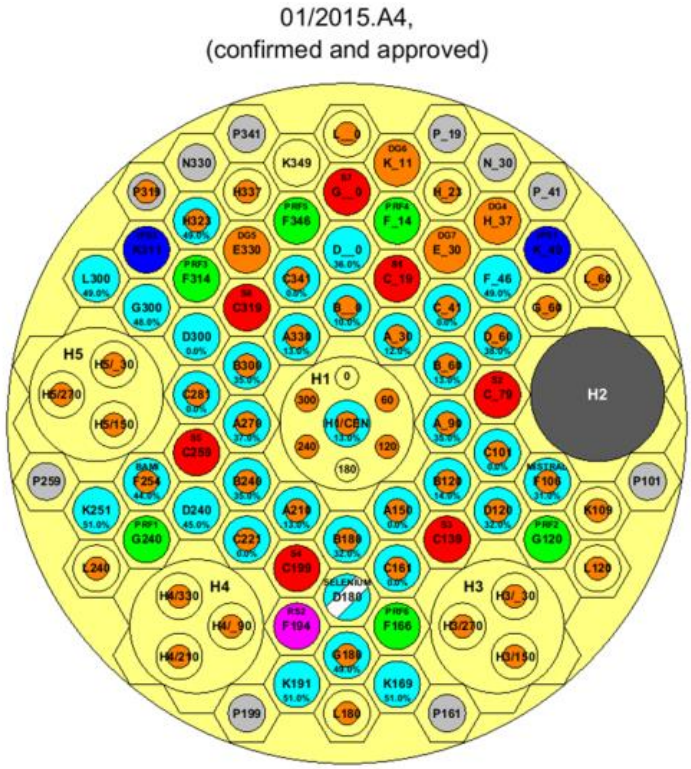

Figure 3.3: The BR2 loading map of cycle 01/2015A. The fuel elements are indicated in blue, the control rods in red, the irradiation experiments in green and light grey, the SIDONIE device for silicon irradiation in dark grey and the reactor's beryllium matrix in yellow. [102]

neutrons. The combined uncertainty on the fission rate of 8.5% is dominated by the uncertainty on the reactor power measurement. For the ^{238}U and ^{239}Pu isotopes, the combined uncertainties are of the same order, while it goes up to 16% for ^{241}Pu.

Table 3.1: Conservative estimates for the relative uncertainties on the main input parameters for the fission rate calculation with the BR2 reactor model. The quoted values concern the ^{235}U isotope. [103]

Parameter	Relative uncertainty
statistical	0.010
geometry	0.016
Be-poisoning	0.005
fission energy	0.010
unique materials	0.011
combined	**0.024**
P_{th}	0.080
combined	**0.085**

An example of the time evolution of the isotopes' fission rates in the BR2 reactor is shown in figure 3.4.

3.1.2 Reactor antineutrino spectra

To derive a number of emitted antineutrinos, N_{em}, from the number of fissions, additional information on the isotopes' neutron-rich fission products, namely their β-decay spectra, is needed. For a given $\overline{\nu}_e$ energy E we can write

$$N_{\text{em}}(E) = \int_t n_f(t) \sum_k \alpha_k(t) S_k(E) \tag{3.9}$$

Here, $S_k(E)$ is the antineutrino yield or spectrum per fission of the isotope k. These spectra are weighed with the fraction of fissions undergone by each isotope, $\alpha_k(t)$, and summed over all four isotopes. The combined antineutrino spectrum can be written as

$$S_{tot}(E,t) = \sum_k \alpha_k(t) S_k(E) \tag{3.10}$$

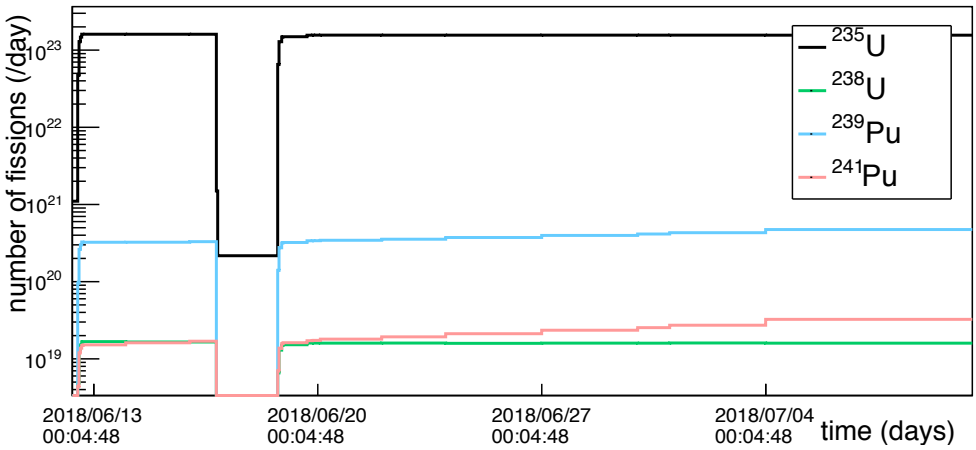

Figure 3.4: The fission rates of the four fissile isotopes: ^{235}U, ^{238}U, ^{239}Pu and ^{241}Pu during cycle 3 of the BR2 reactor in 2018. Given the log scale, it is clear that ^{235}U contributes more than 99.9% of the fissions.

The S_k's need to include all possible outcomes of the fission reaction and depend on the variety of configurations for the β-decays of the resulting daughter nuclides. In practice, the β-spectra emitted by the reactor are calculated first and are then translated to $\overline{\nu}_e$-spectra. To obtain these combined spectra two main methods exist: the summation method and the conversion method.

The summation method is a so-called *ab initio approach*, where the β-spectrum from fissile isotope k is computed by summing the contributions of each of the possible fission products $\mathcal{F}_k$ [104]:

$$S_k(E_\beta) = \sum_{\mathcal{F}_k}^{N_{\mathcal{F}_k}} A_{\mathcal{F}_k}(t) \times S_{\mathcal{F}_k}(E_\beta) \tag{3.11}$$

where $A_{\mathcal{F}_k}(t)$ is the activity of fission product $\mathcal{F}_k$ at time t for fissions of isotope k. $S_{\mathcal{F}_k}(E_\beta)$ is the β-spectrum of the fission product $\mathcal{F}_k$ and is an aggregate of the spectra of all possible β-decay channels, weighed by their branching ratio. The fission product activity and information on the involved β-spectra can be retrieved from nuclear databases. More details on the calculation of the $S_{\mathcal{F}_k}(E_\beta)$ can e.g. be found in reference [104].

A single β-branch spectrum with energy E_β can be translated to an $\overline{\nu}_e$-spectrum in $E_{\overline{\nu}_e}$ by using the simple energy relation $E_{\overline{\nu}_e} = E^b_{0\mathcal{F}_k} - E_\beta$, where

$E^b_{0\mathcal{F}_k}$ is the end-point energy of the branch b of the fission product $\mathcal{F}_k$. This implies that for the summation method the $\overline{\nu}_e$-spectra can be determined with the same accuracy as the β-spectra.

The conversion method relies on measured reference β-spectra of the four fissile isotopes. The electron spectra from ^{235}U, ^{239}Pu and ^{241}Pu fissions were measured with high precision in the 80's at the ILL reactor in Grenoble, France [105]. The fissions were induced by the irradiation of ^{235}U/^{239}Pu/^{241}Pu target foils with reactor neutrons and the β-spectra were acquired after an irradiation time between a few hours and 2 days. The β-spectrum of ^{238}U was measured much later at the FRMII neutron source in Garching, Germany [106].

A method to convert these to $\overline{\nu}_e$-spectra exists in fitting the β-spectrum shape with a large number of virtual β-decay branches of an assumed shape. The fitted spectra of those branches are then converted to antineutrino spectra via the relation $E_{\overline{\nu}_e} = E^v_0 - E_\beta$, where E^v_0 is now the end-point energy of the virtual branch i.

Both methods for the calculation of reactor antineutrino spectra have their advantages and disadvantages. Spectra calculated with the conversion method need to be corrected for so-called *off-equilibrium effects*. This follows from the fact that β-decays have finite lifetimes and as a consequence the spectrum requires some time from the beginning of the fission process to reach a steady equilibrium. Due to the limited measurement time for the ILL reference spectra, compared to that of antineutrino experiments, the flux contributions of long lived fission products are not included. This is taken into account with off-equilibrium corrections.

The summation method, on the other hand, depends on the knowledge of a large number of variables, such as the fission yields, the lifetimes of the daughter nuclei, the individual beta branching ratios, etc.. Systematic effects and missing information in nuclear databases lead to relatively large uncertainties on the predicted spectra.

However, by combining the methods and using information from nuclear databases for the conversion of the reference spectra, very precise predictions of antineutrino spectra can be made.

For the SoLid experiment, spectra calculated with both methods are provided by a team of SCK•CEN and Subatech staff. For each of the calculation methods, they use, in addition to the MCNPX/CINDER90 simulation of the reactor, the MURE (MCNP Utility for Reactor Evolution) code to track the

burn-up of the fissile products.

The conversion method is then implemented by coupling the simulation for the complete reactor model with converted neutrino spectra from a reference of choice; Huber [107], Mueller [104], ... The off-equilibrium effects are implemented as explained in reference [104].

The evaluation of the antineutrino spectra with the summation method is based on a more extensive use of MURE. In addition to the simulation of the reactor core evolution, the MURE code can compute the associated antineutrino energy spectrum. For this purpose, it is coupled to nuclear databases containing all beta decay branches of the fission products for each fissile isotope.

In figure 3.5, examples of the spectra resulting from the conversion model from Huber for ^{235}U, ^{239}Pu and ^{241}Pu and the Mueller prediction for ^{238}U and for a recent summation calculation by Estienne et al. [108] are shown. The ratio of the summation spectra to the conversion results is shown in figure 3.6.

The uncertainties on the predicted spectra are derived from the errors on the input models and/or the variables from nuclear databases. The uncertainty on the ^{235}U yield determined with the conversion method is shown in figure 3.7. The errors increase with increasing energy, but remain below 2% (4%) for the lower (higher) halve of the $E_{\overline{\nu}_e}$ range of interest. For the spectra calculated with the summation method, an overall uncertainty of 2% is generally quoted. However, the actual errors are expected to be larger, as the complex and often unknown correlations between fission yields are not taken into account in these quoted values [109].

3.1.3 Detector acceptance

Since the antineutrino flux from the reactor is assumed to be isotropic, only a fraction of the emitted antineutrinos reaches the detector volume. The number of crossing antineutrinos with energy E, per detector cell i, can be expressed as

$$N_{\text{cross}}(E) = \int_R \frac{A_i}{4\pi L_i^2(\vec{x})}\, N_{\text{em}}(E)\, d^3\vec{x} \tag{3.12}$$

where A_i is the surface area of cell i and the integration runs over the reactor core volume R. The distance L_i depends on the detector cell i and on the $\vec{x} = (x, y, z)$ integration point in the reactor core where the antineutrino originates. The integration will therefore slightly differ between reactor cycles, depending on the reactor fuel loading map. It also follows that the number

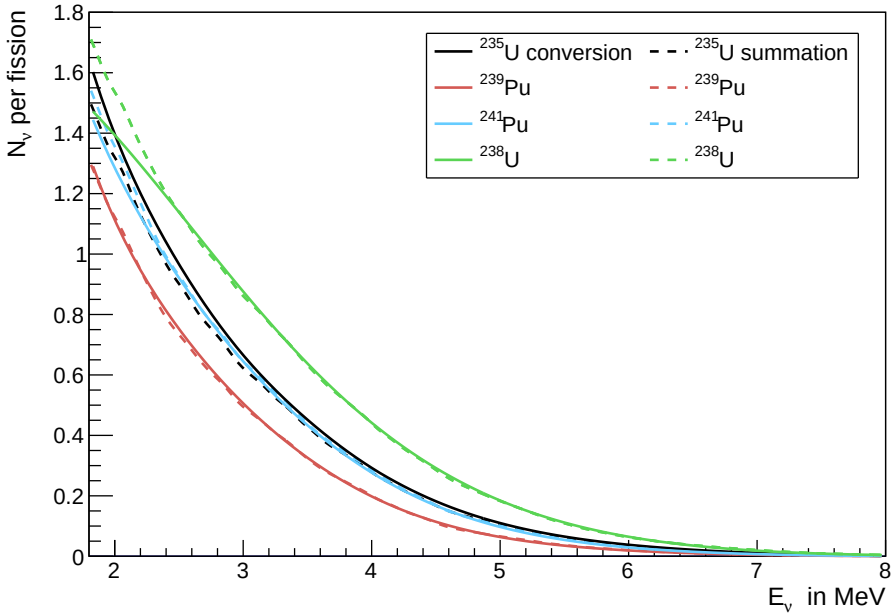

Figure 3.5: The antineutrino yields or spectra for the four fissile isotopes as implemented in the SoLid analysis framework. The conversion results for ^{235}U, ^{239}Pu and ^{241}Pu are taken from the Huber data [107] and from Mueller et al. [104] for ^{238}U. The summations results are taken from the publication by Estienne [108].

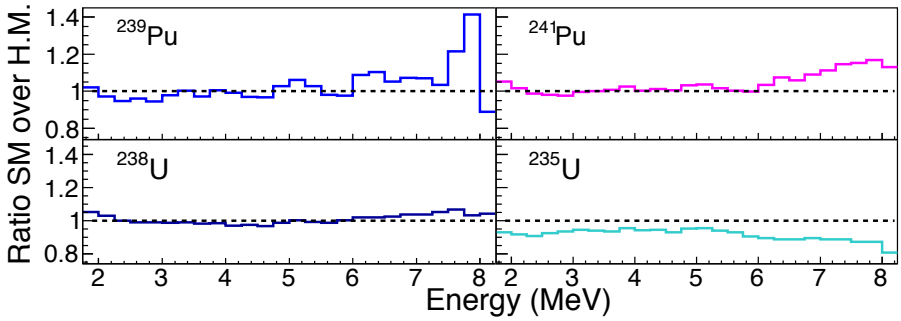

Figure 3.6: Ratio of the antineutrino spectra calculated with the summation method of [108] to the converted spectra for ^{235}U, ^{239}Pu, ^{241}Pu [107] and ^{238}U [104].

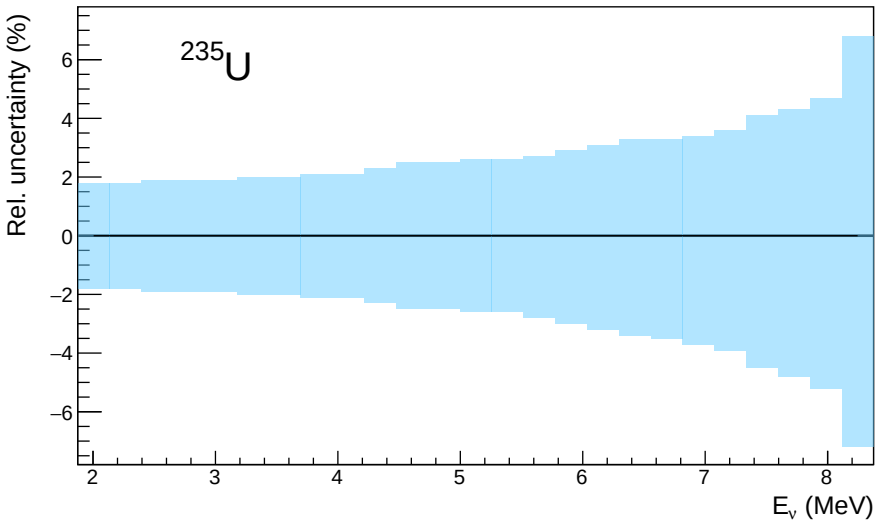

Figure 3.7: Relative uncertainty on the ^{235}U antineutrino spectrum calculated with the conversion method [107].

of crossing antineutrinos decreases quadratically with the distance L_i.

Although the SoLid detector is relatively close to the reactor core, the total detector acceptance, defined as the fraction of emitted antineutrinos that crosses the detector, is only $\approx 0.11\%$. To optimise the signal simulation, an isotropic signal generation should thus be avoided. Therefore, for each event in a certain point of the reactor core volume, a random point in the detector volume is immediately drawn and the distance $L_i(\vec{x})$ is determined. The geometrical efficiency is taken into account by the weight $1/4\pi L_i(\vec{x})^2$. The signal generation will be discussed in more detail in section 3.3.

For now, we will simplify the treatment of the $L_i(\vec{x})$ and write equation 3.12 as

$$N_{\text{cross}}(E)/\text{area} = \frac{1}{4\pi L^2} N_{\text{em}}(E). \tag{3.13}$$

In addition, we note that equations 3.12 and 3.13 neglect possible interactions of the antineutrinos with matter between the point of emission and the detector. In the full neutrino simulation, described in section 3.3, however, additional proton-rich material is taken into account.

3.1.4 IBD cross section

Equation 3.13, together with equation 3.9, shows how the number of crossing antineutrinos can be calculated. To find the number of *interacting* antineutrinos, one needs to take into account the inverse beta decay cross section σ_{IBD}, which defines the probability for an antineutrino to interact with a proton, and multiply with the number of target protons N_p in the detector volume.

The cross section is an energy-dependent variable and, as discussed before, there is a threshold at 1.8 MeV for the IBD reaction to proceed. In order to find a total number of antineutrino interactions, one thus needs to integrate over the full available energy range from 1.8 to approximately 10 MeV (see figure 2.3). We find that

$$N_{\text{int}} = \frac{N_p}{4\pi L^2} \int_E \sigma_{IBD}(E)\ N_{\text{em}}(E)\ dE \tag{3.14}$$

$$= \frac{N_p}{4\pi L^2} \int_E \sigma_{IBD}(E) \int_t n_f(t) \sum_k \alpha_k(t) S_k(E)\ dE\ dt \tag{3.15}$$

In literature, one mostly gathers all energy dependent terms in a separate factor $\langle \sigma_f \rangle$, called the mean cross section per fission. For each fissile isotope k, it is given by

$$\langle \sigma_f \rangle_k = \int_E S_k(E)\ \sigma_{IBD}(E)\ dE \tag{3.16}$$

Summing over all four isotopes, accounting for their fission fractions, we get

$$\langle \sigma_f \rangle(t) = \sum_k \alpha_k(t) \langle \sigma_f \rangle_k \tag{3.17}$$

The IBD cross section $\sigma_{IBD}(E)$ in equations 3.15 - 3.17 can be defined more precisely as the ratio of the probability per target atom for the reaction to occur, to the incident flux of antineutrinos. It depends on the positron energy and momentum - which are directly related to the antineutrino energy - as

$$\sigma_{IBD} = \kappa E_{e^+} p_{e^+}. \tag{3.18}$$

The prefactor κ can be derived from weak interaction theory as

$$\kappa = \frac{G_F^2 |V_{ud}|^2}{\pi} (1 + \Delta^R)(f^2 + 3g^2) \tag{3.19}$$

where G_F is the Fermi coupling constant and V_{ud} is a mixing parameter of the Cabibbo-Kobayashi-Maskawa (CKM) matrix [110]. The Δ^R includes inner

radiative corrections, the f and g are respectively the vector and axial-vector coupling constants. The κ-factor can also be derived from the neutron lifetime τ_n as[2]

$$\kappa = \frac{2\pi^2}{m_e^5 \, f^R \, \tau_n} \tag{3.20}$$

Here, m_e is the positron mass and f^R is a phase space factor that also includes all relevant corrections, except the inner radiative corrections Δ^R. More details on both equations for the cross section can be found in e.g. [111].

Both methods are implemented in the SoLid analysis framework and result in $\kappa = (0.958 \pm 0.003)10^{-43}\text{cm}^2\,\text{MeV}^{-2}$ for equation (3.19) and $\kappa = (0.962 \pm 0.001)10^{-43}\text{cm}^2\,\text{MeV}^{-2}$ for equation (3.20) [112]. The small tension between the results is a well known issue, that is expected to be resolved by future neutron experiments. For the calculation based on the neutron lifetime, radiative corrections are taken from reference [113] or [114].

The proton content N_p is derived from the masses and proton densities of the different detector materials. The masses of all detector components were carefully measured during the construction phase and are listed in table 3.2. The quoted proton densities are given by the producers of the components or taken from literature. The PVT scintillator contributes 94.10% of the total proton content in the active detector volume.

Table 3.2: Overview of the SoLid detector component masses, their proton (H) density and total and relative proton content as implemented in the SoLid detector simulation. The uncertainty on the proton content is 0.1%.

Detector material	Mass [kg]	H $\times 10^{22}$/cm^3	H content	
			abs	rel. [%]
PVT	1.5293×10^3	5.213	7.7921×10^{28}	94.10
^{6}LiF:ZnS(Ag)	3.4190×10^1	2.34267	3.5939×10^{26}	0.43
Li backing	1.6206×10^1	3.4596	4.0633×10^{26}	0.49
Tyvek wrap+sheet	3.2381×10^1	3.2629	2.7826×10^{27}	3.36
WLS fibre core	2.1601×10^1	4.85696	9.9917×10^{26}	1.21
WLS fibre cladding	7.1660×10^0	5.72629	3.4351×10^{26}	0.42

In addition to the materials listed in table 3.2, surrounding plastics such

[2]The involved CKM matrix element and other constants are the same for both processes, since IBD reactions are basically inverse neutron decays.

as HDPE and PPL shielding are taken into account in the detector simulation. These introduce large masses that can produce IBD events near the sensitive volume, of which a small fraction could trigger the detector.

3.1.5 Summary

The final formula, representing the total number of expected events, is

$$N_{\text{int}} = \int_R \int_t \frac{N_p}{4\pi L^2(\vec{x})}\ n_f(\vec{x},t)\ \langle\sigma_f\rangle(t)\ dt\ dx^3 \tag{3.21}$$

We note again that this equation does not include the detection efficiency and reconstruction effects and thus only shows the true number of IBD events.

In addition, we want to stress that a number N^i_{int} can be calculated for each individual detector cell i, by using its distance $L_i(\vec{x})$ and specific proton content N^i_p.

Using all information from the above sections, this expression can be written in more detail as

$$N_{\text{int}} = \int_R \int_t \int_E \ \frac{N_p}{4\pi L^2(\vec{x})} \frac{P_{th}(t)}{\sum_k \alpha_k(\vec{x},t)\langle E_f\rangle_k}\ \sum_k \alpha_k(\vec{x},t) S_k(E)\ \sigma_{IBD}(E)\ dE\ dt\ dx^3. \tag{3.22}$$

where all critical variables are visible.

Equations 3.21 and 3.22 are generally applicable and common for all reactor antineutrino experiments. They represent the expected number of antineutrino interactions in the case of no flavour oscillations. To include the possibility of oscillations to a sterile state, the equations can be multiplied with the disappearance probability of equation 1.26:

$$P_{\bar{\nu}_e \to \bar{\nu}_e} = 1\ -\ \sin^2(2\theta_{14})\ \sin^2\left(\frac{\Delta m^2_{41} L}{4E}\right) \tag{3.23}$$

where $\sin^2(2\theta_{14})$ and Δm^2_{41} are the oscillation parameters and L and E are the same variables as in the equations above, representing the distance and neutrino energy, respectively.

3.2 Binned prediction for the SoLid experiment

To probe sterile neutrino oscillations, the SoLid experiment measures the neutrino flux over a certain baseline, defined by the length of the detector. The

recorded reactor-detector distances are grouped in L-bins with a size that corresponds to a certain number of detector planes. A wider binning groups the events per module, resulting in a total of 5 L-bins. For a data set with higher statistics, a finer binning per 2 detector planes, giving a total of 25 bins, could be chosen. In addition, the detected events vary in energy and the gathered data is binned in measured energy E. As the detector and reconstruction effects have so far been excluded, the signal prediction as given by equation 3.22, can be binned in terms of the true distance $L_{\overline{\nu}_e}$ and true neutrino energy $E_{\overline{\nu}_e}$.

The expected number of IBD events for the ith length bin $[L_i, L_{i+1}]$ and jth neutrino energy bin $[E_j, E_{j+1}]$, where we have dropped the $\overline{\nu}_e$-subscript for simplicity, is written as

$$N_{\text{int}}^{(ij)} = \int_R \int_t \int_{E_j}^{E_{j+1}} \frac{N_p^{(i)}}{4\pi L_i^2(\vec{x})} \frac{P_{th}(t)}{\sum_k \alpha_k(\vec{x},t)\langle E_f\rangle_k} \sum_k \alpha_k(\vec{x},t) S_k(E)\, \sigma_{IBD}(E)\, dE\, dt\, dx^3 \tag{3.24}$$

and, as explained in the previous section, can be modified with the oscillation probability $P_{\overline{\nu}_e \to \overline{\nu}_e}$ for those values of L and E. Note that the range of the integral in E is limited to the bin $[E_j, E_{j+1}]$, which alters the mean cross section per fission:

$$\langle \sigma_f \rangle_k^{(j)} = \int_{E_j}^{E_{j+1}} S_k(E)\, \sigma_{IBD}(E)\, dE. \tag{3.25}$$

3.3 Neutrino generator

To provide representative neutrino spectra that allow a comparison with the measured data, a dedicated framework for the generation of large numbers of neutrino events was designed by the SoLid collaboration. The framework is called SoLO and, as described above, it has to combine the BR2 reactor flux model, the detector acceptance and the neutrino interaction process in the detector. On the one hand, the results of the reactor core simulations, such as the spatial fission distributions, the fission rates and the related energy spectra, are fed to the SoLO code. On the other hand, the full detector geometry is loaded from a GDML file.[3] SoLO thus acts as an interface between the reactor and detector simulations and uses this information to generate a detailed signal prediction.

[3] GDML stands for Geometry Description Markup Language, and is a code specifically designed for the modelling of complex detectors. The GDML file with the SoLid detector geometry is based on the Geant4 detector simulation, described in chapter 4.

The generation of neutrino interaction vertices happens on a voxel-by-voxel basis, where the detector volume is split in voxels of $5 \times 5 \times 5$ cm^3. We would like to emphasise that apart from the SoLid detector cubes, that nicely match one such voxel, all surrounding, inactive material in the simulation is also divided in these voxels. The neutrino generator code then carries out the following steps for each voxel:

1. The signal normalisation is calculated for each isotope k, as deduced from equation 3.24.
2. According to the normalisation, a number of signal events is generated per isotope k. A 100 times more events are generated to reduce statistical fluctuations.
3. For each signal event :
    (a) A position inside the reactor core is picked, according to the given fission map.
    (b) A neutrino energy value is drawn, according to the predicted $E_{\overline{\nu}_e}$ spectrum.
    (c) An interaction point inside the detector voxel is picked.

The SoLO code thus generates events with a certain energy E, momentum $\vec{p}$, a precise reactor-detector distance L based on the fission position in the reactor and the picked interaction point (x, y, z) in the detector. This information allows us to determine the L/E distributions of the neutrinos interacting in each of our detection cells. We should note that the resulting number of events and related histograms need to be scaled back with a factor 100, to obtain the correct normalisation.

The neutrino predictions are generated for each cycle of the BR2 reactor, taking into account the specific power history and the core loading map of that cycle. Table 3.3 shows the predicted number of IBD events in the SoLid detector for the first 5 BR2 reactor cycles of 2018.

An illustration of the distribution of antineutrino interactions over the SoLid detector volume is given in figure 3.8. First of all, the materials with a high proton density, such as the frame lining and shielding plates from HDPE, as well as the cell structure of the PVT cubes are clearly visible in this figure. In addition, one can see the expected quadratic reduction of the number of interacting neutrinos with distance L (= z in the figure), as described in section 3.1.3.

After the antineutrino event generation, the next step is to reproduce the kinematics of the IBD reaction products (e^+, n) and to simulate the particle

Table 3.3: The first 5 BR2 reactor cycles of 2018, with the start and end date, and the corresponding number of calculated reactor fissions and predicted number of IBD events in the active material of the SoLid detector. [115]

Reactor cycle	Start date	End date	N_{fiss} [10^{24}]	N_{IBD}
Cycle 1/18	06/02/18	27/02/18	3.12	24159.3
Cycle 2/18	24/04/18	22/05/18	4.63	35729.4
Cycle 3/18	12/06/18	10/07/18	4.08	31558.6
Cycle 4/18	21/08/18	11/09/18	3.24	25083.3
Cycle 5/18	02/10/18	23/10/18	3.13	24232.0

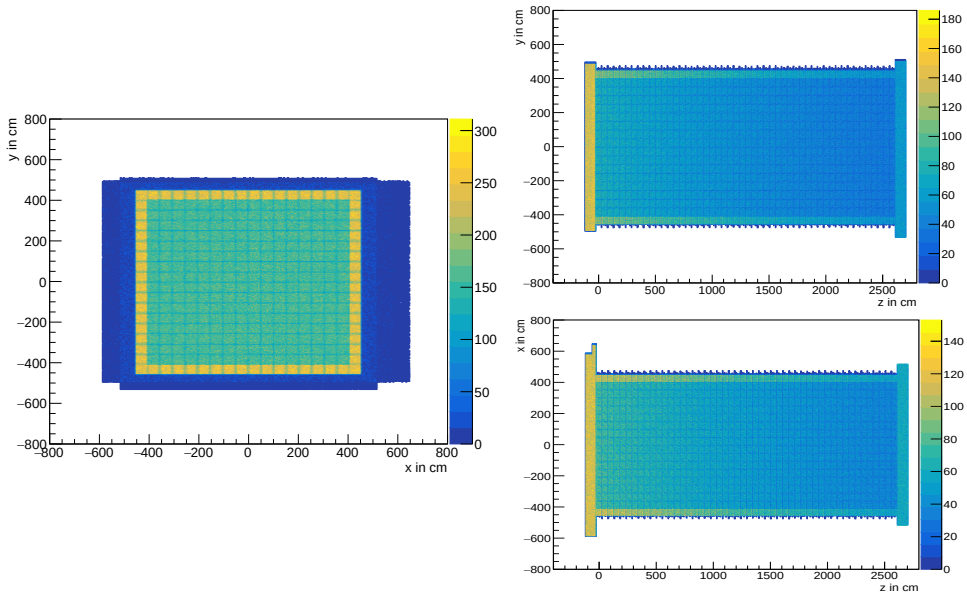

Figure 3.8: The distribution of antineutrino interactions in the SoLid detector volume for a large Monte Carlo sample of $\mathcal{O}(10^5)$ events: front view (left), side view (top right), top view (bottom right).

transport in the detector, which is carried out by the Geant4 detector simulation. The resulting information is then combined with the modelling of the response of our detector in terms of detection efficiency, energy resolution, electronics noise, etc. and the effects of the signal reconstruction algorithms, finally allowing to compare the predicted signal with the measured data. These detector simulation and signal reconstruction steps are discussed in the following chapter.

3.4 Summary

This chapter gave an overview of the inputs required for the IBD signal prediction in the SoLid detector.

A crucial part are the reactor-related calculations, which determine the expected produced antineutrino flux. As discussed in sections 3.1.1 and 3.1.2, these calculations involve the knowledge of an enormous amount of parameters, that are not always directly available. For the SoLid experiment, the error budget on the determination of the flux is mainly driven by the uncertainty on the BR2 reactor power measurement.

In sections 3.1.3 and 3.1.4, the number of interacting antineutrinos was derived by combining the emitted number of antineutrinos with the geometrical efficiency of the SoLid detector, its proton content and the IBD cross section. Equation 3.21 summarises the prediction of the expected IBD signal for the data taking period of the experiment. As discussed in section 3.2, this prediction is in practice binned in the two parameters $E_{\overline{\nu}_e}$ and $L_{\overline{\nu}_e}$, which are the neutrino energy and its distance travelled.

The implementation of the prediction is fully based on Monte Carlo simulations, which are combined in and partly performed by the SoLO framework. In section 3.3 the neutrino generation method of the SoLO code is treated, showing how the SoLid experiment builds a set of neutrino events for a sterile neutrino search.

Detector response and event reconstruction 4

In the previous chapter, the full chain of calculations for the signal prediction was described. The resulting prediction gives a number of expected IBD interactions in the SoLid detector, but - as explained - this does not include the detector response yet. Since the detection and reconstruction effects can not be treated analytically, they are studied and accounted for using Monte Carlo simulations. This chapter briefly describes the detector and readout simulations in the first sections. Next the reconstruction algorithms, that are also applied on real data, are detailed. Further on, a tool to efficiently account for these detector effects when building the signal prediction, called the migration matrix, is discussed.

4.1 Geant4 detector Monte Carlo

The SoLid detector is simulated with a Geant4 [116] Monte Carlo (MC) code, called SoLidSim. It models the transport of particles through the detector materials and determines the energy deposits in the scintillators.

For the implementation of the geometry of the experimental set-up, three levels can be distinguished, according to the degree of detail required and their relative scales [82]:

- The full Phase I detector is simulated with a high level of accuracy. The detailed geometry and composition of the detection cells, the optical fibres, MPPCs and mirrors, the aluminium frames and neutron reflectors are implemented.
- The main volumes and components of the container, including the full instrumentation inside it, are modelled without reproducing the fine patterns, but with the objective of a positioning of the material that is

close to reality. An exception is made for the CROSS calibration system, that is modelled with precision, because of its proximity to the detector.
- The BR2 reactor and its water basin, plus the experimental hall as well as the confinement building are reproduced schematically. These structures affect the transport of cosmic radiation, such as muons and neutrons, and are thus necessary for the estimation of the background radiation in the detector.

Given the geometry and depending on the input particles and the selected physics processes, the particle transport through these implemented volumes is simulated next.

As discussed in section 3.3 of the previous chapter, the collaboration has developed a dedicated neutrino event generator to produce IBD events according to the BR2 specific neutrino energy spectrum and the position distribution of the interaction vertices provided by the SoLO code.

For each of these IBD events, the positron scintillation and annihilation, as well as the neutron thermalisation and capture, are simulated by the SoLidSim code. The modelling of the energy deposited by the positron is relatively straightforward and is based on the standard physics processes available in Geant4. For the neutron modelling in the SoLid detector, however, no analytical models are available. This is a consequence of the particular SoLid detector concept, where the IBD neutrons are thermalised to an energy of about 0.025 eV before they can be captured on ^{6}Li. To simulate the elastic scattering of these thermal neutrons, the collaboration therefore relies on reference cross-sections measured for polyethylene [117], the chemical composition of which is very close to that of PVT. These features are imported in GEANT4 via dedicated neutron libraries.

In addition to these IBD-related generators and other, more standard ones already implemented in the Geant4 software, the collaboration added particle generators for the reproduction of the following calibration sources:

- the ^{252}Cf and AmBe neutron sources, with the radiation energy spectra taken from the ISO reference [118],
- the ^{22}Na, ^{137}Cs and ^{207}Bi gamma and positron sources and their radioactive decay,

and the following experimental backgrounds, see section 5.2:

- the bismuth-polonium decay chain,
- the cosmic muons, with the CRY generator [119], cross-checked with the Guan [120] and Reyna [121] models,
- atmospheric neutrons, using the Gordon parametrisation [122].

As a result, the Geant4 MC provides the collaboration with the spatial and temporal distributions of the expected energy deposits for each of the possible interactions in the SoLid detector.

4.2 Readout simulation

In a next step, the output of the SoLidSim is coupled to a readout simulation, referred to as ROsim. This code aims to reproduce the detector response, first in terms of photon production and collection, and secondly in terms of the response of the MPPCs and readout electronics. As a result, it translates the simulated energy depositions to data-like output waveforms.

For the optical simulation, ROsim generates the production of scintillation photons in the PVT and in the ZnS, taking into account the particle dependent energy response according to Birks' law [123]. The loss of photons due to scattering and absorption in the PVT, ^{6}LiF:ZnS(Ag) sheets or Tyvek is also modelled. The photon transmission by the WLS fibres is then reproduced, correcting for attenuation effects and the reflection on the Mylar mirrors. The number of photons reaching the MPPC is randomised according to a Poisson distribution and spread in time according to the time constants of the PVT and ZnS scintillators. All of the parameters of the implemented model are either derived from the manufacturer's data, or tuned in order to accurately match actual (calibration) measurements obtained with the detector.

To reproduce the response of the MPPCs, studies of various MPPC properties such as the thermal noise and the crosstalk and their dependancy on the gain settings were performed. The obtained MPPC response model then allows to convert the generated photons into digital electrical signals, or waveforms, in units of ADC.

Finally, the same trigger logic (cf. section 4.3.1) as is used in the data acquisition systems can be applied to the simulated waveforms. The resulting simulated data is thus available in the same format as the raw detector data and can be analysed using the same analysis code, called Saffron2, which is described in the next section. In practice, the ROsim code is incorporated in the Saffron2 framework, making the simulation processing more efficient and structured.

4.3 Event reconstruction

For the offline reconstruction and analysis of the (simulated) data, the Saffron2 C++ code was developed. The event reconstruction exists of the selec-

tion, combination and identification of the electronic signals to form physics related objects. We will shortly describe each of these steps in this section. Some of this work, namely the data selection, is already partly addressed by the trigger system in the online readout electronics and is also briefly included here.

4.3.1 Data selection

As mentioned, the trigger system of the online electronics already performs a preselection of the data. Its purpose is to avoid too large amounts of recorded (uninteresting) data, which would make the practical operation and data analysis very inefficient. The SoLid trigger system processes the incoming signals in so-called waveform blocks, which correspond to 256 waveform samples of 25 ns each, or a total time window of 6.4 µs. The triggers are implemented on a per-plane level and use three algorithms [76]:

- a random trigger for a full and simultaneous detector readout at a rate of 1 Hz, that is used to determine the operational properties of the detector and to monitor its stability and proper functioning,
- a threshold trigger based on two or more signals exceeding 20 PA ($\sim$ 1 MeV) that are in coincidence and located on a pair of orthogonal fibres, designed to select scintillation signals created in the PVT,
- and a neutron trigger, based on an algorithm that counts the number of waveform peaks over a certain threshold (PoT) and within a certain time window, as shown in figure 4.1, that selects the signals produced by the ZnS scintillator.

For each trigger type, all channels in the triggered detector plane are read out. In case of a neutron trigger, three planes in front and behind the triggered plane are read out in addition. The time buffer, i.e. the total time window that is read out for a triggered waveform block, is set per trigger type and varies from one (=6.4 µs) or two (=12.8 µs) waveform blocks for the threshold and random trigger respectively, to a long window of [-500 µs, 200 µs] for the neutron trigger. As a consequence, the total recorded data rate of the experiment is dominated by the neutron trigger, and is about 21 MB/s or 1.6 TB/day on average during physics mode.

For the offline reconstruction, the Saffron2 code reads in the recorded waveform blocks and processes them per so-called *cycle*. These cycles are constructed by adding up consecutive waveform blocks, until the time between them exceeds a given value - i.e. when there is a long enough period during which no blocks are recorded - and the cycle is ended. In this way, the method aims to group physically correlated events in one cycle.

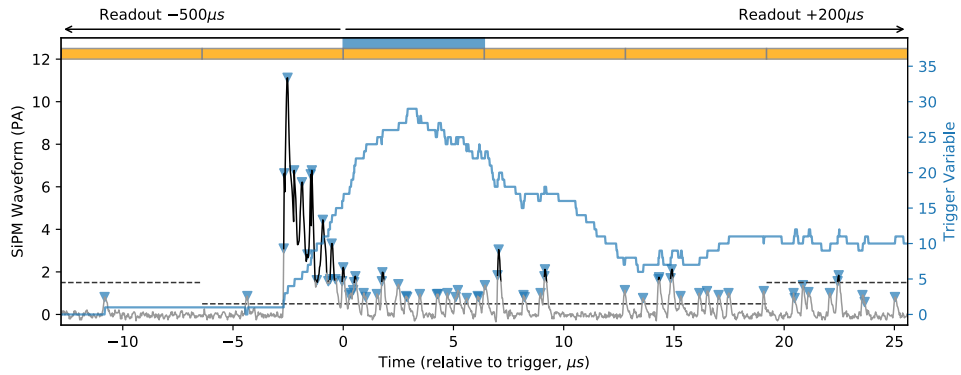

Figure 4.1: Illustration of the neutron trigger algorithm. An example neutron waveform is shown in grey. The dotted black line shows the zero suppression threshold that is set at 1.5 PA per default, but is lowered to 0.5 PA in the time window around a neutron trigger. Local maxima with an amplitude above 0.5 PA, are called *peaks over threshold* (PoT) and are indicated with a blue triangle. The neutron trigger variable, i.e. the number of PoT within a rolling time window of 6.4 µs, is shown in blue. When 17 or more PoT are counted, the corresponding waveform block (rectangles on top) is triggered and an extended time window of 500 µs before and 200 µs after the trigger is recorded to include additional signals that can be useful in the offline analysis.

4.3.2 Event clustering

Although the triggers significantly reduce the data to the signals of interest, the majority of the reconstructed waveforms are still caused by thermal noise. To be able to discern the signal events from this noise, a method of aggregating waveforms based on time coincidence was developed, that allows to combine these waveforms to form coherent events.

In practice, this method exists in the scanning over each waveform within a recorded cycle and searching for waveforms on any other channel that start within less than 175 ns. As a result, all waveforms that originate from correlated light pulses recorded by the MPPCs are aggregated. The set of waveforms building up such a time-related chain form a so-called *cluster*. For each cluster the start and end time (i.e. the detection time of the first sample of the first waveform and last sample of the last waveform, respectively) and the cluster length (i.e. the time between the start and end of the cluster) are determined. The number of waveforms within the clusters and thus the cluster length grow organically and vary for each cluster. A study of this method

has shown that 99% of the waveforms with a peak above 20 PA - that most likely correspond to physical events - are part of a cluster, while the majority of waveforms below 10 PA remain unclustered. The latter waveforms are mostly related to electronics noise and the unclustered waveforms are therefore discarded.

Figure 4.2 shows two examples of clustered waveforms; one for an electromagnetic signal from the PVT scintillator and one coming from scintillation in a neutron screen's ZnS. One can see that the prompt PVT response results in a cluster that is very confined in time, with a small number of included waveform blocks. Due to the relatively large time constant for the ZnS scintillation, on the other hand, the cluster window includes many more consecutive waveform blocks and is significantly longer in time.

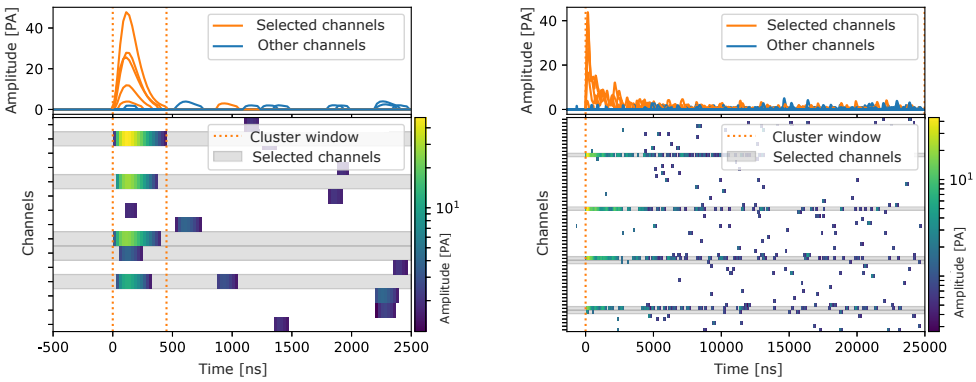

Figure 4.2: Examples of cluster formation for a PVT scintillation signal (left) and a ZnS scintillation signal (right). In the bottom panels, the recorded waveform blocks from different channels are shown. The blocks on the channels indicated in grey are coincident in time and are clustered together. The waveform shapes of the selected channels are shown in orange in the top panels.

4.3.3 Event identification

Once the clusters have been created, the Saffron2 code applies a set of identification algorithms to tag the clusters with their type of interaction. The three types that are differentiated here are successively muons, nuclear signals (NS) and electromagnetic signals (ES). The algorithms mainly use the cluster lengths and the amplitude and/or integral of the included waveforms to perform the identification.

Muons are highly energetic particles, from atmospheric origin. Because of their high energy, they can traverse through multiple detection cells in which they deposit large amounts of energy and leave a clear track. For these tracks, three types are identified:

- Type 0: clipping muons, that cross only one or two cubes at the edge of the detector.
- Type 1: vertical muons, that cross many cubes, but only one detector plane.
- Type 2: muons that traverse multiple detector planes and deposit energy on a large number of detector channels.

Type 1 (2) muons are selected by requiring 11 or more channels in the x- or (and) y-direction, with a detected signal above 200 ADC (∼6.5 PA). The muon track is then reconstructed by combining the horizontal and vertical channels in one (type 1) or multiple (type 2) detector planes, as shown in figure 4.3. The type 0 muons currently have no specific identification procedure implemented and the corresponding clusters will therefore end up in the electromagnetic signal selection, that is explained below.

The total muon signal rate in the Phase I detector is about 250 Hz on average.

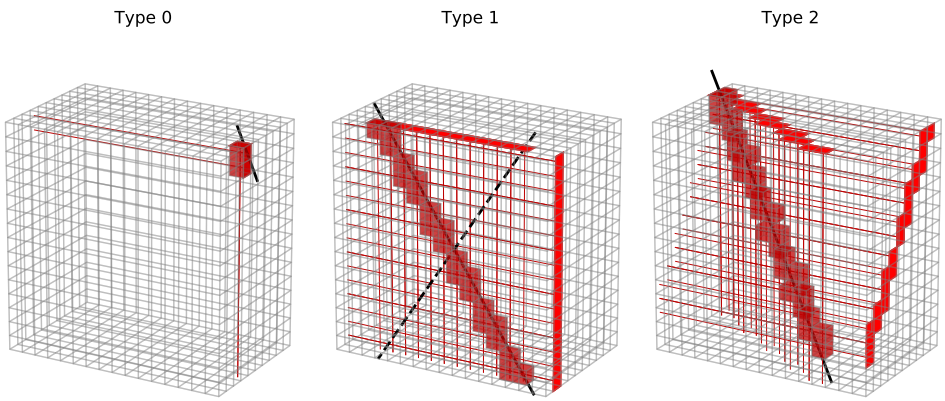

Figure 4.3: Examples of reconstructed muons of type 0, type 1 and type 2 in one module of the SoLid Phase I detector. The black line shows the reconstructed track through the detector. For type 1 muons, that only trigger fibres in one detector plane, two possible tracks can be reconstructed and it is not possible to resolve this ambiguity.

Nuclear signals (NS) are related to the scintillations in the ZnS of the neutron detection screens. NS events thus include the IBD neutrons of interest, but also events induced by neutrons from other processes or α-particles from radioactive decay (cf. section 5.2.2). In a NS candidate cluster, that contains neutron triggered waveforms, the detector cube with the highest recorded number of peaks is first selected. For a further selection, the integral-on-amplitude (IonA) value is evaluated, plus the asymmetry of the energy deposits over the different fibres of the cube. The IonA parameter exploits the fact that NS are mainly characterised by a long scintillation time and multiple waveform peaks, leading to a large integral for relatively low amplitudes. The discrimination power of the asymmetry parameter originates in the position of the four WLS fibres w.r.t. the neutron detection screens in a detector cell (cf. figure 2.5). For the vertical fibre that is fully touching the punched Li-screen, for example, other signal intensities are expected than for the remaining three fibres that have very little or no contact with a neutron screen. A detailed explanation of the NS selection procedure can be found in reference [82]. The NS rate in the SoLid Phase I detector is about 15 Hz.

Electromagnetic signals (ES) are generated by the interactions in the PVT cubes of particles such as photons (γ's), electrons and positrons. We should note that also muons belong to this category, but they are treated separately since they generally deposit a much larger amount of energy over a larger amount of cubes. To first order, the ES are selected as those events that remain after the muon and NS selection. However, since ES are characterised by a very short pulse shape, only clusters with a duration of less than 75 samples are kept. In addition, a signal threshold of 80 ADC ($\sim$ 30 keV) or 144 ADC ($\sim$ 50 keV) is applied, depending on the processing settings. The resulting rate of ES events is of the order of 100 kHz.

4.3.4 Event reconstruction

Once the different signal types are identified, a set of event properties, such as their time, position and energy have to be reconstructed.

For an ES event, the timing is closely related to the trigger time of the event. Its time can be determined very precisely, by exploiting the short and peaked signal shape. For the time reconstruction of an NS event, one can not simply rely on the trigger time, since the PoT requirement is mostly only reached in the tail of the signal. In general, the ES and NS time are therefore determined in the clustering algorithm and are simply taken as the start time

of their corresponding cluster.

As the detected signals are primarily related to channels, and thus to columns or rows of cubes, the position reconstruction is based on combining information of both horizontal and vertical channels. In the ideal case where only two horizontal fibres of the same row of cubes and two vertical fibres of the same column show coincident signals, the result of the cube reconstruction is simple and unambiguous. When more fibres in either or both directions contain a time coincident signal, however, there is no single outcome for the cube position and a more clever reconstruction method is required. The collaboration has therefore implemented the *Maximum-Likelihood Expectation-Maximisation* (ML-EM) method, that selects the most probable outcome based on an iterative study of the different possible configurations, see reference [124].

For the energy reconstruction of the signals two main methods were developed, which are still being evaluated and compared at the time of writing. Both methods are described in more details in the following section.

4.4 Energy estimator

An important aspect of the signal reconstruction is the estimation of the detected prompt energy. As mentioned in section 2.2, this positron energy is directly related to the antineutrino energy. A precise sterile neutrino search thus requires a very good knowledge of the relation between the true positron energy and that of the detected ES event.

As mentioned above, two methods are implemented for the determination of the energy in a reconstructed ES object:

- The first method sums the energies of all recorded channels in the ES event. Its advantage is that it reduces the energy losses in the reconstruction, but the larger number of involved channels makes it more complex.
- The second method selects the reconstructed cube with the maximal detected energy and sums this with the energies in the crown of cubes around it. This method is more robust, as the reconstruction involves less channels, but could have a larger bias and a lower energy resolution.

We should note that the energy reconstruction generally happens in a few steps. First, the ADC values per channel are converted to the corresponding number of PAs, using the gain factor. For the second energy estimator, these per channel values are already combined to get the total number of detected

photons for the selected cubes. Then, the PA value of the cubes (channels) for the second (first) estimator is converted to energy using the light yield per cube (channel), corrected for attenuation and fibre-MPPC coupling, which are determined from calibration data. For the first energy estimator, the per-fibre energies are now summed to determine the total reconstructed energy.

In addition to the choice of the estimator, also the use of a lower or higher threshold in the ES selection has an influence on the reconstructed energy. By using a lower threshold, for example, the efficiency to select the positron annihilation gammas significantly increases, which is very helpful to discriminate the IBD signal from background events, as described in chapter 5. The trade-off is complicated by the increase of thermal noise in the selection with a low threshold and thus an increased complexity of the signal reconstruction.

An simulated example of the detected energy spectrum for both presented estimators is shown in figure 4.4. The two methods are being evaluated at the time of writing, in terms of the resulting energy resolution, the bias and the quality of the data/MC comparison. Once these studies are completed, the effect of the choice of energy estimator on the sensitivity of the SoLid experiment can be derived.

4.5 IBD selection

As described above, different types of events are selected from the recorded data: ES, NS and muons. For the detection of IBD signals, only the related positron and neutron interactions are of interest, which are in principle selected by the ES and NS identification, respectively. However, both ES and NS selections are also populated by a number of events that have a different origin and make up the so-called *background* of the experiment. Additional selection steps, that help in discriminating the IBD signal from the different types of background, are therefore required.

The IBD signal selection is based on the event topology, timing and the reconstructed energies. A full Monte Carlo simulation of the IBD signals and the main background sources, plus on-site measurements of the background rates, are used to determine the most powerful discriminators. The applied IBD event selection methods, with more details on the expected signal properties and the relevant background components, are given in chapter 5. The resulting signal selection for a small sample of the current data set will also be presented there.

We mention this step here to emphasise the actual flow of the analysis, as this IBD selection is already applied before, and included in, the construction

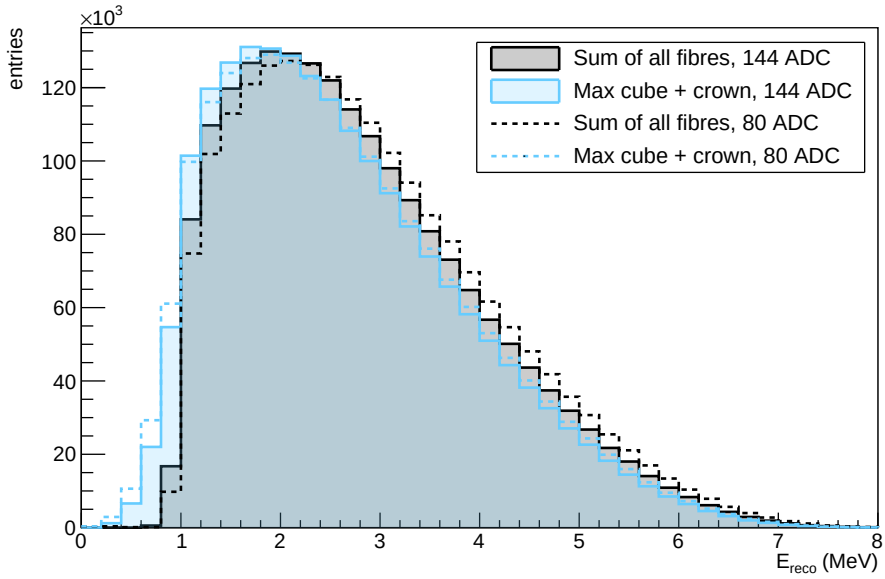

Figure 4.4: The resulting detected energy spectra for the two energy estimators and both reconstruction thresholds of 80 and 144 ADC. The spectra reconstructed with the *max cube + crown* estimator are shifted to lower energies, due to the smaller number of reconstructed fibres. The lower threshold retains more signal and therefore results in a higher reconstructed energy.

of the migration matrix that is described in the following section.

4.6 Migration matrix

The previous sections of this chapter described the steps between an antineutrino interaction in the detector and the set of reconstructed events available for analysis, summarised in figure 4.5.

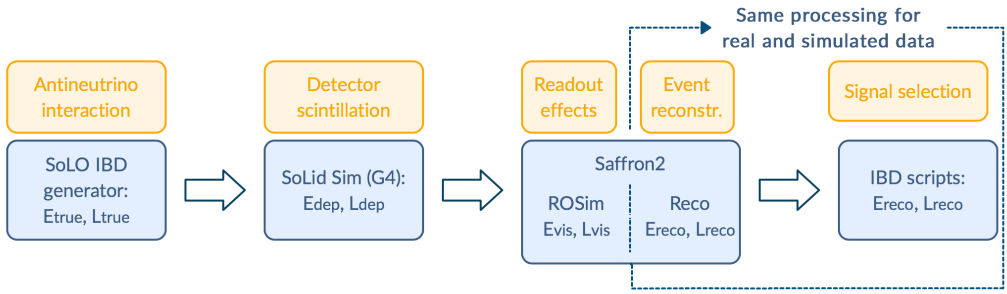

Figure 4.5: Summary of the SoLid simulation scheme from the antineutrino interaction to the reconstructed events. The true neutrino energy, deposited energy, visible energy and reconstructed energy are respectively denoted as E_{true}, E_{dep}, E_{vis} and E_{reco}. The same subscripts are used for the length L. The general processes are given in the yellow boxes, the blue boxes give the related simulation and reconstruction codes. The first three steps involve customised Monte Carlo codes for the signal simulation in the SoLid detector. The last two processing steps in this chain are focussed on the event reconstruction and are shared by the real and simulated data.

For a statistical comparison of the measured data with the predicted reactor antineutrino events, this detector simulation chain has to be applied to all events produced by the *neutrino generator* described in chapter 3. Since the antineutrino prediction depends on the reactor settings as well as on the oscillation parameters Δm^2_{41} and $\sin^2(2\theta_{14})$, many sets of antineutrino events have to be produced. In addition, the detector simulation chain requires a lot of computing time and it is thus not feasible to fully process each antineutrino set.

To address this problem, an object called the *migration matrix* (MM) or *response matrix* is created: a 2D matrix that maps the full detector response. The migration matrix is thus used to translate events from so-called *true space* to *reco space*, a process that is referred to as *folding*. This can be expressed as

a linear relation between the reconstructed events (r_i) and true events (t_j):

$$r_i = \sum_j M_{ij} \cdot t_j \tag{4.1}$$
$$\text{with } M_{ij} = P(\text{reco bin} = i \mid \text{true bin} = j).$$

The opposite process of deducing the original distribution (*true*) from the detected one (*reco*) is called *unfolding*.

A scheme of the MM principle is shown in figure 4.6 and the steps are detailed in the following paragraphs.

4.6.1 Migration matrix construction

For the construction of the MM, the dedicated RooUnfold-package of ROOT [125] was implemented in the SoLO code. First, SoLO is used to combine - event per event - the *true* IBD simulated position and energy ($L_{\text{true}}, E_{\text{true}}$) with the result of the processing of the same event with the full simulation-reconstruction chain ($L_{\text{reco}}, E_{\text{reco}}$). For this purpose, the input and output events are linked one to one throughout the processing chain. The pairs of *true* and *reco* events are then fed to a training algorithm that maps the *migration* of the events. We should note that for a realistic detector modelling, a lot of events are lost in the simulation and reconstruction processes according to the limited detection and reconstruction efficiencies of the experiment. To include these efficiencies, the algorithm keeps track of the missing events as well. Given a large enough number of input events, a reliable response model can be made that maps the probability to retrieve certain reconstructed parameters ($L_{\text{reco}}, E_{\text{reco}}$) for a given ($L_{\text{true}}, E_{\text{true}}$). Since the events are represented by two parameters, we rewrite equation 4.1 to:

$$r_\alpha = \sum_\beta M_{\alpha\beta} \cdot t_\beta \tag{4.2}$$
$$\text{with } \alpha = (i,j) \text{ and } \beta = (k,l)$$

where indices (i,j) now refer to the i^{th} L_{reco} and j^{th} E_{reco} bin, and (k,l) to the k^{th} L_{true} and l^{th} E_{true} bin.

We note that the construction and application of the detector response for folding purposes is rather straightforward. To build the inverse relation for the unfolding of measured events is, however, more complex. This is mainly due to the uncertainties and fluctuations on the limited number of detected events that should not bias or affect the resulting *true* distributions. Various

unfolding algorithms exist and the topic still triggers a lot of interesting discussions between experts. In the remainder of this chapter, we will first of all use the migration matrix to model the SoLid PhaseI detector response and will thus focus on the folding results.

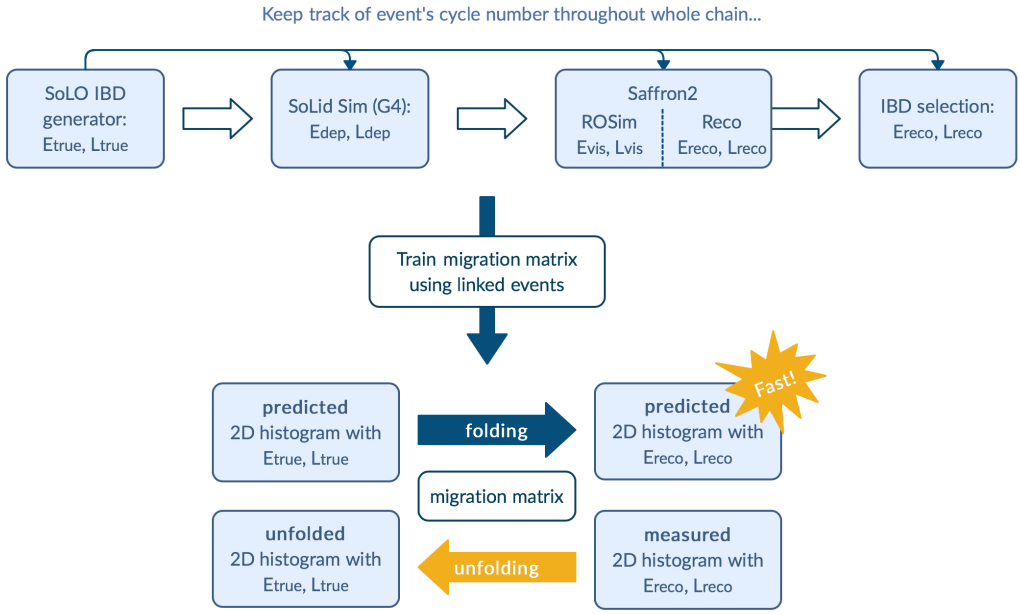

Figure 4.6: Schematic representation of the migration matrix principle.

4.6.2 Resulting migration matrix

The migration matrix that results from the training described above is illustrated in figure 4.7. Here, the response in terms of length reconstruction and that in terms of energy reconstruction are separated to facilitate the interpretation.

When considering the length reconstruction, we should first note that the parameter L_{true} is a three-dimensional parameter, based on the xyz-positions of both the origin and interaction point of the antineutrino. The reconstructed variable L_{reco}, on the other hand, is purely based on the position in the z-direction, that is given by the plane or module in which the event is detected. Therefore, a larger range of L_{true} values will correspond to the same L_{reco} value.

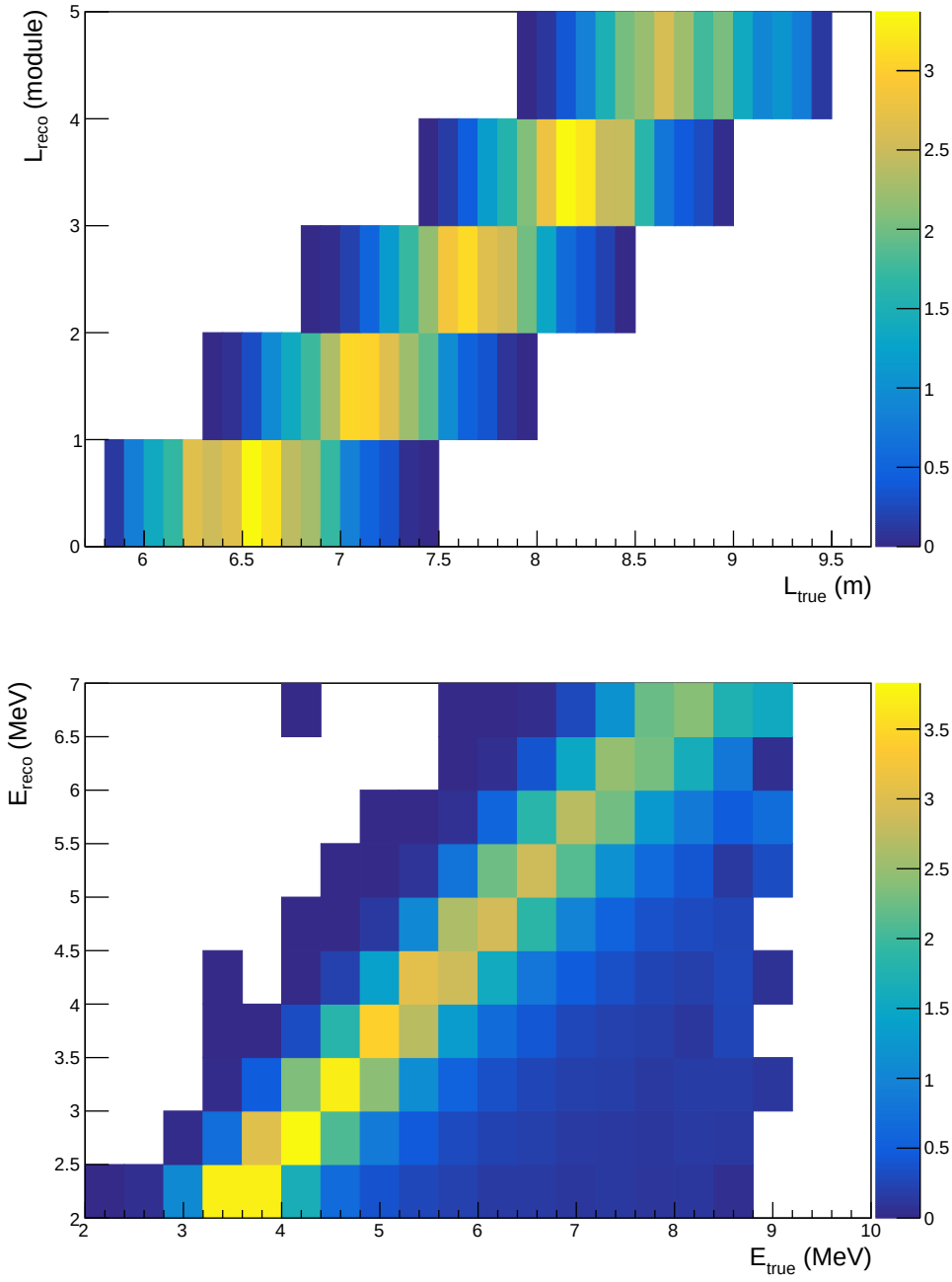

Figure 4.7: Resulting migration matrix, trained on the events of reactor cycle 1-2018, for a reconstruction threshold of 80 ADC and the *sum of all fibres* energy estimator. The MM is projected in length and energy response separately for visualisation purposes. The color scale is in arbitrary units.

In addition, the finite size of the reactor core creates a smearing of the origin of the neutrinos, which causes an overlap of different L_{reco} values for the same the same L_{true} values. Events with $L_{\text{true}} \approx 7.4$m, for example, have almost equal chance of being reconstructed in module 2 or module 3. We therefore also see that some events with L_{true} values below 6.3 and above 8.9 m, which is outside the baseline of the SoLid detector, are also detected.

From the representation of the energy response, in the bottom plot of figure 4.7, we see two main effects. First a shift in energy of about -1.5 to -2 MeV is seen, which is expected from the relation $E_{\overline{\nu}_e} = E_{e^+} + 1.804\,\text{MeV}$, deduced in section 2.2. Secondly, the effect of energy smearing is seen as the broadening of the diagonal. In addition, an effect of energy losses is seen as the slightly higher population below the diagonal.

4.6.3 Migration matrix performance

To test the performance of the MM, it was trained on the IBD prediction of one reactor cycle and applied to the prediction of a second cycle. The number of events generated per reactor cycle is roughly 2.5 to 3.5 million, including the scaling factor of 100 to smoothen the prediction.

Figure 4.8 shows the original distribution of reconstructed events for reactor cycle 3-2018, based on the full simulation chain, compared to the result of the MM trained on reactor cycle 1-2018 and applied to the same set of events in *true space*, i.e. before they are processed with ROsim and the reconstruction and IBD selection algorithms. For visualisation purposes, the distributions are projected in L_{reco} and E_{reco} separately.

The MM reconstruction in L_{reco} matches the expected distribution within statistical errors. Even for the lowest statistics bin, the relative difference is only 3%. The result in E_{reco} shows some more variations from bin to bin, but again stays within statistical errors and a 3% difference at maximum over the full range. We will see in chapter 7 that these differences are well within the statistical errors of the current data set.

Since the MM in principle only represents the detector and reconstruction effects, it should not depend on the shape of the input model on which it is trained. Therefore, the MM performance was also tested by training it on events generated with a flat energy spectrum and looking at the result of its application to a standard set of IBD events.

The resulting IBD distributions in reconstructed position and energy are shown in figure 4.9. A first problem with this MM was that the reconstruction efficiency - i.e. how many IBD events end up in the reconstruction compared

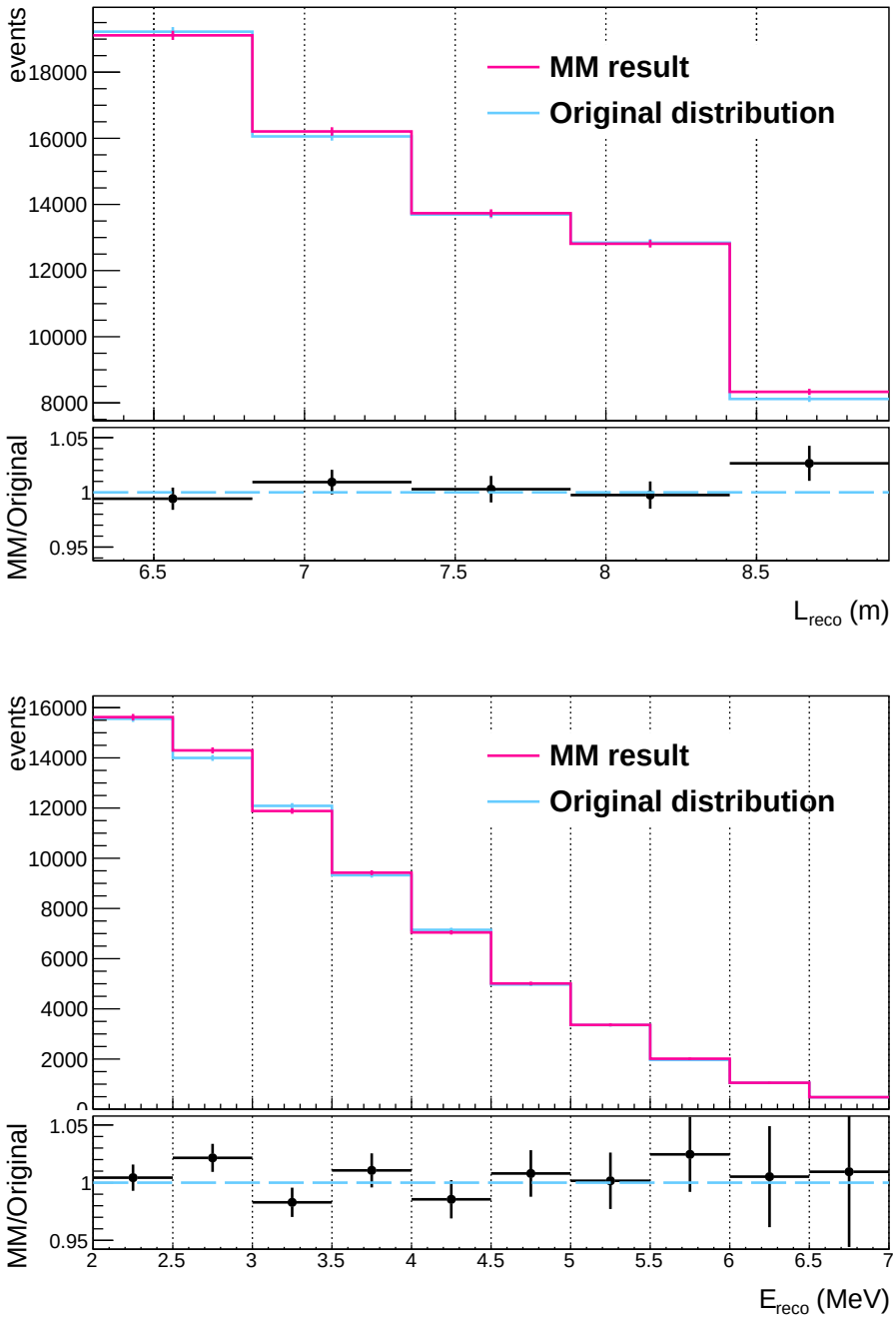

Figure 4.8: Performance of the migration matrix, trained on the events of reactor cycle 1-2018, in terms of the reproduction of the reconstructed distribution in energy (top) and position (bottom) for IBD simulation events of reactor cycle 3-2018.

to the number of simulated interaction - was not well reproduced. This results in a different normalisation of the MM result compared to the original distribution. In figure 4.8, this difference was corrected for by rescaling the MM distribution to match the normalisation of the original one. For the scaled distributions, we see that the energy reconstruction is reproduced very well, but the length reconstruction shows an unexpected outlier of 4% in the first bin that can not be attributed to a statistical fluctuation.

To retrieve the origin of this issue, additional studies with other inputs for the MM training were performed. One is based on events generated with a simplified energy reconstruction model, using a simple shift of 1.8 MeV that represents the loss of the annihilation gammas and a Gaussian smearing of the energy. Further on, a point-like reactor model was used. This study shows similar, but more profound problems, as illustrated in figure 4.10. First of all the reconstruction efficiency does not match the expected one. After scaling, the reconstruction E_{reco}-shape is reconstructed very well, but the length distribution is poorly reproduced.

The studies shown here and additional ones that use different reactor geometries have so far not helped to find a clear solution for the problems described above. Some results indicate that the model has problems training on a data set where the L_{true} simulation is too simplistic. Further tests simulating a finite reactor core with a shifted position will be performed in the near future, to estimate the effect of position reconstruction uncertainties on the MM model. In a second step, a different framework for the construction of the MM, called ReMU [126], will be implemented. This will allow a cross-check of the generated migration matrices and could help to understand the unexpected dependence of the MM performance on the input models.

4.7 Summary

To be able to perform a precise oscillation study, we need to understand all detector effects and how they affect the predicted signal. All steps in the detector response, from the particle transport and scintillation processes (SoLidSim, section 4.1) to the electronics performance (ROsim, section 4.2) are therefore simulated with dedicated Monte Carlo codes. These simulations are based on, and compared to, experimental data to realistically emulate all processes in detail.

Both for real and simulated data, the whole detection process shifts, smears and breaks up the recorded signals. As a consequence, algorithms that conserve as much information as possible and correctly reconstruct the events of interest need to be applied. We have seen that for the SoLid experiment,

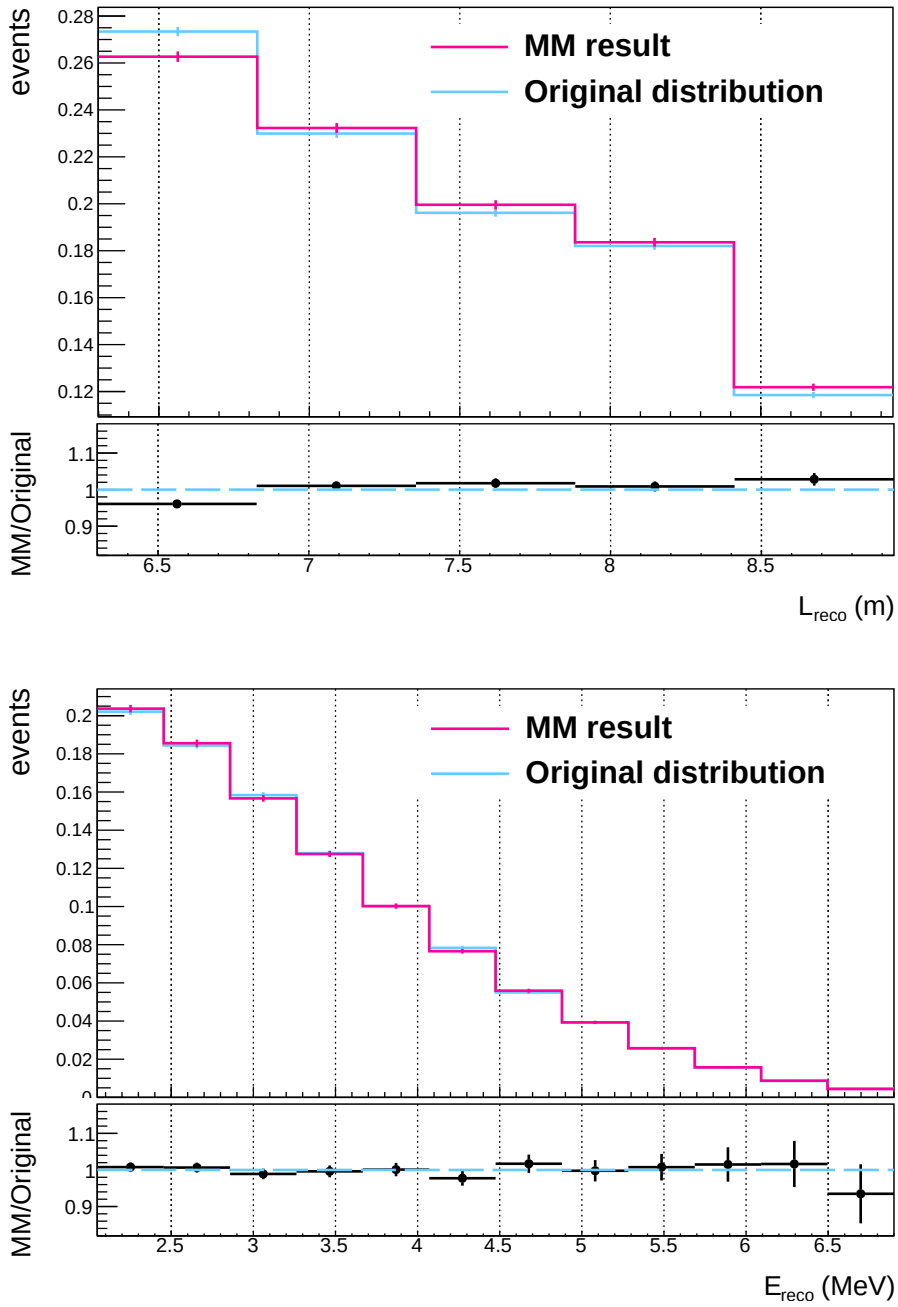

Figure 4.9: Performance of the migration matrix when trained on a flat energy spectrum, in terms of the reconstructed energy (top) and position (bottom).

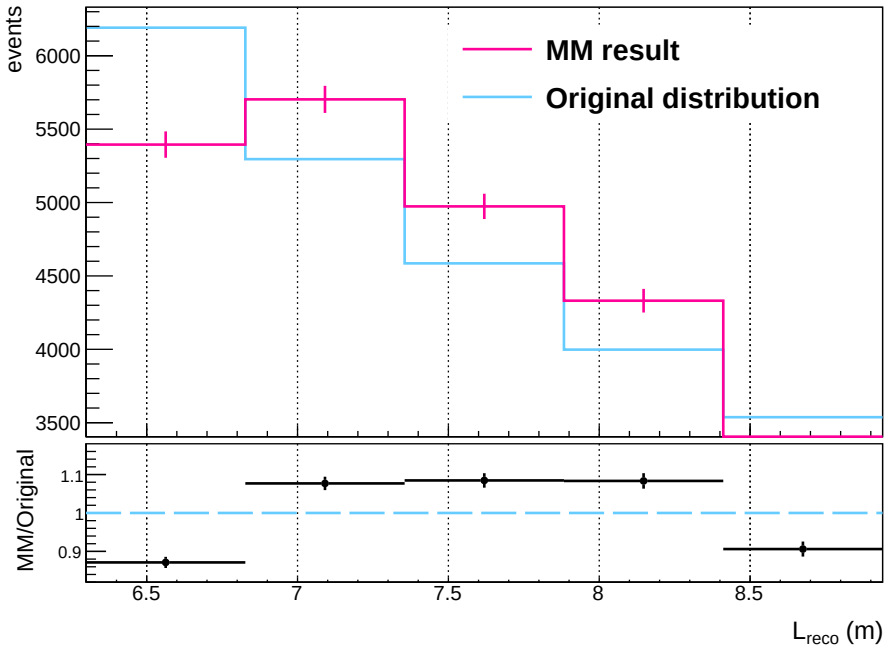

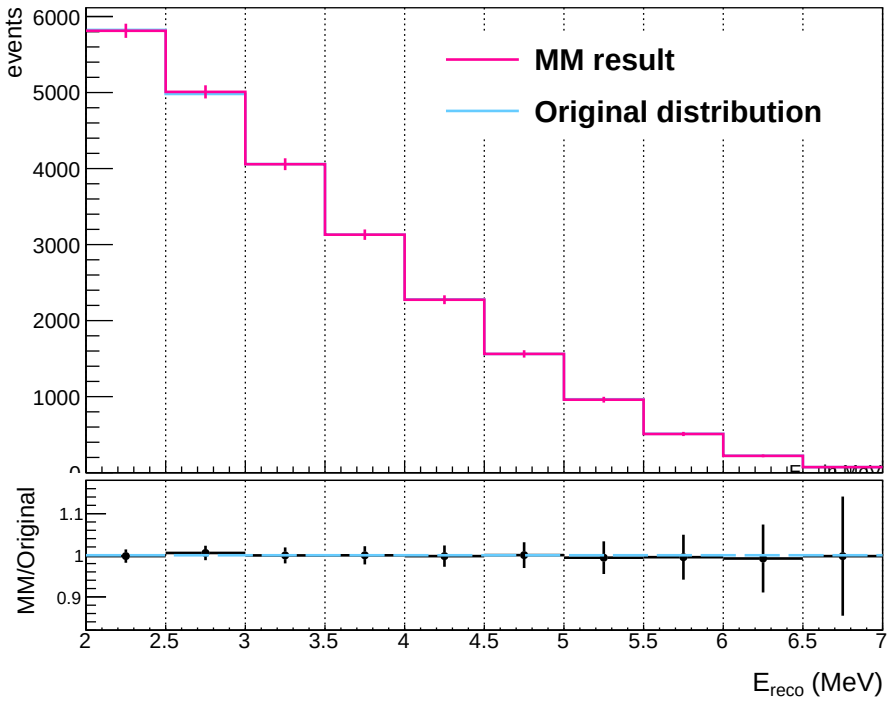

Figure 4.10: Performance of the migration matrix when trained on events with a simplified energy reconstruction, in terms of the reconstructed energy (top) and position (bottom).

these algorithms are implemented in the Saffron2 code. The four main reconstruction steps - selection, clustering, identification and reconstruction - were briefly described in section 4.3. In section 4.4, the importance of the choice of energy estimator in the reconstruction process was discussed.

To highlight the actual sequence of steps, we have already briefly addressed the next step of the data processing chain in section 4.5, which is the IBD signal selection. An in depth discussion on the selection methods is reserved for the following chapter.

Finally, section 4.6 of this chapter gave a description of the migration matrix, an object that is designed to map all relevant detector, reconstruction and selection effects at once, thereby simplifying the translation of the signal prediction from a model in *true space* to an expected signal in *reco space*.

Signal selection 5

As was briefly mentioned in the previous chapter, the event reconstruction is followed by the process of signal selection, where the reconstructed event parameters are exploited to discriminate an IBD signal from the different types of experimental background.

We will first describe the properties expected for the IBD events, based on the study of Monte Carlo simulations and define the most useful parameters for their selection. Next, the background conditions of the SoLid experiment will be discussed. The two main sources of correlated background, induced by natural radioactivity and fast neutrons from atmospheric radiation, will be treated in more detail.

Using the knowledge of the signal and background properties and the general data taking conditions, a set of selection criteria or *cuts* can be defined to reduce the contribution of background noise as much as possible. Of course, these selection criteria also have a significant impact on the signal and it is thus a question of finding the optimal set of cuts to obtain the highest possible IBD detection efficiency and signal-to-background ratio.

Finally, the resulting IBD signal selection for the current data set will be presented.

5.1 The IBD signal

We first investigate the signature of IBD events in the SoLid detector. As mentioned before, an IBD event produces a positron and neutron as reaction products. The positron promptly interacts in the PVT scintillator, the neutron first thermalises and is then captured on ^{6}Li. From the reconstruction processes, described in the previous chapter, we expect to detect the positron and neutron as an ES and NS event, respectively, with a well-determined time

coincidence defined by the neutron capture time. The Saffron2 code is therefore programmed to form a set of associated ES-NS events at the end of the reconstruction chain. The starting point for the IBD signal selection is thus a file with a list of reconstructed ES-NS coincidences and their reconstructed variables.

These reconstructed variables include the detection time t and the x-, y- and z-position for both ES and NS events, as well as the reconstructed energy E_{reco}- based on multiple estimators - of the ES events. Often more interesting for the identification of IBD events, however, are the differences between the ES and NS event for some of these parameters. In general, the difference for parameter u is defined as:

$$\Delta u = u_{NS} - u_{ES}. \tag{5.1}$$

Following this definition, the variables $\Delta t, \Delta x, \Delta y, \Delta z$ and $\Delta r = \sqrt{\Delta x^2 + \Delta y^2 + \Delta z^2}$ are constructed. Figures 5.1 to 5.4 show the simulated distributions for the main reconstructed variables of IBD events, based on the prediction for reactor cycle 3-2018 processed with the full detector and read-out simulation and the Saffron2 reconstruction code.

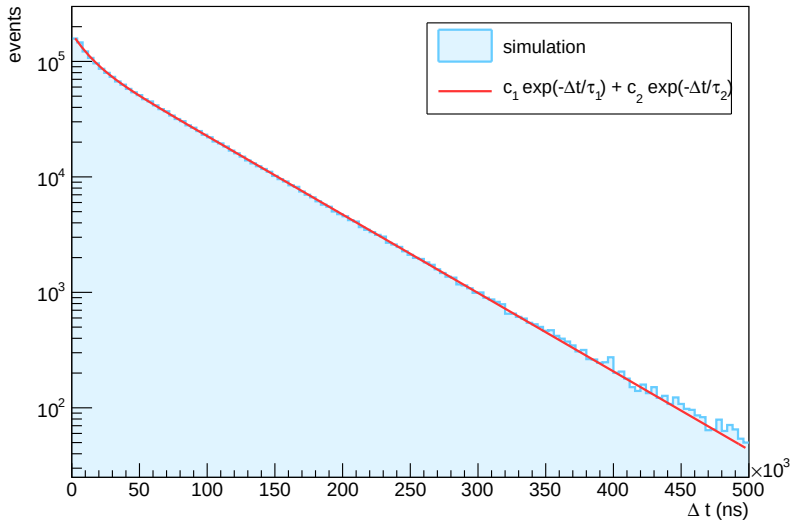

Figure 5.1: The expected Δt distribution of IBD events, based on the full simulation of the prediction for reactor cycle 3-2018. The distribution is fitted with a double exponential function to take into account two types of neutron captures. The resulting time constants are $\tau_1 = 63.9 \pm 0.1 \mu s$ and $\tau_2 = 12.3 \pm 0.2 \mu s$.

Given the definition $\Delta t = t_{NS} - t_{ES}$, we expect a positive Δt distribution for IBD events, as the neutron is delayed with respect to the positron. From figure 5.1 we see that the Δt distribution can be fitted with a sum of two exponentials. The two exponentials in the fit represent two capture processes: one with a larger time constant ($\tau_1 = 63.9 \pm 0.1 \mu s$) for thermal neutron capture, which is the more common process, and a shorter one ($\tau_2 = 12.3 \pm 0.2 \mu s$) that represents the less frequent capture of non-thermal neutrons. With a resulting typical Δt value of about 60 µs, we see that only 8.5% of the expected IBD events has a value $\Delta t > 150$ µs.

In figure 5.2, the typical reconstructed distances between the ES and NS events of an IBD interaction are shown. We note that the position of the ES event is determined by that cube of the event that shows the highest reconstructed energy. Each of the three distributions has a spread of about three cubes at maximum and the Δx and Δy distributions are centred around zero. The ES and NS events are thus also clearly correlated in space, an aspect that can be exploited thanks to the high granularity of the SoLid detector. In addition, the Δz-distribution is boosted towards positive values, indicating that the neutron is likely to keep some momentum in the direction of the incoming antineutrino. As mentioned above, an additional variable, Δr, that combines the three position dimensions can be constructed. By definition, Δr has to be positive and can only take certain values. The expected distribution is shown in figure 5.3.

As discussed in section 4.4, two energy reconstruction methods were developed; the *sum of all fibres* and *max cube + crown* estimators. Both methods have advantages and disadvantages. In addition, two possible threshold settings for the ES selection are being evaluated, that also affect the reconstructed energy. For completeness, the expected energy distributions for the two types of estimators and both thresholds are shown again in figure 5.4. For each of the four illustrated options, the reconstructed ES energy distribution peaks around 2 MeV and becomes very small above 7.5 MeV. The different estimators and thresholds mainly influence the distributions at energies below 1.5 MeV, as lowering the threshold or using more fibre information typically increases the contribution of low-energetic signals.

Given this knowledge of the expected IBD signal timing, topology and prompt energy depositions, we now take a look at the main background components for the SoLid experiment and determine how they can be discriminated from the signal.

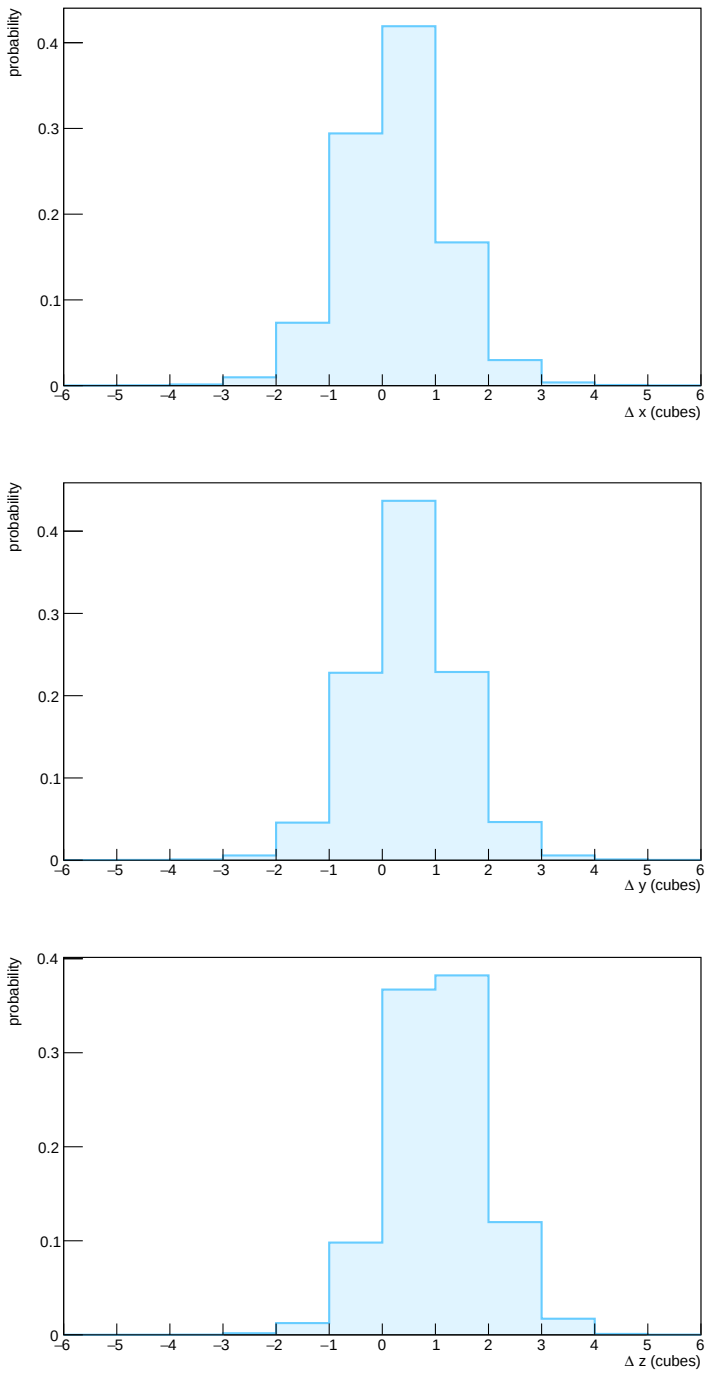

Figure 5.2: The expected Δx, Δy and Δz distributions for reconstructed variables of simulated IBD events, based on the full simulation of the prediction for reactor cycle 3-2018.

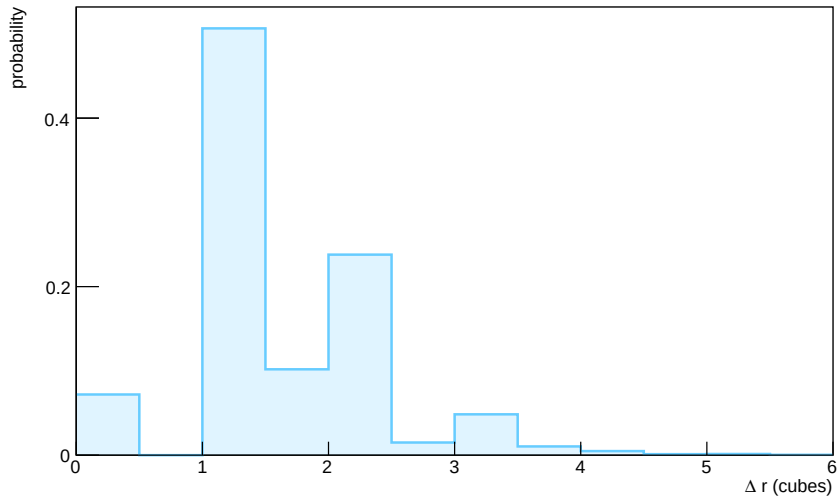

Figure 5.3: The expected Δr distribution of IBD events, based on the full simulation of the prediction for reactor cycle 3-2018.

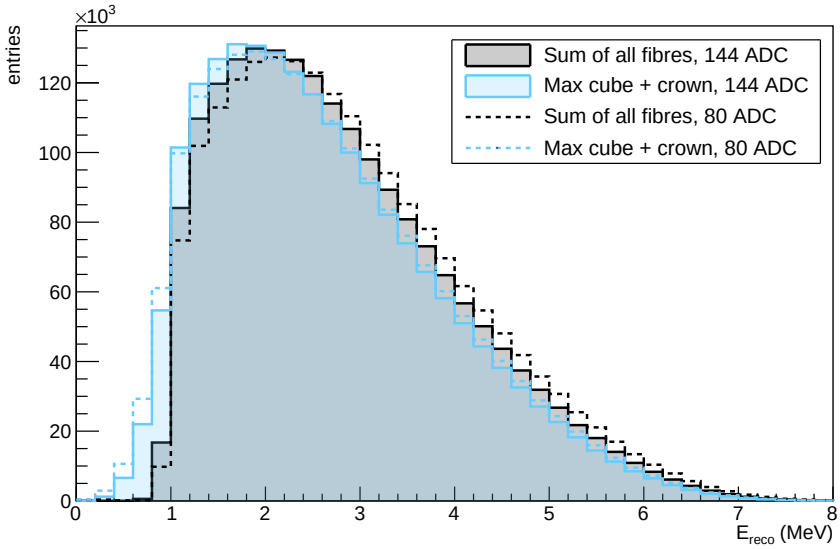

Figure 5.4: The expected E_{reco} distribution of IBD events, based on the full simulation of the prediction for reactor cycle 3-2018. The result of both energy estimators and for two reconstruction thresholds are shown.

5.2 Backgrounds

Given its location near a nuclear reactor, the SoLid detector site sees a lot of reactor induced backgrounds, such as gamma rays and environmental neutrons. Apart from that, since the detector site has very low overburden ($\sim$10 m.w.e.), the experiment is also sensitive to cosmic and atmospheric backgrounds. In general, SoLid's neutron-based trigger system causes the dominant backgrounds to be either induced by neutrons created in processes other than IBDs or by processes that excite the ZnS(Ag) scintillator and as such mimic a neutron capture signal.

We can discriminate two main categories in the background contributions: the correlated backgrounds and the uncorrelated or accidental ones.

5.2.1 Accidental background

The accidental background is mainly caused by the random coincidence of a gamma ray and an environmental neutron interacting in the detector.

As a part of the work for this thesis, I have studied the gamma ray contribution for the SoLid experiment by performing in situ measurements with a Ge-detector. An example of the recorded gamma spectrum is shown in figure 5.5. Some clear gamma peaks for ^{40}K and ^{214}Bi are seen, which are naturally present in (the BR2) building materials. The more intense peaks, however, come from reactor induced elements and thus have a rate that depends on the reactor power. There are two strong gamma lines from ^{60}Co, which is a reactor fission product, and a dominant line at 1294 keV from ^{41}Ar that is created by the capture of reactor neutrons on the natural ^{40}Ar in the air. Because it is an airborne element, the detected rate of ^{41}Ar depends a lot on environmental conditions such as the pressure in and the ventilation of the reactor building.

To reduce the reactor gamma background, the SoLid collaboration has built a water wall and HDPE ceiling to create a 50 cm thick layer of detector shielding. In addition, a small NaI-detector was installed inside the PhaseI container to monitor variations in the gamma background rate.

For the detected accidental coincidences, the ES and NS candidate do not originate from the same physical event and they thus create random configurations in terms of detected topology. As a consequence, the resulting Δx, Δy and Δz parameter distributions for those accidental events are expected to be relatively broad. Topological cuts that make use of the high granularity of

the SoLid detector can therefore largely reduce the contribution of accidental events in the signal selection. The time difference between accidental ES and NS candidates is usually much larger than that of correlated events, and their Δt-distribution can be considered uniform over the relevant range. Since the NS events are not necessarily delayed with respect to the ES event, the coincidences in the dataset with negative Δt can be used to estimate and subtract the remaining accidental background contribution.

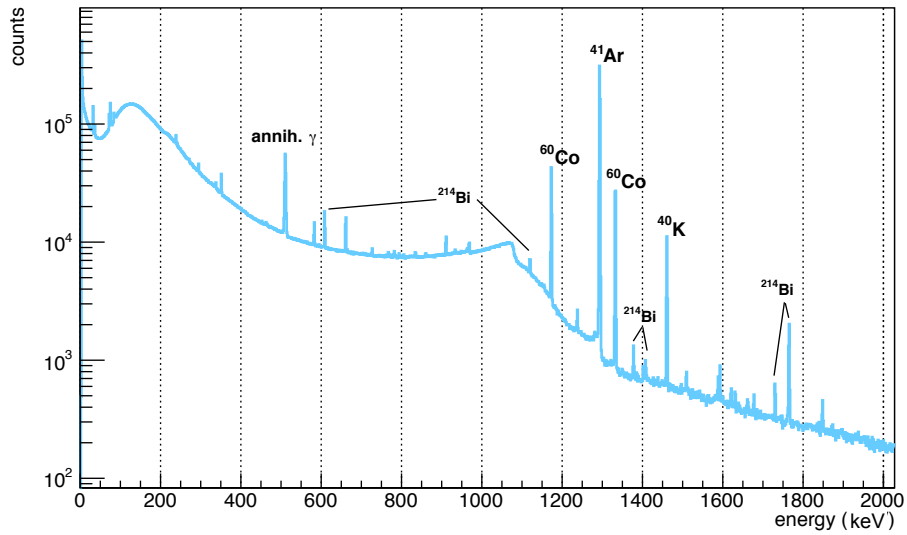

Figure 5.5: The gamma background spectrum measured with a Ge-detector at the position of the SoLid experiment in the BR2 reactor hall. Some of the characteristic gamma lines are labeled with the element they originate from.

5.2.2 Correlated background

The second category of background processes includes those that *do* exhibit a clear time correlation between the reconstructed NS time and preceding ES event and are therefore called correlated. For the SoLid experiment, two main correlated background sources can be identified: fast neutrons and intrinsic radioactivity of the detector materials.

Fast neutrons

One of the largest background contributions for the SoLid experiment comes from fast neutrons, which either come from atmospheric showers or from the

cosmic muon induced spallation of nuclei in the materials surrounding the detector. The fast neutrons can penetrate the shielding and enter the active detector material where they create recoils on hydrogen atoms, as sketched in figure 5.6. These proton recoils cause a scintillation of the PVT and mimic the prompt ES signal; the neutrons themselves are moderated and then detected as the delayed NS. Given the typical time difference between the prompt and delayed signal for fast neutron recoils of $\sim$70 µs, it is clear why this correlated background is hard to discriminate from the IBD processes that have an ES-NS time difference of $\sim$60 µs. The slight difference between these Δt values found for fast neutrons and IBD neutrons is attributed to the generally higher energy of the atmospheric neutrons, that is assumed to increase their thermalisation time.

A first way to reduce the impact of the fast neutron contamination is to reject events close to a muon event, as these are often the precursor of a fast neutron event. For each coincidence, the temporal proximity of the NS to the last detected muon can be determined. If the time difference between the two is too small ($< \mathcal{O}(200\,\mu s)$), the coincidence can be excluded; a selection that is referred to as the *muon veto*. Another way to suppress this background is by looking at the NS and ES signal multiplicities. These multiplicities are usually higher for a fast neutron event than for an IBD interaction, since multiple neutrons can be produced in a spallation process and the energetic proton recoils are often recorded as several ES signals.

As the fast neutron background is independent of the reactor operation, its rate and properties are determined from reactor-OFF data. For a good understanding of both atmospheric and cosmic fast neutrons, detailed MC models were developed, based on respectively the Gordon and CRY generators (cf. section 4.1).

Intrinsic radioactivity

Another important experimental background is an internal one, related to the contamination of the neutron detection screens with elements from the ^{238}U radioactive decay series, shown in figure 5.7. This series contains the decay from ^{214}Bi to ^{214}Po to ^{210}Pb, inducing the subsequent emission of a β- and α-particle. The β-particle escapes the neutron detection screen and annihilates in the PVT scintillator, giving an ES signature. The emitted α has enough energy to excite the ZnS(Ag) and, like neutrons captured on ^{6}Li, induces an NS scintillation signal. This background process is referred to as *BiPo* and is illustrated in figure 5.8. With a β-energy around 3 MeV and half-life for ^{214}Po of 164 µs, the prompt energy and time-correlation of a BiPo process are in the same range as that of the IBD events of interest.

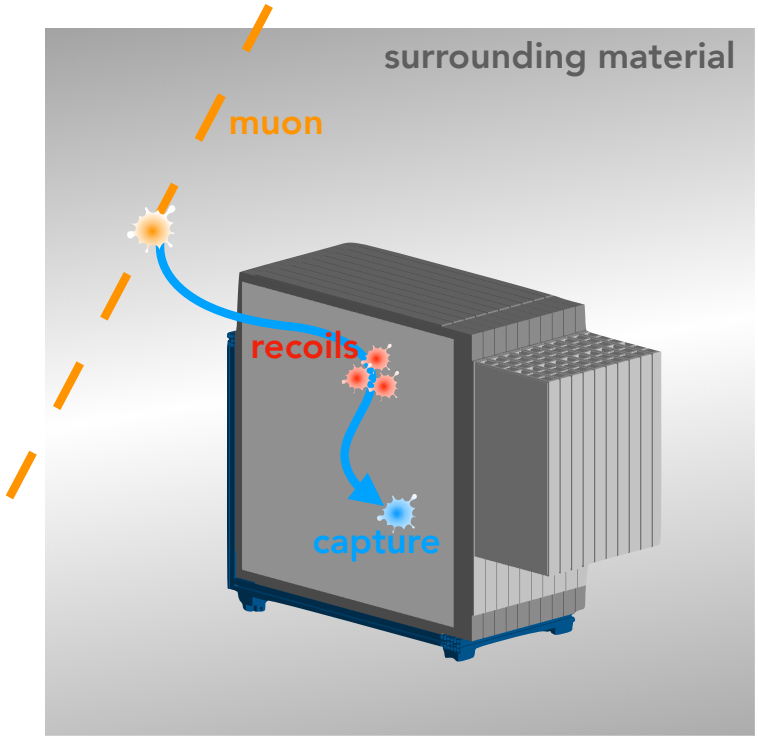

Figure 5.6: Sketch of muon induced spallation in material surrounding the detector and the resulting fast neutron that first recoils on hydrogen and is afterwards captured in ^{6}Li in the detector.

A similar process is caused by the airborne isotope ^{222}Rn, that is part of the same decay chain and can thus produce several α and β-particles. Therefore, a dedicated Rn-detector was installed inside the SoLid container, to constantly monitor the amount of ^{222}Rn.

From a detailed simulation of the BiPo process, it was seen that the use of the event's cube and fibre topology information can be used to discriminate BiPo from IBD events. In addition, some dedicated cuts for the reduction of this background were developed, such as the *BiPonisher* and *energy balance* cuts. The BiPonisher cut is a pulse shape discrimination method that is based on a difference in the ZnS signal for the IBD and BiPo processes, that is driven by the energy of the detected α-particle. From the ^{6}Li break-up in the IBD process, the α is released together with a ^{3}He sharing only 4.78 MeV, while the α-particle resulting from ^{214}Po decay typically carries about 7.69 MeV. This translates to a difference in the NS waveform integral, as shown in figure 5.9, where calibration data taken with an AmBe neutron source is compared to a BiPo selection from reactor-OFF data. By taking the ratio of a short window integral of [0 - 7.5] µs, to the integral over a long window of [0 - 87.5] µs, an optimal separation of the two types of events is obtained.

The energy balance cut makes use of the ratio of the reconstructed energies in the detector cube that shows the largest energy deposit (ES1) and the cube with the second largest deposited energy (ES2) in the prompt ES signal. In the case of an IBD event, the energy deposit in the second cube will often originate from one of the 511 keV annihilation γ's. For a BiPo event, the second cube is very likely related to a γ-signal too, as in more than 80% of the cases the decay of ^{214}Bi results in an excited state of ^{214}Po that de-excites with the emission of one or more γ's. Because the most populated excited states of ^{214}Po have energies more than 1 MeV above the ground state, most emitted γ's will have larger energies than an annihilation γ and the ES2/ES1 balance will be larger for the BiPo background than for the IBD signal, as illustrated in figure 5.10. A cut on this variable can significantly reduce the BiPo background, while retaining most of the IBD events.

At the time of writing, an additional method for BiPo discrimination, based on image recognition with a Convolution Neural Network, is under development. The method was baptised "BiPonator" and its first results promise an improvement of the α-neutron discrimination power with a factor 2.5, compared to the BiPonisher algorithm [129].

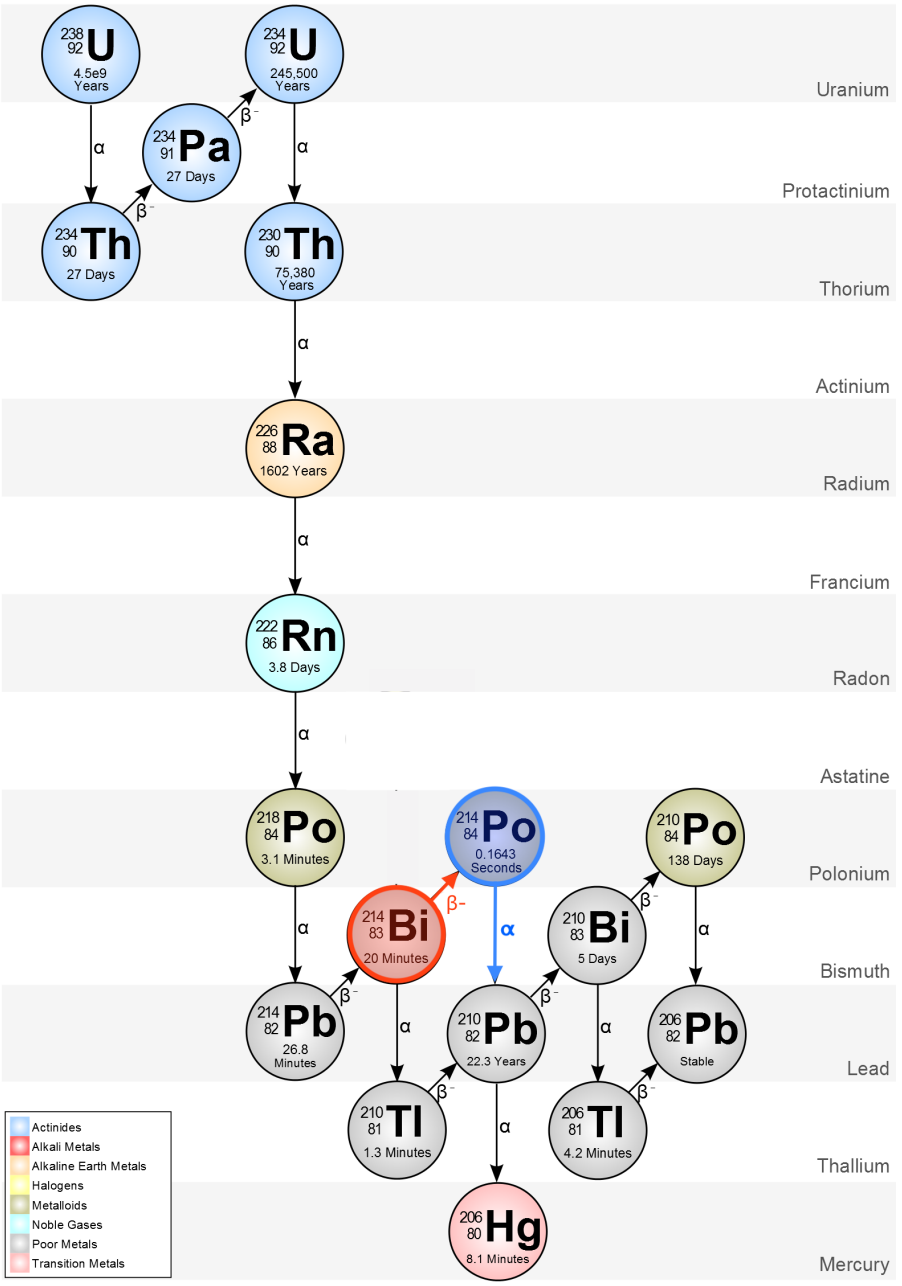

Figure 5.7: The ^{238}U / ^{232}Th radioactive decay chain. The ^{214}Bi β-decay is highlighted in red and the ^{214}Po α-decay in blue. Adapted from [127].

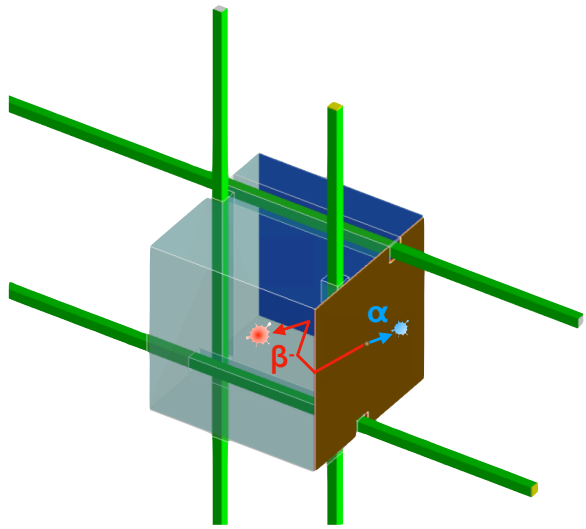

Figure 5.8: Sketch of the Bi-Po background principle. The β-particle from the ^{214}Bi-decay annihilates in the PVT cube, while the α-particle from the ^{214}Po decay is energetic enough to excite the ZnS scintillator.

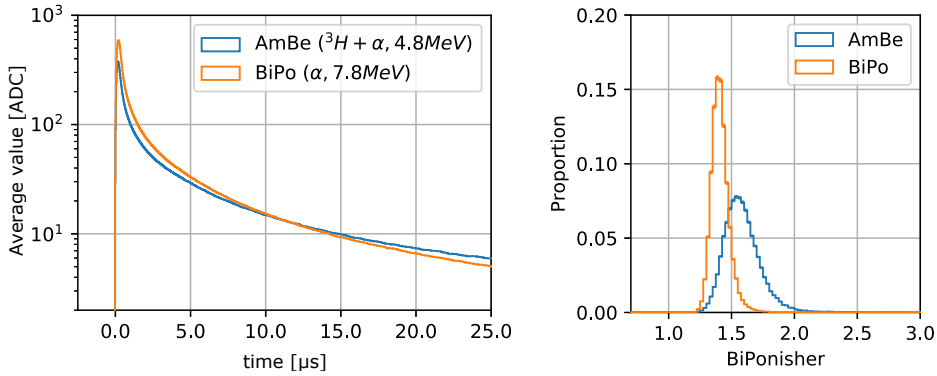

Figure 5.9: Illustration of the BiPonisher method. Left: The averaged NS waveform shape from neutron induced scintillation signals, based on a pure AmBe source sample, and the average waveform from NS signals induced directly by an α, from a pure BiPo selection. Right: The AmBe and BiPo set are reasonably separated in terms of the BiPonisher parameter, which is calculated as the ratio of a short time window integral over a long time window integral.

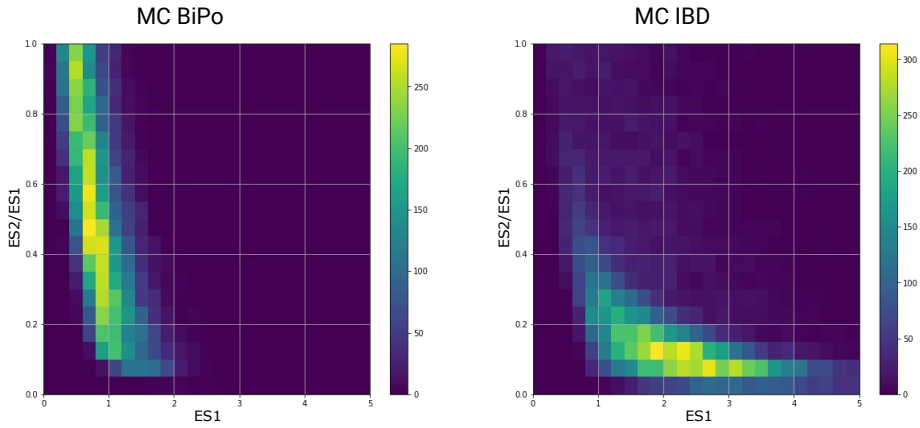

Figure 5.10: Illustration of the energy balance between the highest (ES1) and second highest (ES2) detected energy per cube. For simulated BiPo events (left) and simulated IBD events (right). [128]

5.2.3 General properties

In general, the background component for the SoLid experiment can be evaluated using physics data taken during reactor-OFF periods. From these periods the total background rate (as a function of the environmental conditions) and the parameter distributions of the background-induced coincidences can be determined. A qualitative comparison between the background parameter distributions and those of simulated IBD events is shown in figures 5.11 and 5.12. We note that these figures show the probability distributions for each parameter and not the absolute rates of the background versus signal events. In reality, the total background rate before application of signal selection cuts is much higher ($\sim$100 times) than the signal rate. It is mostly driven by the BiPo event rate, that is most clearly visible in the E_{reco} distribution with a large fraction of the ES events below 3 MeV which can be linked to the β-particle emitted in the ^{214}Bi decay.

5.3 Data quality

The full SoLid PhaseI detector has continuously been taking reactor-ON and -OFF data since April 2018 up to June 2020, apart from the calibration measurements and some short shutdowns for small interventions. A summary of

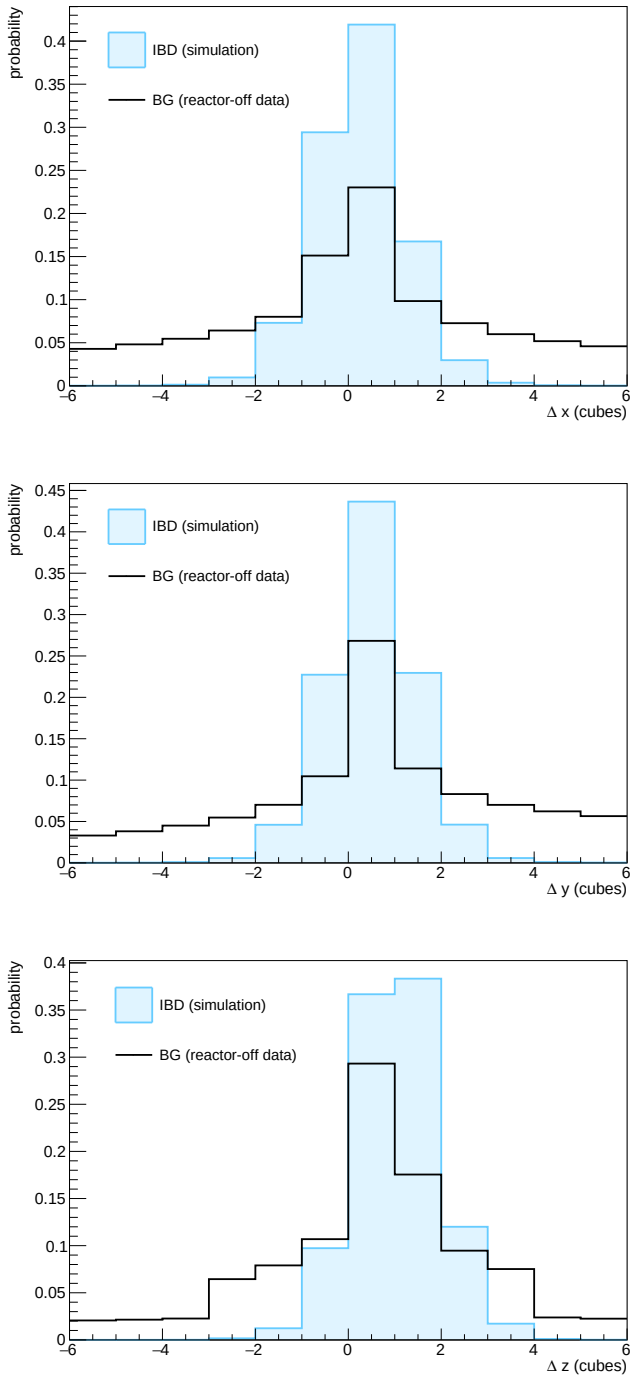

Figure 5.11: The Δx, Δy and Δz background distributions for events with an energy between 0 and 10 MeV based on 10 days of reactor-OFF data (black) compared to the predicted distributions for IBD events (blue).

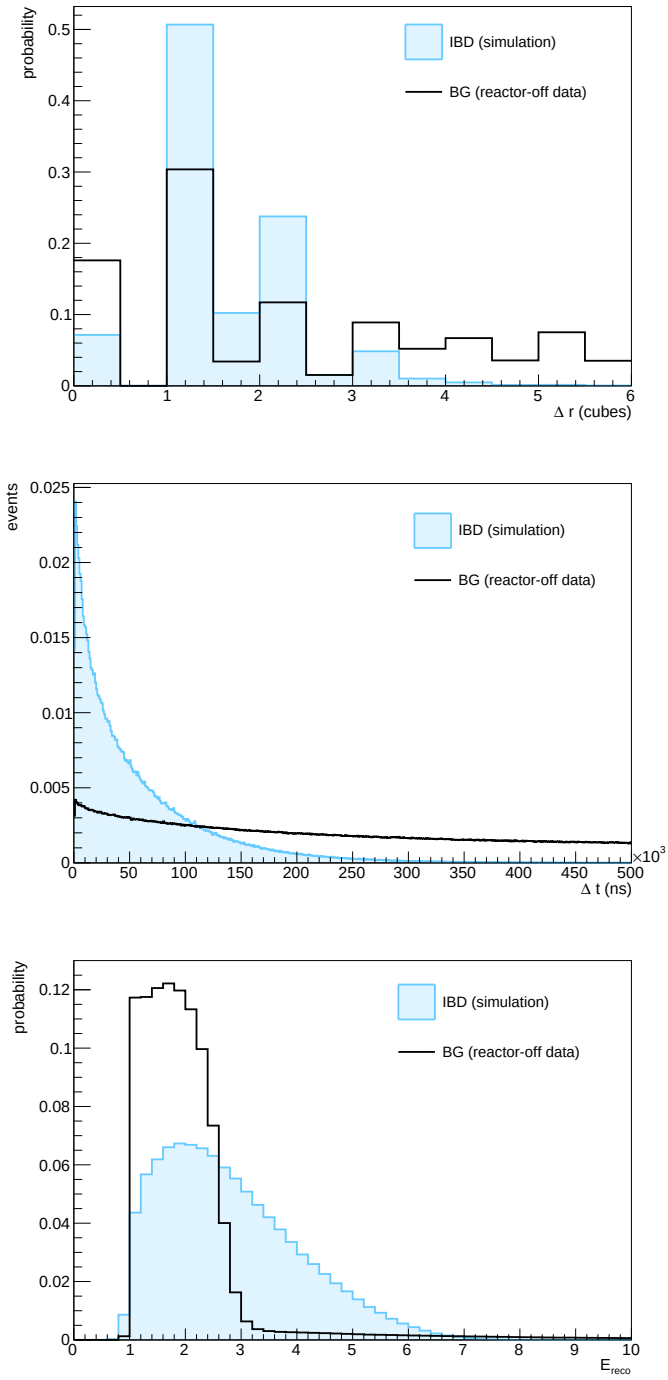

Figure 5.12: The Δr, Δt and E_{reco} background distributions for events with an energy between 0 and 10 MeV based on 10 days of reactor-OFF data (black) compared to the predicted distributions for IBD events (blue).

the reactor-ON periods during which the SoLid detector took quality physics data is given in table 5.1. In total, the PhaseI detector recorded 373 days of physics data. A small part of this data will be rejected in the final analysis, e.g. in case unstable environmental or data taking conditions were noted.

Table 5.1: Reactor-ON periods during which the SoLid PhaseI detector took physics data. The reactor power for each period is also given.

Reactor-ON period	**Nr. of days**	$P_{\text{th}}[MW_{\text{th}}]$
12/06/18 - 10/07/18	28	60
21/08/18 - 11/09/18	21	58
02/10/18 - 23/10/18	21	56
13/11/18 - 11/12/18	28	58
06/02/19 - 05/03/19	27	45
26/03/19 - 30/04/19	35	53
02/07/19 - 06/08/19	35	48
17/09/20 - 22/10/19	35	54
05/11/19 - 03/12/19	28	58
09/01/20 - 07/02/20	29	60
03/03/20 - 31/03/20	28	58
17/04/20 - 18/05/20	31	56
10/06/20 - 07/07/20	27	56
Total	**373**	$< 55 >$

During the full operation time, detector running was monitored via a dedicated web application, called the *SoLid Data Quality Monitor* (SDQM). It runs on Python-based scripts and automatically processes a small part of each run with the Saffron2 reconstruction code. The resulting measurements of the detector are read out periodically, together with the NaI- and Rn-detectors and a number of in-situ environmental sensors that register the pressure, temperature and humidity outside and inside the SoLid container [76]. An example of these trending plots, viewable via the SDQM web application is shown in figure 5.13. The NS rate does not depend on the reactor operation, as it is dominated by the airborne radon background with which it shows a strong correlation. The threshold trigger rate, that selects coincident signals above 20 PA (see section 4.3.1), does show a small difference between reactor-ON and -OFF transitions, which is driven by the change in gamma-background, as seen from the correlation with the NaI-detector measurements.

A significant contribution to the threshold trigger rate comes from cos-

mic muons crossing the detector. As these muons can be reconstructed with high precision, they have proven to be very useful for the verification of the data taking stability over time. Firstly, the known linear relation between the muon rate and the atmospheric pressure was nicely retrieved from the reconstructed data, as shown in figure 5.14. In addition, the energy scale stability of the detector was tested by exploiting the relation of deposited energy per path length (dE/dx) of the reconstructed muon tracks and its variation over time. From figure 5.15 we see that the relative energy scale variations stay below 2%, despite larger variations in environmental conditions, such as the humidity.

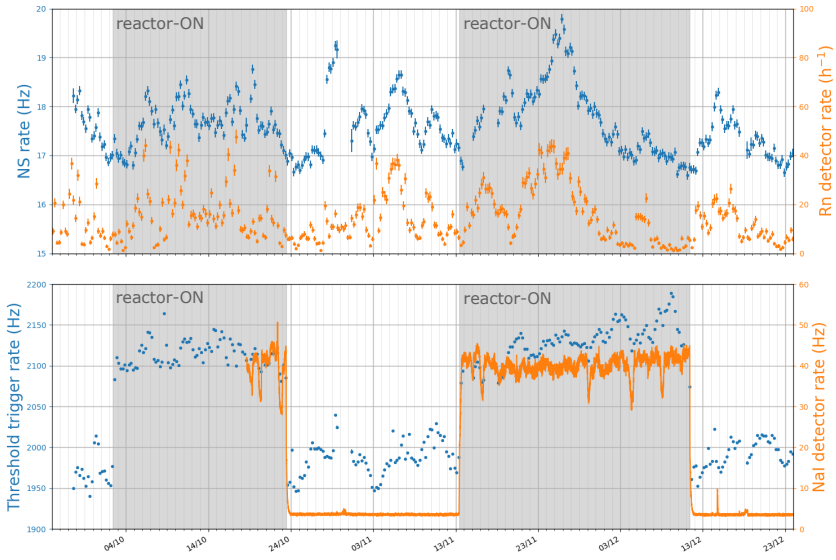

Figure 5.13: Example of the data rates measured with the Phase I detector from October to December 2018. Top: The NS rate after application of a muon veto (blue) and the airborne radon rate measured with the dedicated Rn-detector (orange). Bottom: Trend of the threshold trigger rate (blue), showing a small change between a reactor-ON and -OFF period. The rate is strongly correlated with the gamma-rate measured by the NaI-detector. [78]

5.4 Inverse Beta Decay event selection

As described above, the main backgrounds for the SoLid experiment are fast neutrons from atmospheric origin and radioactivity in the form of BiPo con-

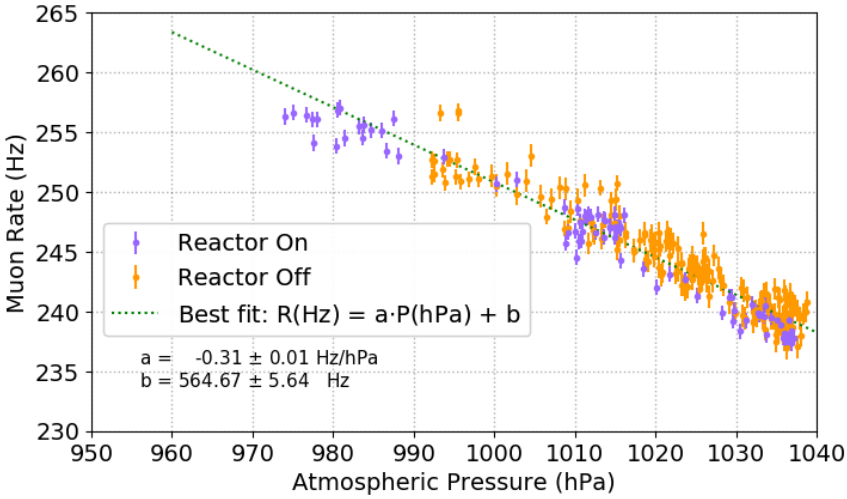

Figure 5.14: The rate of reconstructed muons versus the atmospheric pressure, measured over 9 days of reactor-ON and 14 days of reactor-OFF data. The data shows a strong linear correlation. Thanks to G. Vandierendonck.

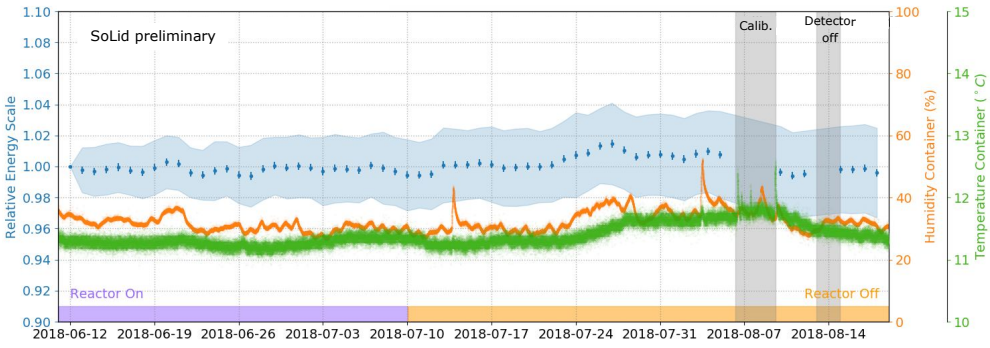

Figure 5.15: Evolution of the relative energy scale determined from the muon data, corrected for gain and baseline variations, and averaged over all detector channels. The error bars on the points represent the statistical uncertainty, the blue band is a measure for the distribution over the different channels. [78]

tamination of the neutron detection screens and airborne radon decays. To select a pure sample of antineutrino induced IBD events with an efficient set of selection methods, the SoLid collaboration is developing a range of techniques and determining the most efficiently discriminating parameters. In this thesis, we will briefly describe three IBD selection analyses that are currently implemented: a classical cut based selection, developed at the CAEN institute, and two codes using machine learning algorithms for the optimisation of the selection, one of which was developed at Imperial College, the other at Subatech. At the time of writing, a fourth IBD analysis is being developed by the group in Clermont-Ferrand.

5.4.1 Cut based

A cut based selection applies sequential, rectangular cuts on the given event parameters. The optimal set of cuts that is currently implemented includes topological and temporal coincidence requirements for the ES and NS event:

- $-2 \leq \Delta x \leq 2$,
- $-1 \leq \Delta y \leq 2$,
- $-1 \leq \Delta z \leq 3$,
- $0 \leq \Delta r \leq 3.4$,
- $0.5 \leq \Delta t \leq 130\,\mu s$,

all of which are very helpful for the reduction of non-correlated backgrounds. In addition, a lower limit on the ES energy[1] is set to reduce electronics noise and light leak effects, and a higher limit is set to exclude high energetic particles such as (clipping) muons;

- $2.5 \leq E_{\text{reco}} \leq 7\,\text{MeV}$.

Further on, a few cuts to reduce the dominant backgrounds - BiPo and fast neutrons - are added:

- an energy balance cut: $ES2/ES1 \leq 0.37$,
- a BiPonisher cut: BiPonisher > 1.495,
- an ES volume ($= \Delta x \times \Delta y \times \Delta z$) cut: $\text{vol}_{ES} < 297$.

A BiPonator cut might be added or could replace the BiPonisher one in the near future. Two possible time-coincidence vetos, that were described above, but are currently not implemented are:

[1] We note that for each of the analyses that are presented in this chapter, it was chosen to use the *sum of all fibres* energy estimator for the ES signal reconstruction.

- a muon veto, excluding all events recorded in a certain time span after a muon signal,
- a NS multiplicity veto, excluding all NS events recorded within a short time from each other.

Both vetos could help to reduce the fast neutron background, but in the current implementation of the event reconstruction they create a too large loss of data because of the dead-time they introduce.

The signal selection with these rectangular cuts results in an estimated IBD selection efficiency of $\sim 10\%$ and a remaining signal-to-background ratio of 0.06. As the high amount of remaining background events introduces a large statistical uncertainty that will reduce the experimental sensitivity, other, more advanced IBD selection methods were developed.

5.4.2 Multivariate analysis techniques

Two machine learning codes for the IBD selection, based on multivariate analyses (MVA) techniques, were developed to explore the use of annihilation gamma reconstruction information, with the goal of increasing the signal selection and background rejection efficiencies. Since the annihilation gammas result in low-energy signals, the data selection with the lower threshold of 80 ADC is used for these studies. In addition, a set of gamma reconstruction variables was introduced, which we will describe first, before treating the MVA codes.

Annihilation gamma variables

The annihilation gamma reconstruction is based on the selection of energy deposits that are not in the direct vicinity of the cube with the maximal detected energy. It is assumed here that the cube where the positron deposits most of its energy is also the cube where it annihilates. The cubes touching this "annihilation cube" (AC) can share some of the positron energy and are therefore directly excluded from the gamma reconstruction. These cubes are said to lie in the *envelope* around the annihilation cube, see figure 5.16. Because the annihilation gammas travel over a distance of about 10 cm, they will anyhow mostly be detected outside this envelope.

An important feature of the annihilation gammas is that they are expected to travel back-to-back. The gamma reconstruction algorithm uses this feature by first tagging the highest energy deposit outside the envelope as (the centre

of) the first annihilation gamma ($C_{\gamma 1}$), and then searching for the second annihilation gamma in the other detector hemisphere. This is done by scanning over all other cubes with reconstructed energy deposits (C') and calculating the cosine of the angle between the vectors $|AC \rightarrow C_{\gamma 1}|$ and $|AC \rightarrow C'|$. The cubes that give a positive cosine value are added to the first gamma cluster, those having a negative cosine value build up the second annihilation gamma cluster. This procedure is illustrated in figure 5.16.

Depending on the topology of the detected ES-NS coincidences, 0, 1 or 2 associated annihilation gammas can be reconstructed. The machine learning codes described below will therefore train on each of these three cases, profiting from more input variables for the cases with a larger number of reconstructed gammas.

Two of these annihilation gamma variables that look promising for signal-versus-background discrimination (for events with two reconstructed gammas) are illustrated in figure 5.17. These are the energies of the reconstructed gammas and the spatial separation between the two gammas, which is defined as the cosine of the angle between $|AC \rightarrow C_{\gamma 1}|$ and $|AC \rightarrow C_{\gamma 2}|$.

MVA method 1: uBDT code

The uBDT method is a machine learning technique, based on the *uBoost* package [130] of the *hep_ml* Python library [131], which is dedicated to machine learning methods used in high energy physics. In general, this technique generates a multi-dimensional space in which cuts on the input variables are formed for an optimal classification of the signal versus the background. The learning method for the cut optimisation is one based on Boosted Decision Trees (BDT). The *u* in uBDT/uBoost stands for *uniform*, as this method is specifically designed to retain a uniform selection efficiency in one or multiple physics variables, while optimising the signal and background discrimination. In the case of the IBD analysis, this is especially useful for the reconstructed z-position and energy variables, as a non-uniform selection in terms of $L_{\text{reco}}(\sim z)$ and E_{reco} would greatly complicate the neutrino oscillation analysis that depends on the ratio L/E. The code and analysis for this method were developed at Imperial College.

MVA method 2: neural network code

The second code is written in C++ and uses the TMVA-package [132] of the ROOT framework. TMVA stands for Toolkit for MultiVariate Analysis and it provides a machine learning environment for the implementation of multivariate classification techniques. The selected type of classification method

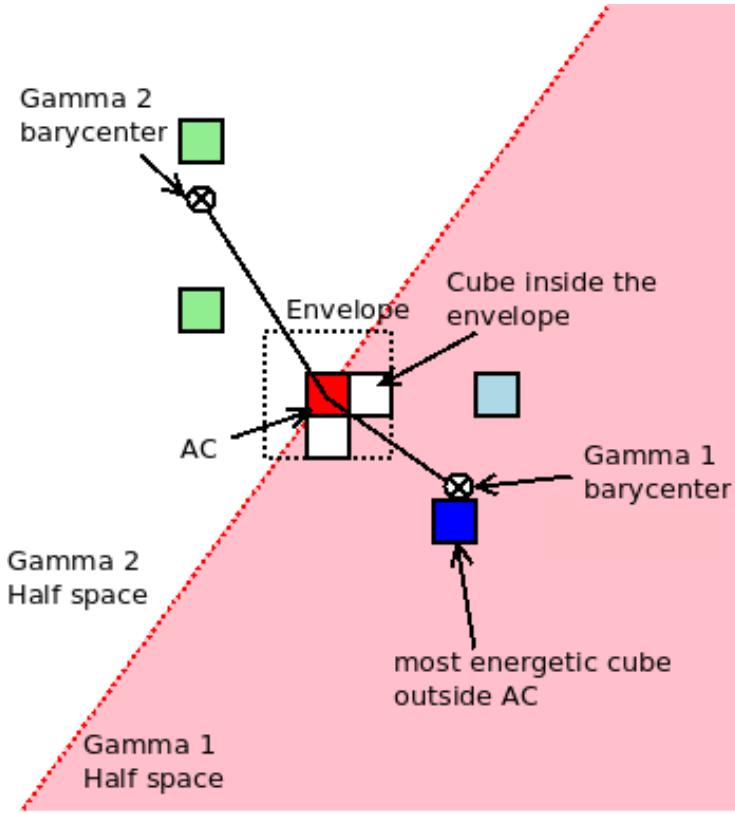

Figure 5.16: The annihilation gamma reconstruction procedure for an event with two detected annihilation gammas. The algorithm searches for the most energetic cube (dark blue) outside the envelope around the reconstructed positron cube (red) that is denoted here as the *annihilation cube* (AC). This cube is associated with a first annihilation gamma. Energy deposits in cubes in the other detector hemisphere (green) are associated with the second annihilation gamma. [124]

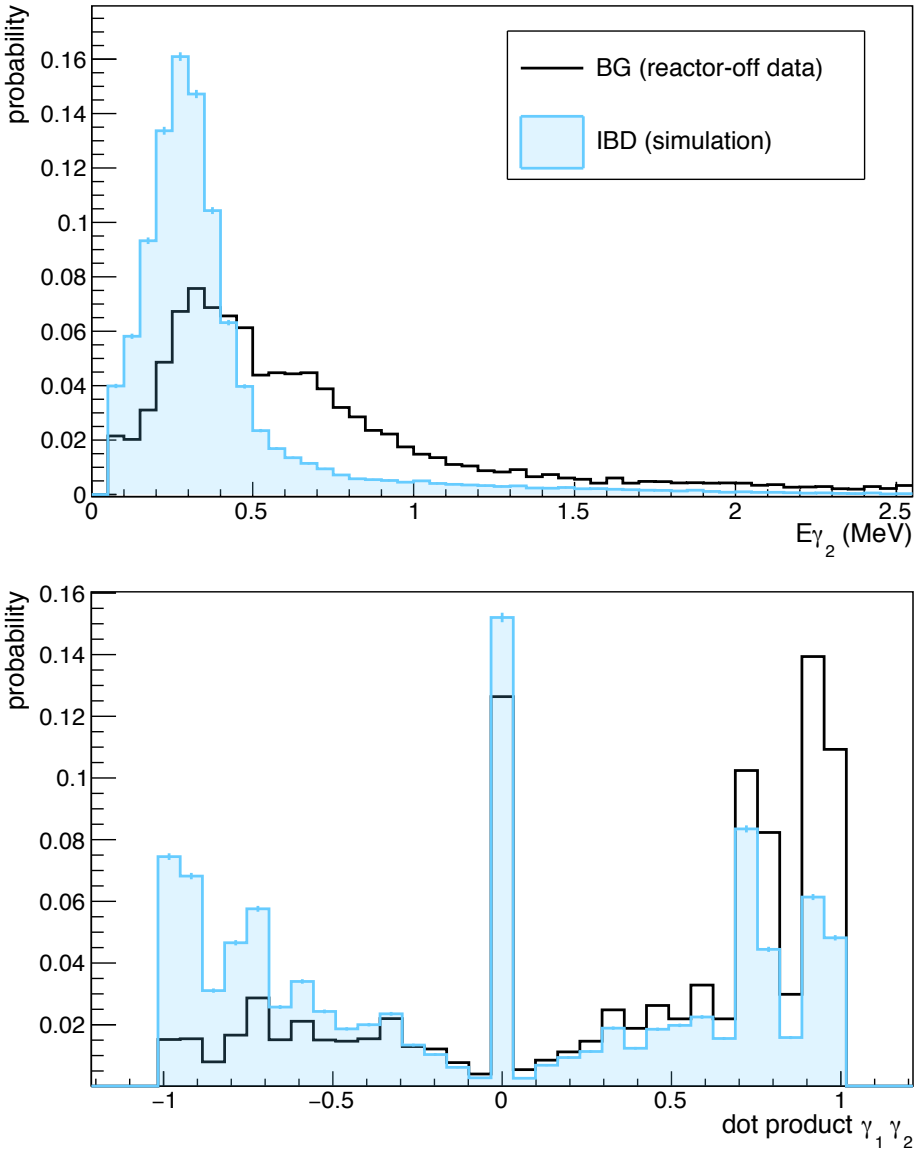

Figure 5.17: Two promising annihilation gamma variables for background discrimination: the reconstructed gamma energies, illustrated using the energy of the second selected gamma, (top) and the cosine of the angle between the two gamma-vectors (bottom).

for the IBD analysis is the MLP one, which stands for *Multi Layer Perceptron* and is an implementation of a neural network. In general, a neural network (NN) can be considered to perform a mapping from a multidimensional space of input variables onto a one-dimensional space of output variables. This mapping is based on associations that the NN has developed from an example set of inputs and outputs, similar to the learning process in a human brain. The code and analysis for this method were developed at Subatech.

Execution and performance of both MVA analyses

The execution of both MVA analyses is very similar and can be summarised as follows:

1. Two training data sets are loaded: a background sample is created from reactor-OFF data and a signal sample from MC generated IBDs.
2. The pre-selection that is listed in table 5.2 is applied to both datasets.
3. These samples are fed to the uBDT/NN classifier, which will do the training, based on predefined functions of the uBoost/TMVA package.
4. The training is performed over three so-called *categories*, corresponding to 0γ, 1γ and 2γ events. Additional input variables related to the reconstructed gammas are each time added to the training for the 1γ and 2γ categories.
5. The output of the training gives a new variable, that we can use to discriminate the signal from the background, as shown in figures 5.18 and 5.19 for the uBDT and NN codes, respectively.

We note that the reconstructed position and energy variables, L_{reco} (equivalent to z_{reco}) and E_{reco}, are not used as a training variable for both codes. In the uBDT code, they are treated as separate input parameters for which a uniform selection efficiency is required. A check of this uniformity is shown in figure 5.20.

The choice of the best ML discriminator cut is driven by the *Figure of Merit (FoM)* that one wants to impose. For both analyses, it was opted to use the value $S/\sqrt{(S+B)}$ as the FoM that is to be maximised.

Using these machine learning codes reduces the background contamination with a factor 3 for the same IBD efficiency of $\sim$10%, as illustrated in figure 5.21.

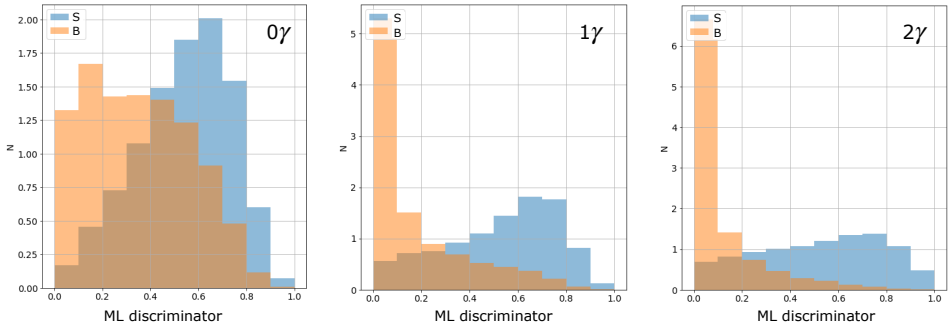

Figure 5.18: Performance of the uBDT principle: the ML discriminator shows a clear separation between the IBD signal (blue) and the background determined from reactor-OFF data (orange) in each of the three categories of the number of reconstructed gammas.

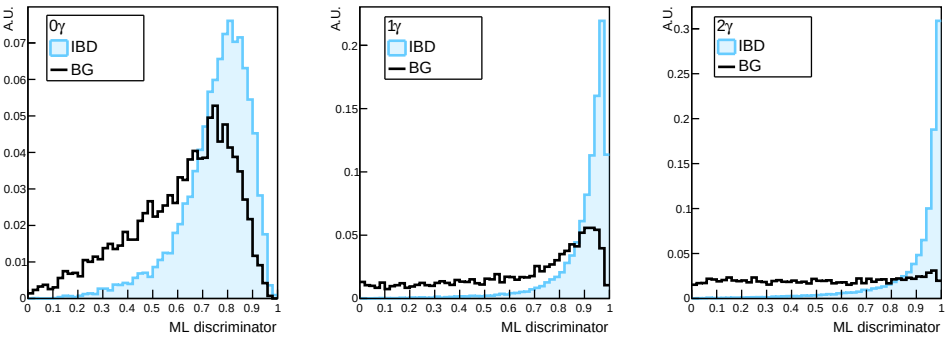

Figure 5.19: Performance of the NN principle: the ML discriminator shows a clear separation between the IBD signal (blue) and the background determined from reactor-OFF data (black) in each of the three categories of the number of reconstructed gammas.

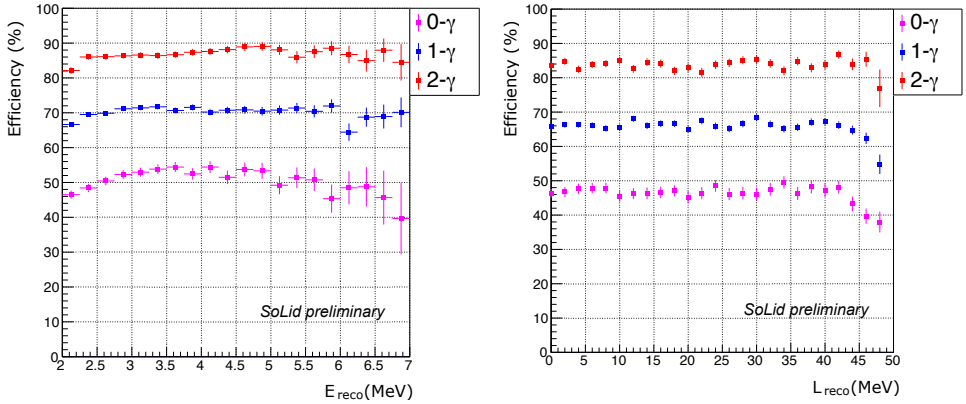

Figure 5.20: Uniformity of the uBDT selection efficiency in reconstructed E and L.

Table 5.2: Preselection cuts applied to the training data sets for both the uBDT and the neural network method.

Variable	Pre-selection
E_{reco}	[2,7] MeV
Δt	[1,141] µs
Δr	]0,4] cubes
Δx	[-3,3] cubes
Δy	[-3,3] cubes
Δz	[-2,3] cubes
BiPonisher	>1.44

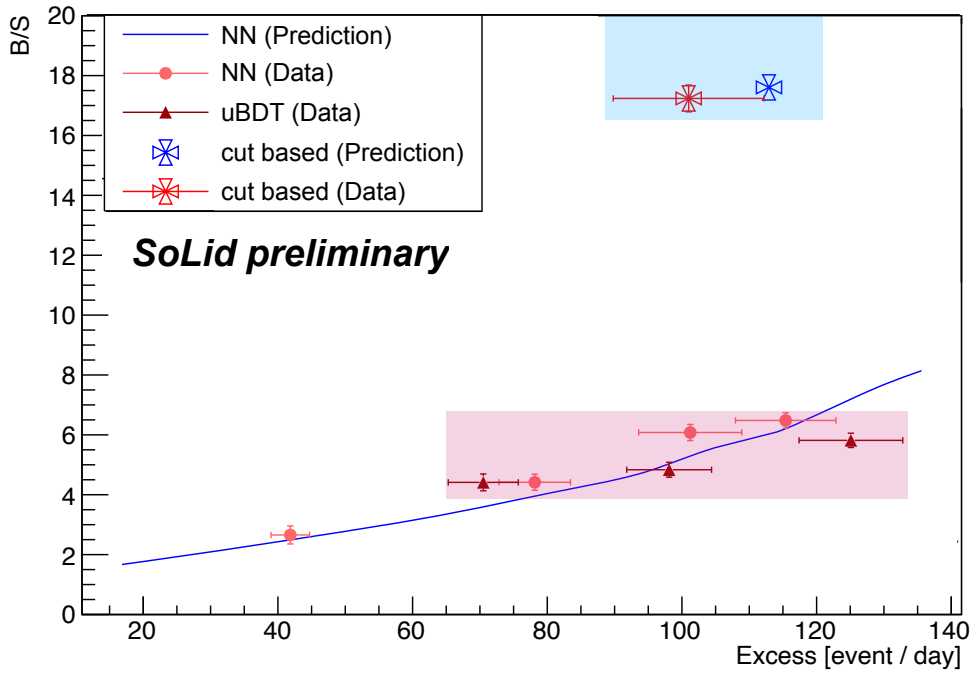

Figure 5.21: Comparison of the IBD selection efficiency versus background-to-signal ratio for the three presented IBD selection methods. Adapted from [133].

5.4.3 Background subtraction

Once all cuts are applied, the resulting data set contains a certain amount of IBD events and a remaining contribution from background events, that occupy the allowed parameter space. To be able to deduce the final signal excess, the remaining background distributions first need to be determined with precision and then subtracted. Based on the knowledge of the various components in the recorded data, we make the following six selections:

- S_{signal} and A_{signal}: the *signal* selections.
  S_{signal} includes all events that are within the allowed parameter space after the IBD event selection. This selection will thus contain the IBD signal, but also the remaining background events.
  A_{signal} is a selection based on the same parameter cuts, but with negative Δt values. It represents the accidental background component that, since it is approximately flat over the relevant Δt values, can be directly extrapolated and subtracted from the S_{signal} window. We will denote the remaining *correlated* events as $C_{signal} = S_{signal} - x_S A_{signal}$, where x_S is a scaling factor that takes into account a possible difference in the width of the accidental Δt window and that of the signal Δt window .
- S_{BiPo} and A_{BiPo}: the *BiPo* selections.
  S_{BiPo} is a selection of pure BiPo events, made by shifting the allowed Δt values to [300 - 500] µs and inverting the BiPonisher cut.
  A_{BiPo} is again selected by switching to negative Δt values and can likewise immediately be subtracted from S_{BiPo}. This results in $C_{BiPo} = S_{BiPo} - x_{BP} A_{BiPo}$, where x_{BP} is a similar type of scaling factor as x_S.
- S_{atm} and A_{atm}: the *atmospheric* selections.
  S_{atm} is a component that can not be selected with the use of a shifted time window or a dedicated parameter, as the atmospheric background parameter values largely overlap with those of the IBD signal. Therefore, this selection is determined from reactor-OFF data. This data, when passed through the same signal selection cuts, will exist of only an accidental, a BiPo and an atmospheric contribution. The first two can be selected by the same methods used for reactor-ON data. When subtracting them, the atmospheric selection remains, as described below in more detail.

Figure 5.22 shows some of these signal and background selections as a function of the Δt parameter.

Starting from these selections, the first step is then the subtraction of the BiPo-component from the signal window. Since the BiPo selection is made by shifting the Δt-window and inverting the BiPonisher cut, we first need to

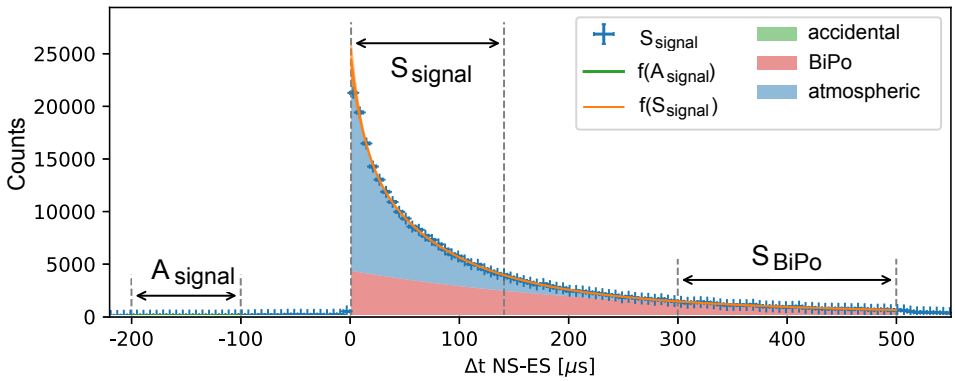

Figure 5.22: Illustration of the distribution in Δt for the signal, accidental and BiPo events. The S_{signal}, A_{signal} and S_{BiPo} selection windows that are used in the background subtraction procedure are indicated. The signal selection for reactor-OFF data consists of only atmospheric background events, while for reactor-ON data, an additional contribution of the IBD events is expected in this window. Adapted from [82].

extrapolate this selection to the expected distribution in the signal region. A dedicated scaling factor χ_{BiPo} can be determined relatively easily by

1. fitting the Δt distribution of the BiPo events, and comparing the integral over the BiPo time window to that over the IBD time window,
2. determining the fraction of α's "polluting" the allowed BiPonisher range of the IBD selection, i.e. those events with BiPonisher value > 1.5.

The signal selection without BiPo contribution is thus:

$$\begin{aligned} C_{signal-BiPo} &= C_{signal} - \chi_{BiPo} C_{BiPo} \\ &= [S_{signal} - A_{signal}] - \chi_{BiPo}[S_{BiPo} - A_{BiPo}] \end{aligned} \tag{5.2}$$

Next, the subtraction of the atmospheric background events is needed. As mentioned, the selection of these events has to be based on reactor-OFF data and, to first order, the atmospheric component can be determined as follows:

$$\begin{aligned} C^{OFF}_{atm} &= C^{OFF}_{signal-BiPo} \\ &= C^{OFF}_{signal} - \chi_{BiPo} C^{OFF}_{BiPo}. \end{aligned} \tag{5.3}$$

An additional challenge comes from the fact that the rate of this background is strongly correlated with pressure, that varies over time. Therefore, a pressure-correction of the C_{atm}^{OFF} is needed, before subtracting it from the reactor-ON selection. For this purpose, the correction factor χ_{atm} is introduced.

This correction factor can be calculated based on a fit of the C_{atm}^{OFF} component as a function of the pressure P. The atmospheric pressure-background correlation is shown in figure 5.23 and the fit is of the form

$$C_{atm,\,j}^{OFF} = f(P_j) = a \times P_j + b, \tag{5.4}$$

for the different time bins j.

The correction factor that compensates for the possible difference in pressure between reactor-ON period i and reactor-OFF period j data then is

$$\chi_{atm} = \frac{f(P_i)}{f(P_j)} \tag{5.5}$$

Using the χ_{atm} factor, the atmospheric background component, estimated from reactor-OFF data is subtracted from the remaining reactor-ON selection, and the signal excess (R_{IBD}) is found:

$$R_{IBD} = C_{signal-BiPo}^{ON} - \chi_{atm} C_{atm}^{OFF} \tag{5.6}$$

We note that this formula represents the excess rate. For the determination of the absolute IBD excess, a scaling factor that takes into account the amount of reactor-OFF data compared to the amount of reactor-ON data is needed. The full subtraction equation then is

$$\begin{aligned} R_{IBD} = \; & (S_{signal} - x_S A_{signal}) - \chi_{BiPo}(S_{BiPo} - x_{BP} A_{BiPo}) \\ & - \left(\frac{t_{ON}}{t_{OFF}}\right) \chi_{atm} \left[(S_{atm}^{OFF} - x_S A^{OFF}) - \chi_{BiPo}(S_{BiPo}^{OFF} - x_{BP} A_{BiPo}^{OFF}) \right] \end{aligned} \tag{5.7}$$

And the statistical uncertainty is found as

$$\begin{aligned} \sigma_{IBD}^2 = \; & (S_{signal} + x_S^2 A_{signal}) + \chi_{BiPo}^2 (S_{BiPo} + x_{BP}^2 A_{BiPo}) \\ & + \left(\frac{t_{ON}}{t_{OFF}}\right)^2 \chi_{atm}^2 \left[(S_{signal}^{OFF} + x_S^2 A_{signal}^{OFF}) + \chi_{BiPo}^2 (S_{BiPo}^{OFF} + x_{BP}^2 A_{BiPo}^{OFF}) \right] \end{aligned} \tag{5.8}$$

We already note that an improved subtraction method, that will be the default for future analyses, will be presented in chapter 8.

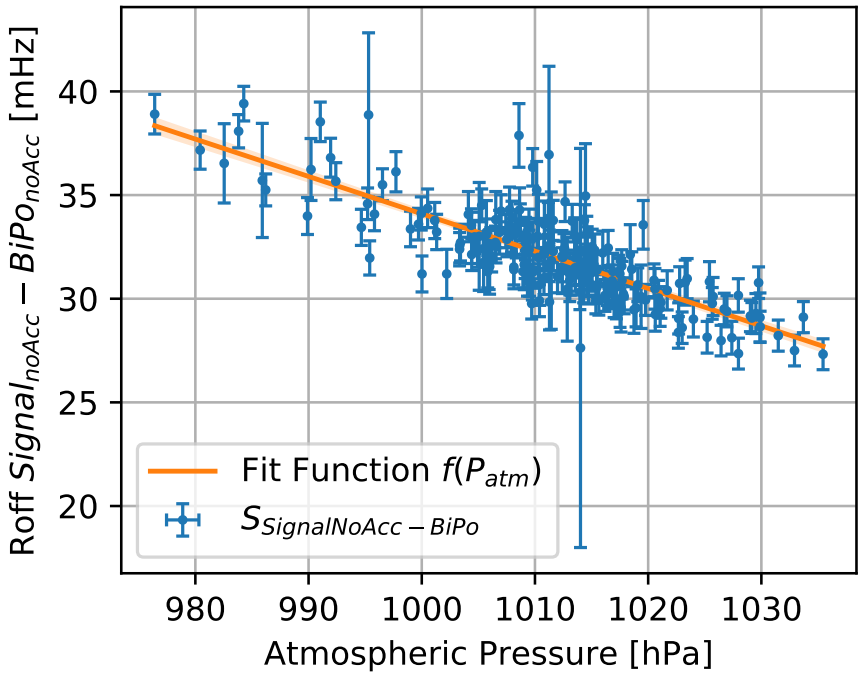

Figure 5.23: Example of the evolution of the atmospheric background component (from reactor-OFF data) as a function of the atmospheric pressure. The linear fit is used to determine the atmospheric correction factor. [134]

5.4.4 Signal excess

Using the methods described above, it is now possible to determine an IBD signal excess from a selected dataset.

We will evaluate here the data taken between June 9 and August 18 of 2018, that includes reactor cycle 3 from the 12th of June to the 10th of July 2018. This is the current Phase I open dataset, that is used for the development, training and testing of the IBD selection methods. The reactor-ON and reactor-OFF samples exist of:

- ON: Every reactor day of cycle 3-2018, except those days at a temporary reactor shutdown. This corresponds to the period from June 13 to 15, 2019 and that from June 20 to July 9, 2019. The days at reactor-ON/-OFF transition periods are taken into account when the average reactor power is above 40 MW. In total 25 days of reactor-ON data are used.
- OFF: Only a few reactor-OFF days between June 9 and August 18, 2019 are used. All days during reactor transition, during which the detector was under maintenance, those used for the uBDT training and of the period from August 7 to August 8 are excluded. This results in a total of 18 days.

We note that this dataset is estimated to be only 7% of the total amount of data recorded with the Phase I detector.

For the evaluation of the IBD excess in this open dataset, we have used the uBDT selection code and the subtraction method described in the previous section. Figure 5.24 shows the recorded excess of IBD events for each day of the reactor-ON and -OFF samples. This excess increases with the reactor power, as expected. Combining all 25 reactor-ON days, a total excess of 2656.85 ± 258.73 was found, which is on average 106.27 ± 10.35 events/day.

The distribution of the signal and background events in energy and position is shown in figure 5.25. The shapes for the IBD excess are compared to the Monte Carlo IBD simulation and show a good agreement within statistical uncertainties.

We note that this excess is the result of data selections and manipulations which are still under evaluation at the time of writing. This preliminary result is thus only used as an example to illustrate the described concepts.

5.5 Summary

In this chapter, we have described the inputs and methods that are used for the IBD signal selection. In section 5.1 the expected IBD signal properties

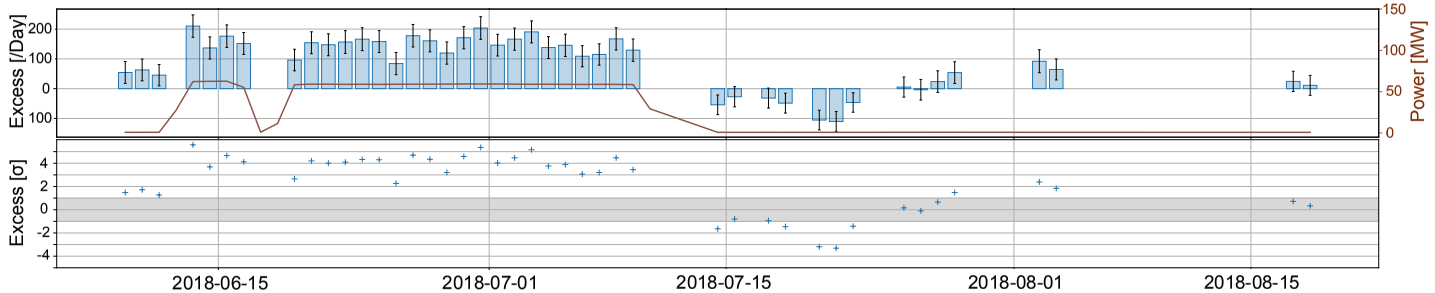

Figure 5.24: Top: The excess of IBD events for each selected day in the period from June 9 and August 18 of 2018. The reactor power evolution is also shown for reference. Bottom: The significance of the excess per day in terms of the standard deviation σ.

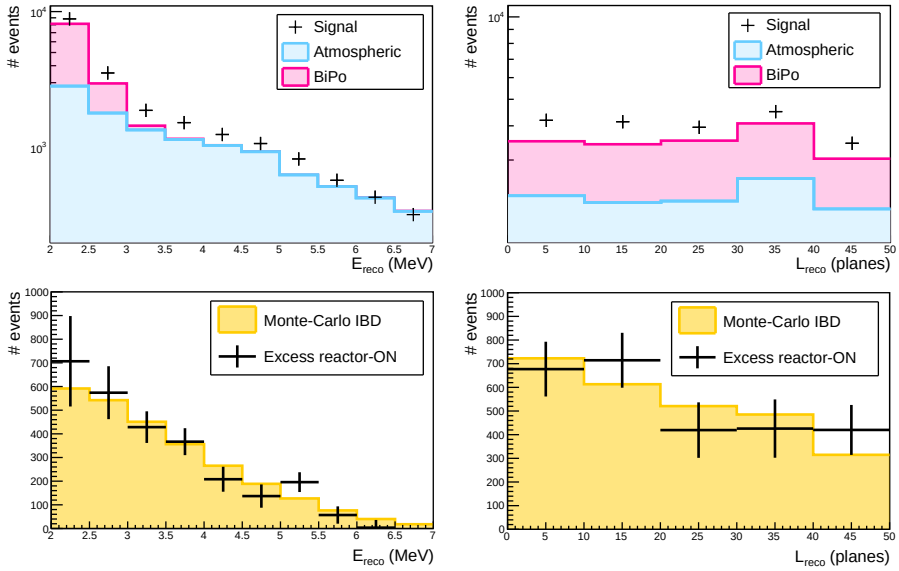

Figure 5.25: Top: The energy and length reconstruction for the C_{signal}, C_{atm} and C_{BiPo} selections, after application of the related scaling factors. Bottom: the energy and length reconstruction for the IBD excess and the Monte Carlo simulation.

were presented, using the information of Monte Carlo simulations, and section 5.2 was dedicated to the background sources and their properties. The two dominant backgrounds are radioactive BiPo events and fast atmospheric neutrons, because of their prompt-delayed timing and energy deposits that are similar to those of IBD events.

Using the knowledge of the signal and background properties and the general data taking conditions, a set of selection criteria or cuts can be defined to reduce the contribution of background noise as much as possible. Of course, these selection criteria can also have an impact on the signal and it is thus a question of finding the optimal set of cuts to obtain the highest possible IBD detection efficiency and signal-to-background ratio. Three IBD selection methods were presented, two of which use multivariate analysis techniques with machine learning codes. We have also shown that the use of annihilation gamma information can be very valuable to improve the background reduction.

In section 5.4.3, a first background subtraction method, that is used for the presented IBD analysis, was discussed. An updated version of the subtraction method will be presented in chapter 8.

Finally, a preliminary version of the resulting signal excess for the current Phase I open dataset was presented.

6 Oscillation Analysis

Using the detected IBD events, an oscillation search for the mixing of the electron antineutrinos with a light sterile neutrino can be performed. This analysis step essentially consists of a comparison of the selected data with a Monte Carlo prediction that contains an oscillation hypothesis. The 3+1-oscillation hypothesis model was introduced in chapter 1, and is probed by the SoLid experiment via the antineutrino disappearance probability:

$$P_{\overline{\nu}_e \to \overline{\nu}_e} = 1 - \sin^2(2\theta_{14}) \, \sin^2\left(\frac{1.27\Delta m^2_{41} L_{\overline{\nu}_e}}{E_{\overline{\nu}_e}}\right). \tag{6.1}$$

The purpose of the oscillation analysis is to determine those mixing parameters $\sin^2(2\theta_{14})$ and Δm^2_{41} that provide a model that best matches the data. As the two variables $L_{\overline{\nu}_e}$ and $E_{\overline{\nu}_e}$ are a priori unknown, the data-to-Monte Carlo comparison will be directly evaluated as a function of the reconstructed $\overline{\nu}_e$'s energy E_{reco} and the reconstructed path length L_{reco}. A thorough determination of the uncertainties on these reconstructed variables is crucial for a correct interpretation of the oscillation analysis results and will be treated in the following chapter.

This chapter will further detail the statistical methods used by the SoLid collaboration to perform the oscillation fit. The work of this thesis existed in the implementation, optimisation and analysis of the techniques presented below.

6.1 Introduction to hypothesis testing

In the previous chapters, we have described the methods for the antineutrino data collection and selection and presented the deduced excess of IBD events.

The next step is now to interpret the characteristics of these IBD events in terms of the physical model of sterile neutrino oscillations. More specifically, we want to test to what extent the data confirms or rejects the assumption of a sterile neutrino oscillation at very short baseline.

In general, the plausibility or validity of a certain model, given the acquired data, can be deduced from a statistical analysis that is called *hypothesis testing*. The hypothesis is basically the assumption that is made about the outcome of the data and it is tested by calculating some quantity of the data under this given assumption. The result of the test allows us to interpret whether the assumption holds or whether it has been violated.

The default assumption of a statistical test is called the null hypothesis H_0; it represents the assumption that nothing has changed. The opposite of the null hypothesis is an alternative hypothesis H_1, that supports the proposed new model. For the SoLid oscillation search, the null hypothesis will for example state that the data can be described by the unaltered SM prediction of the mixing of 3 neutrino flavours or, equivalently, that $(\sin^2(2\theta_{14}), \Delta m^2_{41}) = (0, 0)$. The alternative hypothesis in this case supports the model of an additional, sterile neutrino state that is driven by the non-zero parameters $\sin^2(2\theta_{14})$ and Δm^2_{41}.

Given these hypotheses we now want to make a statement about the *probability* for the outcome of the data. If the experimental data is characterised by one or more parameter values, which we can write as a vector $\vec{x}$, then some probability of this outcome given hypothesis H, $P(\vec{x}|H)$, needs to be determined. How this is done in practice for the SoLid oscillation analysis will be discussed in the following section.

We note that in this thesis we use the classical or *frequentist* approach for the interpretation of *probabilities*. This means that the probability for a certain outcome of an experiment is considered as *the relative frequency of occurrence of this outcome when repeating the same experiment a very large number of times*. A competing approach is the one of Bayesian statistics, that makes use of some prior knowledge as an input for the estimation of a probability. We note that both frequentist and Bayesian approaches are equally "correct" and often result in the same conclusions: the choice is mostly a question of habits and taste.

6.2 Fit statistics

To really quantify the level of agreement between the data and a given hypothesis, one can define a so-called fit statistic or goodness-of-fit parameter. This statistic is a function of the data, and its value can be compared to what one expects under the assumption of H_0. The significance of a discrepancy between data and hypothesis is then quantified by the *p-value*, that is defined as the probability to find a value for the fit statistic in the region of equal or lesser compatibility with H_0 than the level of compatibility observed with the actual data [135].

Let us illustrate this for the concrete case of the goodness-of-fit statistic used for the oscillation analysis. The test that is used here to provide a measure of the agreement between the data and the hypothesised model is the Pearson's χ^2 statistic:

$$\chi^2 = \sum_{ij}^{N} \left(\frac{D_{ij} - P_{ij}}{\sigma_{ij}} \right)^2 , \tag{6.2}$$

where the data is represented by events in the $N = n_L \times n_E$ position-energy histogram bins, D_{ij}, and the hypothesis is contained in the model prediction that is represented by the values P_{ij}. In general, the model is not perfect and is only known within an estimated uncertainty, that is defined as the *standard deviation* σ_{ij}.

In case the data D_{ij} are indeed a statistical representation of the proposed model, then the χ^2 statistic will follow a χ^2 probability density function (p.d.f.) with the number of degrees of freedom (n.d.o.f.) k equal to the number of position-energy bins ($n_L \times n_E$) minus the number of free parameters in the fit:

$$f(\chi^2, k) = \frac{(\chi^2)^{k/2-1} e^{-\chi^2/2}}{2^{k/2}\, \Gamma(\frac{k}{2})}. \tag{6.3}$$

This p.d.f. distribution and its cumulative are plotted in figure 6.1 for values $k = 0, ..., 6$. Using the cumulative distribution, the fraction of possible outcomes for the prediction that result in an equal or larger χ^2 than the one obtained from the data can easily be derived. It represents the probability to find a more extreme fit result than the measured one, in other words the p-value of the test.

When the p-value of the measurement is deduced, it tells us with what confidence the null hypothesis H_0 can be accepted. Often, the level of confidence in the degree of rejection of a hypothesis is quoted in literature. This

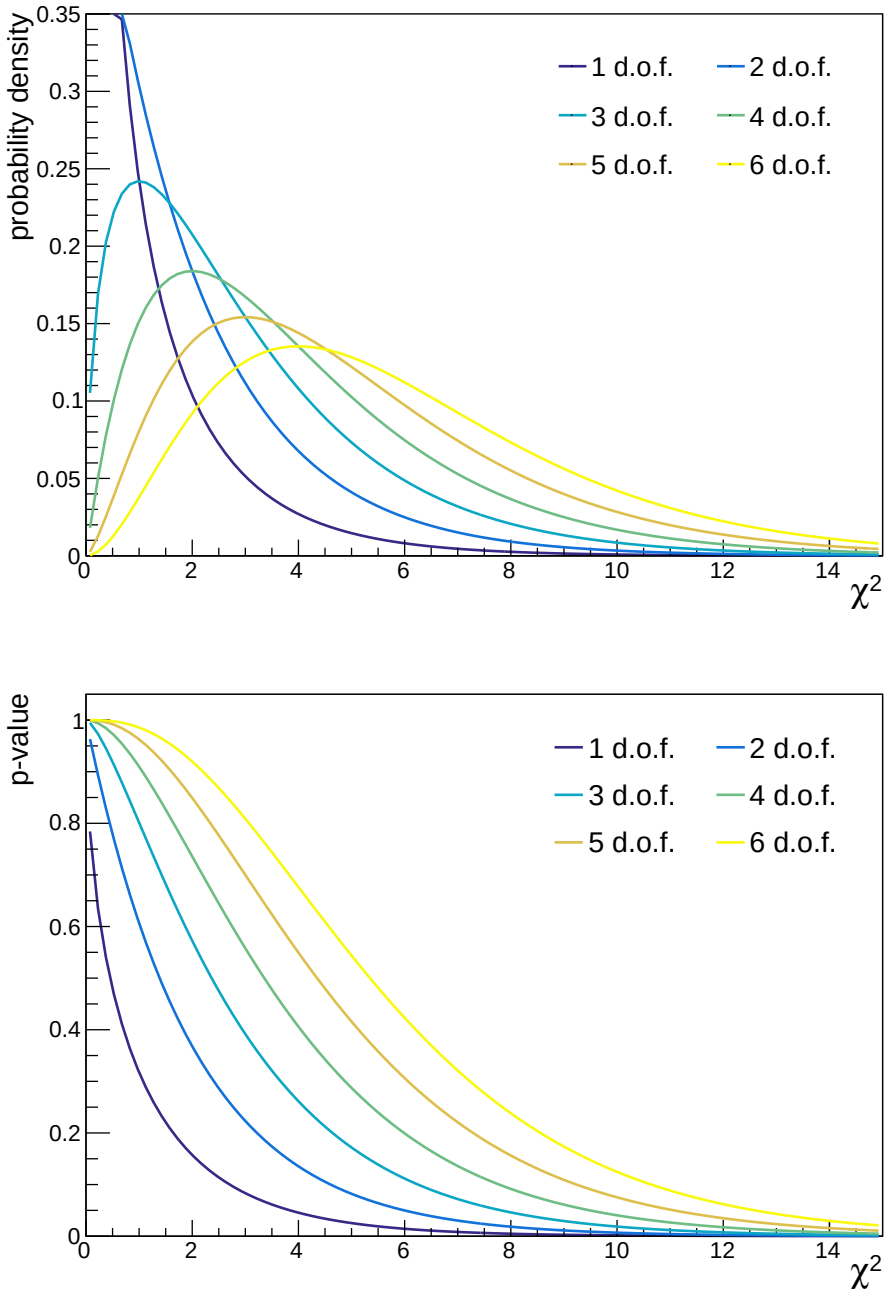

Figure 6.1: The χ^2 probability density function (top) and its complementary cumulative (bottom) for a number of degrees of freedom $k = 0, ..., 6$.

is called an exclusion confidence level (CL) and is the complement of the p-value: $CL = 1 - p$.

In case H_0 is not rejected, i.e. when it has an acceptable p-value, the statistical analysis can continue with tests of the alternative hypotheses H_x and the determination of exclusion contours in the parameter space of the alternative model's parameters. The methods for the construction of those exclusion contours will be discussed in detail in section 6.5.

We should note that equation 6.2 gives the χ^2 fit statistic in its simplest form, where it is assumed that the P_{ij} values, as well as the D_{ij} values are uncorrelated and where no systematic uncertainties are included. In the following paragraphs, we will discuss two methods for the inclusion of (correlated) systematic uncertainties in the χ^2 fit.

6.2.1 Nuisance parameters

One way to improve the model of the hypothesis, is to introduce a number of additional parameters α_k in the fit [136]:

$$\chi^2 = \sum_{ij}^{N} \left(\frac{D_{ij} - P_{ij}(\alpha_k)}{\sigma_{ij}} \right)^2 + \sum_k \left(\frac{\alpha_k}{\sigma_k} \right)^2 . \tag{6.4}$$

These α_k's are so-called *nuisance parameters* and the values σ_k represent their assumed (correlated) errors. The best fit to the data is now found for those values of the α_k that minimise the χ^2, in this way including the effect of (correlated) systematic uncertainties in the updated model $P_{ij}(\alpha_k)$. It is to constrain the values of the nuisance parameters, that the additional *pull terms*, $(\alpha_k/\sigma_k)^2$, are introduced as well.

We want to stress that the fitted values of these α_k parameters are in principle not of interest. They simply help to improve the fit to the data and thus allow to account for some additional systematic uncertainties. However, they sometimes *can* be useful to identify possible biases in the model or to study poorly known systematics.

6.2.2 Covariance matrix

The correlated systematic uncertainties in a model can also be represented by so-called covariance matrices. In such matrices, the statistical and uncorrelated systematic uncertainties for the model prediction construct the matrix diagonal, while the correlated uncertainties populate the off-diagonal matrix elements. Uncertainties related to different sources can be combined in one

full covariance matrix, that we will simply denote here as V^{tot}. The use of the covariance matrix approach is especially useful when detailed information on the systematic uncertainties is available from the experiment.

When working with a covariance matrix, the data - i.e. both measurement and prediction - has to be reshaped from a 2D histogram to a 1D matrix for practical use. For data that is binned in $(L_{\text{reco}}, E_{\text{reco}})$ in a total of $n_L = 5$ by $n_E = 10$ histogram bins, the related data matrix becomes a (1×50)-matrix. For a histogram bin with indices (i, j) that run over the bins in L_{reco} and E_{reco}, respectively, a new matrix position index is determined as

$$\alpha = i * n_E + j, \tag{6.5}$$

where n_E represents the number of E_{reco}-bins. This translation from histogram to matrix is illustrated in figure 6.2, for clarity. One can see that the matrix elements are grouped as one energy spectrum per baseline, running from shortest to longest baseline with increasing α.

Since the uncertainties on the model are evaluated per bin, and the covariance matrix also represents bin-to-bin correlations, this uncertainty matrix V^{tot} will be 50 by 50 large. Each element $V_{\alpha\beta}$ of V^{tot} represents the relation between bin $\alpha(i, j)$ and bin $\beta(k, l)$ in the $(L_{\text{reco}}, E_{\text{reco}})$-data.

With the data and prediction rewritten to matrix format, the χ^2 definition is written as:

$$\chi^2 = (D - P)^T V^{-1} (D - P) \tag{6.6}$$

$$= \sum_{\alpha}^{N} \sum_{\beta}^{N} (D_\alpha - P_\alpha)^T V^{-1}_{\alpha\beta} (D_\beta - P_\beta). \tag{6.7}$$

6.2.3 Nuisance parameters versus covariance matrix

Although it is not straightforward to derive, the use of nuisance parameters or covariance matrices in the χ^2 formalism are known to be fully equivalent. This equivalence between both approaches can be derived analytically, e.g. as demonstrated by Fogli et al in [136]. We should note that, although this assertion of equivalence is consistent for most realistic cases where the systematic errors are not extremely large compared to the statistical ones, there are exceptional cases for which this assumption is incorrect [137].

The choice between both approaches is mostly driven by the practical implementation and use. In particular, it is often a trade-off between the size

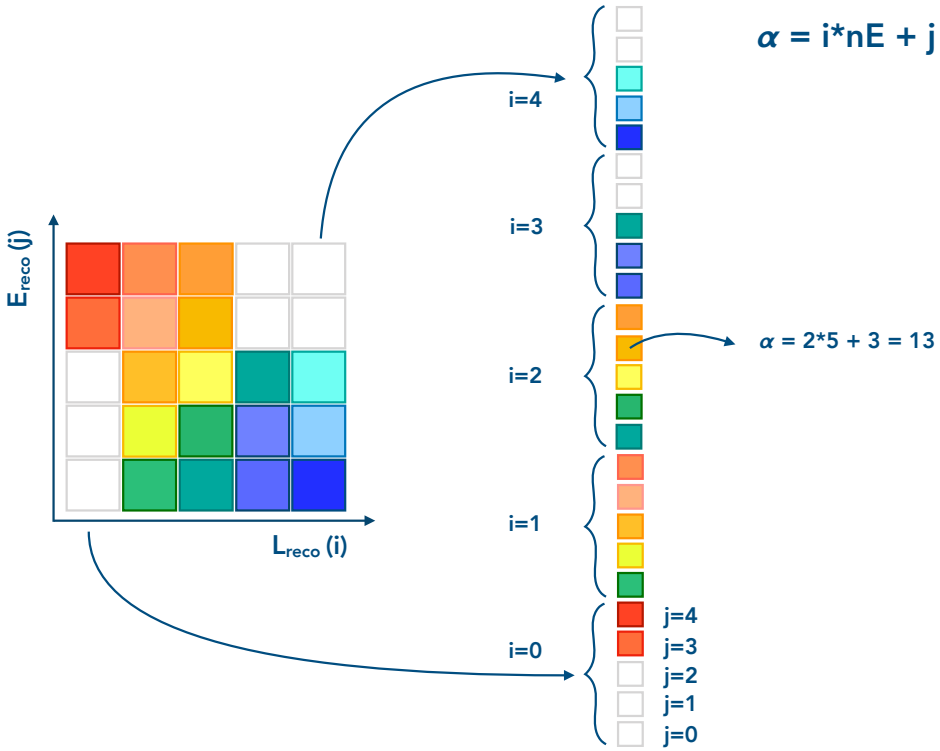

Figure 6.2: Scheme of the data and covariance matrix binning convention.

of the set of measurements, in this case that is the total number of bins in the fit, N, and the number of systematic uncertainty contributors, K.

For the covariance matrix approach, the inversion of an $N \times N$ matrix is required, which becomes increasingly computationally demanding for larger values of N. For the pull terms method, on the other hand, the complexity of the minimisation procedure increases with K and for $K \gg N$, the covariance matrix approach becomes more efficient.

A mixed approach is also possible, where one can exploit good knowledge of some uncertainties in the use of a related covariance matrix, while including one or more nuisance parameters for other systematics.

In this thesis, we will choose to use covariance matrices for the representation of the systematic uncertainties.

6.3 Oscillation fit definitions

Above, the most direct form of the χ^2 fit statistic was presented, where the measurement and predicted histograms are compared bin per bin. Nevertheless, we can define multiple types of fits for the oscillation analysis, that are each (more) sensitive to a different aspect of the oscillation model.

6.3.1 Rate+shape fit

The rate+shape fit is the most general approach and uses the standard χ^2 definition presented above:

$$\chi^2 = \sum_{\alpha}^{N}\sum_{\beta}^{N}(D_\alpha - P_\alpha)^T V_{\alpha\beta}^{-1}(D_\beta - P_\beta). \tag{6.8}$$

This statistic takes into account all potential spectral and temporal information contained in the binned data. It requires a very good knowledge of the predicted reactor model, both in terms of the predicted normalisation and spectrum, and the corresponding uncertainties.

6.3.2 Rate-only fit

The rate-only statistic compares the total measured amount of IBD candidates to the total predicted amount, independent of the spectral shape. By summing over all histogram bins, a ratio N_D/N_P of detected-to-predicted events can be derived. In case the statistical and systematic uncertainties are well-controlled, this ratio can be compared to the RAA, which has shown a

∼6% deficit of measured antineutrinos, see section 1.4.3. This result can be particularly interesting for the SoLid experiment, as it measures a pure ^{235}U flux, compared to the previous generation of experiments that operated at commercial reactors with mixed fuel compositions and can therefore evaluate the fuel-dependence of the RAA.

Secondly, the measured rate can be summed over all energy bins, but per detector module - or over even smaller detector segments, in case of high enough statistics - and fitted to the predicted rate. For this purpose we will note

$$D_i = \sum_j^{n_E} D_{ij} \quad \text{and} \quad P_i = \sum_j^{n_E} P_{ij} \tag{6.9}$$

for the sum of all events in detector module i. The χ^2 fit then becomes

$$\chi^2 = \sum_i^{n_L} \sum_k^{n_L} (D_i - P_i)^T V_{ik}^{-1} (D_k - P_k), \tag{6.10}$$

where the measured number of events is compared to the predicted one in all five detector modules and an oscillation pattern as a function of distance might be discerned.

6.3.3 Shape-only fit

A shape-only chi-squared statistic can be designed to remove the dependence on the normalisation of the signal prediction. This fit can be constructed very simply by normalising the prediction to the measurement:

$$\chi^2 = \sum_\alpha^N \sum_\beta^N (D_\alpha - \epsilon P_\alpha)^T V_{\alpha\beta}^{-1} (D_\beta - \epsilon P_\beta) \tag{6.11}$$

with

$$\epsilon = \frac{\sum_\alpha^N D_\alpha}{\sum_\alpha^N P_\alpha}. \tag{6.12}$$

In a similar way the renormalisation can be accomplished by adding a free parameter ξ to the fit, instead of the fixed ϵ:

$$\chi^2 = \sum_\alpha^N \sum_\beta^N (D_\alpha - \xi P_\alpha)^T V_{\alpha\beta}^{-1} (D_\beta - \xi P_\beta). \tag{6.13}$$

With a shape-only fit, possible length-dependent spectral distortions that point to an oscillation can be probed. The spectra can also be summed over

all position bins and the resulting fit, that is only sensitive to the spectral shape of the $\overline{\nu}_e$-measurement, can be useful for an evaluation of the spectral anomaly at 5 MeV, see section 1.4.4.

6.3.4 Relative fit

For an oscillation analysis that has a minimal dependence on the uncertainties in both the shape and the normalisation of the reactor flux prediction, a relative fit can be defined. In that case, the oscillation result is based on comparisons between the measured spectra for different detector baselines. This approach is thus only possible for experiments that use segmented or multiple detectors. There are different options for the definition of such a relative fit. One method that has been used for a number of neutrino oscillation searches is that using a near-far ratio, where the detected spectrum in one cell is used as the reference for the prediction in the others cells. Usually, the detector cell closest to the reactor is used as reference bin, as it has the highest statistics. We denote the reference values for each energy bin j as R_{0j}, where the 0 subscript refers to the first position bin. The relative prediction P_{ij}^R for the other detector cells ($i > 0$) is then calculated as

$$P_{ij}^R = \frac{P_{ij}}{P_{0j}} R_{0j} = w_{ij} R_{0j} \tag{6.14}$$

The χ^2 sum now runs over one position bin less:

$$\chi^2 = \sum_{i>0}^{n_L-1} \sum_{j}^{n_E} \sum_{k>0}^{n_L-1} \sum_{l}^{n_E} (D_{ij} - P_{ij}^R)^T V_{\alpha\beta}^{-1} (D_{kl} - P_{kl}^R). \tag{6.15}$$

As mentioned, other relative fit definitions are possible as well, and we will summarise here those used by the STEREO and PROSPECT experiments.

The STEREO collaboration has presented a relative fit by assigning a free parameter ξ_j to each energy bin j [87]:

$$\chi^2 = \sum_{i}^{n_L} \sum_{j}^{n_E} \sum_{k}^{n_L} \sum_{l}^{n_E} (D_{ij} - \xi_j P_{ij})^T \; V_{(ij,kl)}^{-1} \; (D_{kl} - \xi_l P_{kl}). \tag{6.16}$$

These ξ_j rescale the number of predicted IBDs per energy bin j, and integrated over all detector cells, to match their average number of measured IBDs. As such, the prediction is made independent of all absolute rate and spectral information.

Alternatively, the PROSPECT collaboration has defined a fit based on the ratio of the detector-wide measured and predicted content of E_{reco} bin j [85]:

$$\chi^2 = \sum_i^{n_L} \sum_j^{n_E} \sum_k^{n_L} \sum_l^{n_E} \left(D_{ij} - D_j \frac{P_{ij}}{P_j} \right)^T V^{-1}_{(ij,kl)} \left(D_{kl} - D_l \frac{P_{kl}}{P_l} \right) \tag{6.17}$$

with

$$D_j = \sum_i^{n_L} D_{ij} \quad \text{and} \quad P_j = \sum_i^{n_L} P_{ij}. \tag{6.18}$$

Here, the rescaling of the prediction to the measurement for each energy bin j, reduces the dependence on the reactor spectrum and rate of the model. In addition, possible relative energy response variations between detector cells are directly corrected for.

6.4 SoLid oscillation fit

For the first oscillation analysis result, the SoLid collaboration will use a relative fit similar to the principle of the PROSPECT- and STEREO-like fits. The difference between these two is mostly determined by the treatment of the uncertainties, where the PROSPECT-like fit uses more a priori information on the uncertainties, summarised in covariance matrices, and the STEREO-fit introduces free nuisance parameters with pull terms.

As the studies on the systematic uncertainties of the current SoLid dataset are still ongoing at the time of writing (see chapter 7), it is left undecided how these uncertainties will be propagated in the final fit. In this thesis, we choose to present the example contours based on the PROSPECT-like fit, with covariance matrices representing the main uncertainties.

6.4.1 Fake dataset

A first contour based on real SoLid data, albeit for only a small data sample, will be presented in chapter 8. To illustrate the concepts presented in the following sections of this chapter, however, we will use a *fake* dataset that has roughly the same size as the total SoLid Phase I dataset.

The predicted IBD events are generated with the neutrino generator, presented in chapter 3, and the migration matrix, presented in chapter 4:

- The simulated IBD interactions are generated requiring a normalisation corresponding to 350 days of reactor-ON data with a thermal power

of 55 MW. This roughly corresponds to the total amount of reactor-ON data gathered by the Phase I detector (see table 5.1), considering a fraction of the days will probably be removed from the analysis due to instabilities. The reactor spectrum is simulated according to the Huber-Mueller prediction, without sterile oscillation, and the antineutrino events are generated based on the average reactor settings and not per individual reactor cycle. The latter choice is motivated by the fact that the shapes of the E_{true}- and L_{true}-distributions are practically the same for each reactor cycle, as illustrated in figure 6.3. The number of events generated in the simulation is increased with a factor 100 with respect to the expected signal normalisation, and then scaled back by dividing the resulting event distributions with 100. This is done to reduce statistical fluctuations in the predicted distributions.

- The reconstructed event distributions are found by applying a simplified detector model to the predicted *true* distribution, that shifts and smears the energy corresponding with the loss of both annihilation gammas and an energy resolution at 1 MeV of 18%, respectively. In addition, the number of events was reduced according to an IBD selection efficiency of 14%. This simple model was used instead of the migration matrix presented in chapter 4, because it significantly speeds up the fit procedures described below.

The fake dataset is then generated by adding fluctuations to the predicted event distributions:

- The fake signal distribution is generated by randomising the (L_{reco}, E_{reco})-distribution bin counts, in agreement with the uncertainty matrix of the prediction. In practice, this construction of the fake experiment happens as follows:
    1. A lower triangular matrix L is derived from the Cholesky-decomposition[1] of the full covariance matrix for the prediction.
    2. Random numbers are drawn from a Gaussian distribution with mean equal to 0 and a standard deviation of 1, to construct a random number vector of the same length as L.
    3. The vector of random values is multiplied with L and the result is added to the original prediction distribution.

[1] Cholesky-decomposition is the operation in which a Hermitian, positive-definite matrix M is decomposed into the product of a lower triangular matrix and its conjugate transpose; $M = L(L)^T$. This makes its use in numerical operations, such as MC simulations, more efficient. [138]

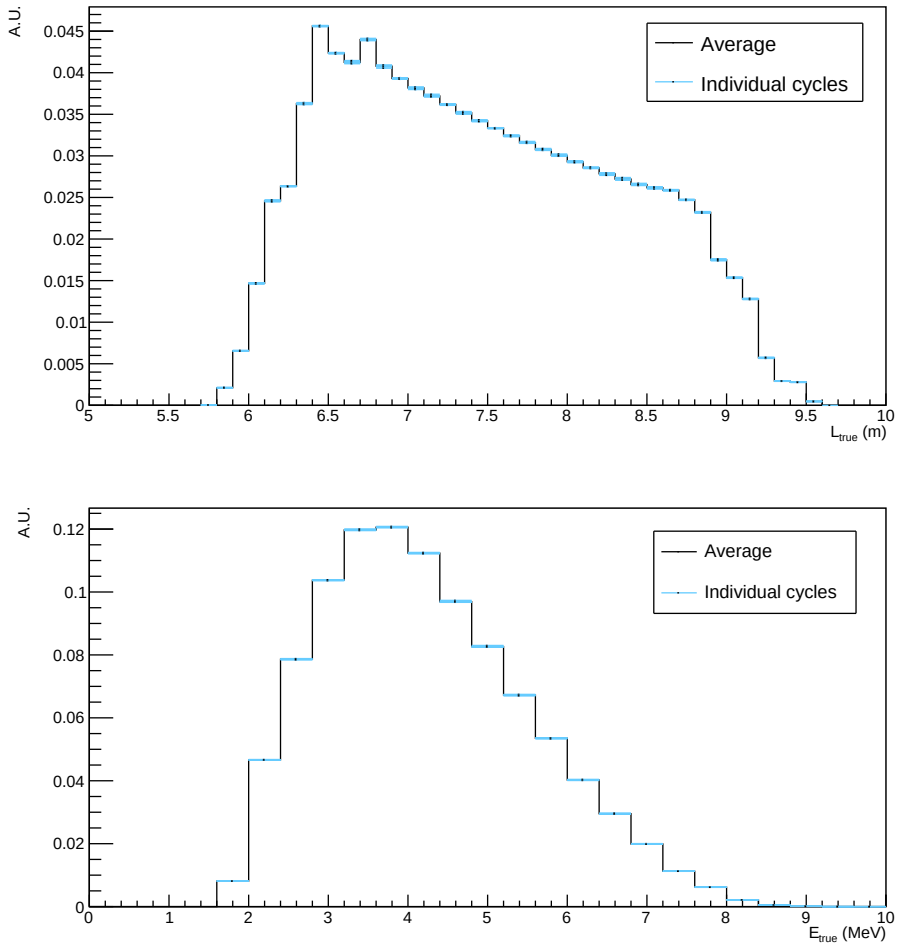

Figure 6.3: The normalised L_{true} (top) and E_{true} (bottom) distributions for simulations of 8 different reactor cycles, shown in blue. The average shape is shown in black.

- The number of background events is determined according to the signal normalisation, scaled with the signal-to-background ratio of 1:5 that was derived with the uBDT selection. The energy distribution of the background events is simulated based on the detected reactor-OFF energy spectrum and the events are assumed to be uniformly distributed over the detector modules after quality cuts.

A plot of the resulting fake data spectrum in the first detector module is shown in figure 6.4. The ratio of this fake data spectrum to the no-oscillation prediction is also shown for each detector module in figure 6.5. This figure also shows this ratio for an oscillated prediction using the RAA best fit oscillation parameters: $\sin^2(2\theta_{14}) = 0.17, \Delta m^2_{41} = 2.3\,\mathrm{eV}^2$.

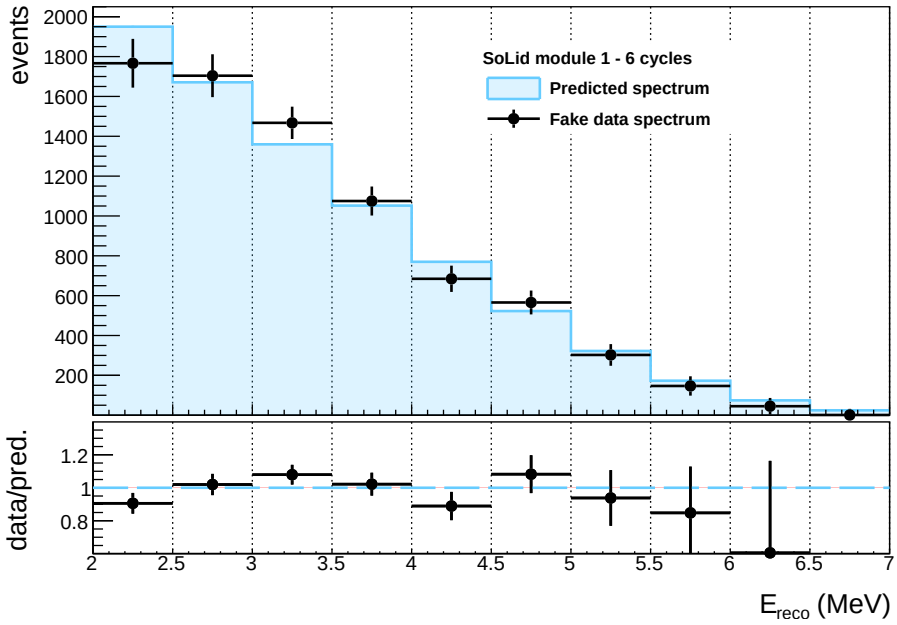

Figure 6.4: Top: Reconstructed energy spectrum of the example dataset in detector module 1 (black points) and the predicted reconstructed energy spectrum in the case of no sterile oscillations (blue). Bottom: Ratio of the fake data spectrum to the predicted no-oscillation spectrum.

We note that only the statistical uncertainties are used for the generation of the toy experiments and for the example plots generated with the fake dataset. This will be the case for all figures shown below. The determination

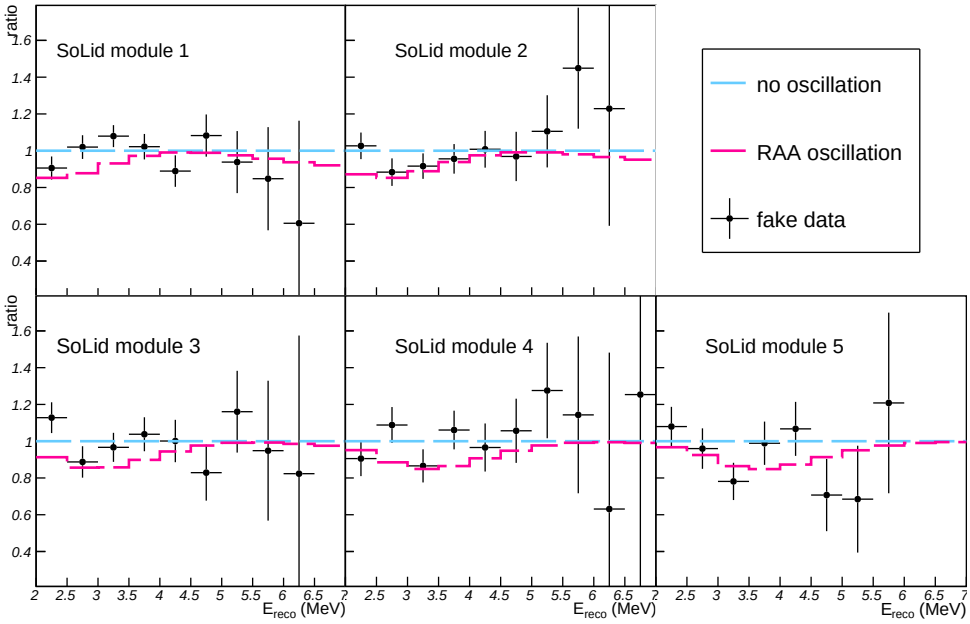

Figure 6.5: Ratio of the reconstructed energy distributions for the fake dataset in each of the 5 detector modules to the prediction containing no sterile oscillation (black points). The ratio for an oscillation prediction according to the reactor antineutrino anomaly best fit oscillation parameters is also shown (pink).

of these statistical uncertainties and of additional systematic uncertainties, as well as their expected effects, will be discussed in chapter 7.

Furthermore, we note that the data binning for the fit is chosen in 10 bins of 0.5 MeV in E_{reco} and per detector module of 10 planes in L_{reco}. Given the $1/L^2$ reduction of IBD signal events with baseline, the event statistics will decrease towards the higher position bins. By segmenting the detector in length such that each position bin has roughly similar IBD signal statistics, one could provide a better statistical coverage and improve the overall oscillation sensitivity. However, this would also require an evaluation of the relative performance and uncertainties per detector plane, rather than per detector module, and a variable L_{reco}-binwidth has therefore not been implemented yet.

Performing a fit of equation 6.17 using this fake dataset, results in a χ^2-value of 43.8. We note that for our relative fit, the number of degrees of freedom is reduced from the 50 $(L_{\text{reco}}, E_{\text{reco}})$-bins to 40, because of the use of the ratios D_j/P_j for each of the 10 E_{reco}-bins. We thus find a reduced χ^2-value of $43.8/40 = 1.095$, which implies a good agreement of the null hypothesis with the (fake) data. This result is as expected, indeed, since the fake dataset was generated based on a no-oscillation prediction. However, it gives us confidence in the implementation of the fit. In addition, one can calculate the χ^2-result for a large number of toys, each generated in the same way as the presented fake dataset, and look at the resulting distribution. The χ^2-distribution made from 10 000 toys is shown in figure 6.6 and agrees well with the χ^2 p.d.f. of 40 degrees of freedom.

6.5 Alternative hypotheses

As was reported in the previous sections, the χ^2 tests defined above are firstly used to test the validity of the null hypothesis H_0. In addition, one can test the confidence level for a range of alternative hypotheses by comparing the data to models including non-zero oscillation parameters $(\sin^2(2\theta_{14}), \Delta m^2_{41})$.

6.5.1 Determining the best-fit point

To start with, one can search for the best fit alternative model by determining those values of $\sin^2(2\theta_{14})$ and Δm^2_{41} that minimise the χ^2. In practice, this is done by scanning across a grid of possible $(\sin^2(2\theta_{14}), \Delta m^2_{41})$ values, in every point adjusting the prediction P, and correspondingly updating the

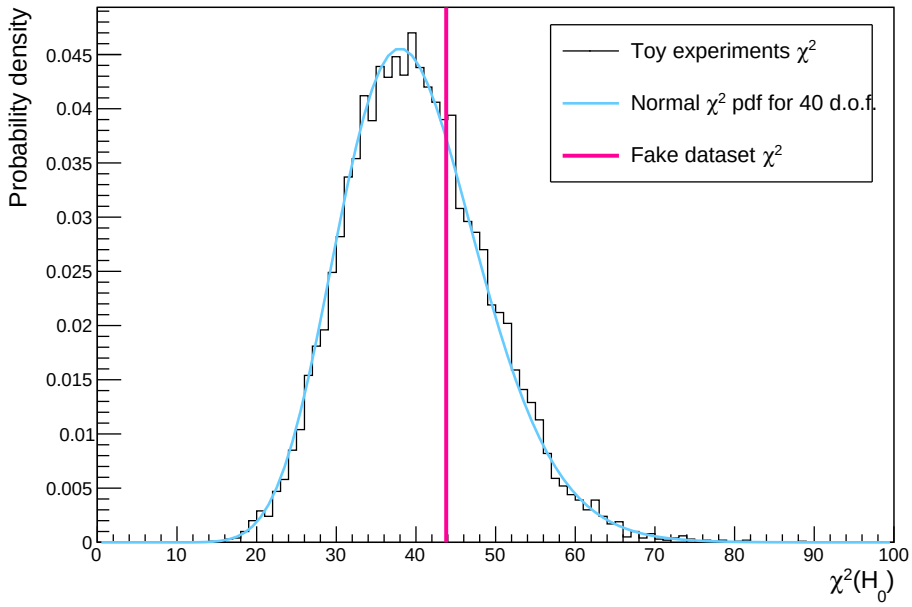

Figure 6.6: The χ^2 value of the fake dataset under the null hypothesis (pink). The χ^2 distribution for 10 000 fake experiments under the null hypothesis (black) is added as a reference and is compared to the normal χ^2 distribution for 40 degrees of freedom (blue).

covariance matrix. The grid point where the χ^2 value is the lowest is called the best fit (BF) point. As a precise determination of the BF requires a fine grid in the $(\sin^2(2\theta_{14}), \Delta m^2_{41})$ parameter space, the allowed $\sin^2(2\theta_{14})$ range from $[10^{-3}, 1]$ is divided in 150 bins and the Δm^2_{41} range is divided in 200 bins in the range $[10^{-2}, 10^2]$. The BF procedure thus runs the χ^2 fit more than 30 000 times.

To speed up this procedure, a method that is based on an iterative χ^2 fit across a grid of $(\sin^2(2\theta_{14}), \Delta m^2_{41})$ parameters was implemented.

Over the first iteration, the covariance matrix is kept fixed at the no-oscillation prediction, i.e. at $\Delta m^2_{41} = 0$ and $\sin^2(2\theta_{14}) = 0$. The grid scan is performed a first time and gives a first BF point $(\sin^2(2\theta_{14}), \Delta m^2_{41})_{min,1}$. The covariance matrix is then updated to match the result of the first iteration and is again kept fixed for the successive iteration, resulting in an updated BF point $(\sin^2(2\theta_{14}), \Delta m^2_{41})_{min,2}$. The error matrix is thus adjusted only once per iteration, which significantly speeds up the fit procedure. The fit iterates until the χ^2 convergence criterion

$$|\chi^2_{min,i} - \chi^2_{min,i-1}| \leq 0.1 \tag{6.19}$$

is met, with a maximum of five iterations.

When allowing free oscillation parameters, a minimal χ^2 of 39.25 was found for parameters $(\sin^2(2\theta_{14}), \Delta m^2_{41}) = (0.14, 2.2\ \text{eV}^2)$. The n.d.o.f for this fit is now 38 instead of 40, as the oscillation parameters introduce two free parameters. The reduced χ^2-value is thus 39.25/38 = 1.033.

6.5.2 $\Delta\chi^2$ statistic

In a following step, we can test all possible alternative hypotheses H_x over a defined range of oscillation parameters $(\sin^2(2\theta_{14}), \Delta m^2_{41})$. It is then possible to say for each alternative hypothesis test whether the oscillation scenario $(\sin^2(2\theta_{14}), \Delta m^2_{41})$ can be excluded according to a confidence level CL, based on the information provided by the measured data. The result of such an analysis are *exclusion contours*, which show regions of the oscillation parameter space that are allowed and rejected by the experiment.

A common test statistic used in each $(\sin^2(2\theta_{14}), \Delta m^2_{41})$ point is the $\Delta\chi^2$ value that is calculated by subtracting the χ^2 value at the best-fit point in parameter space from the χ^2 value at the given point $(\sin^2(2\theta_{14}), \Delta m^2_{41})$:

$$\Delta\chi^2 = \chi^2(\sin^2(2\theta_{14}), \Delta m^2_{41}) - \chi^2_{BF}, \tag{6.20}$$

which enables us to define allowed regions about the best fit point.

It can be shown that for large enough data samples, with a Gaussian behaviour of the uncertainties, the results of this $\Delta\chi^2$ test follow a χ^2 distribution with the degrees of freedom equal to the number of fit parameters[2]. For the case of the presented $\Delta\chi^2$ test the n.d.o.f. is equal to 2, corresponding to the free parameters $\sin^2(2\theta_{14})$ and Δm^2_{41}. As such, the resulting $\Delta\chi^2$ value in each grid point can be compared to the critical χ^2 value (χ^2_c) for a given confidence level and 2 degrees of freedom. Oscillation points with $\Delta\chi^2$ values that are larger than χ^2_c will be excluded. From the bottom plot in figure 6.1, we can deduce a critical value $\chi^2_c = 4.61$ at 90% CL (p-value = 0.1) or $\chi^2_c = 5.99$ for a 95% CL (p-value = 0.05), and so on.

In reality, however, the $\Delta\chi^2$ results will not always follow a χ^2 distribution. For the oscillation search, Wilk's theorem does not hold, for a few different reasons. Firstly, the oscillation probability has a non-linear dependence on the $(\sin^2(2\theta_{14}), \Delta m^2_{41})$ parameters. At high values of Δm^2_{41}, for example, the $\sin^2(1.27\Delta m^2_{41} L/E)$ term averages out to a factor 0.5 and the value of Δm^2_{41} does no longer affect the oscillation probability, effectively reducing the n.d.o.f. to 1 in that region [140]. Secondly, the detected number of selected events in some of the histogram bins can be relatively low, such that Gaussian statistics are not valid. Thirdly, the physical boundaries on the $\sin^2(2\theta_{14})$ parameter do not allow Gaussian errors in oscillation points near minimal and maximal mixing.

A better method to derive the critical $\Delta\chi^2$ values, that is based on simulated datasets, is presented in the following section.

6.5.3 Frequentist method

The frequentist method to construct $\Delta\chi^2$ probability distributions from large samples of simulated data was presented for the first time by Feldman and Cousins [141]. It allows to quantitatively calculate the critical $\Delta\chi^2$ values for any given CL, at every test point of the $(\sin^2(2\theta_{14}), \Delta m^2_{41})$ parameter space.

The general procedure that is executed for each point p in the $(\sin^2(2\theta_{14}), \Delta m^2_{41})$ grid can be summarised as follows:

1. Generate $\mathcal{O}(1000)$ fake experiments with oscillation parameters fixed at this point $(\sin^2(2\theta_{14}), \Delta m^2_{41})_p$.

[2]This statement is known as Wilks' theorem. [139]

2. Calculate the goodness-of-fit $\Delta\chi^2 = \chi^2_p - \chi^2_{BF}$ for each of these fake experiments.
3. Create a distribution from the calculated $\Delta\chi^2$ values of all fake experiments in this point p.
4. Find the critical $\Delta\chi^2_{c,p}$ at the desired CL (e.g. 90%, 95%, 3σ) from the $\Delta\chi^2$ distribution in p.

The production of the fake experiments is performed in a similar manner as presented for the fake dataset in section 6.4, where the full uncertainty matrix governs the size of the fluctuations:

1. Derive the lower triangular matrix L from the Cholesky-decomposition of the full covariance matrix for the prediction in point p.
2. Draw random numbers from a normal distribution to construct a random number vector.
3. Multiply the random number vector with L and add it to the nominal prediction in point p.

We note that the Cholesky-decomposition of the uncertainty matrix is required only once per oscillation point p and only steps 2 and 3 are repeated $\mathcal{O}(1000)$ times.

When all points p are treated, this method results in a map of $\Delta\chi^2_{c,p}$ values corresponding to the chosen CL, as a function of $(\sin^2(2\theta_{14}), \Delta m^2_{41})$. Figure 6.7 shows an example of the $\Delta\chi^2$ distribution for the null oscillation point, compared to the standard χ^2 distribution with 2 d.o.f. that follows from Wilk's theorem. The $\Delta\chi^2 = 4.55$ value for the fake dataset is shown as well and can be compared to the Feldman-Cousins critical value at 90% CL of 12.78, or to the standard critical value of 4.605. In the former case, the null hypothesis is fully compatible with the fake dataset, while it would be excluded at almost 90% CL when using the Wilk's theorem. This example clearly illustrates why the use of Wilk's theorem fails for this type of analysis.

An example of the resulting map of critical $\Delta\chi^2_{c,p}$ values at 90% CL is shown in figure 6.8. This should be compared to a uniform map with all values equal to 4.605 for the standard $\Delta\chi^2$ method, which again illustrates the shortcomings of this assumption.

6.5.4 Drawing of exclusion contours

A confidence interval or exclusion contour is drawn by comparing the $\Delta\chi^2$ statistic of the observed data to the predefined critical values. A particular

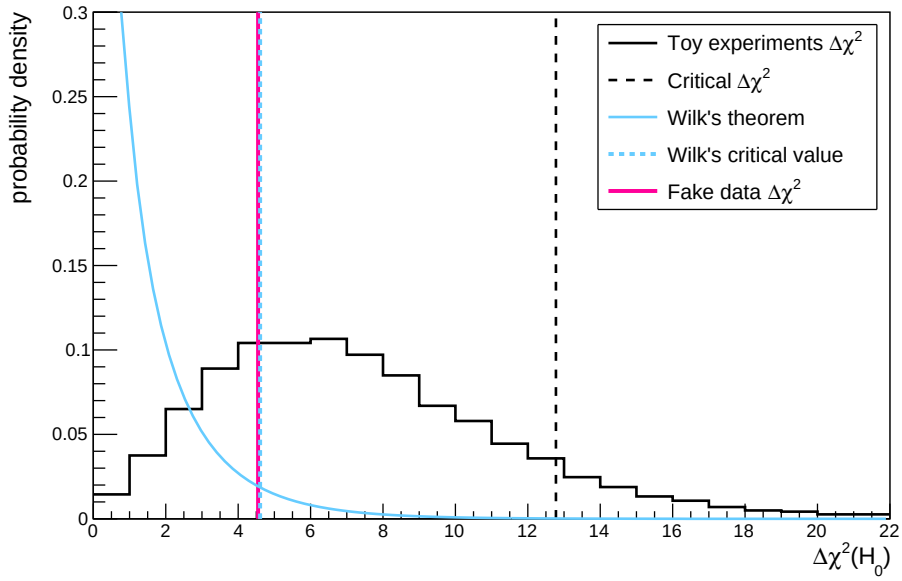

Figure 6.7: The $\Delta\chi^2$ distribution for the Feldman-Cousins method with 10 000 toys (black) compared to a normal χ^2 of 2 degrees of freedom (blue) for the null oscillation hypothesis. The critical value at 90% CL is indicated with the dashed line, the $\Delta\chi^2$ value for the fake dataset is shown in pink.

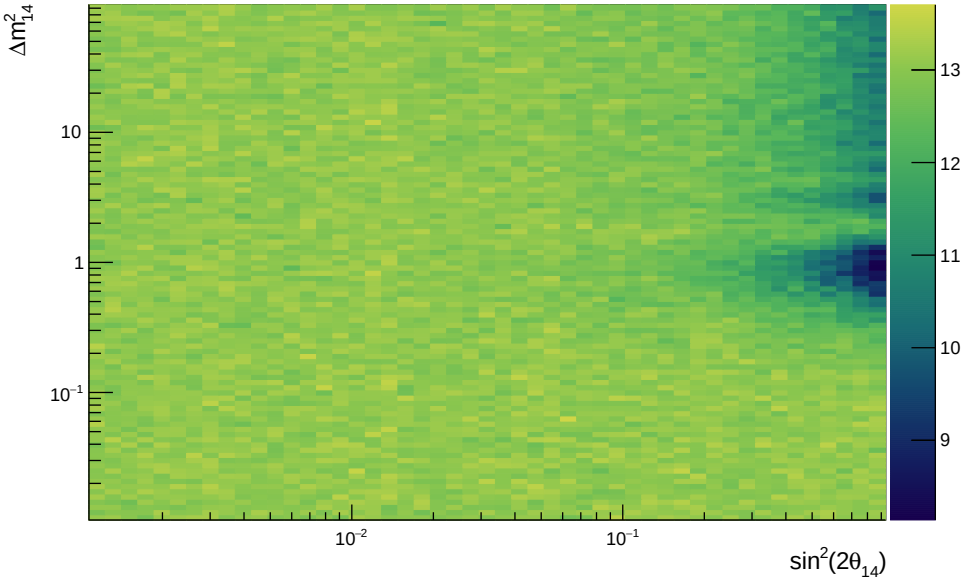

Figure 6.8: The map of critical $\Delta\chi^2$ values in the $(\sin^2(2\theta_{14}), \Delta m^2_{41})$ paramater space, constructed with the frequentist method.

point in the $(\sin^2(2\theta_{14}), \Delta m^2_{41})$ parameter space is said to lie within the inclusion interval, at the prescribed confidence level C, if $\Delta\chi^2(\text{data}) < \Delta\chi^2_{c,p}$ at that point. As a result, a curve can be drawn that divides the parameter space in an allowed region to the left of the curve and an excluded region to the right.

The exclusion contour for the fake dataset is shown in figure 6.9 for the 90% and 95% confidence levels. This contour is made using the raster scan method, as will be explained below.

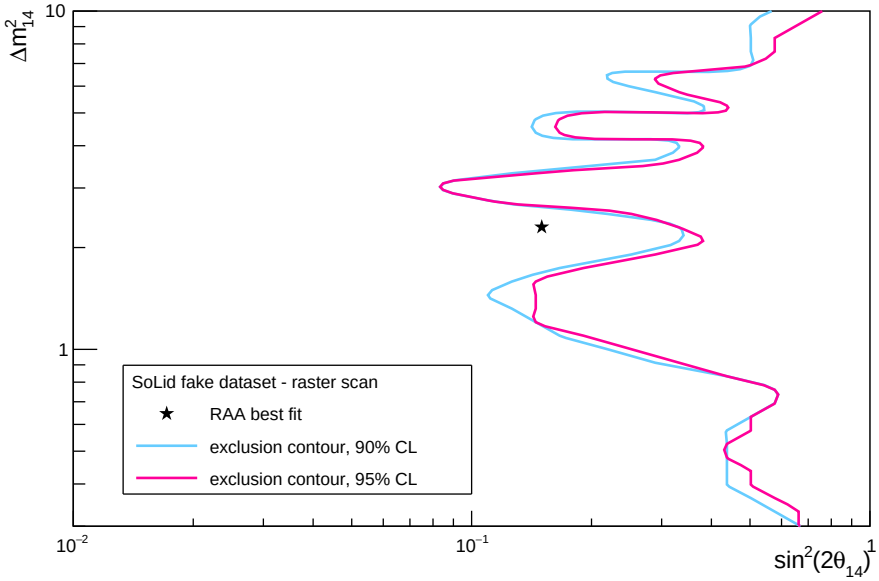

Figure 6.9: Exclusion contour at 90% (blue) and 95% C.L (pink) for the fake SoLid dataset, based on a relative fit.

Global versus raster scan

In principle, the best-fit χ^2 value for a given (fake) dataset is found by scanning over the full range of possible $(\sin^2(2\theta_{14}), \Delta m^2_{41})$ values and finding the point with a minimal χ^2 result. This type of scan is referred to in literature as the *global scan*. When using the Feldman-Cousins method for the construction of $\Delta\chi^2$-distributions, a best-fit scan needs to be performed for each of the many fake experiments and the computation of these distributions becomes

very timeconsuming.

A possible way to reduce the computational effort, is using a *raster scan* instead. This type of scan considers each Δm^2_{41} value separately and then scans over the range of $\sin^2(2\theta_{14})$ values to find the one giving the best-fit, for this fixed value of Δm^2_{41}. As a result, the procedure is sped up a lot with a factor that corresponds to the chosen number of divisions in Δm^2_{41}. In the specific case of the contours presented here, that use a parameter grid of 50 by 100 in $(\sin^2(2\theta_{14}), \Delta m^2_{41})$, the computation time is thus reduced with a factor $\sim$100.

Figure 6.10 shows an example of the $\Delta\chi^2$ distribution built with the raster scan in the oscillation point $(\sin^2(2\theta_{14}), \Delta m^2_{41}) = (0.15, 1.5\text{eV}^2)$. We note that for the raster scan, the $\Delta\chi^2$ fit has only 1 d.o.f. which is the value of $\sin^2(2\theta_{14})$. The distribution is compared to the standard χ^2 distribution of 1 d.o.f. which matches relatively well in this case. This can be explained by the fact that the oscillation is in fact linear in $\sin^2(2\theta_{14})$ and that the distribution of best-fit $\sin^2(2\theta_{14})$ values will be Gaussian for those points that are far enough away from the physical boundaries 0 and 1. The critical value at 90% C.L. in the illustrated example is 3.53, compared to 2.706 for the standard χ^2. We can see that the fake data, with a $\Delta\chi^2$ value of 8.26, is not compatible with the alternative hypothesis in $(\sin^2(2\theta_{14}), \Delta m^2_{41}) = (0.15, 1.5\text{eV}^2)$. This is in agreement with our no-oscillation input for the fake dataset and the results shown in figure 6.7.

It is important to note that for the raster scan case the resulting χ^2_{BF} value might be slightly larger than the actual minimal value for the full parameter space and that the resulting $\Delta\chi^2$-distributions (= $\chi^2_p - \chi^2_{BF}$) will thus be populated with slightly lower values. As a consequence, the raster scan method will shift the contour somewhat to the left and overestimate the discriminating power of the experiment in $\sin^2(2\theta_{14})$.

An example of the contour resulting from a global scan versus that resulting from a raster scan, based on the fake data events, is shown in figure 6.11.

6.6 Sensitivity contour

The *sensitivity* of an experiment is defined as the average expected exclusion limit for many runs of the experiment and without a true signal. In practice, this limit can be derived by generating the exclusion contour based on the fit in which the data is replaced by the null hypothesis prediction. The sen-

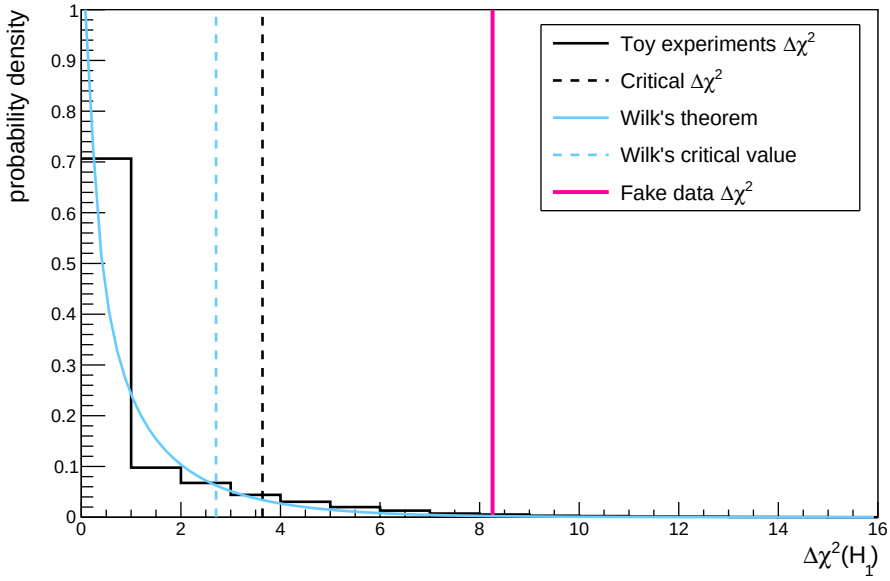

Figure 6.10: The $\Delta\chi^2$ distribution in the oscillation point $(\sin^2(2\theta_{14}), \Delta m^2_{41}) = (0.15, 1.5\text{eV}^2)$ built with the Feldman-Cousins method for 10 000 toys and using a raster scan to determine the best fit point (black) compared to a standard χ^2 of 1 degree of freedom (blue). The critical value at 90% CL is indicated with the dashed line, the $\Delta\chi^2$ value for the fake dataset is shown in pink.

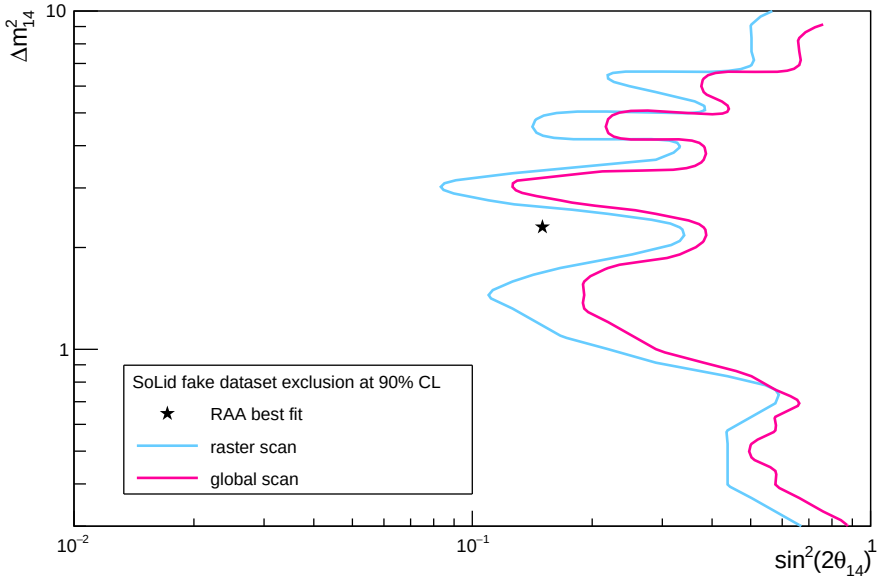

Figure 6.11: The 90% CL contour determined with the raster scan method (blue) versus the contour from the global scan method (pink), based on a relative fit.

sitivity thus shows what is reachable for the experiment, given a predicted amount of events, and is fully driven by the knowledge of the statistical and systematic uncertainties.

As we generally produce our predicted events with increased statistics (scaling factor of 100) to eliminate statistical fluctuations, the χ^2 for this *sensitivity fit* will always have a best fit very close to zero ($\chi^2_{BF} \approx 0$) and Wilk's theorem will thus be valid: $\Delta\chi^2 \approx \chi^2(2 \text{ d.o.f.})$ [142]. As a consequence, the generation of a sensitivity contour does not require the use of toy experiments, which makes the computation much faster.

The sensitivity contour for our fake dataset, based on the relative oscillation fit, is shown in figure 6.12. One can see that the experiment's sensitivity decreases for larger values of Δm^2_{41}. This is due to the fact that for these high values, the oscillation length is smaller than the detector bin size, which results in an average reduction of the detected flux. As the relative fit is independent of the flux normalisation, there is no sensitivity to this reduced flux at high Δm^2_{41} and the contour is pushed to the right. Similarly, low Δm^2_{41} values are only visible for larger values of L/E, and the largest distances covered by the detector modules are not large enough for the experiment to be sensitive there.

The sensitivity contour is shown again, together with the exclusion limit that was presented above, in figure 6.13. We see that the exclusion contour crosses from one side of the sensitivity limit to the other, but generally lies around the predicted limit. This oscillating behaviour of the exclusion contour, that is not present for the sensitivity contour, is explained by the statistical fluctuations of the experimental (fake) data. These fluctuations can sometimes be fitted with oscillation patterns in Δm^2_{41}, which improve the goodness-of-fit, reduce the χ^2 and restrict the rejection power. On the other hand, the statistical fluctuations can also go in the opposite phase of the Δm^2_{41} oscillation, and then the sensitivity is increased. As such, for one experimental dataset, the exclusion limit will go back and forth around the predicted sensitivity that is free from statistical fluctuations. This consistency of the exclusion result with the sensitivity is an important check. Results that are in agreement with the null hypothesis should on average not go beyond the expected sensitivity. In case they do, they indicate a signal or an erratic interpretation of the data.

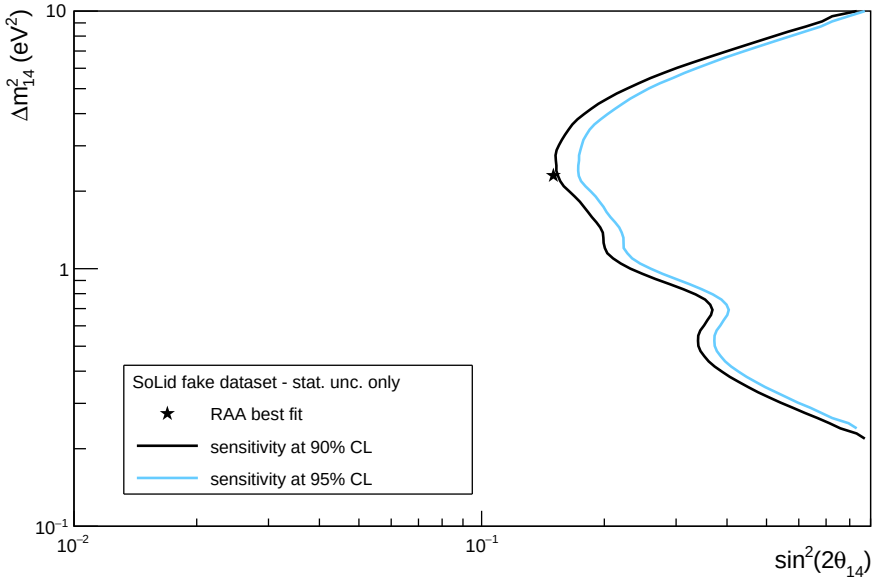

Figure 6.12: The expected sensitivity contour for the fake dataset, based on the statistical uncertainties only and using a relative fit. The 90% confidence limit is shown in black, the 95% confidence limit in blue.

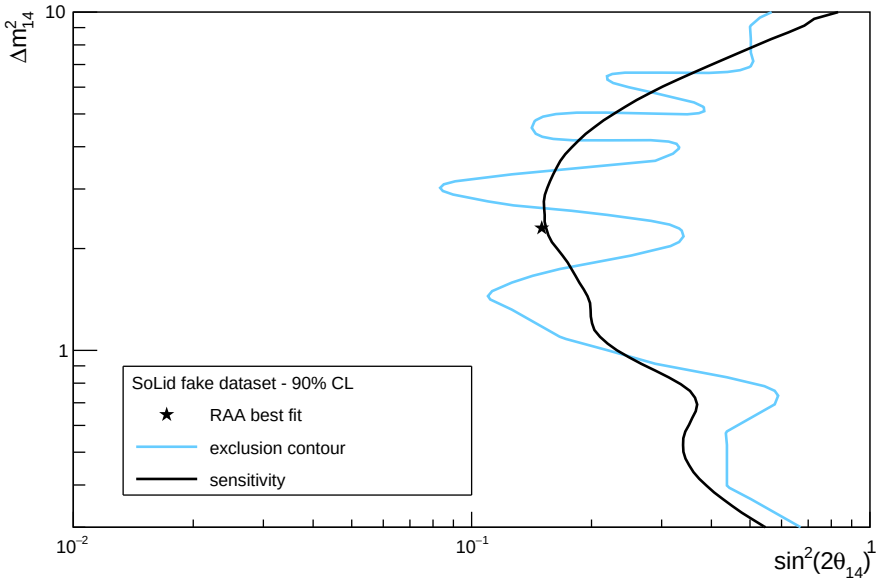

Figure 6.13: The expected sensitivity contour for the fake dataset at 90% confidence level and based on the statistical uncertainties only(black), together with the exclusion contour determined from the data (blue), based on a relative fit.

6.7 Summary

In this chapter we have treated the statistical tests that are used to evaluate the no-oscillation hypothesis H_0 and a range of alternative hypotheses $H_1(\sin^2(2\theta_{14}), \Delta m^2_{41})$, given an experimental dataset. The χ^2 test, that calculates the goodness-of-fit of the data with the prediction based on a bin-per-bin comparison, was introduced in section 6.2. It was mentioned there that two equivalent methods exist for the inclusion of correlated systematic uncertainties in the fit: the use of nuisance parameters or the covariance matrix approach. A more detailed description of these systematic uncertainties will be presented in the following chapter.

In section 6.3, a set of possible definitions of the χ^2 fit statistic for a short-baseline experiment like SoLid were presented, some of which target different aspects of the oscillation search. As explained in section 6.4, the SoLid experiment will use a relative χ^2 fit for the first oscillation analysis, as this fit reduces the dependence on the complex prediction of the reactor antineutrino flux and spectrum. In the same section, we have introduced the fake dataset that was used for the illustration of the principles presented in the last sections of this chapter. In section 6.5, the $\Delta\chi^2$ goodness-of-fit parameter that is used for the evaluation of the alternative hypotheses was treated first, followed by the concepts and machinery necessary to produce data-driven exclusion contours for the experiment. To conclude, we have explained how a prediction-driven sensitivity limit is generated and can be interpreted in section 6.6.

7 Uncertainty propagation

To investigate the possible existence of sterile neutrino oscillations, the measured prompt energy spectra E_{reco} for different baselines L_{reco}, are quantitatively compared to predicted spectra that include oscillation effects. The *goodness-of-fit* parameters used to evaluate the resemblance of measurement and prediction were introduced in chapter 6.

Regardless of the chosen statistical test, a precise knowledge of the uncertainties on the model and the data is of crucial importance. Too large uncertainties will evidently weaken the confidence in the experimental results, while underestimated uncertainties could result in an incorrect interpretation of the outcome of the test.

The processes for the estimation and propagation of these experimental uncertainties are discussed in this chapter.

7.1 Introduction

From a general point of view, three different categories of uncertainty contributions can be distinguished for an oscillation experiment:

- Statistical uncertainties.
  These are directly determined from the number of events in the data bins and the number of subtracted background events, using Poisson statistics. These were already (partly) presented in chapter 5 and will be treated in detail in section 7.3.
- Systematic uncertainties with an effect on the spectrum shape.
  These can have a component that deals with a global distortion of the energy scale, common to all detector cells, and a local component that allows each detector cell to have its own distortion independently of the others.

- Systematic uncertainties with an effect on the measured rate.
  These come from parameters that affect the determination of emitted or detected flux, such as the reactor power, the number of detector target protons, the electronics dead-time, etc.. These can be also be plane-dependent.

The choice for a relative oscillation fit for the analysis presented here results in a large reduction of the number of uncertainties that need to be evaluated. As mentioned before, the fit is independent of the reactor model and the related uncertainties become irrelevant. In addition, absolute detector uncertainties cancel out as well and energy response variations between detector cells are corrected for. On the other hand, this relative fit also introduces correlated statistical uncertainties between the detector modules, as we will see in section 7.3.

As was shown in chapter 6, there are two main methods to account for the (correlated) systematic errors in a statistical test, i.e. by introducing nuisance parameters or by using a covariance matrix. It was discussed there that the two methods are perfectly interchangeable, but since it was chosen to use a fit method that uses covariance matrices for the representation of the uncertainties, we will present the statistical and systematic uncertainties and their correlation between bins in the form of such covariance matrices in this chapter.

7.2 Covariance matrix construction

For each uncertainty contributor u, a separate covariance matrix V^u can be constructed. The full covariance matrix for the analysis V^{tot} will then be composed of the sum of all individual matrices.

Depending on the available information on a given uncertainty contributor, there are a few possible methods for the construction of the related covariance matrix. For parameters that are part of an analytical model describing the data, the covariance matrix can be deduced analytically. In case the parameter's effect on the data is derived empirically, a computational approach for the deduction of the covariance matrix is more appropriate. We will shortly describe the two general procedures in this section and will give more details on the treatment of the actual parameters of concern in sections 7.3 to 7.8.

7.2.1 Analytical approach

From general error propagation theory we know that the uncertainty on the model prediction $P(u)$, induced by a certain parameter u, can be found by using the partial derivative of this prediction function P to u. In matrix notation, we can write this derivative as

$$J^u_\alpha = \frac{\partial P_\alpha}{\partial u}, \tag{7.1}$$

where J is commonly referred to as the Jacobian matrix.

In case the uncertainty on this component u can be restricted to one single parameter σ_u, we can deduce the model uncertainty as

$$V^u_{\alpha\beta} = J^u_\alpha \, \sigma^2_u \, J^u_\beta, \tag{7.2}$$

where the indices α and β denote the position of the covariance matrix element, as described above.

In case the uncertainty is governed by multiple correlated parameters (u_X, u_Y, ...), one needs to include the cross-terms of those parameters

$$V^u_{\alpha\beta} = \sum_{X,Y} J^{u_X}_\alpha \, m^u_{XY} \, J^{u_Y}_\beta \tag{7.3}$$

with m^u_{XY} the covariance matrix relating the uncertainties on parameters u_X and u_Y.

7.2.2 Computational approach

For each systematic uncertainty parameter u, a covariance matrix V^u can also be produced computationally, based on systematically fluctuated toy datasets. This method generally requires three inputs;

- the nominal value u_{nv} of the input parameter u,
- the uncertainty σ_u on the input parameter,
- and the response model; i.e. the simulation code or model that depends on the input parameters to generate a corresponding output $P(u)$.

Based on these inputs, a large number of fluctuated datasets ($N_{\text{sim}} \geqslant 1000$) are generated. For this purpose, the value u is varied with respect to its nominal value u_{nv}, by randomly drawing a value u_i from a Gaussian distribution with mean u_{nv} and a width σ_u. Then, this updated value u_i is fed to the MC chain (= the response model) to produce a new prediction P^i.

By calculating the average difference between each fluctuated dataset P^i and the non-fluctuated dataset $\overline{P}$, the variance as a function of u is determined:

$$V^u_{\alpha\beta} = \frac{1}{N_{\text{sim}}} \sum_{i=1}^{N_{\text{sim}}} (P^i_\alpha - \overline{P}_\alpha)(P^i_\beta - \overline{P}_\beta). \tag{7.4}$$

In the case of n correlated parameters $\vec{u} = \{u_1, u_2, ..., u_n\}$ a similar method can be applied by using their covariance matrix m^u, instead of the single uncertainty σ_u, to determine the fluctuations. The toy datasets are then generated according to the scheme that was already presented in sections 6.4 and 6.5.3:

1. First a Cholesky-decomposition of the matrix m^u is needed, that results in a lower triangular matrix L^u.
2. By multiplying L^u with a vector of n random values $\vec{\rho}$, picked from a Gaussian with mean equal to 0 and standard deviation equal to 1, a random fluctuation can be generated for each u_i:

$$\delta u_i = L^u_{ij}\, \rho_j \tag{7.5}$$

3. The updated values $\vec{u}'$ are found as

$$\vec{u}' = \vec{u} + \vec{\delta u} \tag{7.6}$$

The $\vec{u}'$ now serve as input for the generation of a new toy prediction. After generating a large number of such toys, equation 7.4 can be used again to construct the resulting covariance matrix $V^{\vec{u}}_{\alpha\beta}$ for the prediction $P(\vec{u})$.

We note that this toys-method is very versatile as it can be applied to any parameter at any level of the simulation. However, it generally requires a lot of computing resources and time and a careful assessment of the relevant parameters is therefore recommended.

7.3 Statistical uncertainties

The statistical uncertainties represent the standard deviation of the count rate for each $(L_{\text{reco}}, E_{\text{reco}})$-bin. As the excess number of IBD events is calculated by subtracting the accidental, BiPo and atmospheric background components, the total statistical uncertainty follows from the propagation of the statistical errors on each of these components.

For each component, the statistical uncertainty is determined using Poisson statistics, i.e. the statistical uncertainty is computed per bin as the square root of the number of events in that bin. We have seen in chapter 5 that the error propagation in the background subtraction process leads to a total statistical uncertainty of

$$\begin{aligned}\sigma^2_{IBD} = \; & (S_{signal} + x_S^2 A_{signal}) + \chi^2_{BiPo}(S_{BiPo} + x^2_{BP} A_{BiPo}) \\ & + \left(\frac{t_{ON}}{t_{OFF}}\right)^2 \chi^2_{atm} \left[(S^{OFF}_{signal} + x_S^2 A^{OFF}_{signal}) + \chi^2_{BiPo}(S^{OFF}_{BiPo} + x^2_{BP} A^{OFF}_{BiPo})\right]\end{aligned} \tag{7.7}$$

These uncertainties are calculated per (L_{reco}, E_{reco})-bin and are treated as fully uncorrelated.

In addition to these Poisson errors, the use of a relative oscillation fit method requires an additional statistical component. Let us have a look at the PROSPECT-like fit introduced in the previous chapter:

$$\chi^2 = \sum_i^{n_L} \sum_j^{n_E} \sum_k^{n_L} \sum_l^{n_E} \left(D_{ij} - D_j \frac{P_{ij}}{P_j}\right)^T V^{-1}_{(ij,kl)} \left(D_{kl} - D_l \frac{P_{kl}}{P_l}\right). \tag{7.8}$$

with

$$D_j = \sum_i^{n_L} D_{ij} \quad \text{and} \quad P_j = \sum_i^{n_L} P_{ij} \tag{7.9}$$

Since this fit calculates the predicted spectra (P_{ij}) based on the measured data (D_{ij}), the prediction will also contribute to the statistical uncertainty. The variance on the term $(D_{ij} - D_j \frac{P_{ij}}{P_j})$ can be determined from error propagation and results in [143]:

$$V^{stat}_{ij} = \sigma^2_{stat,ij} \left(1 - 2\frac{D_{ij}}{D_j}\right) + \sigma^2_{stat,j} \left(\frac{D_{ij}}{D_j}\right)^2, \tag{7.10}$$

where $\sigma^2_{stat,ij}$ is the regular statistical uncertainty on bin ij, defined by equation 7.7, and the $\sigma^2_{stat,j}$ are the statistical uncertainty on the detector-wide spectrum:

$$\sigma^2_{stat,j} = \sum_i^{nL} \sigma^2_{stat,ij} \tag{7.11}$$

Additionally, the use of the detector-wide measurement as reference for each baseline bin introduces correlations between different baselines. These correlations between $M_{l,e}$ and M_e need to be taken into account in the statistical covariance matrix and can be determined using Monte Carlo toys.

7.3.1 Fake dataset example

For our fake dataset, introduced in the previous chapter, an approximation of the statistical uncertainties was made. It is based on two assumptions:

1. that the accidental background is negligible once the selection cuts are applied, resulting in $x_S^2 A_{signal} \approx 0$, $x_{BP}^2 A_{BiPo} \approx 0$,
2. that all scaling factors in equation 7.7 are close to 1, i.e. that the available reactor-OFF time is the same as the reactor-ON time, the atmospheric pressure was comparable for both periods and the BiPo selection window is of similar size as the signal window.

In this simplified case, the statistical uncertainty formula is reduced to the sum of the signal selection and the total background component:

$$\sigma_{IBD}^2 = S_{signal} + BG_{tot} = R_{IBD} + 2 \times BG_{tot}, \tag{7.12}$$

where we have used the fact that the signal selection is the sum of the excess IBD events and the background component. The total resulting statistical covariance matrix of the fake dataset, including correlations introduced by the measurement-based prediction, is shown in figure 7.1. Here, the elements are again grouped per baseline-bin, such that positions 1 to 10 run over all energy bins of L_{reco}-bin 1, positions 11 to 20 over all energy bins of L_{reco}-bin 2, and so on. The matrix is shown in its *reduced* or *fractional* format, i.e. the relative uncertainties are shown, which have to be multiplied in each position $\alpha\beta$ with the corresponding number of events $N_\alpha * N_\beta$ in the related bins, to obtain the covariance matrix for a given dataset.

Figure 7.2 shows the fractional statistical uncertainty for each of the (L_{reco}, E_{reco})-bins. They can be derived by taking the square root of the diagonal elements of the reduced statistical covariance matrix: $\sigma_{stat} = \sqrt{V_{\alpha\alpha}^{red}}/N_\alpha$. It can be seen that the lowest statistical uncertainty on the fake dataset bins is about 7.5% and quickly increases towards higher energy bins. It is therefore expected that for the actual SoLid Phase I dataset, the total covariance matrix will be primarily dominated by the statistical uncertainties.

7.4 Systematic uncertainties

As uncertainties are combined by summing them quadratically, the addition of a relatively small error to a larger one will have little or no effect. Given the lowest statistical uncertainty of 7.5% on the first (L_{reco}, E_{reco})-bin for the fake dataset (see figure 7.2), we can estimate what the effect of additional

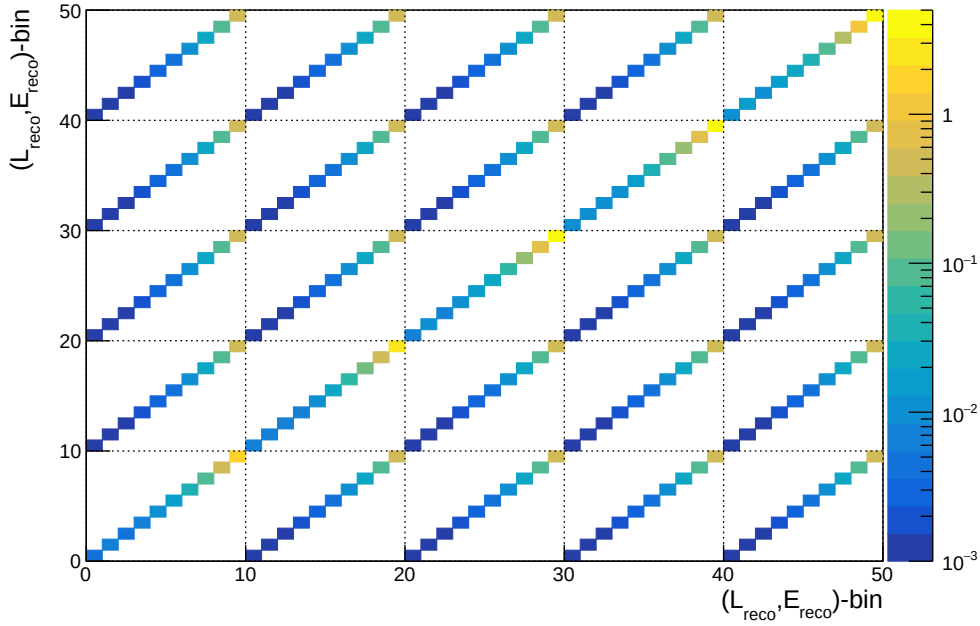

Figure 7.1: Example of the reduced statistical covariance matrix for the relative fit method. The off-diagonal elements represent the correlated uncertainties that are introduced by the relative χ^2 fit definition.

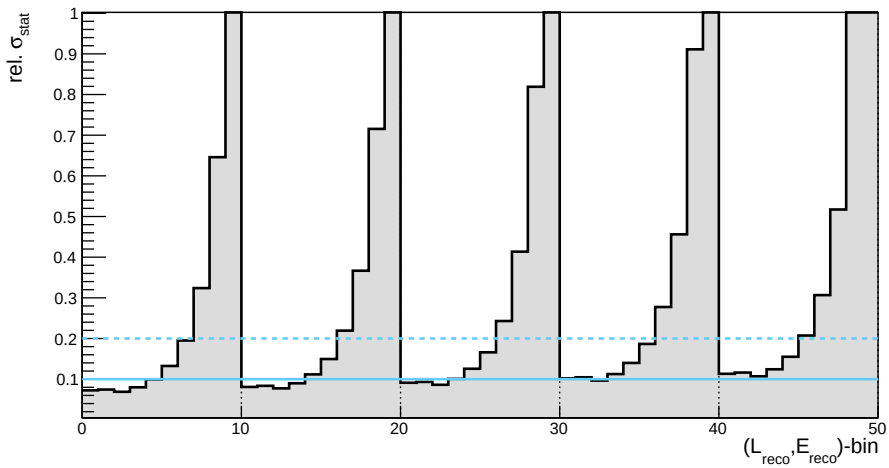

Figure 7.2: Example of the fractional size of the diagonal elements of the statistical covariance matrix for the relative fit method: $\sqrt{V_{\alpha\alpha}}/N_\alpha$, produced with a simulated dataset. The solid blue line indicates 10% relative uncertainty, the dotted blue line indicates 20%.

uncertainties could be. By adding a systematic uncertainty on the signal of 3%, for example, the combined uncertainty becomes

$$\sigma_{tot} = \sqrt{0.075^2 + 0.030^2} = 0.081 \tag{7.13}$$

which is an increase of only 0.6%.

It should therefore be safe to assume that systematic uncertainties on the signal up to 3% will be negligible for the first SoLid analysis, provided that no improvements on the statistics of the dataset can be made.

In the following sections, we will introduce the systematic uncertainties that are expected to give a significant contribution to the error matrix and that will thus be most relevant for a future relative oscillation fit. As most of these systematic studies are ongoing or not started yet at the time of writing, the sections will be limited to a short description of, or proposal for, the methods that are, or can be, used.

The uncertainty contributors are listed in order of expected importance. Given the relatively large signal-to-background ratio for the current implementation of the IBD selection, systematic uncertainties on the background components are assumed to have a dominant effect and are treated first in section 7.5. Secondly, the uncertainties on the reactor fission loading map

could have a significant effect on the detector acceptance, as will be described in section 7.6. In the remaining two sections, the energy reconstruction and relative detection efficiency uncertainties will be discussed.

7.5 Background uncertainties

A first systematic uncertainty on the background selection arises from the pressure correction of the reactor-OFF atmospheric component before subtracting it from the reactor-ON signal selection. For the subtraction method presented in section 5.4.3, the uncertainty is thus related to the uncertainty on the scaling factor χ^{av}_{atm}. However, we will see in the following chapter that an improved subtraction method was developed for future analyses, which uses a different approach for the removal of pressure-dependant background fluctuations. In any case, the scaling of the reactor-OFF component is assumed to be energy-independent and will thus only result in an uncertainty on the background normalisation.

A second systematic could be introduced due to unexpected background component variations over time. These can be studied by comparing the recorded spectra for different reactor-OFF periods, corrected for relative atmospheric differences. In addition, the time stability of events that are vetoed by the IBD selection cuts, for example those in the BiPo-selection time window of [300 - 500]µs, can also be compared between reactor-OFF and -ON periods. Both comparisons give information on the accuracy and time-stability of the estimation of the different correlated background components.

Once the current IBD selection methods are finalised, these studies of the background uncertainties will start.

The uncertainty on the selection and subtraction of the accidental background can safely be neglected, as the selection in the negative Δt window is very pure and the remaining number of accidental events after application of the IBD selection cuts is small.

7.6 Detector acceptance

As discussed in chapter 3, the detector acceptance is determined as the ratio of the number of crossing antineutrinos to the number of emitted antineutrinos. As these numbers depend on the spatial fission distribution in the reactor core, which can vary according to the fuel loading map of a cycle, the geometrical acceptance needs to be determined per reactor cycle. And any uncertainty on these fission distributions will introduce an uncertainty on the

detector acceptance.

As the antineutrino disappearance depends on the ratio $L_{\overline{\nu}_e}/E_{\overline{\nu}_e}$, uncertainties on the baseline-dependent acceptance do not only influence the rate normalisation, but also the predicted oscillation pattern. Therefore, an evaluation of this uncertainty is also necessary for a relative oscillation fit.

The effect of the geometrical uncertainties can be evaluated using toy simulations. In this case, the spatial fission distribution is varied within its uncertainty and the reactor simulation is each time rerun and compared to the nominal reactor prediction.

We note that the resulting reactor uncertainty matrix V^R_{ab} is constructed in terms of the true neutrino coordinates $(L_{\text{true}}, E_{\text{true}})$. In practice, however, the oscillation fit is performed using events binned in reconstructed space and an additional step for the conversion of V^R_{ab} to $V^R_{\alpha\beta}$ is needed.

This conversion can again be performed by using the computational toy-method. In this case the three inputs for the toy generation will be

- the nominal values for the reactor related input parameters
- the covariance matrix V^R_{ab}
- and the migration matrix, presented in chapter 4, that serves as the response model.

To speed up this procedure, each generated toy prediction P^i_a can be fitted with a spline. By comparing this fit to the spline fit of the nominal prediction, a ratio can be made that then serves for the re-weighting of the set of MC prediction events that were produced with the SoLO generator. After the rescaling of the events, the migration matrix can be applied to give an updated prediction in reconstructed space P^i_α. By applying equation 7.4 to a set of these resulting P^i_α, the covariance matrix $V^R_{\alpha\beta}$ is now available in reconstructed space.

Because of the need of this translation step, the procedure for the evaluation of any reactor-related uncertainty is in general much more time consuming than the evaluation of uncertainties in the signal reconstruction processes.

A team of researchers from CAEN, Subatech and BR2 is evaluating this uncertainty at the time of writing. The first results of this study are expected within a few months.

7.7 Energy reconstruction uncertainties

The energy reconstruction of the detected events is largely based on three main concepts: the detector light yield, the energy linearity of the PVT scintillator and the propagation of energy losses. All three properties are measured or verified with calibration sources and implemented in the ROsim and reconstruction code. The uncertainties on these parameters will each introduce an uncertainty on the reconstructed energy spectrum that can be evaluated with the use of randomised MC toys.

Light yield and energy linearity

As presented in section 2.6, the LY values of all SoLid detector cubes are determined based on calibration runs with a ^{22}Na source. An average detector LY was determined and by including effects such as the fibre specific attenuation and the individual fibre-MPPC couplings, the per-cube LY variations are understood within 3%. To study the effect of the remaining LY uncertainties, a large set of simulations was generated, each time simultaneously varying the LY values for all cubes in the detector simulation within the known 3% uncertainty, as described in section 7.2.2. The variations were propagated to the resulting measured energy spectrum and compared to the nominal value, following equation 7.4. Figure 7.3 shows a first result for the expected uncertainties on the energy spectrum, based on a set of 100 toys. More toys are being generated for a precise determination of the resulting covariance matrix.

As mentioned in chapter 2, PVT is assumed to have a linear response to energy deposits. This energy linearity of the SoLid detector material was verified with the use of multiple calibration points, spanning a relatively large energy range. The result, averaged over the full detector, was shown in figure 2.21. The uncertainties on this linear fit were derived by performing the same linearity study, but restricted to individual cubes. It was first verified for a large number of cubes that the relation between deposited and detected energy is indeed consistent with a linear law. Then, the energy response slope was evaluated cube-per-cube by fitting the LY/MeV values obtained for 4 calibration points. The cube-to-cube variations on the fit parameters compared to the full detector parameters indicate a 2% uncertainty on the slope. This value can be used to simulate new MC toys, varying the energy response slope within 2%, to propagate the uncertainty to the reconstructed energy spectrum.

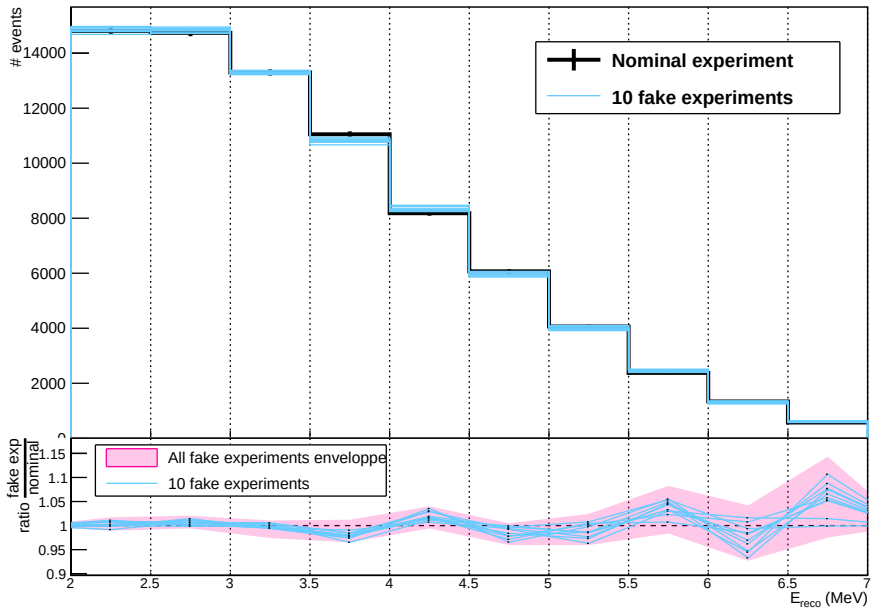

Figure 7.3: Top: The predicted E_{reco}-spectra for 10 example toy experiments with randomised light yield values (blue), compared to the nominal spectrum using the standard light yield values (black). Bottom: the ratio of each toy to the nominal value prediction (blue), showing the relative variation on the E_{reco}-spectra. The envelope (pink) shows the maximal variations for the full set of toys

Low energy signals

Another source of systematic uncertainty originates in the difference in the reconstruction efficiency for small energy deposits between data and MC. This difference is seen when comparing the detected energy from annihilation gammas produced by a ^{22}Na source, to the MC simulation of these interactions. As mentioned before, these annihilation gammas have an energy of 511 keV, which is low compared to the minimal required energy of 2 MeV for the ES signals in the IBD selection. In case all energy of an annihilation gamma is deposited and detected, this corresponds to a signal of $\sim$50 PA. Most of the detected signals will however be smaller. The measured and simulated energy distributions for annihilation gammas detected in a SoLid cube are shown in figure 7.4. A discrepancy of 20% per cube or 5% per WLS fibre is found between the two distributions over the full energy range from 10 to 50 PA.

This seemingly large uncertainty can be explained by the fact that each of the fibres can only detect a few PAs for these low energy deposits. As a consequence, the $\sqrt{N}$ behaviour of statistical fluctuations causes large variations in the resulting signal efficiency as a function of the actual deposited energy. The evaluation of the impact of this uncertainty on the reconstructed energy spectrum is just starting at the time of writing. The procedure will exist in generating toys for which 20% of the cubes with detected energies below 500 keV is randomly removed from the reconstruction of each event. For the cubes that share their row or column with the maximal amplitude cube, i.e. that cube where the positron deposited most of its energy, the cube removal will be reduced to only 10%, as 2 out of the 4 fibres will most probably be above threshold.

7.8 Relative detection efficiency

The effect of an error on the IBD selection efficiency can act as a bias in the signal normalisation. The absolute selection efficiency uncertainty does not affect a relative oscillation analysis, but variations in this efficiency between detector modules *will* have an impact on a relative oscillation search and should therefore be correctly included in the MC detector simulation. Therefore, the differences in selection efficiencies between the Monte Carlo simulation and what is measured from calibration data need to be determined in order to derive an uncertainty interval on each effect.

The IBD selection efficiency is a combination of the neutron detection efficiency and the ES reconstruction efficiency.

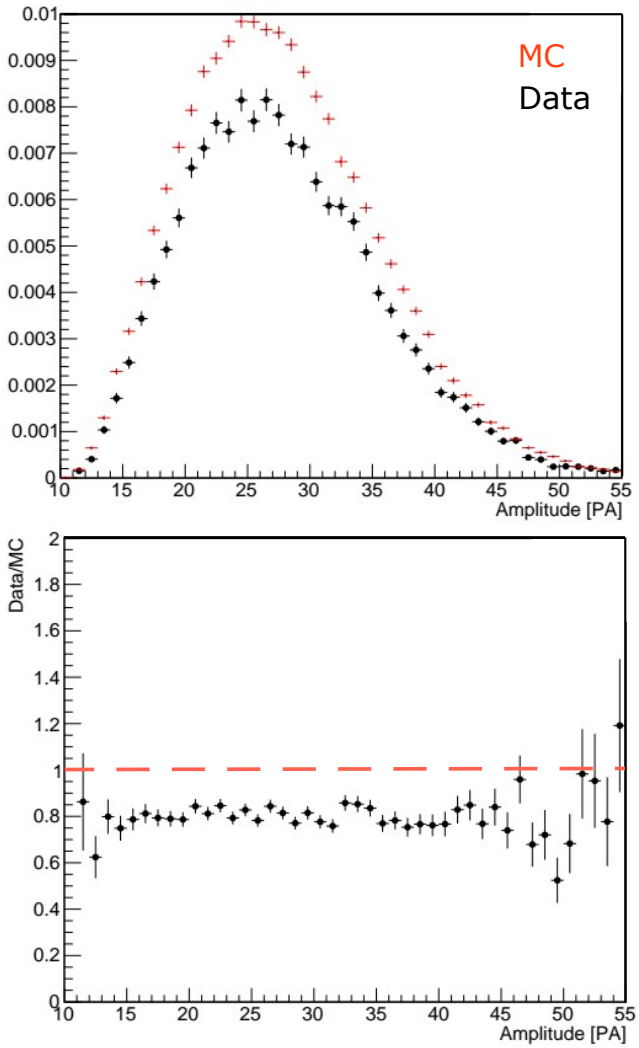

Figure 7.4: Data/MC comparison of the reconstructed energies for energy deposits below 55 PA ($\sim$ 600 keV), based on the measured and simulated reconstruction of annihilation gammas from a ^{22}Na source. A discrepancy of 20% is seen for these low energetic signals.

In figure 2.18, the neutron reconstruction efficiency, determined from calibration data, was shown for each individual Phase I detector plane. From this calibration data, an average neutron reconstruction efficiency was determined within 4% uncertainty. The uncertainty per detector module will be of the same order. The neutron capture efficiency might vary between modules due to geometrical differences between the outer and inner modules, but is automatically taken into account in the Monte Carlo simulation.

For the ES reconstruction, the plane-per-plane variation in the efficiency mostly depends on the variations in the average LY between planes. These variations are included in the detector simulation.

A direct way to evaluate the remaining systematic uncertainties is to look at the data-to-MC comparison of the L_{reco}-distribution of the excess events. However, such a study might not be precise enough, due to limited statistics.

Another possible method is to compare the distribution of ES events over the detector planes in a BiPo data sample and in a MC sample. To match the IBD topology, a subsample of BiPo events can be made that have a cube with a reconstructed NS signal and at least one other cube that tagged a radiative gamma. This study will not cover effects due to light leaks at higher energies. To evaluate this, two IBD simulations that have different simulated light leakage values can be used.

7.9 Summary

In this chapter, we have presented the general methods used for an evaluation of the systematic uncertainties on the prediction for the experiment. In a second step, we have listed the most relevant uncertainty contributors for a relative oscillation search. The statistical uncertainties are determined from the different signal and background selections and are based on Poisson statistics, as described in section 7.3. We have also seen in this section that a relative fit, that uses the measured data as a reference for the prediction, introduces correlated statistical uncertainties.

On the other hand, a relative fit removes a large part of the systematic uncertainties. For the current SoLid dataset, the dominant systematic uncertainties are expected to come from the background selection, the dependence of the detector acceptance on the reactor loading map, the energy reconstruction and relative detection differences between detector modules. We have briefly discussed the methods that can and/or will be used to quantitatively determine these uncertainties for the first full SoLid oscillation analysis.

Results and analysis outlook

8

In this chapter, we present a first SoLid sensitivity contour using real data, determined according to the oscillation analysis steps that were described in chapter 6. The contour will be based on the preliminary IBD excess presented in chapter 5, determined from a limited open dataset containing only 1 reactor-ON cycle. As a consequence, the result will lack sensitivity and is not useful for a final oscillation search. The purpose is, however, to demonstrate the readiness of the oscillation analysis code for the study of the full Phase I dataset. In addition, we summarise the remaining steps and studies that are required to produce the full Phase I dataset exclusion contour.

8.1 Current status

As mentioned, the SoLid collaboration is currently still working on the validation of the IBD analysis techniques and the full Phase I dataset is not available yet for further analysis. For the production of a first exclusion contour with real SoLid data, the same limited dataset is used as the one for which a first IBD excess study was presented in chapter 5. This set includes 25 days of reactor-ON data, taken during the third BR2 reactor cycle of 2018. The goal is to evaluate the implementation of the oscillation analysis machinery, which was my dominant contribution to the SoLid analysis.

The input for the oscillation fit is the measured L_{reco} versus E_{reco} distribution of the IBD signal excess, which is shown in figure 8.1. All statistical uncertainties were propagated during the event selection and background subtraction procedures and are stored per histogram bin. A projection of these uncertainties is shown in figure 8.2. Systematic uncertainties are not taken into account for this study, as they are negligible compared to the statistical uncertainties on this limited dataset.

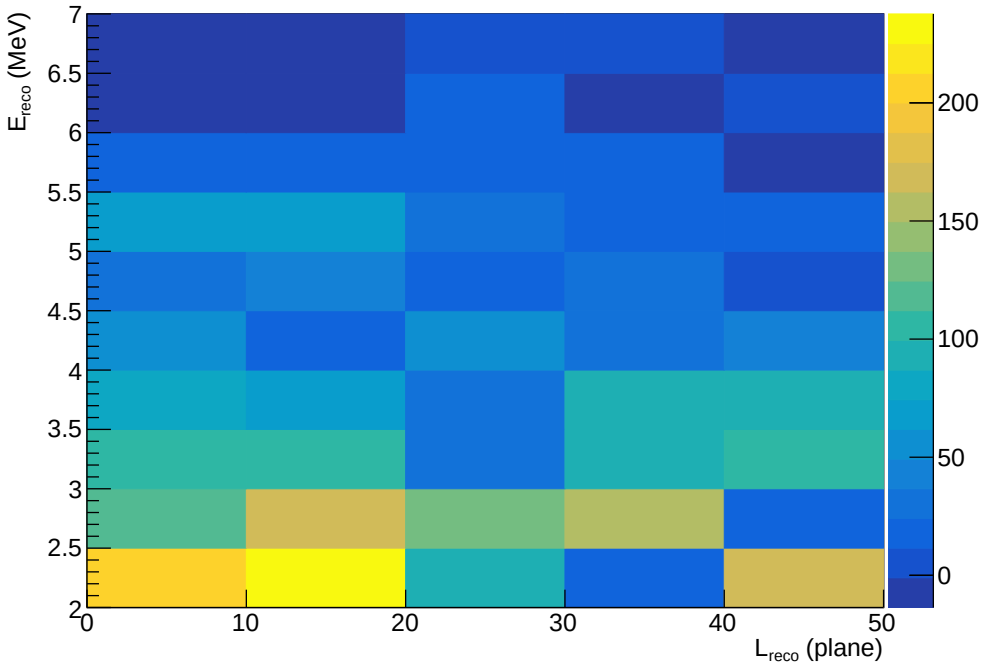

Figure 8.1: Signal excess measured by the SoLid experiment for BR2 reactor cycle 3-2018, presented in terms of L_{reco} versus E_{reco}. This is the data input for an oscillation analysis.

For the prediction, the full simulation of reactor cycle 3-2018 was used. The simulated IBD interactions were folded with the detector response, using a migration matrix trained on the data of reactor cycle 1-2018, that was processed with the full ROsim and uBDT selection method. This migration matrix was already presented in chapter 4. The prediction was then scaled to match the number of events in the open dataset. The background effects were included via their contribution to the statistical uncertainties. The expected sensitivity, based on this prediction and using the relative, PROSPECT-like fit, is shown in figure 8.3. Because of the low statistics, the fit is only sensitive to a very limited part of the parameter space where the $\sin^2(2\theta_{14})$ mixing terms are larger than about 0.6.

A fit of the data with the null-oscillation prediction results in a χ^2-value of

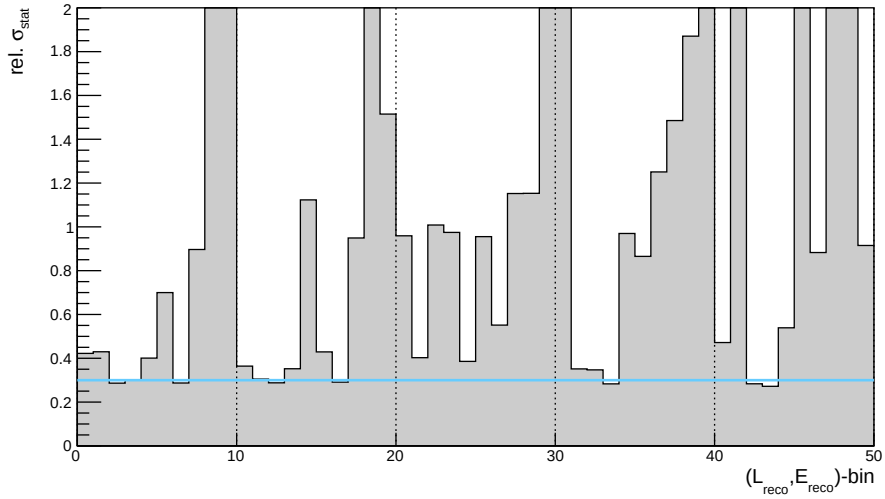

Figure 8.2: The total relative statistical uncertainties on the small open dataset used for a first oscillation analysis. The uncertainties are grouped per baseline bin, with 10 reconstructed energy bins for each. The blue line indicates 30% relative uncertainty.

39.21. Given the 40 d.o.f. in the fit (see chapter 6), we find a good agreement of the data with the null hypothesis. When performing the best fit search, this point is found for $\sin^2(2\theta_{14}) = 0.001$. For this very small mixing angle, the oscillation is negligible for any value of Δm^2_{41}, and the best fit point is in fact in line with the no-oscillation hypothesis.

The exclusion contour for the open dataset is shown in figure 8.4. We see that the exclusion limit is consistent with the predicted sensitivity. However, the limit does not provide a useful result, which can be attributed to the very limited statistics of the available dataset. We note that this open dataset contains only 7% of the total Phase I data on-tape that is of a similar size as the fake dataset presented in chapter 6.

8.2 Steps towards a Phase I exclusion contour

In this section we briefly list the remaining items that need to be studied and determined by the SoLid collaboration, in order to produce a first exclusion contour with the full Phase I dataset.

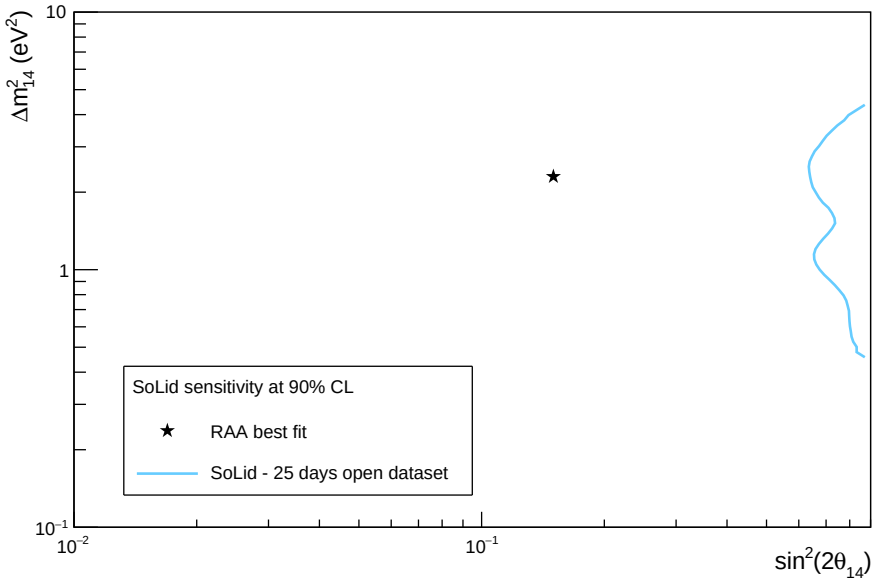

Figure 8.3: The sensitivity contour at 90% confidence level for the SoLid open dataset, based on a relative fit including statistical uncertainties only (blue). The RAA best fit point is indicated with a black star.

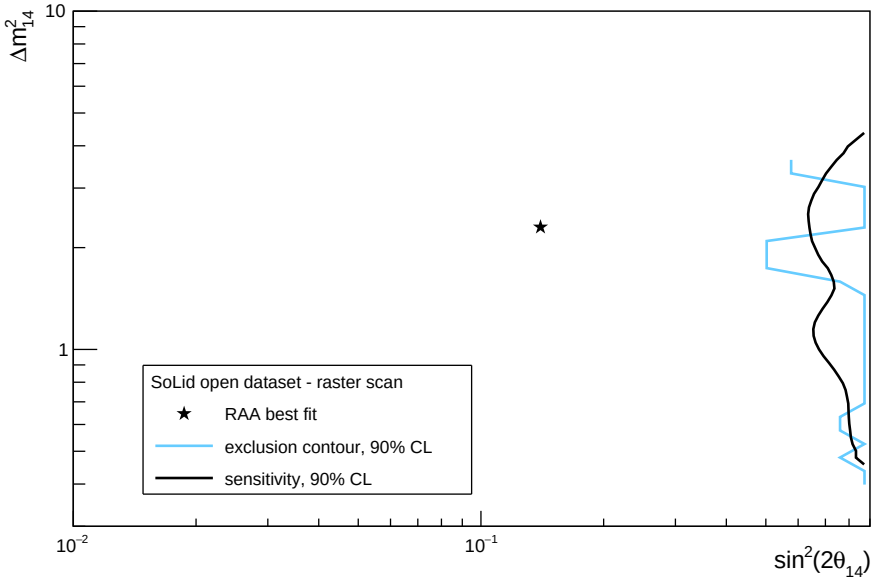

Figure 8.4: The exclusion contour at 90% confidence level for the SoLid open dataset, based on a relative fit including statistical uncertainties only (blue). The predicted sensitivity is added for reference (black). The RAA best fit point is indicated with a black star.

8.2.1 Improved subtraction method

As mentioned in chapter 5, an improved background subtraction method, compared to the one described in section 5.4.3, was recently developed. The reason were the results from data stability studies, that indicated a dependence of the IBD excess on the pressure correction factor χ_{atm}. This correlation showed that the atmospheric background component was not well controlled.

The concept of the improved method is to first subtract pressure induced fluctuations, before subtracting the full reactor-OFF atmospheric selection from the reactor-ON selection. For this purpose, a fit function $f(P)$ is used to determine the fluctuations of the atmospheric component, based on the pressure evolution per time bin (j):

$$\Delta C_{atm,\,j} = C_{atm,\,j} - \overline{C}_{atm} = f(P_j) = \chi^{ref}_{atm}(P_j - \overline{P}), \tag{8.1}$$

where $\overline{C}_{atm}$ and $\overline{P}$ are the average atmospheric rate and pressure for the reactor-OFF period and where we have dropped the OFF superscript for notation simplicity. An example of the fit is shown in figure 8.5.

Once the factor χ^{ref}_{atm} is determined from the fit, and the pressure evolution is known, the pressure correlated background rate for any other time bin (k) can be found:

$$\begin{aligned} C^{OFF}_{atm-\Delta,\,k} &= C^{OFF}_{atm,\,k} - \Delta C_{atm,\,k} \\ &= C^{OFF}_{signal-BiPo,\,k} - \chi^{ref}_{atm}(P_k - \overline{P}) \end{aligned} \tag{8.2}$$

As such, this component $C^{OFF}_{atm-\Delta,\,k}$ represents the expected atmospheric background, corrected for pressure induced fluctuations.

Since the varying pressure during reactor-ON periods causes the same kind of fluctuations in the atmospheric background, a similar subtraction of the $\Delta C_{atm,\,k}$ is done first:

$$C^{ON}_{signal-BiPo-\Delta,\,k} = C^{ON}_{signal-BiPo,\,k} - \chi^{ref}_{atm}(P_k - \overline{P}). \tag{8.3}$$

In principle, this $C^{ON}_{signal-BiPo-\Delta,\,k}$ component now only contains the excess IBD signal and a pressure corrected atmospheric background.

Finally, the remaining atmospheric background component, estimated from reactor-OFF data is subtracted from the remaining reactor-ON selection,

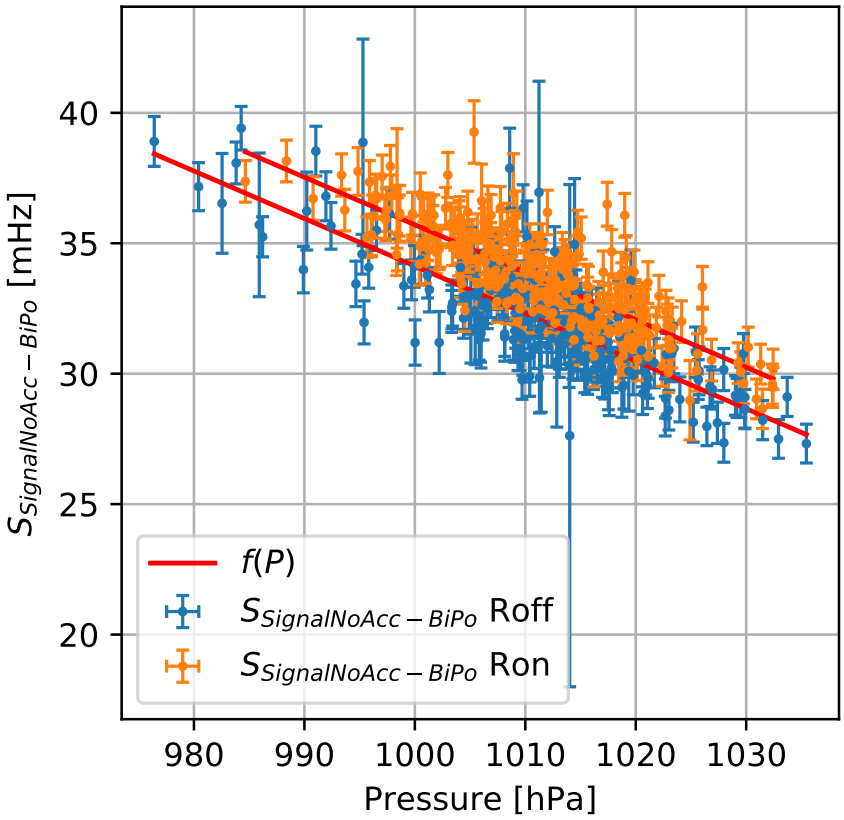

Figure 8.5: Evolution of the atmospheric background component with respect to the atmospheric pressure for reactor-ON and -OFF data. The fit of the reactor-OFF data is used to determine the atmospheric correction factor. [134]

and the signal excess (R_{IBD}) is found:

$$R_{IBD} = \sum_k C^{ON}_{signal-BiPo-\Delta,\ k} - \sum_l C^{OFF}_{atm-\Delta,\ l} \tag{8.4}$$

We note that this formula represents the excess rate. For the determination of absolute numbers a scaling factor for the amount of reactor-OFF data to amount of reactor-ON data is needed.

This method has already been implemented and tested for the excess rate determination, but needs some additional work to be able to precisely determine the effect on the event distributions in length and energy, for which an individual atmospheric fit of each $(L_{\text{reco}}, E_{\text{reco}})$-bin will be needed. For a full discussion, see [144].

8.2.2 IBD signal selection on full dataset

Currently, the IBD selection methods described in section 5.4 were trained and tested on the open dataset of only one reactor-ON cycle. Once the methods are fully validated, the processing of all Phase I data with the latest reconstruction software version can start.

After the processing, some data stability checks will have to be performed first. These include investigations of the total data rate for reactor-ON and -OFF periods, and of rates of individual event types. Muon event rates will be correlated with logs of atmospheric pressure to test the detector efficiency and energy scale stabilities. If needed, unstable periods can be excluded from the final dataset.

When the detector performance over all selected data taking periods is well understood, the total signal excess of the Phase I dataset can be determined.

8.2.3 Systematic uncertainties

As described in chapter 7, the evaluation of the systematic uncertainties is mostly based on data-to-MC comparisons and toy MC datasets. A first step for the determination of systematics is thus to process MC samples with the latest SoLidSim and ROsim software versions. Then, the procedures described in the same chapter will have to be tested further or will need to be implemented. It is assumed that the most optimal strategy is to start with an evaluation of the background, detector acceptance and energy reconstruction uncertainties.

8.2.4 Migration matrix tests

To verify the migration matrix method and performance, a second toolkit for the construction of response matrices, called ReMu [126], will be implemented and tested. As such, a cross-check of the results found with the currently implemented RooUnfold framework can be made.

8.2.5 Sensitivity studies

Once the statistical and systematic uncertainties on the full open dataset are known, a new sensitivity projection of the SoLid Phase I experiment can be produced. It will need to be determined which of the fit methods, described in chapter 6, best matches the available data and goals of the first oscillation analysis. This choice will mostly be driven by the set of systematic uncertainties.

For the production of the contours, the expected background shape will need to be updated in the SoLO framework, depending on the used IBD selection method. Currently, only one background shape is implemented in the SoLO analysis code. This background spectrum is made using the overall reactor-OFF spectrum in the signal selection region. For future studies, however, it would be useful to be able to study the effect of increasing or reducing one of the background components. This requires a separate implementation of the individual background spectra and the use of relative normalisation factors between components.

Depending on the final statistics of the Phase I dataset, the choice of binning in L_{reco} and E_{reco} could also be revised. As mentioned in section 6.4, the L_{reco}-bins could be chosen in such a way that each position bin has roughly the same signal statistics. This kind of binning should result in a better statistical coverage, which improves the overall oscillation sensitivity.

8.3 Summary

In this chapter we have presented a first sensitivity and exclusion contour based on real SoLid data. The purpose of this analysis was to test the full analysis chain and to validate my work for this thesis. As only a small part of the SoLid Phase I dataset was available for this first analysis, these preliminary results are not sensitive enough for an evaluation of the sterile neutrino hypothesis. We have therefore also listed the remaining items that require additional work from the SoLid collaboration, in order to produce an exclusion contour with the full Phase I dataset.

9 SoLid Phase II

In July 2020 the SoLid Phase I detector was shut down after two and a half years of operation at the BR2 reactor site. The detector modules were taken out of the container and shipped to the University of Antwerp for an upgrade of the readout sensors. The SoLid collaboration is currently replacing all 3200 MPPCs with a new, more performant type. The aim is to take more physics data with the upgraded *Phase II* detector for about 1 additional year and profit from an increased sensitivity for the final oscillation analysis. In this chapter we briefly present the expected improvements and the resulting increase of the experiment's sensitivity.

9.1 New generation MPPCs

For the SoLid Phase II detector, the Hamamatsu S12572-050P MPPCs are replaced with the new ones of the type S14160-3050HS. They have a similar photosensitive area of 3 by 3 mm, such that they still match the cross-section of the WLS fibres and fit in the same connectors. This new generation of photon multipliers should achieve a higher photon detection efficiency (PDE) for a lower operation voltage than their predecessors [145].

To test the performance of the new MPPCs, a test bench with one SoLid cube that was read out by two short WLS fibres was set up at Imperial College. One end of each fibre was connected to an MPPC, that was connected to readout channels on a SoLid-type analogue electronic board. To allow a high statistics measurement and good comparison between the performance of both old and new MPPCs, a ^{90}Sr calibration source was used, placed on top of the cube. The data was recorded with a threshold trigger set at a relatively high threshold to eliminate the effect of dark counts. To ensure stable data

taking conditions, this test set-up, with all connected electronics, was placed in a small dark box that additionally acted as Faraday cage.

A summary of the test bench results for the cross-talk probability, dark count rate and light yield of the MPPCs is shown in figure 9.1. This shows that switching to the new MPPCs, and operating them at the same over voltage (OV) settings as the old MPPCs, would result in:

- a decrease of the cross talk,
- an increase of the dark count rate,
- and an increase of the light yield.

Moreover, because of the reduced cross-talk probability of the new MPPCs, it would be possible to operate them at a larger over voltage. By setting the OV at 3.5 V, the cross-talk level is comparable to that of the Phase I experiment, while significantly increasing the light yield by 40%. The dark count rate would increase by about 25%. We note that switching to a new over voltage involves changing other related operation settings and will therefore require a small update of the SoLid read-out electronics too.

9.2 Expected improvements

For the upgraded Phase II detector, a range of different improvements is expected, the most dominant ones being:

- The increased photon statistics will improve the energy resolution, providing a better sensitivity to the measured IBD spectral shape.
- The signal reconstruction threshold could be lowered, since the higher photon statistics help discriminate low energy signals from electronics noise. As a consequence, more annihilation gammas will be reconstructed for IBD events, improving the performance of the uBDT and NN codes.
- The neutron signals will produce more peaks over threshold, increasing the discriminative power of the BiPonisher and/or BiPonator variables.

The actual changes resulting from the MPPC upgrade can only be retrieved from a detailled simulation, based on results from calibration runs with the newly instrumented detector planes. In addition, a re-evaluation of the reconstruction processes and event variables, as well as a new optimisation of the IBD selection procedure, will be required. A precise determination of the expected improvements is beyond the scope of this thesis and in the following section we will therefore present some general cases that will impact the Phase II sensitivity.

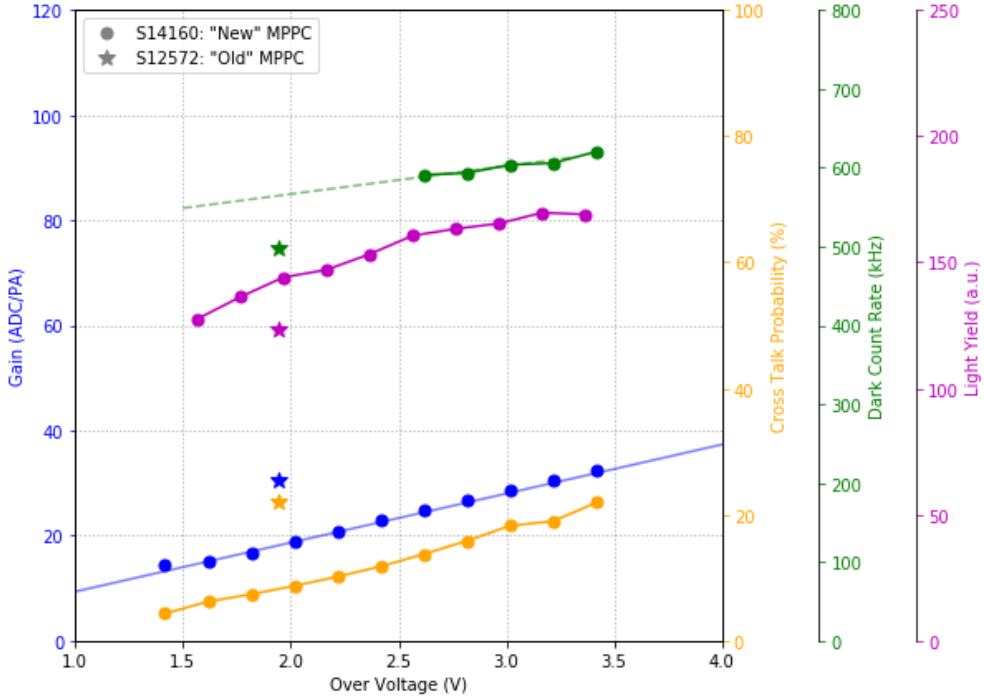

Figure 9.1: The cross-talk probability, dark count rate and light yield for the new S14160-3050HS Hamamatsu MPPCs (dots), compared to the older generation of S12572-050P MPPCs (stars), as tested with a small set-up at Imperial College. [146]

9.3 Phase II sensitivity

From the previous chapters of this work, it is clear that the sensitivity of an experiment to sterile neutrino oscillations depends on a large amount of parameters. In this section we will discuss a few general parameters that have the most dominant effect on the sensitivity, as an illustration of the possible improvements for the Phase II SoLid experiment.

9.3.1 Run time

A straight-forward advantage of the Phase II run lies in the experiment's increased run time. By gathering an additional year of data, the number of detected events will be larger and the statistical uncertainties will decrease. In figure 9.2 the sensitivity of the current estimated dataset (see chapter 6) and that for a dataset with an additional year of data taking are shown. We have assumed here that in 1 year there will be 6 reactor cycles, each with about 25 reactor-ON days per cycle.

From figure 9.2 we can see that a longer run time primarily results in an increased sensitivity to lower $\sin^2(2\theta_{14})$ values.

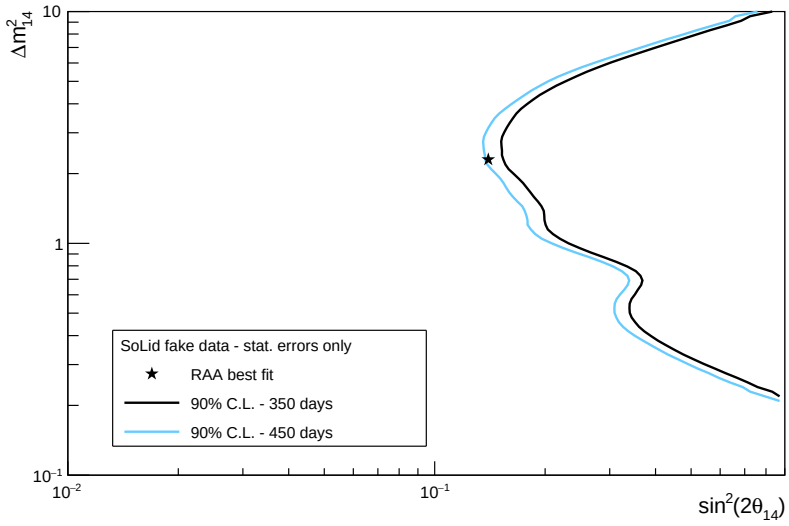

Figure 9.2: Example of the effect of a longer run time on the sensitivity of the SoLid experiment. All other parameters are fixed at the Phase I values.

9.3.2 Energy resolution

As mentioned above, the increased light yield will improve the energy resolution of the detector. This resolution is about 18% (stat.+sys.) for the Phase I detector, and is estimated to be between 10 and 15% for the Phase II detector. An increased energy resolution implies less smearing of the energy and thus a more correct energy reconstruction. Figure 9.3 shows that this improvement pushes the sensitivity to larger values of Δm^2_{41}. This can be explained from the inverse relation between the Δm^2_{41} parameter and the energy in the frequency term $\sin^2(\Delta m^2_{41} L/E)$. [79]

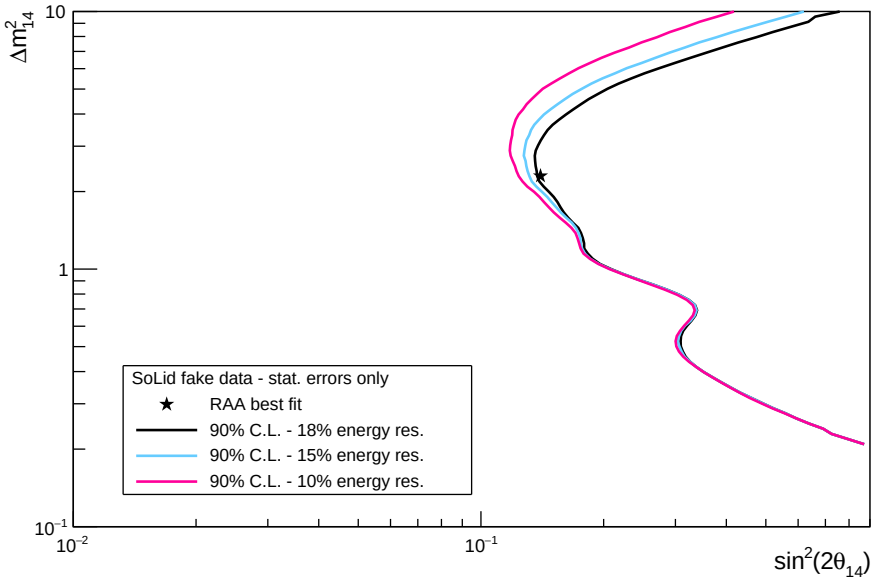

Figure 9.3: Example of the effect of an improved energy resolution on the sensitivity of the SoLid experiment. The used run time corresponds to 450 days, all other parameters are fixed at the Phase I values.

9.3.3 IBD efficiency

With an improved performance of the IBD selection methods, it is possible to increase the IBD detection efficiency. Of course, the trade-off between the selection of more signal events or the discrimination of more background events always remains.

The effect of a larger IBD efficiency is shown in figure 9.4. It is the same as that of increasing the run time, as both parameters affect the number of signal events and more events reduce the statistical uncertainty.

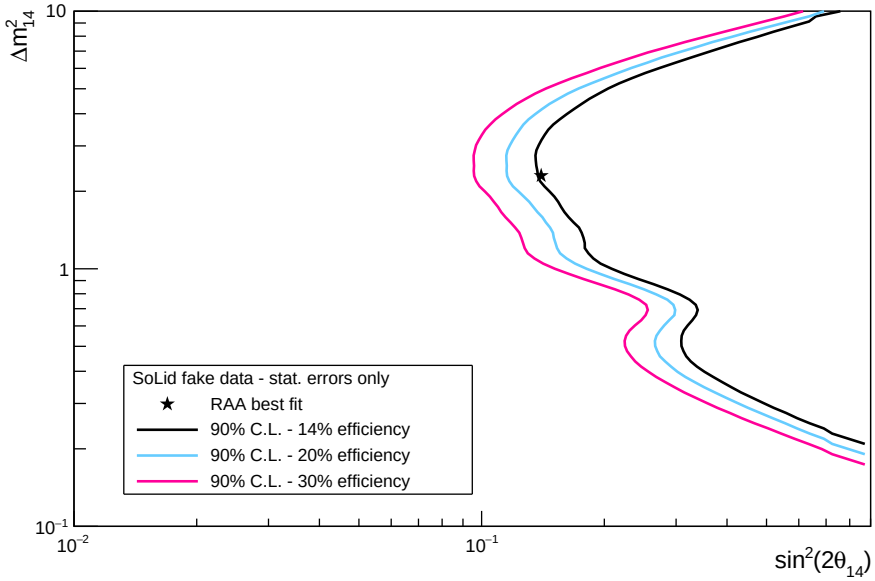

Figure 9.4: Example of the effect of an increased IBD efficiency on the sensitivity of the SoLid experiment. The used run time corresponds to 450 days, all other parameters are fixed at the Phase I values.

9.3.4 Signal-to-background ratio

With the Phase II upgrade, it is expected that the signal-to-background ratio can significantly be improved. Firstly, the possibility to lower the reconstruction thresholds is expected to increase the annihilation gamma reconstruction efficiency for the IBD signal. As a consequence, the MVA codes will be more discriminative between signal and background events. In addition, it is expected that, when the machinery is ready to take full advantage of the BiPonator tool, the BiPo background can be reduced by at least a factor 2. For a reduction of the atmospheric background component, the collaboration will optimise and implement the NS multiplicity and muon vetos.

Given these future prospects, a total signal-to-background ratio of 1 over 3 seems achievable. Figure 9.5 shows the impact of this improvement on the

sensitivity. As can be expected, the contour is again shifted towards lower values of $\sin^2(2\theta_{14})$, because the reduced number of background events for the same number of signal events improves the statistical uncertainty.

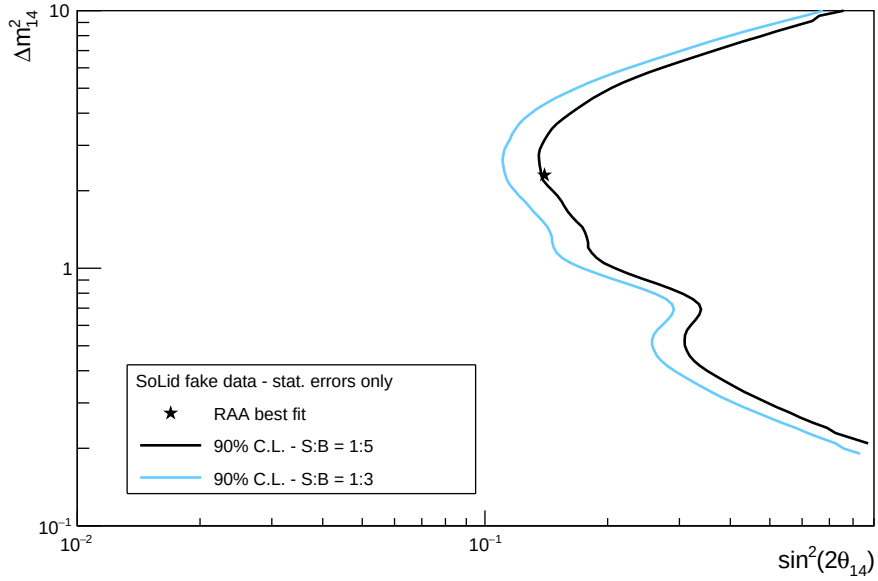

Figure 9.5: Example of the effect of a larger signal-to-background ratio on the sensitivity of the SoLid experiment. The used run time corresponds to 450 days, all other parameters are fixed at the Phase I values.

9.3.5 Position binning

Depending on the final gathered statistics, the choice of the binning in L_{reco} can be optimised. When the statistical uncertainties are small enough, a finer binning results in a higher precision on the frequency term $\sin^2(\Delta m^2_{41} L/E)$ and thus improves the sensitivity of the experiment to the Δm^2_{41} parameter.

Figure 9.6 shows the projected SoLid sensitivity for 450 days of reactor-ON data, with the Phase I energy resolution, IBD efficiency and signal-to-background parameters, for varying bin sizes in L_{reco}. The top plot is based on the relative fit method including the effect of correlated statistical uncertainties induced by this fit method. It can be seen that, in this case, a finer binning in L_{reco} worsens the sensitivity of the experiment.

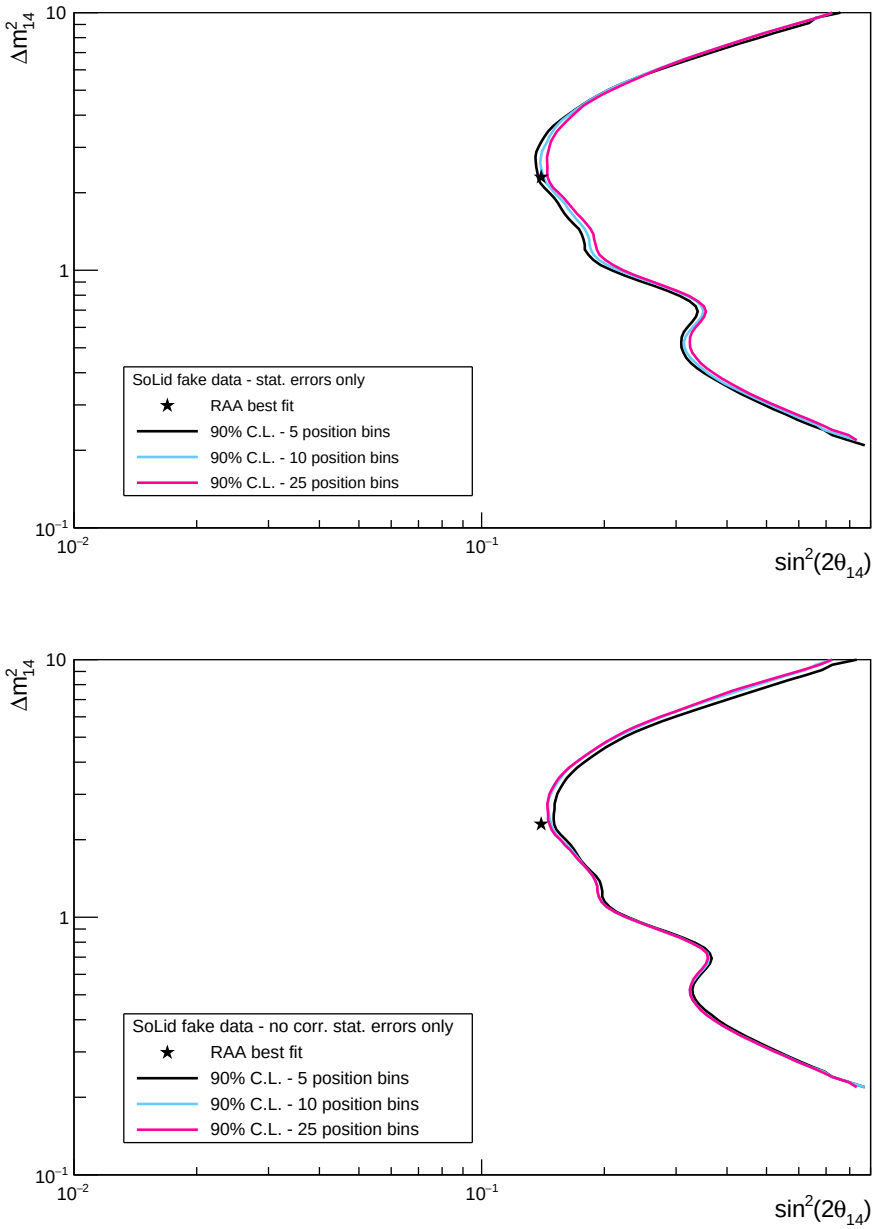

Figure 9.6: Example of the effect of different L_{reco}-binning on the sensitivity of the SoLid experiment, based on a relative fit including correlations between the statistical uncertainties (top) and without these correlation terms (bottom). The used run time corresponds to 450 days, all other parameters are fixed at the Phase I values.

This reduced sensitivity can be addressed to the correlation terms of the statistical uncertainties, which enlarge the effect of the reduced statistics per bin when spreading the events over a larger number of bins. This is confirmed by the results of the relative fit without the statistical correlation terms, that are shown in the bottom plot of figure 9.6. These results are less affected by statistical uncertainties and the expected, but small effect, where a finer binning improves the sensitivity to Δm^2_{41}, remains visible here.

We can thus conclude that for a final analysis, the choice of the binning in L_{reco} will have to be evaluated as a function of the available statistics and the systematic uncertainties, as a finer binning does not necessarily imply a better sensitivity.

9.4 Phase I + II sensitivity

The sensitivity contours shown above are each derived from one set of simulated data for which all parameter values were fixed. In reality, however, the SoLid collaboration will have to combine two datasets with different settings for both phases of the experiment. The combination of two sets for the calculation of the sensitivity limits can be done by simply adding the individual χ^2 values:

$$\chi^2_{I+II} = \chi^2_I + \chi^2_{II}. \tag{9.1}$$

This can be understood intuitively, as the addition of a second dataset is practically the same as the addition of extra data bins in the χ^2 sum. The $\Delta\chi^2$ value of the combined dataset can be calculated by searching for the minimal value of χ^2_{I+II} over the parameter grid. For the approach following Wilk's theorem, the critical value can be determined from a standard χ^2 distribution with 2 degrees of freedom. The production of toys of the combined dataset for the Feldman-Cousins approach is less trivial: it requires the simulation of individual toys from both datasets and individual χ^2 calculations and then a best fit scan for the summed χ^2_{I+II} values of each toy pair. A dedicated code that executes this process will have to be implemented in the SoLO framework.

An example of a combined Phase I+II sensitivity contour is shown in figure 9.7. The fake Phase II dataset is based on 150 days of reactor-ON data, with an IBD efficiency of 20%, a signal-to-background ratio of 1:3 and an energy resolution of 12%. One can see that this smaller Phase II fake dataset already shows a better sensitivity than the Phase I dataset of 350 days. This can be verified with a quick calculation of the statistics:

- The improved efficiency from an assumed 14% for Phase I to an assumed 20% for Phase II increases the statistics with a factor 1.43. The 150 days of Phase II are thus equivalent to 214 days with an efficiency of 14%.
- The effect of the reduced background contribution from 5-to-1 to 3-to-1 on the statistics can be deduced as follows: using the simplified calculation of the statistical uncertainties as described in section 7.3.1, we have

$$\begin{aligned} \sigma^2_{IBD} &= N_{IBD} + 2 \times N_{BG} \\ \text{and thus } \sigma^2_{IBD,I} &= N_{IBD} + 2 \times (5 \times N_{IBD,I}) \\ \text{and } \sigma^2_{IBD,II} &= N_{IBD,II} + 2 \times (3 \times N_{IBD,II}) \end{aligned} \tag{9.2}$$

  Using these equations we can deduce that the reduced statistical uncertainty of Phase II is comparable to increased signal statistics for Phase I:

$$\begin{aligned} N_{IBD} + 10 \times N_{IBD,I} &= N_{IBD,II} + 6 \times N_{IBD,II} \\ \text{or } N_{IBD,II} &= \frac{11}{7} N_{IBD,I} \end{aligned}$$

  The 214 days with an efficiency of 20% and S:B = 1:3 become 337 days of data with 20% efficiency and S:B = 1:5. At this point, the statistics of Phase I are already reached.
- In addition, the energy resolution is improved to 12%, which shows as a higher sensitivity to larger values of Δm^2_{41}, as explained in section 9.3.

We can conclude from this preliminary study of the combined Phase I and Phase II sensitivity that the SoLid experiment is expected to be able to reject or confirm the sterile neutrino hypothesis as the cause of the reactor antineutrino anomaly at 90% confidence level or more.

The current sensitivity and exclusion contours published by the STEREO and PROSPECT experiments, are shown in figure 9.8, as a reference. Taking into account the use of different confidence levels, it can be seen that these contours exclude a slightly larger part of the oscillation parameter space, compared to the SoLid Phase I+II combined sensitivity contour.

To obtain a competitive result, the SoLid collaboration will thus have to maximise the signal selection efficiency and reduce the background contamination as much as possible. In addition, the systematic uncertainties will need to be well-controlled, as the presented SoLid Phase I+II sensitivity projection is based on statistical uncertainties only.

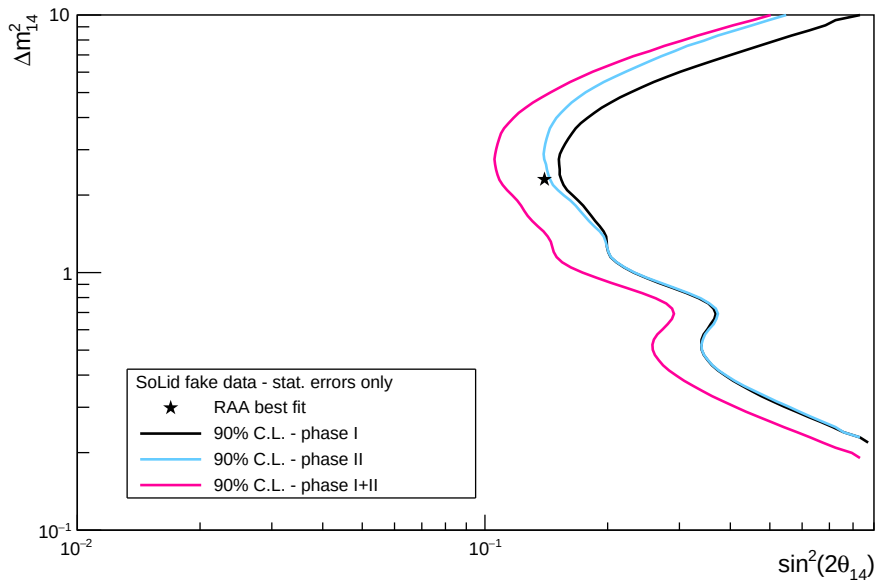

Figure 9.7: Example of a combined Phase I and Phase II sensitivity contour (pink), based on fake SoLid data. The individual Phase I (black) and Phase II (blue) contours are added for reference.

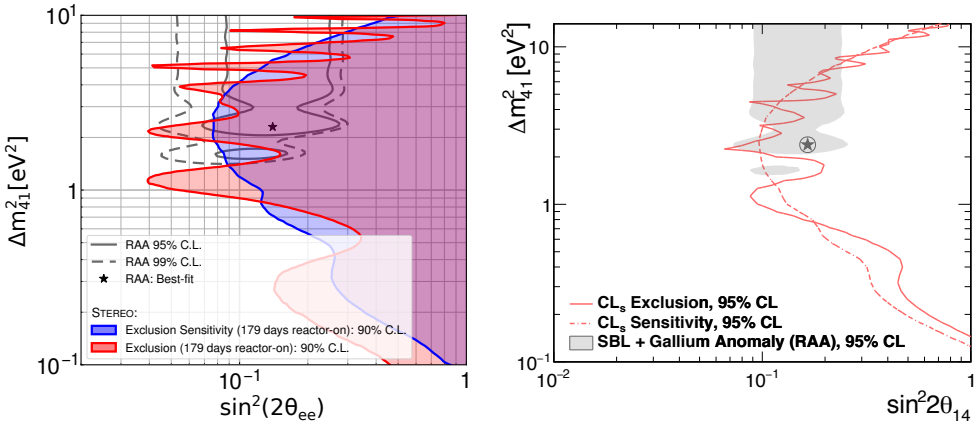

Figure 9.8: The current exclusion and sensitivity contours published by the STEREO experiment [87] (left) and PROSPECT experiment [85] (right).

9.5 Summary

In this chapter, we have presented the currently ongoing upgrade to the SoLid Phase II detector. We briefly discussed the expected improvements and gave an outlook on the resulting sensitivity of the SoLid experiment to the reactor antineutrino anomaly and the related sterile neutrino hypothesis.

Conclusion 10

Despite the enormous experimental progress that has been made since the first detection of the neutrino in 1956, this elementary particle is still not fully understood. Neutrino experiments using different sources have shown tensions with the current theoretical framework of 3 flavours of neutrinos oscillating into each other, and led to the so-called *accelerator, Gallium* and *reactor antineutrino anomalies*. One of the proposed solutions for these anomalies is that of the *light sterile neutrino* with a mass of about 1 eV, causing additional oscillations over relatively short distances.

To resolve the reactor antineutrino anomaly and evaluate the sterile neutrino solution, many new reactor neutrino experiments are developed to explore $\overline{\nu}_e$-oscillations at very short distances. One of these is the SoLid experiment, that operates at less than 10 m distance from the core of the BR2 reactor, at the SCK•CEN in Mol, Belgium. The SoLid detector principle is based on the detection of inverse beta decays (IBD) from antineutrino interactions, using small cells of a composite scintillator technology. The cells exist of $(5 \times 5 \times 5)$ cm^3 polyvinyl toluene (PVT) cubes for the detection of electromagnetic interactions and ^{6}LiF:ZnS(Ag) screens for the capture and detection of neutrons.

The full scale SoLid detector, called *Phase I*, exists of 12 800 of these detection cells and weighs about 1.6 tonne. It was constructed over the course of about 1 year from December 2016 to November 2017. Since the largest part of the detector construction took place at Ghent University, I was closely involved in the planning and organisation of this effort. I helped with the cube wrapping, plane assembly, quality assurance tests and the final installation of the Phase I modules in their container at the BR2 site. This installation was finished in the winter of 2017-2018 and since then, the Phase I detector has continuously been taking data until July 2020, when it was shut down for an

electronics update. In total, 373 days of data were gathered during operation of the BR2 reactor.

To be able to understand the recorded data and compare it with what is expected, a large set of simulation codes is needed. First, a full simulation of the fissions of the reactor fuel is needed to retrieve a predicted antineutrino flux and spectrum per reactor cycle. This information is provided to the SoLid collaboration by a team of reactor calculation specialists from the SCK•CEN and Subatech institutes. A dedicated code called *SoLO* that links this reactor information to the SoLid detector simulation was developed within the SoLid collaboration.

Then, when the antineutrino interactions in the SoLid detector material are generated, the SoLidSim code runs a simulation of the particle transport and interactions in the detector materials. This simulation takes into account all densities and geometrical information of the SoLid detector, the housing container and the BR2 reactor hall. Next, the response of the readout electronics to the detected light emissions from the particle interactions, as well as the signal reconstruction of the recorded waveforms are emulated by the ROsim code. For a fast application of the overall detector response to a set of simulated IBD interactions, an object called the *migration matrix* was trained. I have worked on the implementation of this object in the SoLO analysis framework and tested its performance and use in the data analysis.

All these simulation steps are needed to be able to predict the signature of the inverse beta decays in the SoLid detector. Given this signature, it is possible to define selection criteria which help to discriminate the antineutrino signal from a large amount of background events. The main sources of background for the SoLid experiment are atmospheric neutrons and radioactive *BiPo* decays.

With the use of machine learning codes some powerful signal-to-background discriminators were developed. By using these discriminators, in addition to rectangular cuts on the event topology, time coincidence, energy, etcetera, a signal excess of 106.27 ± 10.35 events/day can be reached. The statistical uncertainty is relatively large, due to the rather low signal-to-background ratio of about 1:5 in the current analysis.

In the final step of the SoLid analysis, the signal excess for a given dataset is compared to the predicted excess that is deduced from the full simulation of the corresponding reactor period. In practice, the quantitive comparison is based on the χ^2 goodness-of-fit parameter, taking into account all statistical and systematic uncertainties of the experiment. This analysis allows to reject or confirm the sterile neutrino hypothesis as underlying model of the recorded data.

The work of this thesis mainly existed in the development of the oscillation analysis framework. I have worked on the implementation of different χ^2 fit methods and the extension of the framework for the use of the Feldman-Cousins method. I have updated the sensitivity contours along the course of the experiment and tested the full oscillation analysis chain for the production of exclusion contours.

A first oscillation analysis, based on a small fraction of the SoLid Phase I dataset, was performed to test the readiness of the full analysis chain. To allow an oscillation analysis of the full dataset, a reprocessing of the data with the latest software versions and additional data quality studies are needed. In addition, a full evaluation of the systematic uncertainties is necessary to present a more precise result. The SoLid experiment expects to conclude the study of the SoLid Phase I dataset in the coming year.

The collaboration is currently also working on the installation of the Phase II detector, that will use upgraded photosensors with a higher light detection efficiency. The new photosensors are expected to increase the energy resolution and the overall IBD detection efficiency and reduce the background noise, resulting in an improved sensitivity of the SoLid experiment to sterile neutrino oscillations.

Nederlandstalige samenvatting

Ondanks de enorme experimentele vooruitgang die is geboekt sinds de eerste detectie van het neutrino in 1956, wordt dit elementaire deeltje nog steeds niet volledig begrepen. Neutrino-experimenten die gebruik maakten van verschillende bronnen hebben onenigheden aangetoond met het huidige theoretische model van 3 families van neutrino's die in elkaar oscilleren. Deze hebben geleid tot de zogenaamde *versneller*, *Gallium* en *reactor antineutrino* anomalieën. Eén van de voorgestelde oplossingen voor deze anomalieën is die van het lichte steriele neutrino met een massa van ongeveer 1 eV, dat extra oscillaties zou veroorzaken over relatief korte afstanden.

Om een verklaring te vinden voor de reactor antineutrino anomalie en om de hypothese van het steriele neutrino te evalueren, worden veel nieuwe reactor neutrino-experimenten ontwikkeld die antineutrino oscillaties op zeer korte afstanden kunnen onderzoeken. Eén daarvan is het SoLid experiment, dat opereert op minder dan 10 m afstand van de kern van de BR2-reactor, aan het SCK•CEN in Mol, België. Het SoLid detectorprincipe is gebaseerd op de detectie van invers beta-verval (IBV) veroorzaakt door antineutrino-interacties, en dit met behulp van kleine detectie-cellen gemaakt van scintillatiemateriaal. De cellen bestaan uit polyvinyl tolueen (PVT) kubusjes van $(5 \times 5 \times 5)$ cm^3, die dienen voor de detectie van elektromagnetische interacties, in combinatie met 2 plaatjes ^{6}LiF:ZnS(Ag) die dienen voor het invangen en detecteren van neutronen.

De eerste grootschalige SoLid detector, genaamd *Phase I*, bestaat uit 12 800 van deze detectie-cellen en weegt ongeveer 1.6 ton. Phase I werd gebouwd in ongeveer 1 jaar tijd, in de periode van december 2016 tot november 2017. Aangezien het grootste deel van de detectorconstructie plaatsvond aan de UGent, was ik nauw betrokken bij de organisatie en uitvoering van deze taak. Ik hielp mee met het samenstellen van de individuele kubusjes en van de detector frames, met het uitvoeren van kwaliteitstests en met de uiteindelijke installatie van de Phase I onderdelen in hun container op de BR2

site. Deze installatie werd voltooid in de winter van 2017-2018 en sindsdien heeft de Phase I detector continu data genomen tot juli 2020, toen hij werd uitgeschakeld voor een elektronica-update. In totaal werden 373 dagen aan gegevens verzameld tijdens de werking van de BR2-reactor.

Om de verzamelde data te kunnen begrijpen en te kunnen vergelijken met wat wordt verwacht zijn er meerdere simulatie codes nodig. Ten eerste is een volledige simulatie van de kernfissies in de reactor nodig om een voorspelling van de antineutrino-flux en -spectrum per reactorcyclus te maken. Deze informatie wordt aan de SoLid collaboratie verstrekt door een team van reactor-experten van de SCK•CEN en Subatech instituten. De SoLid collaboratie zelf heeft een speciale code ontwikkeld, SoLO genaamd, die deze reactorinformatie koppelt aan de simulatie van de SoLid detector.

Wanneer de antineutrino-interacties met het detectormateriaal worden gegenereerd, voert de SoLidSim-code een simulatie uit van het deeltjestransport en van de verschillende reacties van deze secundaire deeltjes met de detectormaterialen. Deze simulatie houdt rekening met alle dichtheden en geometrieën van de SoLid detector, de container errond en de BR2-reactorhal. Vervolgens worden de respons van de elektronica op de gedetecteerde lichtsignalen, evenals de reconstructie van de geregistreerde elektronische signalen gesimuleerd door de ROsim-code. Voor een snelle toepassing van de algehele detectorrespons op een reeks gesimuleerde IBV-interacties, werd een object genaamd de *migratiematrix* getraind. Ikzelf heb gewerkt aan de implementatie van dit object in de SoLO code en de prestaties en het gebruik ervan in de data-analyse procedure getest.

Al deze simulatiestappen zijn nodig om de kenmerkende eigenschappen van de inverse beta-vervallen in de SoLid detector te kunnen voorspellen. Door gebruik te maken van deze kenmerken is het mogelijk om selectiecriteria te definiëren die helpen om het antineutrino-signaal te onderscheiden van een grote hoeveelheid achtergrondruis. De belangrijkste bronnen van deze ruis voor het SoLid experiment zijn atmosferische neutronen en radioactief BiPo-verval.

Met behulp van machine learning-codes werden enkele krachtige discriminatoren ontwikkeld om signaal en achtergrondruis van elkaar te onderscheiden. Door deze discriminatoren te gebruiken samen met meer simpele selecties op basis van de topologie, tijdscoïncidentie, energie, e.d. van het event, kan boven de achtergrondruis een signaal onderscheiden worden van 106.27 ± 10.35 events/dag. De statistische onzekerheid op dit signaal is relatief groot vanwege de vrij lage signaal-tot-achtergrondverhouding in de huidige analyse van ongeveer 1 op 5.

In de laatste stap van de SoLid analyse wordt het resterende aantal IBV

events voor een bepaalde dataset vergeleken met de voorspelde hoeveelheid signaal die wordt afgeleid uit de volledige simulatie van de bijbehorende reactorperiode. In de praktijk is de kwantitatieve vergelijking gebaseerd op de χ^2 *goodness-of-fit* parameter, die ook alle statistische en systematische onzekerheden van het experiment in rekening brengt. Deze zogenaamde *oscillatie analyse* maakt het mogelijk om de steriele neutrino-hypothese te aanvaarden of te verwerpen als onderliggend model van de geregistreerde data.

Het werk van deze thesis bestond voornamelijk uit de ontwikkeling van de code voor de oscillatie analyse. Ik heb gewerkt aan de implementatie van verschillende χ^2 fit-methoden en de uitbreiding van het framework voor het gebruik van de Feldman-Cousins methode. Ik heb de verwachtingen voor de sensitiviteit van het experiment gedurende de vordering van het project bijgewerkt en de volledige oscillatie analyse-procedure getest op de productie van exclusie-contouren.

Een eerste oscillatie analyse, gebaseerd op een kleine fractie van de SoLid Phase I dataset, werd uitgevoerd om de gereedheid van de volledige analyse procedure te testen. Om een oscillatie-analyse van de volledige dataset mogelijk te maken, zijn een nieuwe verwerking van de data met de meest recente softwareversies en een aanvullende studie van de kwaliteit van de data nodig. Bovendien is een volledige evaluatie van de systematische onzekerheden nodig om een nauwkeuriger resultaat te presenteren. Naar verwachting zal de studie van de SoLid Phase I dataset binnen het volgende jaar worden afgerond.

De SoLid collaboratie werkt momenteel ook aan de installatie van de Phase II detector, die verbeterde fotosensoren met een hogere foton detectie-efficiëntie zal gebruiken. De nieuwe fotosensoren worden verondersteld de energieresolutie en de algemene IBV detectie-efficiëntie te verhogen en de achtergrondruis te verminderen, wat zal resulteren in een verbeterde gevoeligheid van het SoLid experiment voor steriele neutrino-oscillaties.

List of Abbreviations

A

- ADC: analogue-to-digital

B

- BDT: Boosted decision tree

C

- Calipso: Calibration per plane for SoLid
- CL: Confidence level
- CROSS: Calibration on site SoLid

D

- DAQ: Data acquisition

E

- EB: Electronics box
- EM: Electromagnetic
- ES: Electromagnetic Signal

H

- HEU core: Highly enriched uranium core
- HDPE: High density polyethylene

I

- IBD: Inverse beta decay
- ID: Identification
- IonA: Integral-on-amplitude

L

- LWR: Light water reactor
- LY: Light yield

M

- MC: Monte Carlo
- MCNP: Monte Carlo N-Particle
- ML-EM: Maximum Likelihood Expectation-Maximisation
- MM: Migration Matrix
- MPPC: Multi-pixel photon counter
- MVA: Multivariate analysis
- m.w.e.: metre water equivalent

N

- n.d.o.f. : number of degrees of freedom
- NN: Neural network
- NS: Nuclear signal

O

- OV: Over voltage

P

- PA: Pixel avalanche
- PDE: Photon detection efficiency
- p.d.f.: probability density function
- PMNS matrix: Pontecorvo Maki Nakagawas Sakata matrix
- PoT: Peak over threshold
- PVT: Polyvinyl toluene

Q

- QCD: Quantum chromodynamics

R

- RAA: Reactor antineutrino anomaly
- ROsim: Readout simulation

S

- Saffron2: SoLid analysis framework, version 2
- SBL: Short baseline
- SDQM: SoLid Data Quality Monitor
- SiPM: Silicon Photomultiplier
- SM: Standard Model of particle physics

- SM1: SubModule 1
- SoLid: Search for Oscillations with a ^{6}Li detector

V

- VSBL: Very short baseline

W

- WLS fibres: Wavelength shifting fibres

List of Figures

List of Tables

Bibliography

[1] K. Harrison. "Discovering particles: fundamental building blocks of the Universe". In: *http://www.ep.ph.bham.ac.uk/* (2019).

[2] Wikipedia. "Standard Model". In: *https://en.wikipedia.org/wiki/Standard_Model/* (2020).

[3] F. Englert and R. Brout. "Broken Symmetry and the Mass of Gauge Vector Mesons". In: *Phys. Rev. Lett.* 13 (9 Aug. 1964), pp. 321–323.

[4] Peter W. Higgs. "Broken Symmetries and the Masses of Gauge Bosons". In: *Phys. Rev. Lett.* 13 (16 Oct. 1964), pp. 508–509.

[5] P.W. Higgs. "Broken symmetries, massless particles and gauge fields". In: *Physics Letters* 12.2 (1964), pp. 132–133. ISSN: 0031-9163.

[6] ATLAS Collaboration. "Observation of a new particle in the search for the Standard Model Higgs boson with the ATLAS detector at the LHC". In: *Phys. Lett. B* 716 (2012), pp. 1–29.

[7] CMS Collaboration. "Observation of a new boson at a mass of 125 GeV with the CMS experiment at the LHC". In: *Phys. Lett. B* 716 (2012), p. 30.

[8] A. Bettini. *Introduction to elementary particle physics*. 6th ed. Cambridge, 2008.

[9] S. M. Bilenky. "Neutrino. History of a unique particle". In: *arXiv: 1210.3065* (2012).

[10] F. Reines and C. Cowan. "The Reines-Cowan Experiments: Detecting the Poltergeist". In: *Los Alamos Science* 25 (1997), pp. 4–27.

[11] F. Reines et al. "Detection of the free antineutrino". In: *Phys. Rev.* 117 (1960), p. 159.

[12] L.Lederman et al. "Observation of High-Energy Neutrino Reactions and the Existence of Two Kinds of Neutrinos". In: *Phys. Rev. Letters* 9 (1962).

[13] M. L. Perl. "The new particles produced in electron-positron annihilation". In: *SLAC-PUB-1652* (1975).

[14] DONUT collaboration. "Observation of tau neutrino interactions". In: *Phys. Lett. B* 504 (2000), pp. 218–224.

[15] H. Burkhardt and J. Steinberger. "Tests of the electroweak theory at the Z resonance". In: *Ann. Rev. Nucl. Part. Sci.* 41 (1991), pp. 55–96.

[16] B. Povh et al. *Particles and Nuclei: An Introduction to the Physical Concepts*. Graduate Texts in Physics. Springer Berlin Heidelberg, 2015. ISBN: 9783662463215.

[17] R. Davis, Jr. and D. S. Harmer and K. C. Hoffman. "Search for neutrinos from the sun". In: *Phys. Rev. Lett.* 20 (1968), p. 1205.

[18] John N. Bahcall. "Solar neutrinos. I: Theoretical". In: *Phys. Rev. Lett.* 12 (1964), pp. 300–302.

[19] K. S. Hirata et al. "Observation of ^{8}B solar neutrinos in the Kamiokande-II detector". In: *Phys. Rev. Lett.* 63.1 (1989), p. 16.

[20] GALLEX Collaboration. "Final results of the ^{51}Cr neutrino source experiments in GALLEX". In: *Phys. Lett. B* 420.1 (1998), pp. 114–126.

[21] J. N. Abdurashitov et al. "The Russian-American gallium experiment (SAGE) Cr neutrino source measurement". In: *Phys. Rev. Lett.* 77 (1996), p. 4708.

[22] R. Clark et al. "Atmospheric Muon Neutrino Fraction above 1 GeV". In: *Phys. Rev. Lett.* 79 (3 July 1997), pp. 345–348.

[23] K. S. Hirata et al. "Observation of a small atmospheric muon-neutrino / electron-neutrino ratio in Kamiokande". In: *Phys. Lett.* B280 (1992), pp. 146–152.

[24] The Super-Kamiokande Collaboration, Y. Fukuda et al. "Evidence for oscillation of atmospheric neutrinos". In: *Phys. Rev. Lett.* 81 (1998), pp. 1562–1567.

[25] The University of Tokyo Kamioka Observatory ICRR (Institute for Cosmic Ray Research). "Neutrino and Neutrino Oscillations". In: *http://www-sk.icrr.u-tokyo.ac.jp/sk/sk/neutrino-e.html* (2020).

[26] The SNO Collaboration. "Measurement of Charged Current Interactions Produced by 8B Solar Neutrinos at the Sudbury Neutrino Observatory". In: *Phys. Rev. Lett.* 87.071301 (2001).

[27] B. Pontecorvo. "Neutrino Experiments and the Problem of Conservation of Leptonic Charge". In: *Sov. Phys. JETP* 26 (1968), pp. 984–988.

[28] S. Eidelman et al. “Particle Data Group - The Review of Particle Physics”. In: *Phys. Lett. B* 592 (revised 2005), chapter 13.

[29] D. Perkins. *Particle Astrophysics*. Oxford University Press, 2013.

[30] C. Giunti and M. Laveder. *Neutrino Mixing*. 2004. arXiv: `hep-ph/0310238v2 [hep-ph]`.

[31] S. Adrián-Martínez et al. “Letter of intent for KM3NeT 2.0”. In: *Journal of Physics G: Nuclear and Particle Physics* 43 (Jan. 2016).

[32] S.P. Mikheyev and A. Yu. Smirnov. “Resonance enhancement of oscillations in matter and solar neutrino spectroscopy”. In: *Soviet Journal of Nuclear Physics* 42 (1985).

[33] L. Wolfenstein. “Neutrino oscillations in matter”. In: *Phys. Rev. D.* 17 (1978).

[34] P. A. Zyla et al. (Particle Data Group). *The Review of Particle Physics*. To be published in Prog. Theor. Exp. Phys. 2020, 083C01. (2020).

[35] LSND Collaboration. “Evidence for $\bar{\nu}_\mu \to \bar{\nu}_e$ oscillations from the LSND Experiment at the Los Alamos Meson Physics Facility”. In: *Phys. Rev. Lett.* 77 (1996), p. 3082.

[36] B. Armbruster et al. “Upper limits for neutrino oscillations $\overline{\nu}_\mu \to \overline{\nu}_e$ from muon decay at rest”. In: *Phys. Rev. D* 65 (11 June 2002), p. 112001.

[37] A. A. Aguilar-Arevalo et al. (MiniBooNE Collaboration). “Search for electron neutrino appearance at the $\delta m^2 \sim \text{eV}^2$ scale”. In: *Phys. Rev. Lett.* 98.23 (2007).

[38] A. A. Aguilar-Arevalo et al. (MiniBooNE Collaboration). “Event excess in the MiniBooNE search for $\bar{\nu}_\mu \to \bar{\nu}_e$ oscillations”. In: *Phys. Rev. Lett.* 105 (2010), p. 181801.

[39] A. A. Aguilar-Arevalo et al. “Significant Excess of Electronlike Events in the MiniBooNE Short-Baseline Neutrino Experiment”. In: *Phys. Rev. Lett.* 121 (22 Nov. 2018), p. 221801.

[40] J. N. Abdurashitov et al. “Measurement of the response of a Ga solar neutrino experiment to neutrinos from a ^{37}Ar source”. In: *Phys. Rev. C* 73 (4 Apr. 2006), p. 045805.

[41] F. Kaether et al. “Reanalysis of the Gallex solar neutrino flux and source experiments”. In: *Physics Letters B* 685.1 (2010), pp. 47–54. ISSN: 0370-2693.

[42] J. Kostensalo et al. “The gallium anomaly revisited”. In: *Physics Letters B* 795 (Aug. 2019), pp. 542–547. ISSN: 0370-2693.

[43] C. Giunti and T. Lasserre. "eV-Scale Sterile Neutrinos". In: *Annual Review of Nuclear and Particle Science* 69.1 (2019), pp. 163–190. eprint: https://doi.org/10.1146/annurev-nucl-101918-023755.

[44] M. Thomson. *Modern particle physics*. Cambridge University Press, 2015.

[45] The Daya Bay Collaboration. "Observation of Electron-Antineutrino Disappearance at Daya Bay". In: *Phys. Rev. Letters* 108 (2012).

[46] F. P. An et al. "New measurement of θ_{13} via neutron capture on hydrogen at Daya Bay". In: *Phys. Rev. D* 93 (7 Apr. 2016), p. 072011.

[47] Y. Abe et al. "Measurement of θ_{13} in Double Chooz using neutron captures on hydrogen with novel background rejection techniques". In: *Journal of High Energy Physics* 2016.1 (2016), p. 163.

[48] RENO Collaboration. "Observation of Reactor Electron Antineutrinos Disappearance in the RENO Experiment". In: *Phys. Rev. Lett.* 108 (2012), p. 191802.

[49] S. H. Seo et al. "Spectral measurement of the electron antineutrino oscillation amplitude and frequency using 500 live days of RENO data". In: *Phys. Rev. D* 98 (1 July 2018), p. 012002.

[50] S. Abe et al. "Precision Measurement of Neutrino Oscillation Parameters with KamLAND". In: *Phys. Rev. Lett.* 100 (22 June 2008), p. 221803.

[51] Y. Declais et al. "Study of reactor anti-neutrino interaction with proton at Bugey nuclear power plant". In: *Phys.Lett. B* 338 (1994).

[52] J.L. Vuilleumier et al. "New Limits on Oscillation Parameters for Electron Anti-neutrinos". In: *Phys.Lett. B* 114 (1982).

[53] H. Kwon et al. "Search for neutrino oscillations at a fission reactor". In: *Phys. Rev. D* 24 (5 Sept. 1981), pp. 1097–1111.

[54] A.A. Kuvshinnikov et al. "Measuring the anti-electron-neutrino + p $\rightarrow$ n + e cross-section and beta decay axial constant in a new experiment at Rovno NPP reactor". In: *JETP Lett.* 54 (1991), pp. 253–257.

[55] K. N. Abazajian et al. "Light sterile neutrinos: A white paper". In: *arXiv:1204.5379* (2012).

[56] Double Chooz Collaboration. "Improved measurements of the neutrino mixing angle θ_{13} with the Double Chooz detector". In: *JHEP* 10 (2014), p. 086.

[57] J. H. Choi et al. "Observation of Energy and Baseline Dependent Reactor Antineutrino Disappearance in the RENO Experiment". In: *Phys. Rev. Lett.* 116 (21 May 2016), p. 211801.

[58] D. Adey et al. "Extraction of the U235 and Pu239 Antineutrino Spectra at Daya Bay". In: *Physical Review Letters* 123.11 (Sept. 2019). ISSN: 1079-7114.

[59] G. Bak et al. "Fuel-Composition Dependent Reactor Antineutrino Yield at RENO". In: *Physical Review Letters* 122.23 (June 2019). ISSN: 1079-7114.

[60] C. Buck et al. "Investigating the spectral anomaly with different reactor antineutrino experiments". In: *Physics Letters B* 765 (Feb. 2017), pp. 159–162. ISSN: 0370-2693.

[61] P. Huber. "NEOS data and the origin of the 5 MeV bump in the reactor antineutrino spectrum". In: *Phys. Rev. Lett.* 118 (2017), p. 042502.

[62] J. I. Crespo-Anadón. "Double Chooz: Latest results". In: *Nucl. Part. Phys. Proc.* 265-266 (2015), pp. 99–104. arXiv: 1412.3698 [hep-ex].

[63] M. G. Aartsen et al. "An eV-scale sterile neutrino search using eight years of atmospheric muon neutrino data from the IceCube Neutrino Observatory". In: *arXiv:2005.12942* (2020). arXiv: 2005.12942 [hep-ex].

[64] SCK•CEN. *BR2: Research reactor with multiple applications*. SCK•CEN, 2011.

[65] John Lilley. *Nuclear Physics: Principles and Applications*. John Wiley & Sons Ltd, 2001.

[66] SCK•CEN. "BR2 refurbishment operation". In: *https://science.sckcen.be/* (2015).

[67] The SoLid Collaboration. "A novel segmented-scintillator antineutrino detector". In: *arXiv:1703.01683* (2017).

[68] G. F. Knoll. *Radiation detection and measurement*. Wiley, 2000.

[69] Eljen Technology. "GENERAL PURPOSE: EJ-200, EJ-204, EJ-208, EJ-212". In: *www.eljentechnology.com* (2016).

[70] Scintacor. "Neutron screens". In: *https://scintacor.com/* (2015).

[71] Dupont. "DUPONT TYVEK® 1082D". In: *https://www.dupont.com/* (2020).

[72] Saint-Gobain. "Plastic Scintillating Fibers". In: *https://www.crystals.saint-gobain.com* (2019).

[73] Hamamatsu. "MPPC (multi-pixel photon counter)". In: *https://www.hamamatsu.com/* (2018).

[74] Celine Moortgat. "The SoLid antineutrino detector: construction and commissioning with cosmic ray muons". PhD thesis. UGent, 2018.

[75] The SoLid Collaboration. "Performance of a full scale prototype detector at the BR2 reactor for the SoLid experiment". In: *JINST* (2018).

[76] Y. Abreu et al. "Commissioning and operation of the readout system for the SoLid neutrino detector". In: *Journal of Instrumentation* 14.11 (Nov. 2019), P11003–P11003.

[77] Y. Abreu et al. "Optimisation of the scintillation light collection and uniformity for the SoLid experiment". In: *Journal of Instrumentation* 13.09 (Sept. 2018), P09005–P09005.

[78] Y. Abreu et al. "SoLid: A short baseline reactor neutrino experiment". In: (2020). arXiv: 2002.05914 [physics.ins-det].

[79] S. Vercaemer. "Commissioning of the SoLid experiment for the observation of electron antineutrinos at the BR2 reactor". PhD thesis. UAntwerpen, VUB, 2018.

[80] Paul Adamson. *A general quantum mechanical method to predict positron spectroscopy*. Jan. 2007.

[81] Y. Abreu et al. "Development of a quality assurance process for the SoLid experiment". In: *Journal of Instrumentation* 14.2 (2019), P02014–P02014.

[82] V. Pestel. "Détection de neutrinos auprès du réacteur BR2: analyse des premières données de l'expérience SoLid". PhD thesis. Université de Caen Normandie, 2019.

[83] A. P. Serebrov et al. "First Observation of the Oscillation Effect in the Neutrino-4 Experiment on the Search for the Sterile Neutrino". In: *JETP Letters* 109.4 (2019), pp. 213–221.

[84] PROSPECT Collaboration. "PROSPECT—A Precision Oscillation and Spectrum Experiment". In: *https://prospect.yale.edu/* (2018).

[85] M. Andriamirado et al. *Improved Short-Baseline Neutrino Oscillation Search and Energy Spectrum Measurement with the PROSPECT Experiment at HFIR*. 2020. arXiv: 2006.11210 [hep-ex].

[86] H. Almazán et al. "Sterile Neutrino Constraints from the STEREO Experiment with 66 Days of Reactor-On Data". In: *Phys. Rev. Lett.* 121 (16 Oct. 2018), p. 161801.

[87] H. Almazán et al. "Improved sterile neutrino constraints from the STEREO experiment with 179 days of reactor-on data". In: *Phys. Rev. D* 102 (5 Sept. 2020), p. 052002.

[88] I. Alekseev et al. "DANSS: Detector of the reactor AntiNeutrino based on Solid Scintillator". In: *Journal of Instrumentation* 11.11 (Nov. 2016), P11011–P11011.

[89] Y. J. Ko et al. "Sterile Neutrino Search at the NEOS Experiment". In: *Phys. Rev. Lett.* 118 (12 Mar. 2017), p. 121802.

[90] I. Alekseev et al. "Search for sterile neutrinos at the DANSS experiment". In: *Physics Letters B* 787 (Dec. 2018), pp. 56–63. ISSN: 0370-2693.

[91] S. Gariazzo et al. "Model-independent $\bar{\nu}_e$ short-baseline oscillations from reactor spectral ratios". In: *Physics Letters B* 782 (July 2018), pp. 13–21. ISSN: 0370-2693.

[92] M. Dentler et al. "Updated global analysis of neutrino oscillations in the presence of eV-scale sterile neutrinos". In: *Journal of High Energy Physics* 2018.8 (2018), p. 10.

[93] C. Giunti. "Statistical significance of reactor antineutrino active-sterile oscillations". In: *Phys. Rev. D* 101 (9 May 2020), p. 095025.

[94] M. Danilov. "New results from the DANSS experiment". In: EPS-HEP. July 2019.

[95] K.-H Schmidt et al. "Benefits of extended capabilities of the driver accelerator for EURISOL". In: *Physical Review Special Topics - Accelerators and Beams* 10 (Jan. 2007), p. 014701.

[96] D. Lhuillier. *Reactor Neutrino Spectra and Sterile Neutrino Searches*. Seminar given at Ghent University. Feb. 2019.

[97] J. van Muiden. *Determination of the Accuracy and Precision of BR2*. Tech. rep. University of Antwerp, 2015.

[98] A. C. Hayes and P. Vogel. "Reactor Neutrino Spectra". In: *Annual Review of Nuclear and Particle Science* 66.1 (2016), pp. 219–244. eprint: `https://doi.org/10.1146/annurev-nucl-102115-044826`.

[99] D. B. Pelowitz et al. *MCNPX 2.7.0 Extensions*. LA-UR-11-02295. LANL. 2011.

[100] F. X Gallmeier et al. "The CINDER 90 transmutation code package for use in accelerator applications in combination with MCNPX". In: ICANS XIX. 2010.

[101] M. Fallot S. Kalcheva and L. Giot. *BR2 reactor simulation and antineutrino spectrum - Status*. Private communication. 2019.

[102] S. Kalcheva et al. “Reactor Core Simulations for Determination of the Antineutrino Spectrum for the SoLid Experiment at BR2 Reactor”. In: *M& C 2017*. International Conference on Mathematics Computational Methods Applied to Nuclear Science Engineering. Jeju, Korea, 2017.

[103] M. Fallot, L. Giot, and S. Kalcheva. *The BR2 reactor simulation and antineutrino spectrum status*. Private communication. 2019.

[104] T. A. Mueller et al. “Improved predictions of reactor antineutrino spectra”. In: *Phys. Rev. C* 83 (2011), p. 054615.

[105] N. Haag et al. “Re-publication of the data from the BILL magnetic spectrometer: The cumulative β spectra of the fission products of ^{235}U, ^{239}Pu, and ^{241}Pu”. In: (May 2014). arXiv: `1405.3501 [nucl-ex]`.

[106] N. Haag et al. “Experimental Determination of the Antineutrino Spectrum of the Fission Products of ^{238}U”. In: *Phys. Rev. Lett.* 112 (12 Mar. 2014), p. 122501.

[107] P. Huber. “Determination of antineutrino spectra from nuclear reactors”. In: *Physical Review C* 84.2 (Aug. 2011). ISSN: 1089-490X.

[108] M. Estienne et al. “Updated Summation Model: An Improved Agreement with the Daya Bay Antineutrino Fluxes”. In: *Phys. Rev. Lett.* 123 (2 July 2019), p. 022502.

[109] A.A. Sonzogni and E.A. McCutchen. *Development of Cumulative Fission Yield Covariances for Uncertainty Quantification*. Presented at WANDA 2020 conference.

[110] Particla Data Group. “CKM Quark-Mixing Matrix”. In: *http://pdg.lbl.gov/2019/reviews/rpp2018-rev-ckm-matrix.pdf* (2019).

[111] P. Vogel and J. F. Beacom. “Angular distribution of neutron inverse beta decay,$\overline{\nu}_e + p \rightarrow e^+ + n$”. In: *Physical Review D* 60.5 (July 1999). ISSN: 1089-4918.

[112] L. Kalousis. *Anti-neutrino signal generation with SoLO*. Private communication. 2018.

[113] A. Kurylov, M.J. Ramsey-Musolf, and P. Vogel. “Radiative corrections to low-energy neutrino reactions”. In: *Phys. Rev. C* 67 (2003), p. 035502. arXiv: `hep-ph/0211306`.

[114] P. Vogel. “Analysis of the antineutrino capture on protons”. In: *Phys. Rev. D* 29 (9 May 1984), pp. 1918–1922.

[115] G. Lehaut, B. Guillon, and the Reactor Group. “Reactor Simulation For SoLid”. In: *SoLid Technical note* (2020).

[116] S. Agostinelli et al. "Geant4—a simulation toolkit". In: *Nuclear Instruments and Methods in Physics Research Section A: Accelerators, Spectrometers, Detectors and Associated Equipment* 506.3 (2003), pp. 250–303. ISSN: 0168-9002.

[117] J.R. Granada et al. "Thermal neutron cross section and transport properties of polyethylene". In: *Nuclear Instruments and Methods in Physics Research Section A: Accelerators, Spectrometers, Detectors and Associated Equipment* 261.3 (1987), pp. 573–578. ISSN: 0168-9002.

[118] *ISO. Reference neutron radiations - part 1 : Characteristics and methods of production.* Tech. rep. ISO, Feb. 2001.

[119] D. et al. Wright. "Monte Carlo Simulation of Proton-induced Cosmic-ray Cascades in the Atmosphere". In: *http://nuclear.llnl.gov/simulation/doc_cry_v1.7* (2018).

[120] M. Guan et al. "A parametrization of the cosmic-ray muon flux at sea-level". In: *arXiv:1509.06176* (Sept. 2015). arXiv: 1509.06176 [hep-ex].

[121] D. Reyna. "A simple parameterization of the cosmic-ray muon momentum spectra at the surface as a function of zenith angle". In: *arXiv:hep-ph/0604145* (2006).

[122] M. Gordon et al. "Measurement of the flux and energy spectrum of cosmic-ray induced neutrons on the ground". In: *Nuclear Science, IEEE Transactions on* 51 (Jan. 2005), pp. 3427–3434.

[123] J B Birks. "Scintillations from Organic Crystals: Specific Fluorescence and Relative Response to Different Radiations". In: *Proceedings of the Physical Society. Section A* 64.10 (Oct. 1951), pp. 874–877.

[124] H. Chanal et al. "The CCube Algorithm". In: *SoLid Technical note* (2020).

[125] CERN. "ROOT". In: *root.cern.ch* (2018).

[126] L. Koch. *ReMU - Response Matrix Utilities*. http://github.com/ast0815/remu.

[127] UC Berkeley. "Nuclear Forensic Search Project". In: *http://metadata.berkeley.edu/nuclear-forensics* (2020).

[128] K. Graves. *Further discrimination of BiPo*. Private communication. 2019.

[129] V. Buridon et al. "Deployment of a 1D-CNN reduces further the BiPo background over the current PSD method". In: *Neutrino2020 Conference* (2020).

[130] J. Stevens and M. Williams. "uBoost: a boosting method for producing uniform selection efficiencies from multivariate classifiers". In: *Journal of Instrumentation* 8.12 (Dec. 2013), P12013–P12013. ISSN: 1748-0221.

[131] A. Rogozhnikov and contributors. "hep_ml documentation". In: *https://arogozhnikov.github.io/hep_ml/#hep-ml-documentation* (2020).

[132] A. Hoecker et al. *TMVA - Toolkit for Multivariate Data Analysis*. 2007. arXiv: physics/0703039 [physics.data-an].

[133] D. Hefnaff. *Status of the SoLid experiment*. Private communication. 2020.

[134] G. Vandierendonck. *The background subtraction method*. Private communication. 2020.

[135] K.A. Olive. "Review of Particle Physics". In: *Chinese Physics C* 40.10 (Oct. 2016), p. 100001.

[136] G. L. Fogli et al. "Getting the most from the statistical analysis of solar neutrino oscillations". In: *Physical Review D* 66.5 (Sept. 2002). ISSN: 1089-4918.

[137] Alekhin Sergey. *Statistical properties of the estimator using covariance matrix*. 2000. arXiv: hep-ex/0005042 [hep-ex].

[138] "Cholesky decomposition". In: *https://en.wikipedia.org/wiki/Cholesky_decomposition* ().

[139] S.S. Wilks. "The Large-Sample Distribution of the Likelihood Ratio for Testing Composite Hypotheses". In: *Annals Math. Statist.* 9.1 (1938), pp. 60–62.

[140] J. M. Conrad and M. H. Shaevitz. "Sterile Neutrinos: An Introduction to Experiments". In: *arXiv:1609.07803* (2016). arXiv: 1609.07803 [hep-ex].

[141] G. J. Feldman and R. D. Cousins. "Unified approach to the classical statistical analysis of small signals". In: *Physical Review D* 57.7 (1998), pp. 3873–3889. ISSN: 1089-4918.

[142] L. N. Kalousis and S. Vercaemer. *SoLid sensitivity contours*. Private communication. 2017.

[143] Pranava Teja Surukuchi. "Search for sterile neutrino oscillations with the PROSPECT experiment". PhD thesis. Illinois Institue of Technology, May 2019.

[144] G. Vandierendonck. *Discussion on the improved subtraction method*. Private communication.

[145] Hamamatsu. "MPPC (multi-pixel photon counter) - S14160/S14161 series". In: *https://www.hamamatsu.com/* (2019).

[146] G. Vandierendonck. *The MPPC upgrade tests*. Private communication. 2019.